Electron Transport in Single Molecule Transistors

by

Jiwoong Park

B.S. (Seoul National University) 1996

A dissertation submitted in partial satisfaction of the

requirements for the degree of

Doctor of Philosophy

in

Physics

in the

GRADUATE DIVISION

of the

UNIVERSITY OF CALIFORNIA, BERKELEY

Committee in charge:

Professor Paul L. McEuen, Co-chair
Professor John Clarke, Co-chair
Professor Steven G. Louie
Professor A. Paul Alivisatos

Fall 2003

Electron Transport in Single Molecule Transistors

Copyright © 2003

by

Jiwoong Park

Abstract

Electron Transport in Single Molecule Transistors

by

Jiwoong Park

Doctor of Philosophy in Physics

University of California, Berkeley

Professor Paul L. McEuen, Co-chair

Professor John Clarke, Co-chair

Electron transport through single molecules is strongly affected by single-electron charging and the energy level quantization. In this thesis, we investigate electron transport in single molecule transistors made with several different molecules, including fullerene molecules (C_{60}, C_{70} and C_{140}) and single Co molecules with different lengths. To perform transport measurements on these small (<3 nm) molecules, electrodes with a gap that is 1~2 nm wide are fabricated using the electromigration-junction technique. We also studied single-walled carbon nanotube devices that are fabricated using a more conventional method.

At low temperatures, most single molecule devices exhibit Coulomb blockade with discrete conductance peaks that correspond to quantum excitations of the molecule. The origin of the observed quantum excitation varies from molecule to molecule depending on how tunneling electrons interact with various molecular degrees of freedom. Vibrational excitation is the one that is most frequently observed. The most prominent vibrational excitation was identified as the bouncing-ball mode in C_{60} and C_{70} transistors, whereas it was assigned to the intercage stretching mode in C_{140} transistors. Magnetic excitation was also studied, and the spin state of a single Co molecule was determined by analyzing the Zeeman splitting in a magnetic field.

The overall conductance of single molecule transistors is determined mainly by the coupling with electrodes. In single Co transistors, the coupling could be controlled by changing the length of insulating handles. With a longer handle, the conductance is lower as the single Co forms a quantum dot. With a shorter handle, the coupling between

Co and electrodes as well as the overall conductance becomes large and the Kondo effect was observed.

Finally, the conductance of carbon nanotubes was studied in two different temperature regimes. At low temperatures, they form a single quantum dot (p-doped) or a double quantum dot (n-doped) due to a local doping by the electrodes. In room temperature measurements, a highly efficient electrolyte gate was used to investigate the field effect transistor properties of carbon nanotubes, which unveiled excellent device performances.

To my parents

Table of Contents

Acknowledgements

Several people deserve additional comments. First, special thanks to Hongkun, who gave me lots of good lessons from the early days till now. I cherish the crazy days (and nights) spent in the lab with him at Berkeley. Also many thanks to Abhay, who, with his cheerful manners and creative energy, kept my days at Clark Hall very pleasant and fun. Many chapters of this thesis are the results of the wonderful collaboration with him. I thank my dear friend Michael as well. He impresses me in many ways inside and outside of the lab with his talent in cooking and singing, just to name a few.

I also want to acknowledge some other members of my very special "support system." I had lots of fun with my old friends who all happened to be living in the Bay Area. Especially, Seokhwan, Eunsun, Haktae and Jinbaek all paid many visits to my place to keep me entertained and happy throughout my days at Berkeley.

Special thanks, of course, go to my family. My dear Dad and Mom, with their usual positive advice and unceasing love, gave me the strength to finish this work. Without their support and love, I cannot be here finishing up this thesis. I also thank my cheerful brother Chulwoong, who supported me through his quiet but very warm caring. I am also deeply indebted to EoJean's family for their strong support and love. I thank my parents-in-law for lending me their wisdom and insight in many occasions.

Finally, my warmest thanks to my wife, EoJean. Without her love and support, this thesis cannot exist. Through her creative energy and witty insights, she has made my life full of excitement and joy. Thank you and I love you, EoJean.

Chapter 1

Introduction and Background

1.1 Introduction: Electron Transport in Nanoscale Systems

Electrical conductance of a macroscopic object is described by the well-known Ohm's law. The conductance (G) of a rectangular conductor is proportional to its width (W) and inversely proportional to its length (L). Namely,

$$G = \frac{\sigma W}{L} \tag{1.1}$$

Here σ is the conductivity of the conductor, which is decided mainly by the charge carrier density and the mean free path.

As the conductor gets smaller, several effects that are negligible in a macroscopic conductor become increasingly important. In a very small object such as nanostructures and molecules, electron transport usually does not follow Ohm's law. There are several reasons why Ohm's law fails at such exceedingly small scale. First, the size is smaller than the mean free path. Thus electron transport is not a diffusive process as described by Ohm's law. Instead, it is in a ballistic conduction regime, where a charge carrier experiences no scattering within the conductor. Second, the contact between macroscopic electrodes and the nanoscale conductor strongly affects the overall conductance. Depending on the properties of the contact, the overall transport behavior can be very different and hence understanding the nature of the contact is extremely important. Third, a nanoscale object has a large charge addition energy and a quantized excitation spectrum. Both of these strongly affect electron transport especially at low temperatures.

Studying transport behaviors of these extremely small objects is a very interesting scientific problem, and it also has many practical implications, especially to the microelectronic industry. In recent years, studying electron transport in nanoscale objects has become one of the most active fields in condensed matter physics and also attracted huge research efforts from various other disciplines of science. To date, many nanoscale

systems have been investigated, including solid-state nanostructures[1-3] as well as chemical nanostructures such as carbon nanotubes[4-6] and nanocrystals[7, 8]. Transport measurements on such systems displayed a plethora of exciting new behaviors that cannot be explained within the framework of the conventional macroscopic theory. The subject of this thesis is also to study electron transport in nanoscale objects, especially the devices made from single molecules.

1.2 Electron Transport in a Single Molecule Device

Single molecules as an active electronic unit have attracted huge attention both from the research community and industry[9-11]. Single molecules can offer several unique properties as an electronic unit. The size is within several nanometers for most simple molecules and hence the electronic spectrum is quantized with the typical energy scale of ~ eV. They also allow self-assembly, which is very useful in fabricating electronic devices at such a small length scale. Another huge advantage is their tremendous diversity and functionality. There exist an incredibly large number of chemicals and their different chemical and electrical functions can open up many new possibilities that have never been available.

In this section, we will first review the history of this field briefly and then discuss a model that describes electron transport in single molecule devices.

Short history

Molecules were first proposed as an active electronic unit by Aviram and Ratner[12] in 1973. They proposed that one can expect a current rectifying behavior from a certain types of molecules that are represented by D-σ-A, where D represents an electron-donor unit with a large ionization energy, A represents an electron-acceptor unit with a large electron affinity and σ is a conducting molecular bridge that connects D with A. In such molecules, the zwiterionic state D^{+}-σ-A^{-} is expected to be energetically more accessible than D^{-}-σ-A^{+}, which will lead to an asymmetric current-bias curve. Other types of molecules for key electronic units are also proposed, including molecular wires and molecular switches. Reviews on such candidate molecules can be found in other references[10, 11, 13, 14].
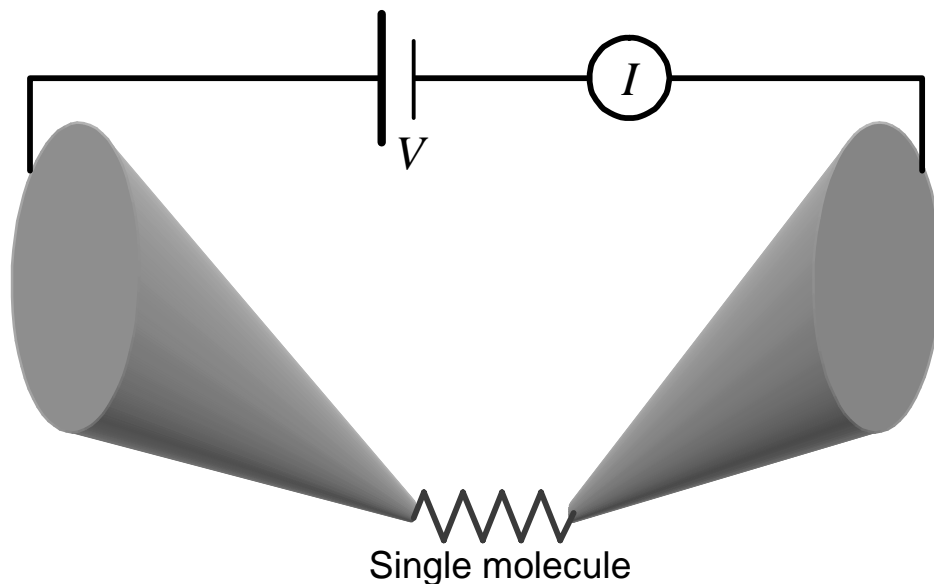
Figure 1.1 Conductance measurement of a single molecule. A bias is applied between the electrodes while the current flowing through the molecule is measured.

Electron transport measurements on single molecules require what is, in principle, a relatively simple experimental scheme (Figure 1.1). A molecule is contacted by two macroscopic metal electrodes. These electrodes are connected to outside equipment for measuring the current and voltage. To measure the conductance, one applies a bias voltage (*V*) between the electrodes and then measures the current (*I*) flowing through the device.

However, molecular-scale transport measurements could be performed only after necessary experimental techniques were developed. The advent of the scanning probe microscopy (SPM) techniques such as scanning tunneling microscopy (STM) and atomic force microscopy (AFM) allowed the conductance measurements down to a single molecule level[15, 16]. The development of nanolithography techniques also led to the fabrication of nanoscale electrodes, which can be used to "wire up" multiple or single molecules. Most early experiments were two-terminal measurements and observed interesting conduction behaviors such as the electromechanical current amplification[14], oxidation-induced negative differential resistance[17] and logic gates[18].

In these earlier experiments, current versus voltage (*I-V*) curves were measured at relatively high bias voltages to add (subtract) extra charges to (from) the molecules, or a molecule was subjected to a significant mechanical deformation to form a good contact.

Such experimental conditions, even though they allow observation of interesting behaviors, are expected to strongly perturb the original electronic structure of a molecule and hinder one from performing a careful study on electron transport through a handful of well-defined quantum molecular levels.

Sequential electron tunneling in single molecule devices

One regime that allows a careful study on electron transport through well-defined quantum molecular states is the sequential tunneling limit. In this regime, electric current in single molecule devices flows by the sequential tunneling process described below.

First, we draw the energy landscape of a single molecule device as illustrated in Figure 1.2. Electronic levels of the electrodes are filled up to the electrochemical potential (Fermi level) of each electrode that is represented by μ_S and μ_D (S and D denote source and drain). The electrodes are connected to an outer circuit, which controls the difference between μ_S and μ_D using the bias voltage V. The relation between them is $\mu_S - \mu_D = eV$, where e is the electron charge ($e = -1.602 \times 10^{-19}$ C). To reflect the quantum nature of the electronic structure, we represent available electronic states of the molecule using several discrete lines. The physical meaning (electrochemical potential) of these lines will be carefully defined in the following section. All the states below μ_S and μ_D are occupied by an electron and all the electronic states above μ_S and μ_D are
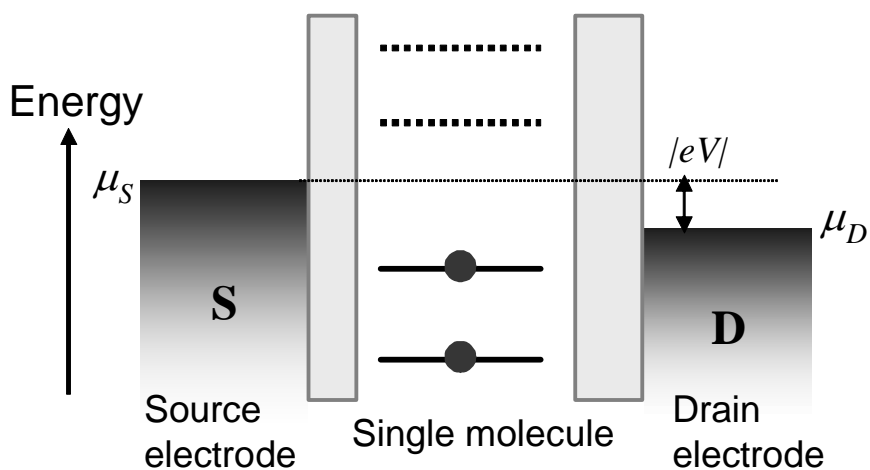
Figure 1.2 Schematic diagram of the energy landscape of a single molecule between two macroscopic electrodes. Electronic levels of the molecule are represented by discreet lines. The electronic levels whose energy is below electrode Fermi levels (μ_S and μ_D) are occupied by an electron (red dot).

empty. The contact between the molecule and an electrode is represented by a barrier that separates them.

We assume that the barrier at either contact is opaque enough that it serves as a tunnel barrier. Then an electron can be considered located either on the molecule or one of the electrodes. Electric current will flow when an electron can tunnel onto the molecule and subsequently off from it to the other electrode. When a state is available between μ_S and μ_D, the sequential tunneling process can occur via this state while changing the number of electrons on the molecule between *N* and *N*+1. A large current will flow in this case ("on" state). On the other hand, when there are no available states between μ_S and μ_D, the current will be blocked and the number of electrons *N* on the molecule is fixed. Only a small current will flow in this case by a direct tunneling between the two electrodes ("off" state).

The "on" and "off" behavior is caused by the quantized electronic structure of a molecule. This quantized structure can be attributed to two main reasons – the charge addition energy and the electronic excitation spectrum. To illustrate how these affect electron transport in single molecules, we will first review the single electron transistor theory in the following section.

The model presented here assumes that the contacts are behaving as tunnel barriers. Even though some molecules can be connected to the leads without forming a tunnel barrier at the contacts[19, 20], the single molecule devices described in this thesis forms tunnel contacts and their electrical conductance can be explained based on the sequential tunneling process.

1.3 Single Electron Transistor Theory

The theory of a single electron transistor (SET) can be found in several review papers on this topic[21-25]. We will follow a similar path that has been used by Kouwenhoven *et al*.[26]

Figure 1.3 shows a device schematic of a single electron transistor, where a dot is surrounded by three electrodes. All three electrodes are coupled to the dot capacitively; a potential change in any of them can cause an electrostatic energy change in the dot. Only
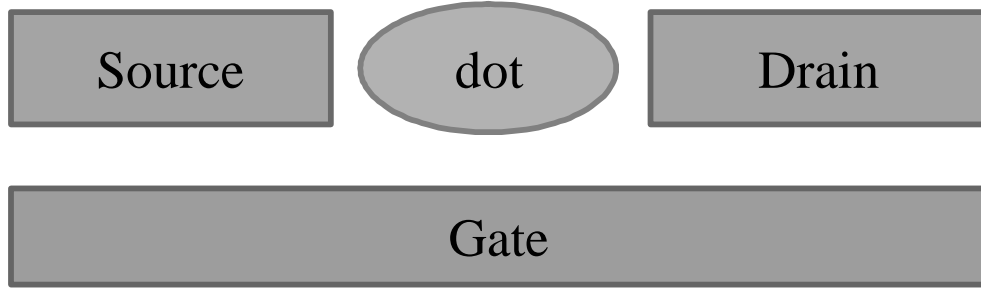
Figure 1.3 The single electron transistor. A small dot is separated from the source and drain electrodes by tunnel barriers. It is also coupled to the gate electrode capacitively.

two electrodes (source and drain) are tunnel coupled to the dot and electron transport is allowed only between the dot and these two electrodes. Since the dot is connected to the source and drain electrodes by a tunnel barrier (meaning an electron is either on the dot or one of the electrodes), the number of electrons on the dot, N is well defined. We assume that all interactions between an electron on the dot and all other electrons on the dot or on the electrodes can be parameterized by the total capacitance C. We also assume that C does not depend on different charge states of the dot. Then the total electrostatic energy for a dot with N electrons will become $Q^2/2C = (Ne)^2/2C$.

When N electrons reside on the dot, the total energy is $U(N) = \sum_{i=1}^{N} E_i + (Ne)^2/2C$. After an additional electron is added to the dot, the total energy increases to $U(N+1) = \sum_{i=1}^{N+1} E_i + ((N+1)e)^2/2C$. Here E_i is the chemical potential of the dot with i electrons. This is the energy of the orbital of the dot that the i-th electron would occupy if there were no electron-electron interactions. The electrochemical potential μ_N is then,

$$\mu_N \equiv U(N) - U(N-1) = E_N + (N-1/2)e^2/C. \qquad (1.2)$$

By definition, the electrochemical potential μ_N is the minimum energy required for adding N-th electron. As long as μ_N is below both μ_S and μ_D, the N-th electron will be added to the dot. Likewise, to add one more electron to a dot with N electrons, $\mu_{N+1} = \mu_N + e^2/C + \Delta E$ needs to be lower than both μ_S and μ_D, where $\Delta E = E_{N+1} - E_N$. For simplicity, we will assume that ΔE does not change for different charge states of the dot. This allows us to drop the subscript N for ΔE. Therefore, the $N+1$-th electron needs to have an energy larger than the one for the N-th electron by $e^2/C + \Delta E$. This is

the charge addition energy. The first term $e^2/C \equiv E_C$, which is called the charging energy, is the energy that is required to overcome the Coulomb repulsion among different electrons. The second term ΔE is the result of quantized excitation spectrum of the dot.

Figure 1.4(a) illustrates the energy diagram of a single electron transistor with $\mu_{N+1} > \mu_S, \mu_D > \mu_N$. The dot will have N electrons and the solid lines below μ_N represent all the filled electrochemical levels. The lowest dotted line represents μ_{N+1} and it cannot be occupied since it is above the electrode Fermi levels. Therefore, the dot is stable with N electrons and hence the current cannot flow through the dot. In other words, the current is "blocked" due to the charge addition energy. Figure 1.4(b) illustrates another case where $\mu_D > \mu_{N+1} > \mu_S$. In this case, the $N+1$-th electron can be
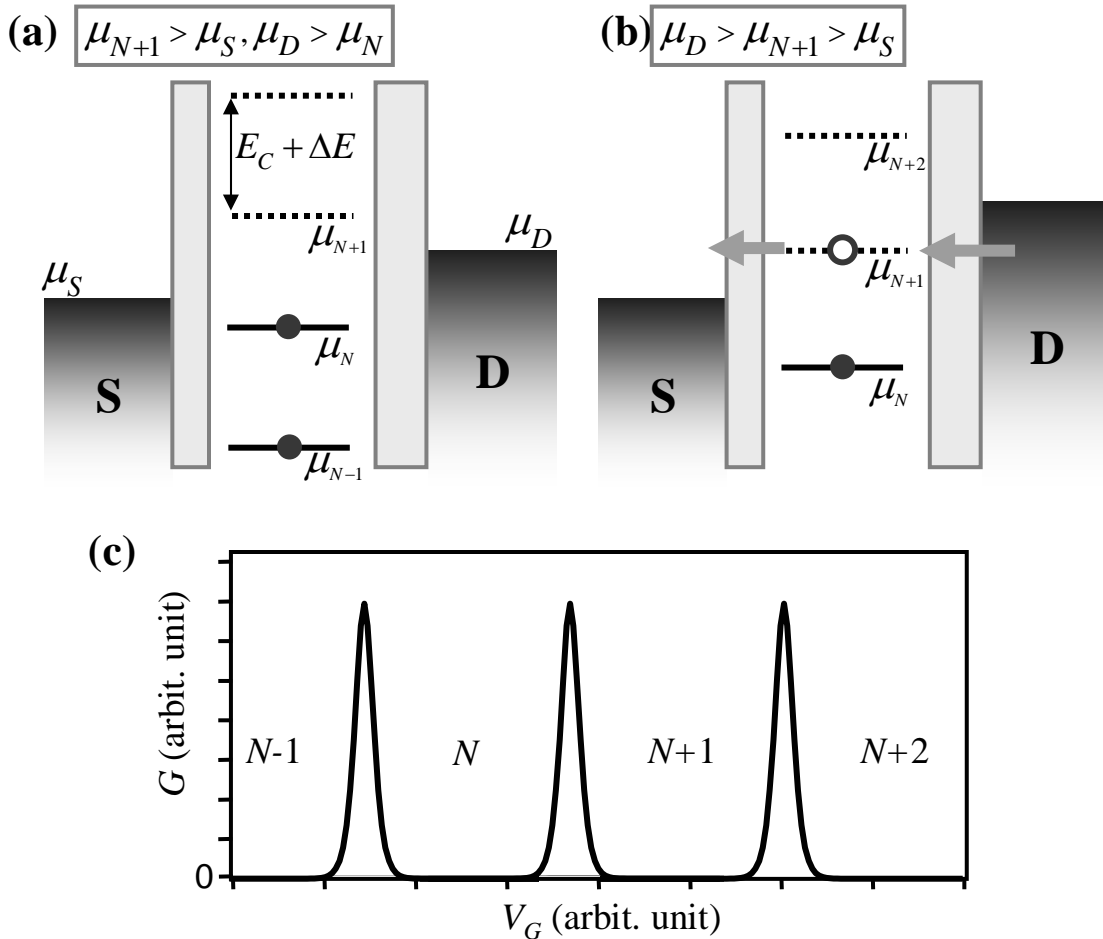
Figure 1.4 Electron transport in a single electron transistor. Energy diagrams for two different energy configurations are shown. In (a), the number of electrons on the dot is fixed at N ("off"-state) and the current is blocked. In (b), the electron number on the dot oscillates between N and $N+1$ ("on"-state). (c) The linear conductance (G) as a function of the gate bias (V_G) displays the Coulomb oscillation. Each conductance valley is labeled by the number of electrons on the dot.

added from the drain and then it can leave to the source electrode. This process allows electric current to flow by constantly switching the charge state of the dot between *N* and *N+1*.

When we sweep the gate voltage V_G, the electrochemical potential of the dot changes linearly with V_G and this allows one to change the number of electrons on the dot. Equation (1.2) will be later modified in Chapter 2 to include this gate effect. The conductance (*G*) as a function of V_G at a low bias is illustrated in Figure 1.4(c). The conductance curve shows a series of peaks as well as valleys of low conductance. In the valleys, the number of electrons on the dot is fixed and the current is blocked by the charge addition energy $e^2/C + \Delta E$. This corresponds to the case depicted in Figure 1.4(a). The dot has a well-defined electron number in each valley; *N*, *N+1*, *N+2* and so on. The conductance peak in this plot corresponds to the case depicted in Figure 1.4(b), where the dot can oscillate between two adjacent charge states. For example, the conductance peak located between the *N*-electron valley and the (*N+1*)-electron valley represents the dot carrying current by oscillating between *N* and *N+1* electron states. These conductance peaks are called Coulomb oscillations.

To be able to observe Coulomb oscillations, the charge addition energy should be much larger than the thermal energy $k_B T$. Otherwise, thermal fluctuation effect will be dominant and the Coulomb oscillation will disappear. Also the electron number on the quantum dot should be a well-defined observable, which requires the contact between the dot and the leads to be resistive. Quantitatively, the contact resistance needs to be larger than the resistance of a single conductance channel (*e.g.* a point contact), $h/e^2 \sim 25.81 k\Omega$. These conditions are summarized below.

$$e^2/C + \Delta E >> k_B T \tag{1.3}$$

$$R_{contact} >> h/e^2 \tag{1.4}$$

To date, single electron transport behavior has been observed from many different nanostructures. They include metallic nanoparticles[27], semiconductor heterostructures [28, 29], carbon nanotubes[30, 31] and semiconducting nanocrystals[8]. More recently, similar behaviors were observed from devices made from single molecules[32-34].

1.4 The Charging Energy and Excitation Spectrum in a Single Molecule Device

Electron transport in many single molecule devices can be described based on the SET theory we just described. Figure 1.5 shows various small molecules that we have successfully incorporated into a single electron transistor. To illustrate how this theory can be used to understand electron transport in single molecules, let's first study the electronic structure of a fullerene molecule, C_{60}.

Figure 1.6 shows the electronic level structure of an isolated neutral C_{60} and its anion C_{60}^{1-} calculated using a density functional method[35]. In both charge states, the electronic levels display a quantized and non-uniform structure. In neutral C_{60}, there is a 1.65 eV HOMO-LUMO energy gap. Here HOMO and LUMO represent the highest occupied molecular orbital and the lowest unoccupied molecular orbital, respectively. In the language of the SET theory, this corresponds to the energy splitting $\Delta E(C_{60} \rightarrow C_{60}^{1-})$ for the C_{60} to C_{60}^{1-} charge state transition. When looking at C_{60}^{1-}, the highest electronic
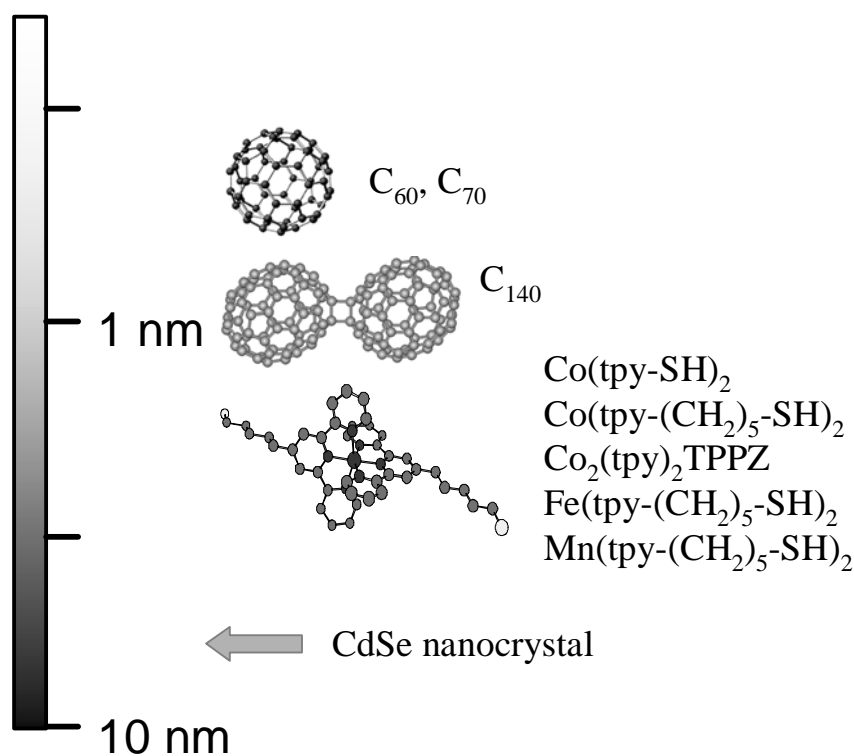
Figure 1.5 Various molecules measured using the SET geometry. All of them are smaller than 3 nm. For comparison, the size of the CdSe nanocrystal (5.5 nm) that was measured in a previous experiment (Klein, *et al.*, *Nature* **389**, 699 (1997)) is marked.
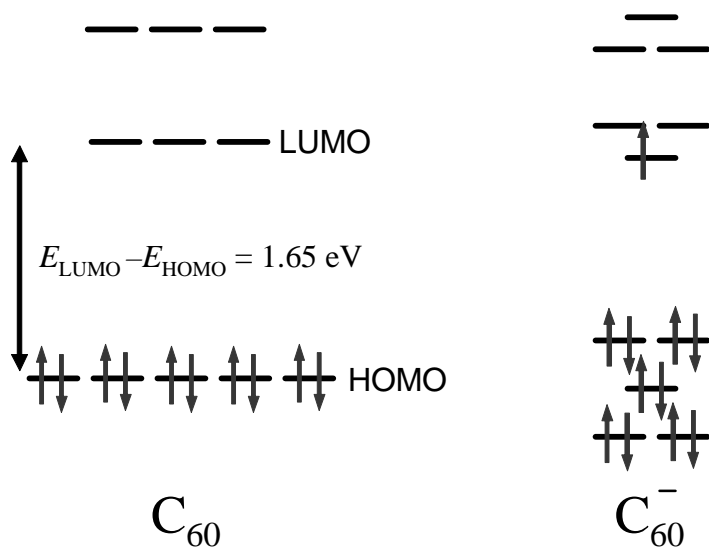
Figure 1.6 Electronic level structure of C_{60} and C_{60}^- calculated using the density functional method. Only the levels near the HOMO-LUMO gap are shown in this figure. (from Green *et al.*, *J. of Phys. Chem.* **100**, 14892 (1996))

level is occupied by only one electron and hence the next electron can occupy the same orbital. Thus, $\Delta E(C_{60}^{1-} \rightarrow C_{60}^{2-})$ will become zero. This clearly shows that the electronic excitation energy (or level splitting) ΔE changes according to the specific charge state transition. However, neither for C_{60} nor for C_{60}^{1-}, the electrochemical potential can be determined from the individual electronic level calculations shown in Figure 1.6.

Instead, an electrochemical potential needs to be obtained from the total energy difference between the two charge states involved, using $\mu_N = U(C_{60}^{N-}) - U(C_{60}^{(N-1)-})$. The first ionization energy and the electron affinity of a neutral C_{60} is ~ 7.7 eV[36] and 2.7 eV[35] each. By the definition of an ionization energy and electron affinity, these correspond to,

$$\mu_0 = U(C_{60}) - U(C_{60}^{1+}) \approx -7.7 \text{ eV (ionization energy)}$$
$$\mu_1 = U(C_{60}^{1-}) - U(C_{60}) \approx -2.7 \text{ eV (electron affinity)}$$

(1.5)

Here the reference energy is the energy of a free electron infinitely away from the C_{60} molecule. The electrochemical potential (Fermi energy) of gold is about –5 eV[37]. Therefore, if we assume that electron transport is allowed between a C_{60} molecule and a gold electrode located far away from C_{60}, electrons will be transferred to C_{60} until it

reaches the neutral charge state, and then the charge transfer will stop because $\mu_1 > \mu_{gold} > \mu_0$. The energy diagram of this case is shown in Figure 1.7(a).

The difference between the two C_{60} electrochemical potentials in equation (1.5) is 5.0 eV. According to the SET theory discussed in the previous section, it comprises two parts, the charging energy E_C and the electronic level splitting ΔE. Since $\Delta E(C_{60} \rightarrow C_{60}^{1-}) = 1.65$ eV (the HOMO-LUMO gap of C_{60}), it leaves approximately 3.3 eV for E_C. In comparison, the charging energy ($e^2 / 4\pi\varepsilon_0 R$) of a metal sphere with a radius (R) of 4 Å (the outer radius of C_{60}) is roughly 3.6 eV, which is in good agreement with the value obtained above. From the electronic structure of C_{60}^{1-}, we previously inferred $\Delta E(C_{60}^{1-} \rightarrow C_{60}^{2-}) = 0$, and hence we expect that $\mu_2 = U(C_{60}^{2-}) - U(C_{60}^{1-})$ is larger than μ_1 only by E_C. The calculated electron affinity of C_{60}^{1-} is -0.2 eV[35], corresponding to $\mu_2 \approx 0.2$ eV. This value is larger than $\mu_1 \approx$ -2.7 eV by 2.9 eV, which gives another estimate for E_C. It is 12 % smaller than the previous estimate 3.3 eV, but the model seems to work reasonably well considering its simplicity.
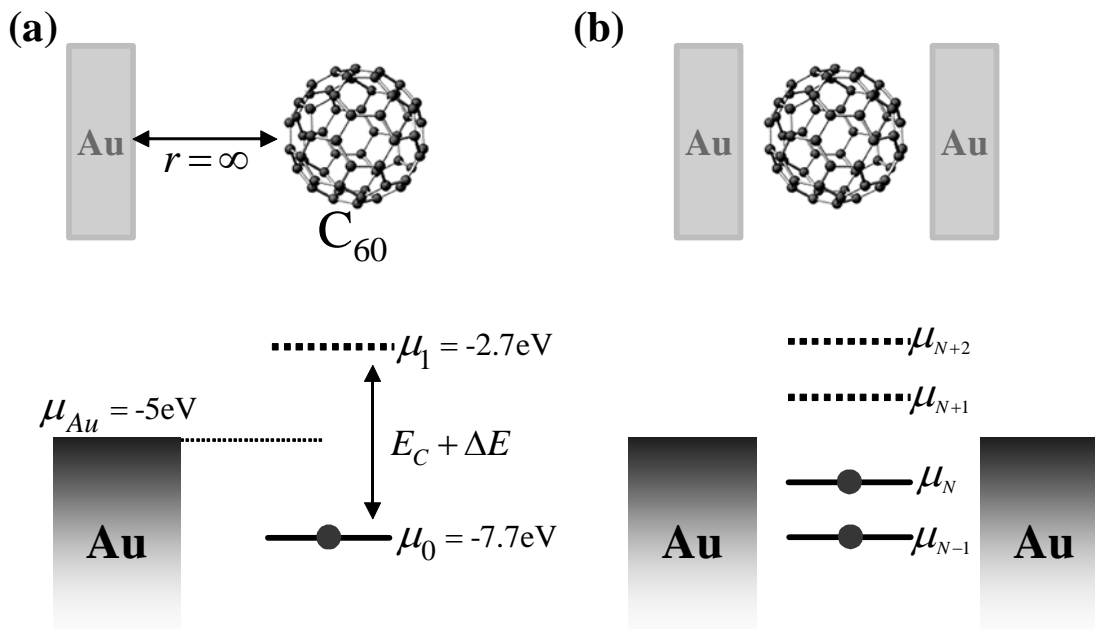
Figure 1.7 The electrochemical potential of C_{60} in different charge states. (a) When C_{60} is located far away from gold, the electrochemical potential for its neutral charge state is below the Fermi level of gold. (b) When C_{60} is located near gold electrodes, the energy spacing between neighboring electrochemical potentials becomes smaller due to the molecule-electrode interaction. The stable charge state of C_{60} is not necessarily neutral in this case.

The energy landscape described above is for a C_{60} located far from gold electrodes. As C_{60} moves closer to the electrodes, its electrochemical potentials will be modified due to the electron-electron interaction between C_{60} and gold. Most importantly, the presence of gold near C_{60} will increase the total capacitance, leading to a smaller charging energy. The lower bound on the charging energy in this case can be obtained using the capacitance ($4\pi\varepsilon_0/(1/r_1 - 1/r_2)$) of two metallic shells, whose radii are r_1 and r_2, respectively. The inner shell represents C_{60}, while the outer shell represents the gold electrodes. When r_1 is 4 Å and the second shell is 10 Å apart (r_2 = 14 Å), the charging energy is calculated to be 2.6 eV, 1 eV smaller than the charging energy of a single metallic shell, 3.6 eV. As the second shell moves much closer to the inner shell (r_2 = 5 Å), the charging energy further decreases to 0.7 eV.

These estimates can be even smaller when one uses high dielectric constant when estimating the total capacitance. Indeed, a similar mechanism affects the electrochemical redox-potential measurements of C_{60} when it is performed in a high dielectric medium. The spacing between adjacent redox potentials, which corresponds to $\Delta\mu$, decreases significantly in such measurements[35] because the high dielectric constant diminishes the charging energy.

Therefore, the energy diagram of C_{60} with gold electrodes nearby (Figure 1.7(b)) will be different from the one shown in Figure 1.7(a). The spacing between chemical potentials is smaller and each chemical potential will shift accordingly. As a result, the stable charge state of C_{60} is not necessarily neutral in this case. In fact, several experiments suggest that C_{60} can be in its (1-) charge state when it is deposited on a gold surface[38].

This C_{60} example teaches us that the energy landscape of a single molecule device cannot be inferred directly from a calculated or measured molecular electronic structure for a certain charge state. One needs to compare various electrochemical potentials, which can be obtained from electron affinity or ionization energies measured for an isolated molecule. To get a correct picture, one should also take into account the interactions between the molecule and the surrounding environment, especially the metal electrodes. However, very useful information can be still obtained from the electronic structure of an isolated molecule. One example is the HOMO-LUMO gap. When the

molecule shows a large HOMO-LUMO gap (let's say, larger than 5 eV) for its neutral charge state, one can expect a very low conductance from the molecule since the electrode Fermi level will be most likely located within the gap. This behavior will not change even when the charging energy becomes smaller due to the molecule-electrode interaction. Such interaction changes only E_C strongly, but not ΔE.

1.5 Examples of Single Molecule Devices

In this section, we discuss transport properties of several single molecule devices. These examples will show us how the general description developed in previous sections can be used in real single molecule devices. Each example will also bring up different aspects of electron transport in single molecule devices.

(1) Electron tunneling in alkanedithiol

The monolayer of alkanedithiol, HS-$(CH_2)_n$-SH (Figure 1.8(a)) is a well-known insulator and its insulating behavior is caused by its large HOMO-LUMO gap (~ 9 eV for decanedithiol[39]). Regarding the contact, alkanedithiol strongly binds to gold thanks to a strong S-Au bond (binding energy ~ 2 eV[9]). Recently, Cui *et al.*[40] successfully measured the resistance of a single octanedithiol (HS-$(CH_2)_8$-SH) molecule using a gold coated AFM tip as one of the electrodes. The measured resistance is 900 ± 50 MΩ, a large resistance for such a short molecule (~ 1 nm). This large resistance is consistent with its energy landscape (Figure 1.8(a)). Due to the large HOMO-LUMO gap, there is no available charge state (or its electrochemical potential) near the Fermi level of the electrodes. Therefore, the main conduction mechanism in this molecular junction is a direct electron tunneling between the source and drain electrodes.

(2) Single electron tunneling in [Co(tpy-$(CH_2)_5$-SH)$_2$]$^{2+}$

Unlike alkanedithiols, this molecule with a single cobalt atom (Figure 1.8(b)) has an electrochemical potential $\mu(Co^{3+} \rightarrow Co^{2+})$ near the Fermi level (μ_S, μ_D) of gold electrodes. The additional electron that is added to the molecule at its (3+) charge state is, however, highly localized near the cobalt atom at the center of the molecule, and hence it needs to tunnel from one of the electrodes to the cobalt ion. $\mu(Co^{3+} \rightarrow Co^{2+})$

(a) alkanedithiol

LUMO

S   D

Au-S-(CH$_2$)$_8$-S-Au

(b) [Co(tpy-(CH$_2$)$_5$-SH)$_2$]

Co

S   D

Gate

Co^{2+}/Co^{3+}

S

D

(c)

Carbon
nanotube

S   D

Gate

good
contact

S   D

e^-

$G \approx 4e^2 / h$

tunnel
Contact
(SET)

S

D
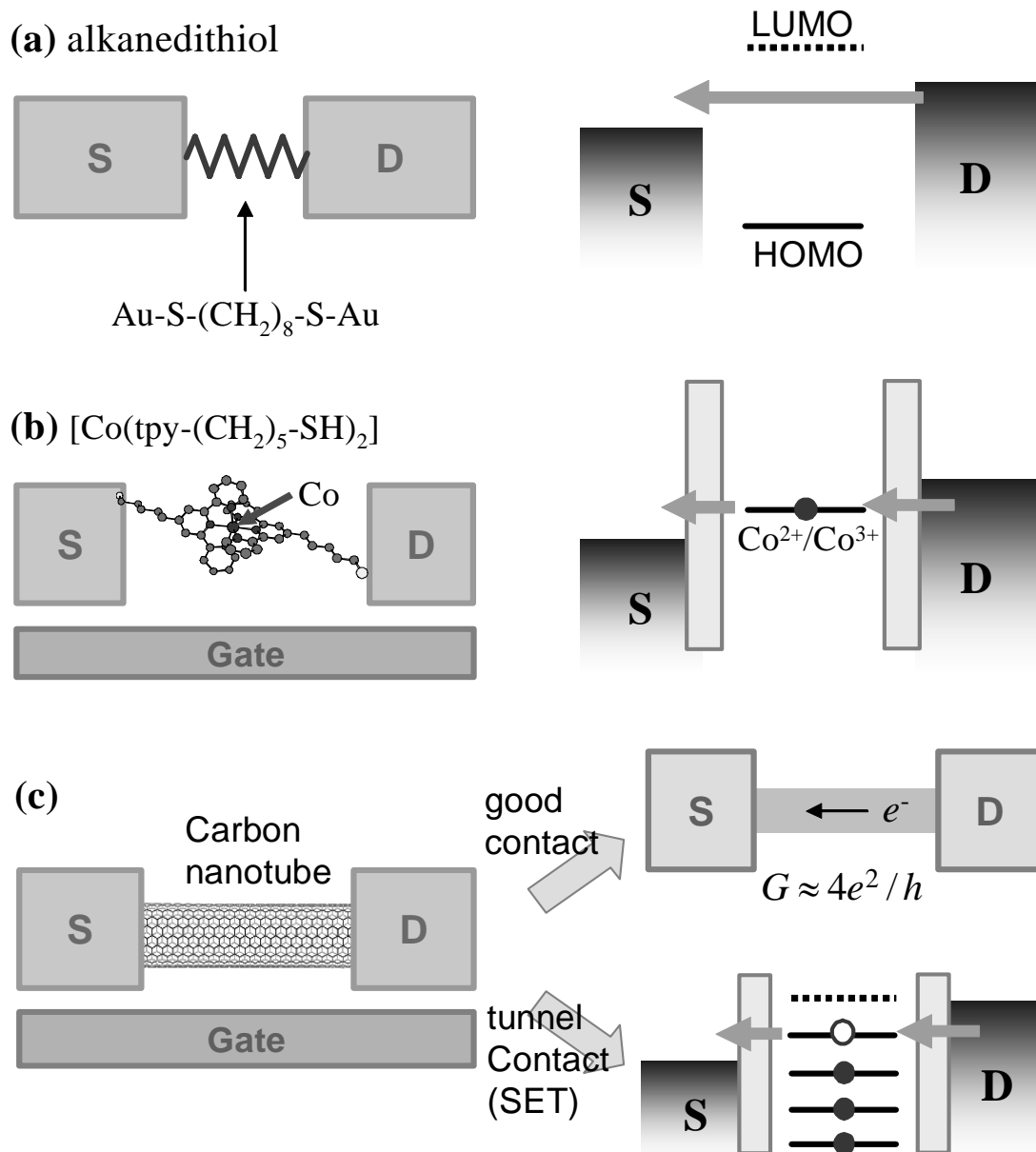
Figure 1.8 Examples of single molecule devices. **(a)** Electron transport in a gold/alkanedithiol/gold junction. Due to a large HOMO-LUMO gap of alkanedithiol, the main transport mechanism is a direct tunneling between the two gold electrodes. **(b)** A [Co(tpy-(CH$_2$)$_5$-SH)$_2$] molecule has an electrochemical potential corresponding to the Co^{3+}/Co^{2+} charge transition near the Fermi level of gold electrodes. This allows the sequential tunneling process as the main electron transport mechanism in this device. **(c)** A single-walled carbon nanotube device. A nanotube behaves like a good electrical wire when the contacts are good, but it shows the SET behavior when the contacts are poor.

can be aligned closer to μ_S, μ_D by applying a gate potential, and then a relatively large

electric current will flow at a small bias voltage. As explained in sections 1.2 and 1.3, the

conduction mechanism in such case is sequential tunneling. An electron tunnels onto the

molecule and then leaves to the other electrode, and then the next electron can tunnel onto the molecule. The overall conductance of a device made from [Co(tpy-(CH$_2$)$_5$-SH)$_2$] molecule is, therefore, mainly decided by the tunnel resistances adding ohmically. Since the cobalt ion is separated from the electrodes by a five-carbon alkyl-chain, the tunnel resistance will be large.

However, a much higher conductance is expected from a similar molecule [Co(tpy-SH)$_2$], which differs from [Co(tpy-(CH$_2$)$_5$-SH)$_2$] by an omission of the alkyl-chain at either ends. Obviously, the tunneling barrier between electrodes and the cobalt ion is much narrower than before and this leads to the higher conductance of this shorter molecule. From this example, we not only see how an insertion of a certain (electrically active) metal ion to a molecule can change the overall conductance dramatically, but we also understand how the conductance can be changed by modifying the insulating (electrically inactive) parts of the molecule. Electron transport in these molecules will be discussed in Chapter 6 in greater detail.

In the previous two examples, the contact was made by the strong S-Au bonding. This serves as a very good mechanical and chemical bonding for a single molecule device, which leads to a good electrical contact, too. If the thiol end group (-SH) is replaced by another end group (for example, -CH$_3$), it does not form a stable bond to gold any more and the conductance is predicted to change according to the exact placement of the end group relative to gold[40].

(3) Contact effects in carbon nanotubes

The importance of the contact between a molecule and macroscopic electrodes is well illustrated by different transport behaviors observed from the single carbon nanotube devices (Figure 1.8(c)). For simplicity, we will limit our discussion to a metallic carbon nanotube only. When the contacts between a carbon nanotube and electrodes are poor, it forms a tunnel barrier at either contacts and electrons need to tunnel through them to reach the nanotube. Therefore, the conductance will be low in this case. The nanotube behaves as an electron box, over which electrons can be delocalized. Due to the charging energy and electronic level quantization, the conductance of a nanotube device measured

at cryogenic temperatures shows characteristic behaviors of an SET, including Coulomb oscillations introduced in section 1.3[30, 31].

In contrast, transport measurements on a nanotube device display completely different behaviors when the contacts are good. With good contacts, the nanotube behaves as a good electronic wire and it becomes a ballistic conductor. The Coulomb oscillation disappears and the overall conductance increases significantly, almost approaching the theoretical maximum value, $4e^2/h \approx 155\,\mu\mathrm{S}$. Low temperature measurements further revealed the interference effect between propagating electron waves[20] (the Fabry-Perot resonator).

This example clearly shows that the transition from the high resistance regime (sequential tunneling) to the low resistance regime (ballistic conductor) in nanotube devices is dictated by the property of the contacts. Even though a reproducible way for controlling the contact is still not known for most single molecule devices, understanding the nature of contacts is critical for finding the correct picture for the electron transport mechanism in a specific single molecule device.

1.6 Summary and Outline

In this chapter, we reviewed several basic concepts that are necessary for the description of electron transport in single molecule devices. When electric current flows through a single molecule, the conductance is mainly decided by the quantized electronic structure of the molecule. The presence of accessible charge states near the electrode Fermi levels can help electron transport through a molecule. The properties of the contact between the molecule and the leads are also important, and they strongly affect the overall conductance of a single molecule device.

This thesis is organized as followings. We first discuss the Coulomb blockade theory, which describes single electron transport in an SET (Chapter 2). In particular, we will focus on the case where only one or two quantum levels are accessible. By analyzing such cases, we can understand how different parameters of an SET can affect the conductance pattern and also how one can extract information about quantum excitations from it (transport spectroscopy).

In Chapter 3, we will review the experimental issues, focusing on the electromigration technique. The fabrication procedure and the measurement setup will be also discussed.

Chapters 4 through 7 are the main body of this thesis and will describe the experimental results on various molecules. In Chapter 4, we study the conductance of single C_{60} transistors. The bouncing ball mode of C_{60} was observed in these devices and we will describe a theoretical model for a vibrating dot. In Chapter 5, excited levels that correspond to an internal vibration of C_{140} will be discussed and the results will be compared with the case of C_{70}. In Chapter 6, we study two similar molecules with a cobalt atom at the center. They show different conductance behaviors depending on the length, the longer one showing Coulomb blockade and the shorter one showing the Kondo effect.

In Chapter 7, we will steer our discussion to a much longer molecule, a carbon nanotube. We study the conductance of a single-walled carbon nanotube (SWNT) in two different temperature regimes. The low temperature study shows the SET behavior of a semiconducting SWNT in both *p-* and *n*-doped regime, while the contact effect causes a double dot configuration in the *n*-doped regime. Then a room temperature study using an electrolyte gate will be presented. The highly-efficient electrolyte gating is used to study the field effect transistor behavior of semiconducting SWNTs.

Finally, Chapter 8 will summarize the results along with the future directions.

Chapter 2

The Coulomb Blockade Theory

2.1 Overview

Basic concepts of the single electron transistor (SET) theory, which is also known as the Coulomb Blockade theory, were introduced in Chapter 1. In this chapter, we continue our study on this theory to further details. We first modify the energy landscape description of an SET to include the effect of all the capacitive couplings between the dot and three electrodes. Again the charging energy E_C and the excitation energy ΔE cause an energy gap in the dot near the Fermi level of the leads, leading to the single electron transport phenomena.

We will then concentrate on the quantum dot regime where ΔE is larger than the thermal energy $k_B T$. The distinction between a classical dot and a quantum dot will be discussed again in the following section. In the quantum dot regime, electrons tunnel through the dot using individual quantum levels and transport measurements on a quantum dot provide spectroscopic information on these quantum levels. In particular, we will limit our discussions to the case of a single-level quantum dot (section 2.3) and a two-level quantum dot (section 2.4) to elucidate how various SET parameters can be related to transport measurements.

The theory of an SET has been extensively studied in the past and there exist a number of review articles on this topic[21-26]. By no means is this chapter intended to be a comprehensive overview of this well-studied topic. Instead, it is written in such a way that it can provide basic theoretical tools for analyzing transport data measured from an SET. In the early part of this chapter, we again follow the path used by Kouwenhoven *et al*[26]. The discussions on the few-level quantum dot cases are similar to the one found in Bonet *et al*[41].

Throughout this chapter, we assume a negative value for the electron charge e (*i.e.* $e = -|e|$).

2.2 Basic Concepts of a Single Electron Transistor

Figure 2.1 describes the configuration of a single electron transistor with all the important parameters. A small dot is surrounded by three electrodes - the source, drain and gate electrode. The dot is capacitively coupled to all three electrodes; a potential change in any electrode will modify the electrostatic potential of the dot. The dot is also tunnel coupled to the source and drain electrodes, allowing electrons to move between the dot and either of these two electrodes. Therefore, electric current can flow between the source and the drain by electrons tunneling on and off the dot.

The electrochemical potential μ_N of a dot with N electrons was previously obtained in Chapter 1 from the energy difference between the total energy $U(N)$ for the N electron state and $U(N-1)$ for the N-1 electron state (equation (1.2)). In this calculation, the effect of individual electrode potentials was not included in the estimation of the total energy, and the electrochemical potential in equation (1.2) thus does not depend on any electrode potential. Once we include such effects in the calculation of $U(N)$ for all different charge states, the electrochemical potential μ_N changes to the following[26]:

$$\mu_N \equiv U(N) - U(N-1) = E_N + (N-1/2)e^2/C_{total} + eV_{dot}. \qquad (2.1)$$
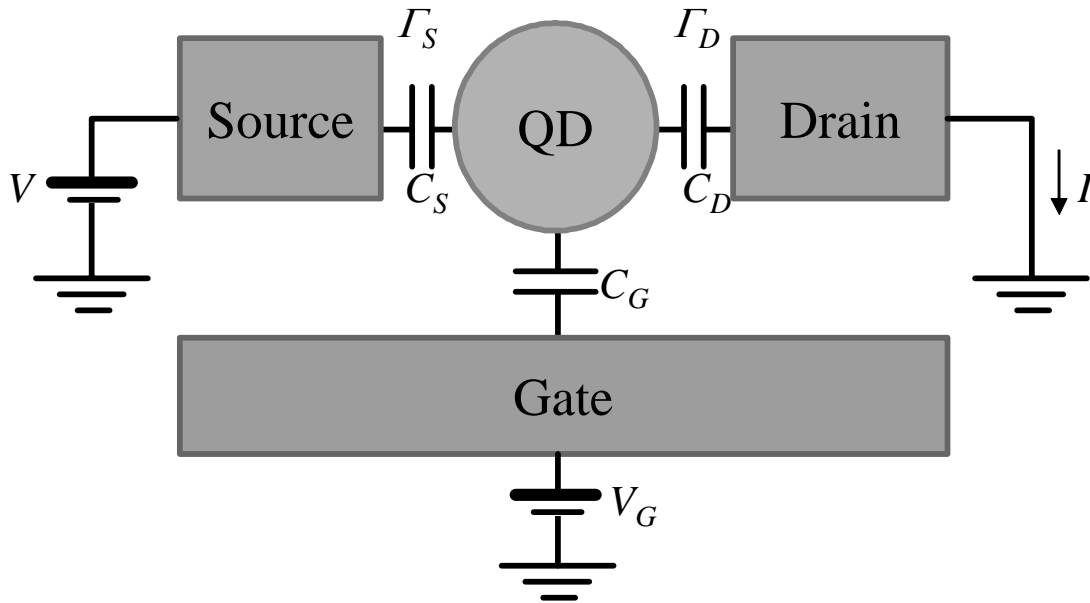
Figure 2.1 A schematic of a single electron transistor and its parameters.

Now there is a new term eV_{dot} in the equation that describes the effect of capacitive couplings with individual electrodes. Here V_{dot} is a function of the gate bias V_G and the source bias V, which is described by the following equation.

$$V_{dot} = \frac{1}{C_{total}} \sum_{i=S,D,G} C_i V_i = \frac{C_S}{C_{total}} V + \frac{C_G}{C_{total}} V_G \qquad (2.2)$$

In the last step, a term related to the drain electrode is dropped because it is grounded in the diagram shown in Figure 2.1 ($V_D = 0$). In fact, the drain electrode is always kept grounded in all experiments discussed in this thesis. The results that are derived using (2.2), therefore, are consistent with experimental conditions. In (2.1) and (2.2), C_{total} is the sum of all three capacitances, $C_{total} = C_S + C_D + C_G$.

Since V_{dot} does not depend on the number of electrons on the dot N, the charge addition energy $E_C + \Delta E$ does not change in this case. However, the position of μ_N relative to the electrode Fermi levels μ_S, μ_D changes according to V and V_G. Therefore, one can control the electrochemical potential of a dot for an arbitrary charge state by changing the bias voltage V and/or the gate voltage V_G. Using (2.1) and (2.2), we can calculate how much change in μ_N is expected for a certain ΔV and ΔV_G.

$$\Delta \mu_N / e = \frac{C_S}{C_{total}} \Delta V + \frac{C_G}{C_{total}} \Delta V_G \qquad (2.3)$$

As we can clearly see from (2.3), the efficiency of an electrode potential in controlling μ_N is proportional to the ratio between the electrode capacitance and the total capacitance.

As explained in Chapter 1, the number of electrons on the dot (N) is decided by the maximum N whose electrochemical potential μ_N is below μ_S and μ_D. When μ_{N+1} is above μ_S and μ_D, the (N+1)-th charge state is not accessible and hence the current does not flow. This current blockade is caused by a large charge addition energy $E_C + \Delta E$, which is equal to the difference between μ_N and μ_{N+1}. On the contrary, when μ_{N+1} is located between μ_S and μ_D, the charge state of the dot oscillates between N and N+1, allowing electric current to flow by the sequential electron tunneling process. This

alternating conductance behavior leads to the Coulomb oscillation curve shown in Figure 1.4(c).

As mentioned earlier (equation (1.3)), such single electron transport behavior can be observed only when the charge addition energy $E_C + \Delta E$ is significantly larger than the thermal energy $k_B T$. The charging energy E_C increases as a dot becomes smaller, and the value of E_C can be roughly estimated from the size of the dot. For example, E_C of a metal sphere with a radius R is $e^2/(4\pi\varepsilon_0 R)$ using $C = 4\pi\varepsilon_0 R$. For a metal sphere with 1 μm radius, this becomes 1.44 meV, which is fairly small and can be important only at cryogenic temperatures. E_C increases to 144 meV if R = 10 nm, which is large enough to be observable even at room temperatures ($k_B T$ = 25.9 meV at 300K). However, these values provide an upper bound of the real charging energy, since the total capacitance C will be always larger than $4\pi\varepsilon_0 R$ due to the additional capacitance between the dot and the electrodes. For example, the total capacitance for the same sphere (R = 10 nm) surrounded by a spherical shell (R = 11 nm) is 11 times larger than the capacitance of the sphere alone. This will reduce the charging energy to 13 meV. Therefore, one should take into account not only the size of a dot, but also the local electrostatic environment when estimating the charging energy.

The other constituent of the charge addition energy is the electronic excitation energy ΔE, which also increases as the dot becomes smaller. In general, the characteristic energy scale of ΔE is $\pi^2 \hbar^2 / m R^2$ [26]. ΔE also depends on N, but the quantitative relation between the two varies depending on the dimensionality of the dot[26]. For example, ΔE of a 100 nm 2D dot (GaAs/AlGaAs heterostructure) is ~30 μeV, which is large enough to be observable below 100 mK. In comparison, similar ΔE can be expected for a 3D metallic cluster near its Fermi level only at a much smaller size, $R \sim 5$ nm.

Depending on whether ΔE is larger than $k_B T$ or not, a single electron transistor has different names. When $\Delta E < k_B T$, it is called a "classical dot", and when $\Delta E > k_B T$, a "quantum dot". The distinction between these two cases is necessary because the theoretical description for one regime is somewhat different from the other. In the

classical dot regime, a tunneling electron can access what is in effect a continuum of excited states of the dot, and the overall conductance can be described by the tunneling rates averaged over many electronic levels. On the contrary, in the quantum dot regime,

(a) Summary of various energies in an SET model

- Total energy $\qquad\qquad\qquad\qquad U(N)$
- Electrochemical potential $\qquad\qquad \mu_N \equiv U(N) - U(N-1)$
- Charge addition energy $\qquad\qquad \mu_{N+1} - \mu_N = E_c + \Delta E$
- Charging energy $\qquad\qquad\qquad E_c = e^2/C$
- Electronic level spacing $\qquad\qquad \Delta E$
- Thermal energy $\qquad\qquad\qquad k_B T$
- Intrinsic broadening $\qquad\qquad\quad \gamma \sim h(\Gamma_S + \Gamma_D)$
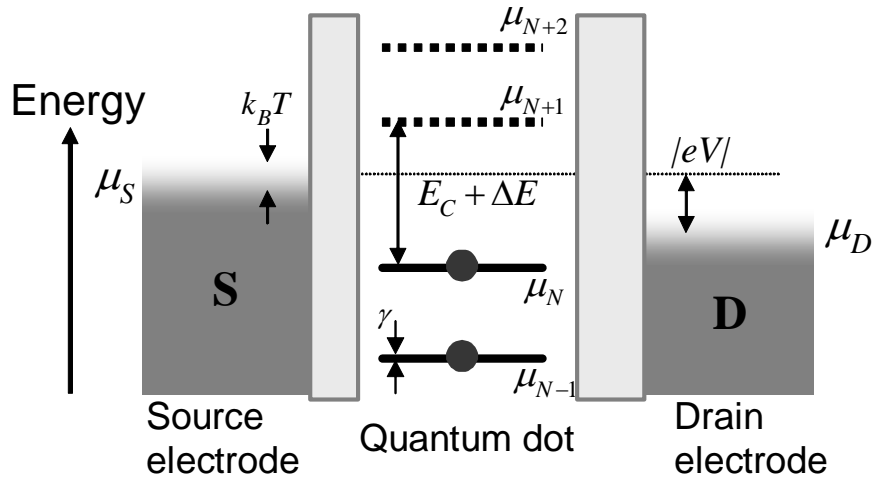
(b) Assumptions in the current model

- Single electron transport $\qquad\qquad E_c + \Delta E >> k_B T$
- Quantum dot regime $\qquad\qquad\quad \Delta E >> k_B T$
- Single-level quantum dot $\qquad\qquad E_c, \Delta E >> |eV_{\max}|$
- Negligible intrinsic broadening $\qquad \gamma << k_B T$

Figure 2.2 (a) The summary of various energies of a single electron transistor with an energy diagram. (b) The energy regime (quantum dot regime) associated with the model.

each quantum state of the dot can be identified and specific tunneling rates are assigned to each quantum state.

Single molecules, the main subject of this thesis, fall in the category of the quantum dot, especially at cryogenic temperatures. The charge addition energy of a molecule is typically on the order of eV and the excitation energy is also much larger than $k_B T$ at liquid helium temperatures ($k_B T = 0.36$ meV at 4.2 K). The electronic structure of a C_{60} molecule discussed in Chapter 1 (section 1.4) is a good example. It is interesting to note that many molecules have not only a stable charge state but also a certain electronic ground state at room temperature, because both the charge addition energy and the electronic excitation energy are large.

In a single electron transistor, tunnel barriers separate the dot from the source and drain electrodes. In the quantum dot regime the rate of electron tunneling between the dot and the source or drain electrode is represented by the tunneling rates Γ_S and Γ_D. In general, these rates can be different for each quantum level of the dot. They are defined as the number of electrons that tunnel through one of the tunnel barriers per unit time. Thus the unit of Γ_S and Γ_D is s^{-1} or Hz. If one of them is much larger than the other (for example, $\Gamma_S >> \Gamma_D$), the current flowing through the device when it is turned on will become $|e|\Gamma_D$. In real experiments, the current flowing through a single quantum level of a quantum dot is usually less than 1nA, which is equivalent to approximately 6 GHz for Γ's. The general relation between Γ's and the current in the device's on-state can be decided by solving the rate equations, which will be described in the next section.

For reference purposes, definitions of various different energies introduced in the SET theory are summarized in Figure 2.2(a) with an energy diagram. In the next section, we concentrate on the single-level quantum dot regime. The assumptions for this regime are summarized in Figure 2.2(b).

2.3 Single-Level Quantum Dots

So far we introduced three energy scales; the charging energy E_C, the thermal energy $k_B T$, and the quantum excitation energy ΔE. In order to understand the electron

transport properties of a single electron transistor, it is necessary to develop a theoretical model that is valid within a specific energy range. From this point, we will assume $E_C >$ $k_B T$ and $\Delta E > k_B T$ (the quantum dot regime). We also assume that E_C and ΔE are large enough that only one additional charge state (N+1) is accessible and that no quantum excited states are accessible for the quantum dot. Therefore, we will be dealing with only two charge states (N and N+1) in their own ground states.

If the electrochemical potential of the N+1 electron state (μ_{N+1}) when $V = V_G = 0$ is defined as E_0, μ_{N+1} can be written as the following.

$$\mu_{N+1} = E_0 + eV_{dot} \qquad (2.4)$$

For convenience, we also define $\mu_D = 0$ from now on.

In Figure 2.3, energy diagrams of a quantum dot with $E_0 > 0$ and V ~ 0 (*i.e.* $\mu_D \sim \mu_S$) is illustrated. When $V_G = 0$ (case A), the quantum dot is always in its N electron state because μ_{N+1} is above the Fermi level of both source and drain electrodes ($\mu_{N+1} > \mu_D \sim \mu_S$). The current will not flow in this case. When $|e|V_G > E_0(C_{total}/C_G)$ (case C), electric current is blocked again because the N+1 electron state is always occupied. Electron transport is allowed only when $|e|V_G \sim E_0(C_{total}/C_G)$ (case B), where μ_{N+1} is aligned with the source and drain electrodes. In this case, an electron can jump
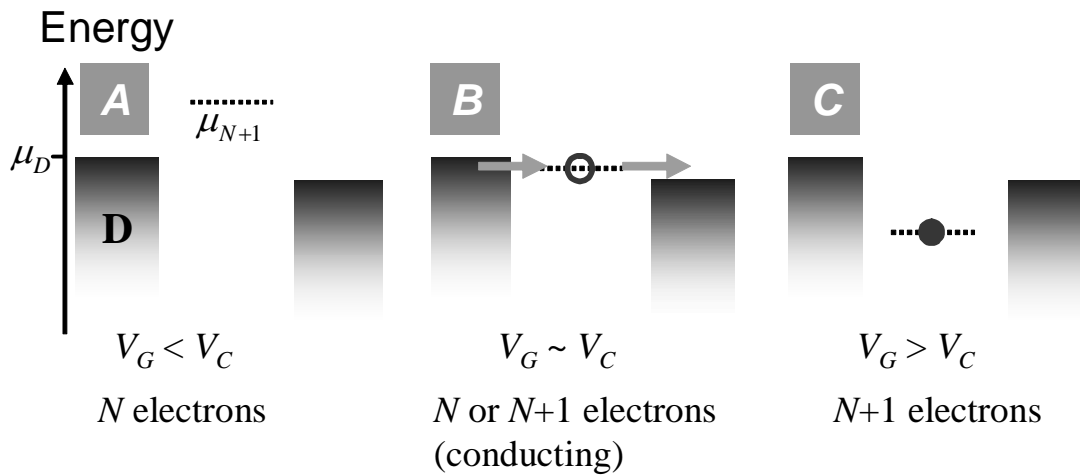
Figure 2.3 The energy diagrams of a quantum dot with a single level. Initially the level is empty (case A). As the gate voltage increases the level becomes occupied sometimes (case B) and finally gets completely occupied (case C). The current flows only in case B because the dot can change the charge states freely.
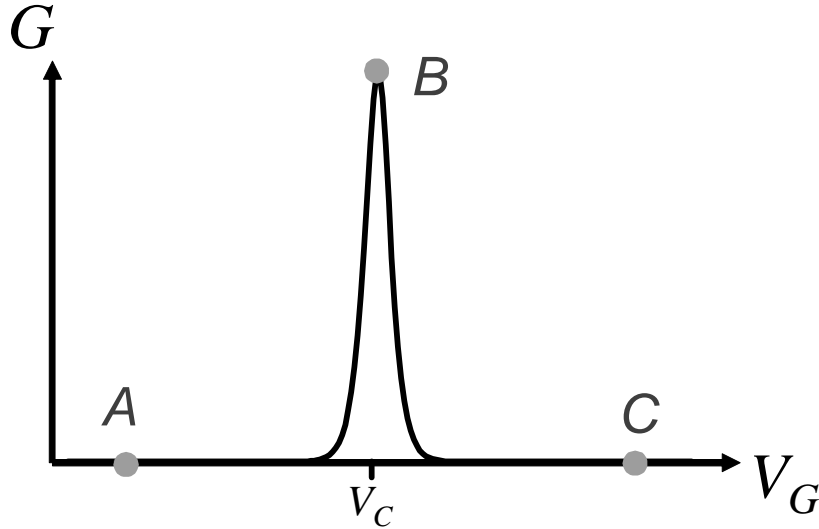
Figure 2.4 The Coulomb oscillation. The low bias conductance ($|e|V < k_BT$) measured as a function of the gate voltage will show a peak (Coulomb oscillation) that corresponds to the charge degeneracy of case B in Figure 2.4.

between the dot and the source or drain electrode freely. We define the crossing potential V_C, where electric current is allowed at low bias.

$$V_C = \frac{E_0}{|e|} \frac{C_{total}}{C_G} \tag{2.5}$$

By monitoring the current that flows through the device with a small bias voltage $\delta V < k_BT$ applied, we can measure the conductance of the device as a function of the gate voltage V_G. The resulting low-bias conductance curve will look like the Figure 2.4. As explained above, the conductance will be zero below and above the crossing potential, V_C. It will show a sharp peak only near at $V_G = V_C$. The peak height and the shape of this curve can be calculated by solving the rate equation, which will be described in this section.

As we already discussed in Chapter 1, the conductance peak in Figure 2.4 is called the Coulomb oscillation. At $V_G = V_C$, the two charge states N and $N+1$ of the quantum dot have the same energy, hence an electron can hop on and off the dot freely. This charge degeneracy of the quantum dot is the origin of the low-bias conductance that produces the conductance peak in Figure 2.4.

Before we move on, let us introduce the final energy scale of this model; the intrinsic broadening, γ. Since the quantum dot is coupled to the source and drain

electrodes by tunnel barriers, an electron on the dot can decay to one of the electrodes over time. The lifetime τ of an electron on the dot will be dictated by the two tunnel rates, Γ_S and Γ_D and it will be expressed as $\tau \sim (\Gamma_S + \Gamma_D)^{-1}$. By the uncertainty principle, $\tau\gamma \sim h$ (h is the Planck constant). Therefore, the intrinsic broadening γ is expressed as $\gamma = h(\Gamma_S + \Gamma_D)$. For a quantum dot with $\Gamma_S = \Gamma_D = 10$ GHz, $\gamma \sim 0.083$ meV ~ 1K. As this example shows, the intrinsic broadening of a quantum state of a quantum dot can be large enough to be measurable at cryogenic temperatures. For the rest of this chapter, we will assume $\gamma \ll k_B T$ to simplify the analysis. However, in reality one should keep in mind that the data could be affected by the intrinsic line broadening.

Solving the rate equations for a one-level quantum dot

For a quantum dot with one level (μ_{N+1}), there are only two states available to the dot; one with an empty level (state 0; N electron state) and the other with an occupied level (state 1; N+1 electron state). During electron transport measurements, current will flow while the quantum dot fluctuates between the two states. It is a stochastic process and therefore should be approached using a statistical method.

First, we define P_0 and P_1, the probability that the dot is in a specific state. P_0 corresponds to the probability that the dot is in the state 0 (empty dot) and P_1 corresponds to the state 1 (occupied dot). For a certain set of conditions (bias voltages and temperature, etc.), the time change rate of P_0 and P_1 can be readily written as the following.

$$\frac{\partial P_0}{\partial t} = -P_0(\Gamma_S f_S + \Gamma_D f_D) + P_1(\Gamma_S(1-f_S) + \Gamma_D(1-f_D)) \tag{2.6}$$

$$\frac{\partial P_1}{\partial t} = P_0(\Gamma_S f_S + \Gamma_D f_D) - P_1(\Gamma_S(1-f_S) + \Gamma_D(1-f_D)) = -\frac{\partial P_0}{\partial t} \tag{2.7}$$

These are called the rate equations. They can be written in a matrix form as

$$\begin{pmatrix} \partial P_0 / \partial t \\ \partial P_1 / \partial t \end{pmatrix} = \begin{pmatrix} a_{00} & -a_{11} \\ -a_{00} & a_{11} \end{pmatrix} \begin{pmatrix} P_0 \\ P_1 \end{pmatrix}. \tag{2.8}$$

The rate equation in a matrix form is useful when we solve quantum dots with multiple states.

In (2.6) and (2.7), f_S and f_D are the Fermi functions calculated at μ_{N+1} for the source and drain electrodes, and they will depend on such parameters as temperature, source-drain bias, gate bias and all the capacitances. The complete form of f_S and f_D is as follows.

$$f_D = \left(1+\exp\left(\frac{\mu_{N+1}-\mu_D}{k_BT}\right)\right)^{-1} = \left(1+\exp\left(\frac{\mu_{N+1}}{k_BT}\right)\right)^{-1}$$

$$f_S = \left(1+\exp\left(\frac{\mu_{N+1}-\mu_S}{k_BT}\right)\right)^{-1} = \left(1+\exp\left(\frac{\mu_{N+1}+|e|V}{k_BT}\right)\right)^{-1} \qquad (2.9)$$

$$\mu_{N+1} = E_0 - |e|\frac{C_GV_G+C_SV}{C_{total}} = -|e|\frac{C_G(V_G-V_C)+C_SV}{C_{total}}$$

Then the electric current flowing from the source electrode to the drain electrode in equilibrium can be obtained by setting $\partial P_0/\partial t = \partial P_1/\partial t = 0$. Using $P_1 = 1 - P_0$, we can solve (2.6) for P_0 to get,

$$P_0 = \frac{\Gamma_S(1-f_S)+\Gamma_D(1-f_D)}{\Gamma_S+\Gamma_D}. \qquad (2.10)$$

Finally, the electric current I will be,

$$\frac{I}{|e|} = -P_0\Gamma_Sf_S + P_1\Gamma_S(1-f_S) = \frac{\Gamma_S\Gamma_D}{\Gamma_S+\Gamma_D}(f_D-f_S) \equiv \Gamma(f_D-f_S). \qquad (2.11)$$

The final equation (2.11) is rather simple and has two major parts. Γ decides the maximum current amplitude, while $f_D - f_S$ decides whether the current will flow or not. At low temperatures, the value of f_D and f_S is either 0 or 1 in most cases. The current is zero when they have the same value and will become non-zero when they have different values.   Therefore, the conducting case corresponds to those regions where the electrochemical potential of the $N+1$ electron state μ_{N+1} is located between the Fermi levels of the source (μ_S) and the drain (μ_D) electrodes. Figure 2.5 plots f_D, f_S and $f_D - f_S$ as a function of V and V_G along with energy diagrams of the quantum dot for each case. It clearly shows that the current is allowed only when the quantum dot level is located between the two Fermi levels of the electrodes.
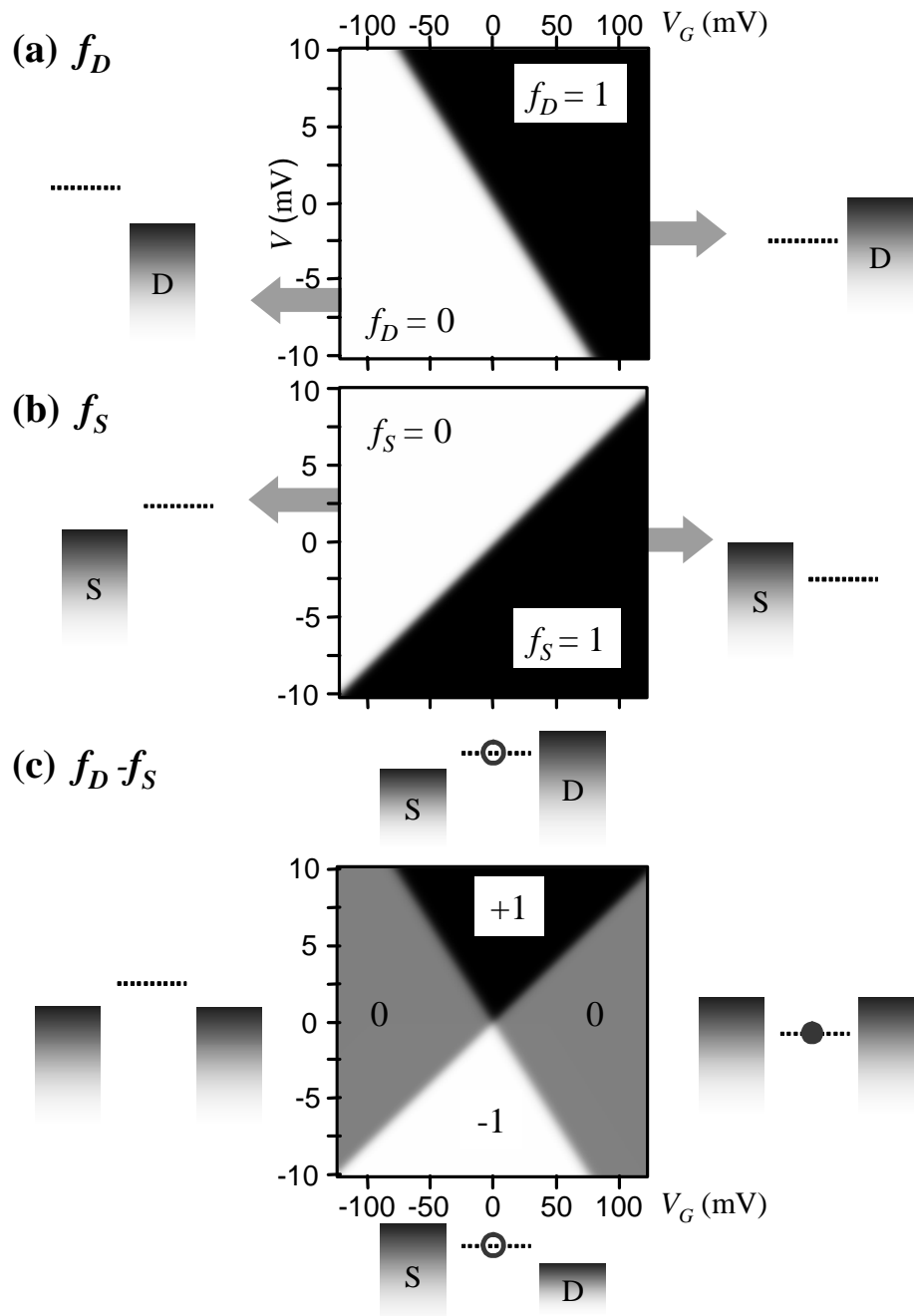
Figure 2.5 The values of the Fermi functions. These values are calculated using the equations in the text. The conditions are the following. $T = 1.5$ K, $E_0 = 0$ ($V_C = 0$), $C_D{:}C_S{:}C_G = 38{:}57{:}5$

Figure 2.6(a) plots the calculated current (I) as a function of V and V_G and Figure 2.6(b) shows calculated I-V curves at different gate voltages. Each curve in Figure 2.6(b) shows a non-conducting region up to a certain bias and then starts conducting with a current $\pm e\Gamma$. This suppression of conductance at low biases is a direct result of the

charge addition energy and it is called the Coulomb blockade. The width of the Coulomb blockade changes according to V_G and becomes zero at $V_G = V_C$. The Coulomb blockade is a signature behavior of single electron transistors together with the Coulomb oscillation that we already encountered.
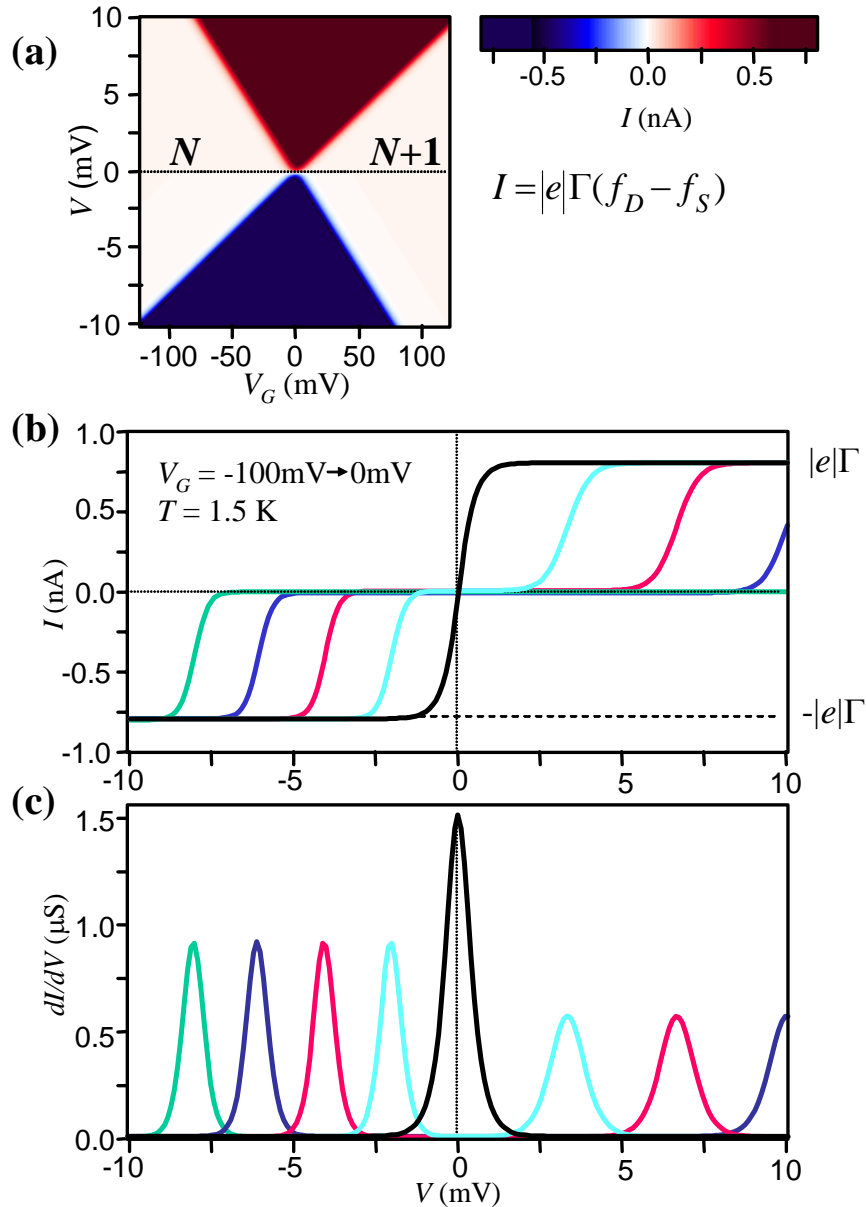
Figure 2.6 The Coulomb blockade. (a) The current (I) calculated using the parameters in Figure 2.5 with $\Gamma_S = \Gamma_D = 10$ GHz. The number of electrons on the dot is shown in each blockade region. (b) Five I-V curves taken at different V_G's. They show a conductance suppressed region near zero bias followed by a current step (Coulomb blockade). (c) dI/dV as a function of V. They show peaks corresponding to the current steps in (b).

In Figure 2.6(c), we also plot the differential conductance dI/dV, as a function of V for different gate voltages. Each dI/dV-V curve shows a peak near each current step present in the corresponding I-V curve. A dI/dV-V-V_G map calculated for the same parameters is shown in Figure 2.7. The analytical form of the differential conductance dI/dV can be obtained by differentiating (2.11) in V.

$$\frac{dI}{dV} = |e|\Gamma\left(\frac{\partial(f_D - f_S)}{\partial\mu_{N+1}}\frac{\partial\mu_{N+1}}{\partial V} - \frac{\partial f_S}{\partial V}\right) = \frac{e^2\Gamma}{k_B T}\left((1-f_D)f_D\frac{C_S}{C_{total}} + (1-f_S)f_S\frac{C_D+C_G}{C_{total}}\right) \quad (2.12)$$

Since both f_D and f_S are either 0 or 1 for most cases at low temperatures, dI/dV
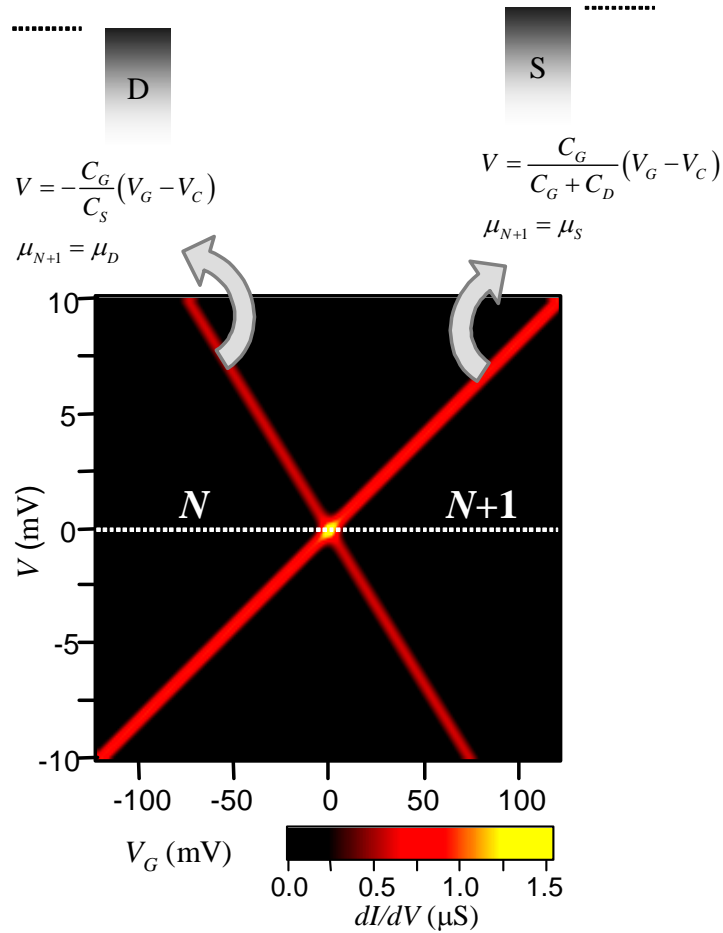
Figure 2.7 Color scale plot of the differential conductance as a function of V and V_G. It shows two dI/dV lines, each corresponding to the current steps in Figure 2.6 (b). These lines also signify the event of the quantum dot level (μ_{N+1}) aligning to the Fermi level of either the source (positive slope) or the drain (negative slope) electrode. It is calculated for a quantum dot with the same parameters used in Figure 2.5 and 2.6.

is zero for most cases. The first term of the right side of (2.12) will be non-zero when the value of f_D is between 0 and 1, which corresponds to the case where μ_{N+1} is aligned to μ_D, the Fermi level of the drain electrode. Likewise, the second term of the right side of (2.12) will be non-zero only when the value of f_S is between 0 and 1, corresponding to the case where μ_{N+1} is aligned to μ_S, the Fermi level of the source electrode. Equivalently, the non-zero region in Figure 2.7 signifies an event that the electron energy level of the quantum dot (μ_{N+1}) is aligned to one of the Fermi levels of the source and the drain electrodes. Therefore, we can measure μ_{N+1} by measuring *dI/dV* of a single electron transistor while changing the Fermi levels of the electrodes by varying V and V_G. This is the first example of the transport spectroscopy in a quantum dot. We shall see more examples in the following sections.

To better understand this important subject, let's figure out the condition for the level alignment between the quantum dot level and the source electrode ($\mu_{N+1} = \mu_S$). By using (2.2), (2.4) and (2.5), we can rewrite this equality as follows.

$$\mu_{N+1} = E_0 + e\left(VC_S + V_G C_G\right)/C_{total} = e\left(VC_S + \left(V_G - V_C\right)C_G\right)/C_{total} = eV = \mu_S \quad (2.13)$$

We solve this for V to get,

$$V = \frac{C_G}{C_{total} - C_S}\left(V_G - V_C\right) = \frac{C_G}{C_G + C_D}\left(V_G - V_C\right) \quad \text{(aligned to source).} \quad (2.14)$$

Similarly, the alignment condition between the quantum dot and the drain electrode is,

$$V = -\frac{C_G}{C_S}\left(V_G - V_C\right) \quad \text{(aligned to drain).} \quad (2.15)$$

(2.14) and (2.15) show that the non-zero region in a *dI/dV-V-V$_G$* plot will form a line with a slope that corresponds to a capacitance ratio. For example, the alignment between the quantum dot and the source will be represented by a *dI/dV* line with a slope $C_G/(C_G + C_D)$ that crosses $V = 0$ at $V_G = V_C$. Therefore, we can obtain information about the capacitance ratio among the three capacitances by measuring the slopes of *dI/dV* lines in a *dI/dV-V-V$_G$* plot. One can notice that the absolute value of the slopes are different in (2.14) and (2.15) even when $C_S = C_D$. It happened because we earlier introduced an

asymmetry to the system by grounding the drain electrode. These results are summarized in Figure 2.7.

The Coulomb oscillation curve and its temperature dependence

We earlier discussed the conductance of a quantum dot as a function of V_G at low biases (Figure 2.4). It conducts when $V_G \sim V_C$, but the conductance will be zero, otherwise. Using (2.12), we can obtain the analytic form of the dI/dV-V_G curve at $V = 0$. The equation (2.12) simplifies significantly since $f_S = f_D$ in this case.

(a)

$$\frac{dI}{dV}\bigg|_{V=0} = \frac{e^2 \Gamma}{4k_B T}\left(\cosh\frac{|e|\alpha(V_G - V_C)}{2k_B T}\right)^{-2}$$

(b)

$$G_{max} = \frac{e^2 \Gamma}{4k_B T}$$

(c)

$$FWHM = 3.525\frac{k_B T}{|e|\alpha}$$
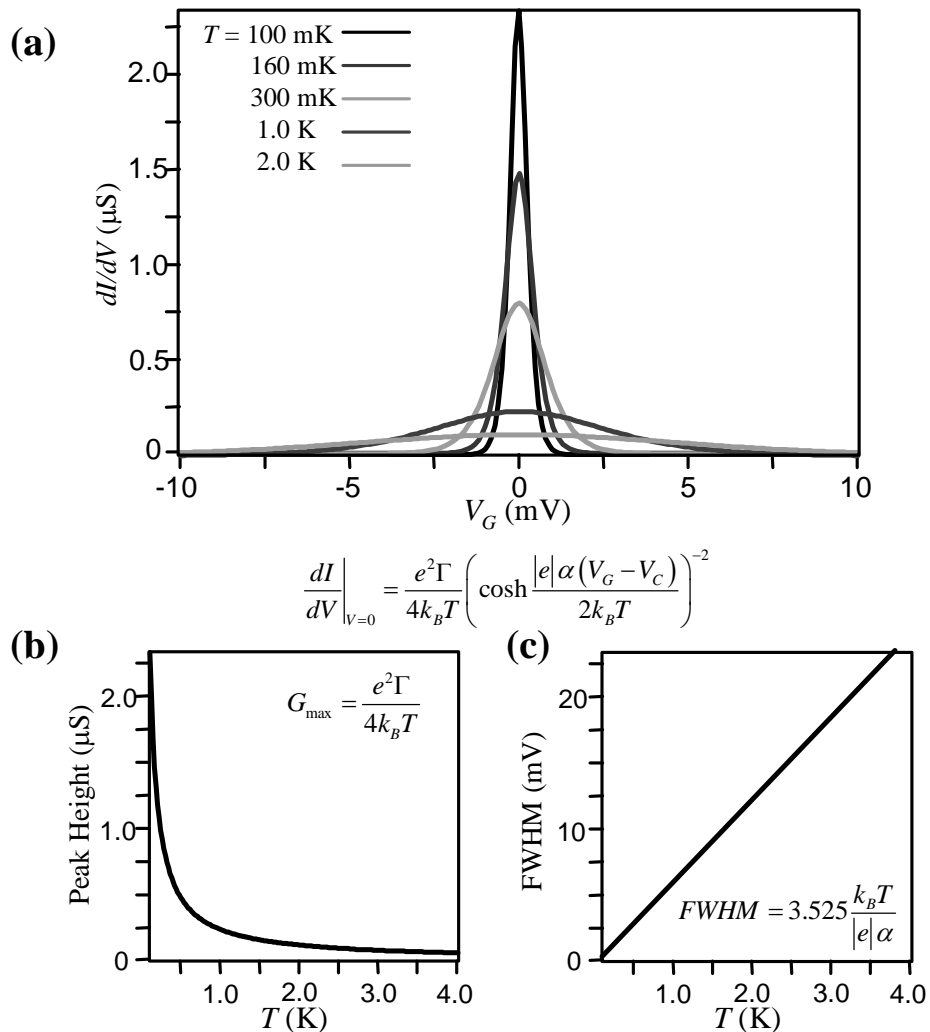
Figure 2.8 (a) Temperature dependence of the Coulomb oscillation peak. (b) The peak height decreases with an increasing temperature. (c) The peak width increases linearly with the temperature. The same parameters as in Figure 2.5 were used and $\Gamma_S = \Gamma_D = 1$ GHz.

$$\frac{dI}{dV}\bigg|_{V=0} = \frac{e^2\Gamma}{k_BT}(1-f_D)f_D = \frac{e^2\Gamma}{4k_BT}\left(\cosh\frac{|e|\alpha(V_G-V_C)}{2k_BT}\right)^{-2} \tag{2.16}$$

We used $\alpha \equiv C_G/C_{total}$, the gate efficiency factor in the exponent of the right side. In Figure 2.8, we plot (2.16) as a function of V_G for a set of parameters. It has a peak centered at $V_G = V_C$, and the peak height is $e^2\Gamma/4k_BT$. The full width at the half maximum (FWHM) of the peak is $3.525\,k_BT/|e|\alpha$. This plot gives a quantitative description for the analysis we performed earlier.

The temperature dependence of a Coulomb oscillation peak is one of the signature behaviors of a quantum dot as opposed to a classical dot. As we can see in (2.16) and Figure 2.8, the height of a Coulomb oscillation peak is proportional to $1/T$ and its width is linearly proportional to T. Unlike these, a classical dot shows a peak whose height does not change with increasing temperatures.

This temperature dependence of a Coulomb oscillation peak can be used for measuring quantum dot parameters, such as T, γ, α or V_C. In real experiments, however, the temperature dependence of a Coulomb oscillation peak often shows a deviation from the theoretical $1/T$ dependence. It occurs for mainly two reasons. First, the electrons in the device might not be as cold as the cryostat thermometer indicates. Due to electrical noise in the leads or a poor coupling between electrons and phonons in the sample, the electron temperature is often higher than the cryostat temperature. A second possibility is the intrinsic line width γ of the quantum dot level. Once the temperature gets comparable to γ ($k_BT \sim \gamma$), the Coulomb oscillation peak does not get any narrower and additional cooling does not affect the shape of the peak. Therefore, by measuring the temperature dependence of the Coulomb oscillation peak, we can measure the electron temperature or the intrinsic level broadening. It is usually difficult to determine which is to blame when additional cooling does not change the peak, especially at very low temperatures ($T < 100$ mK).

We can also measure α, the gate efficiency from the width of a Coulomb oscillation peak using the following formula.

$$FWHM = 3.525 \frac{k_B T}{|e| \alpha} \tag{2.17}$$

The width should be measured within the temperature range where the Coulomb oscillation peak follows the $1/T$ dependence. α can also be independently measured from the slopes of dI/dV lines in a dI/dV-V-V_G plot using (2.14) and (2.15).

A quantum dot with multiple charge states: The Coulomb diamond

So far we have dealt with a quantum dot with only two charge states (N and $N+1$). However, many quantum dots can be occupied by more than one additional electron and show multiple Coulomb oscillations, each of them corresponding to a different charge degeneracy. Studying the Coulomb blockade behavior in different charge states of a quantum dot (or so called an artificial atom) produces a variety of interesting results, such as the observation of Hund's rule in a side-gated vertical quantum dot[42].

Electron transport through different charge states of a quantum dot can be also calculated using the rate equations. Unlike the case with only two charge states, now there are more than two states for the quantum dot and we need to solve the rate equations for P_0, P_1, …, P_n (n is the maximum number of additional electrons that can be added to the dot). It is too cumbersome a task to put down the general equations and solve them in this thesis. Rather, let's see the results for a quantum dot with only three accessible charge states.

Figure 2.9 is the dI/dV-V-V_G plot for three different charge states of a quantum dot, which we will call 0, 1- and 2- states (corresponding to the N, $N+1$ and $N+2$ electron state, respectively). There are two Coulomb oscillation peaks, one for the charge degeneracy between 0 and 1- charge states (at $V_G = V_{C1}$) and the other for 1- and 2- states (at $V_G = V_{C2}$). There is one pair of dI/dV lines that cross each charge degeneracy point. For example, the lines crossing $V = 0$ at $V_G = V_{C1}$ correspond to the configurations where the electrochemical potential of the (1-) state (μ_{N+1}), is aligned to the Fermi level of either source or drain electrode. The slopes of corresponding dI/dV lines for different charge states are usually the same since the capacitances rarely change between different charge transitions. However, the intensity of dI/dV lines can differ for different charge

states due to variations in Γ. The Coulomb blockade region between the two degeneracy points looks like a diamond, which is why it is called the Coulomb diamond.

One important parameter we can measure from Figure 2.9 is the charge addition energy $E_C + \Delta E$. The point A in Figure 2.9(a) denotes a crossing point between two *dI/dV* lines, one for the source alignment of the (1-) charge state and the other for the drain alignment of (2-) charge state. The energy diagram clearly shows that the bias at the crossing point A is equal to the difference between the two chemical potentials μ_{N+1}
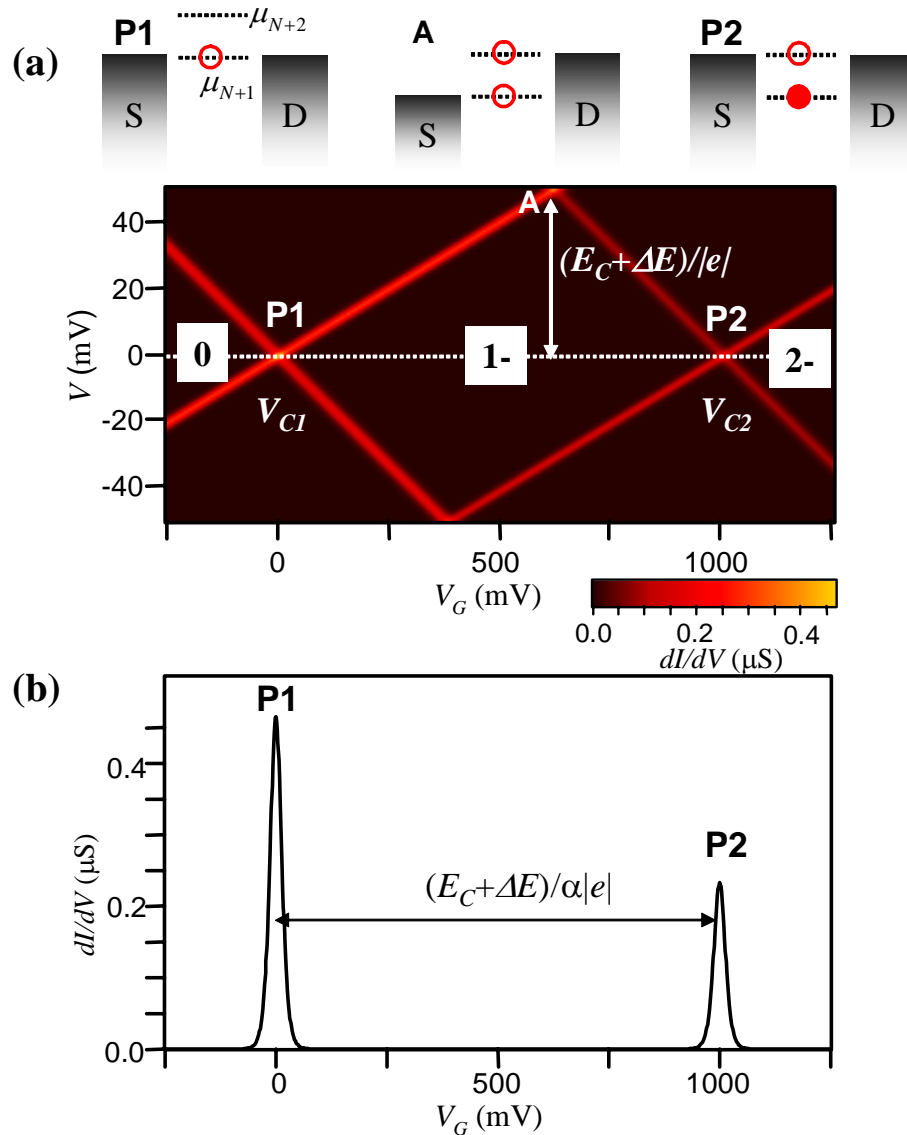
Figure 2.9 A quantum dot with multiple charge states. (a) The diamond plot calculated for $T = 5$ K, $E_{01} = 0$ ($V_{C1} = 0$), $E_{02} = 50$ meV ($V_{C2} = 1$ V), $C_D:C_S:C_G = 38:57:5$ ($\alpha = 0.05$), $\Gamma_{S1} = \Gamma_{D1} = 10$ GHz, $\Gamma_{S2} = \Gamma_{D2} = 5$ GHz. (b) Multiple Coulomb oscillation peaks are expected from the same quantum dot.

and μ_{N+2}, which is equal to the charge addition energy.

$$\left|eV_{cross}\right| = E_C + \Delta E_{N+2} \tag{2.18}$$

If there is an independent estimate of the level spacing ΔE_{N+2}, we can measure the charging energy E_C using (2.18).

The method we described above is a general way to measure an energy difference between two states. A *dI/dV* line with a positive slope corresponds to a case where a state (different quantum excited levels, different charge states, etc.) is aligned to the Fermi level of the source electrode, whereas the crossing *dI/dV* line with a negative slope corresponds to a case where another state is aligned to the Fermi level of the drain electrode. Therefore, the bias at the crossing point corresponds to the energy difference between the two states, regardless of the origin of these states.

2.4 Quantum Dots with Excited Levels

All the quantum dots we encounter in real experiments come with more than one quantum state. There is also intrinsic degeneracy of the ground state (*e.g.* spin degeneracy) that requires a theory that can handle more than just one state. As we shall see in later chapters, most electron transport measurements in single molecule quantum dots show interesting results that are related to the properties of quantum excitations. This is the motivation why we would like to understand how excited levels affect electron transport in quantum dots.

The rate equations introduced in the previous section can be readily modified for a quantum dot with more than one level to explain the behaviors that are expected from the excited levels. However, let's first remind ourselves of the meaning of some basic notions before we solve the rate equations.

The energy diagram for excited levels

In section 2.3, we described the Coulomb blockade theory for a quantum dot with one level. However, there are two states involved in the description of this single level; the ground state of the quantum dot without an additional electron (state 0; N electron state) and the ground state of the quantum dot with an additional electron (state 1; $N+1$

electron state).   The energy of the quantum dot level, which is equivalent to the electrochemical potential μ_{N+1}, is therefore the difference between the total energies of the two ground states.

$$\mu_{N+1}^0 = U^g(N+1) - U^g(N) \tag{2.19}$$

In (2.19), g represents the ground state and the superscript 0 on μ_{N+1} denotes the fact the all the relevant states are ground states.

If the $N+1$ electron state is in one of its excited states, the corresponding μ_{N+1} will be larger, whereas it will be smaller when the N electron state is in its excited state. The energy diagram in Figure 2.10(a) shows all three levels. μ_{N+1}^{-1}, the level below μ_{N+1}^0 corresponds to an excited state of the N electron state, and μ_{N+1}^{+1}, the level above μ_{N+1}^0 corresponds to an excited state of the $N+1$ electron state.

(a)

(b)
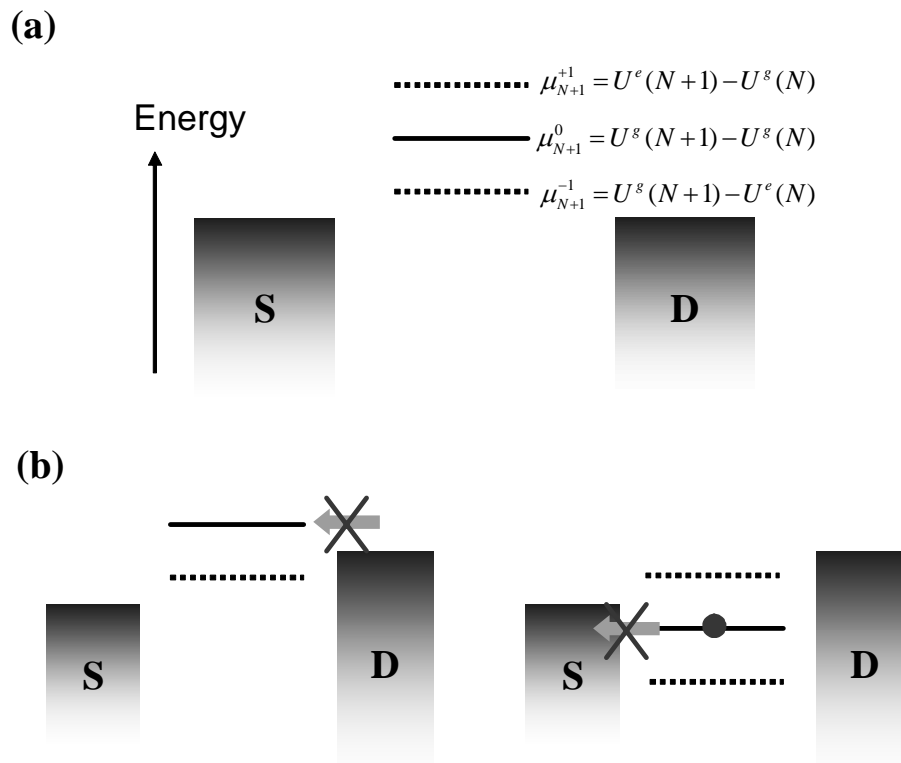
Figure 2.10 A quantum dot with excited levels. (a) Energy levels (electrochemical potentials) associated with excited states of either charge state. Depending on the origin of the excited state it can be located above or below the ground level. (b) When only an excited level is within the bias window, current does not flow because the ground level is not available. The current blocking processes are marked by crossed arrows.

For the rest of this chapter, we assume that all the tunneling processes involve at least one ground state. The tunneling processes between excited states of the N electron state and the $N+1$ electron state will not be considered. This assumption is closely related to the lifetime (or relaxation time) of excited states and the calculations based on this assumption can describe transport data well if the excited-level lifetimes are shorter than the electron tunneling time (the inverse of the tunneling frequencies).

The cases that may cause confusion are illustrated in Figure 2.10(b), where only μ_{N+1}^{-1} or μ_{N+1}^{+1} is located between the two Fermi levels of electrodes. Unlike the case where μ_{N+1}^{0} is located in the bias window, these cases will not sustain any electric current. The reason is the following for the first case where only μ_{N+1}^{-1} is located within the bias window. In this energy configuration, an electron can tunnel onto the dot only when the N electron state is in its excited state. If an additional electron tunnels out of the dot leaving it in the ground state of the N electron state, an electron cannot jump onto the dot any more because it will require μ_{N+1}^{0}, which is above the Fermi level of both electrodes. This current blocking process is marked by a crossed arrow in Figure 2.10(b). In short, μ_{N+1}^{0} is always required to be located within the bias window for a quantum dot to conduct.

Solving the rate equations for a two-level quantum dot

To understand how excited levels affect electron transport properties of a quantum dot, let's study the special case of a quantum dot with only one excited state for the $N+1$ electron state. In this case the quantum dot has only the ground state for the N electron state but it has both the ground and excited state for the $N+1$ electron state. As in the previous section, we can define P_0, P_1^g and P_1^e, where P_1^g (P_1^e) is the probability that an additional electron is in the ground (excited) state of the $N+1$ electron state. Then we can set up the rate equations as follows.

$$\frac{\partial P_0}{\partial t} = -P_0 \left(\Gamma_S^g f_S^g + \Gamma_D^g f_D^g + \Gamma_S^e f_S^e + \Gamma_D^e f_D^e \right)$$

$$+ P_1^g \left(\Gamma_S^g \left(1 - f_S^g \right) + \Gamma_D^g \left(1 - f_D^g \right) \right) + P_1^e \left(\Gamma_S^e \left(1 - f_S^e \right) + \Gamma_D^e \left(1 - f_D^e \right) \right)$$

$$\frac{\partial P_1^g}{\partial t} = P_0 \left(\Gamma_S^g f_S^g + \Gamma_D^g f_D^g \right) - P_1^g \left(\Gamma_S^g \left(1 - f_S^g \right) + \Gamma_D^g \left(1 - f_D^g \right) \right)$$

$$\frac{\partial P_1^e}{\partial t} = P_0 \left(\Gamma_S^e f_S^e + \Gamma_D^e f_D^e \right) - P_1^e \left(\Gamma_S^e \left(1 - f_S^e \right) + \Gamma_D^e \left(1 - f_D^e \right) \right)$$

(2.20)

Here the superscripts *g* and *e* represent a ground state and an excited state, respectively. For simplicity, we assume that the relaxation rate from the excited state to the ground state of the *N*+1 electron dot is zero. This does not violate the earlier assumption because each tunneling process involves at least one ground state (the ground state of the *N* electron state). However, one should include relaxation terms to develop better quantitative models for a real quantum dot.

By setting $\frac{\partial P_0}{\partial t} = \frac{\partial P_1^g}{\partial t} = \frac{\partial P_1^e}{\partial t} = 0$ for the equilibrium state, we can solve (2.20) for

P_0 and P_1^g using $P_0 + P_1^g + P_1^e = 1$. Then the current can be calculated as follows.

$$\frac{I}{|e|} = -P_0 \left(\Gamma_S^g f_S^g + \Gamma_S^e f_S^e \right) + P_1^g \Gamma_S^g \left(1 - f_S^g \right) + P_1^e \Gamma_S^e \left(1 - f_S^e \right)$$

$$= \frac{\Gamma_S^g \Gamma_D^g \left(f_D^g - f_S^g \right) \left[\Gamma_S^e (1 - f_S^e) + \Gamma_D^e (1 - f_D^e) \right] + \Gamma_S^e \Gamma_D^e \left(f_D^e - f_S^e \right) \left[\Gamma_S^g (1 - f_S^g) + \Gamma_D^g (1 - f_D^g) \right]}{\left(\Gamma_S^g + \Gamma_D^g \right) \left(\Gamma_S^e + \Gamma_D^e \right) - \left(\Gamma_S^g f_S^g + \Gamma_D^g f_D^g \right) \left(\Gamma_S^e f_S^e + \Gamma_D^e f_D^e \right)}$$

(2.21)

The solution is already quite bulky for this simple two-level quantum dot. As in a one-level quantum dot, the current amplitude is decided by $\left(f_D^g, f_S^g, f_D^e, f_S^e \right)$, a set of the four Fermi functions. Figure 2.11(a) shows them for different regions of the *V-V_G* map at *T* = 0 K. There are nine different regions shown in this map and any two regions have different sets of values of the Fermi functions. There are a total of four lines separating these regions; two of them cross *V* = 0 at $V_G = V_C$, and the other two at $V_G = V_C^e$. The first two lines correspond to an alignment event of the ground level to one of the Fermi levels of the electrodes and the second set of lines correspond to the cases where the excited level is aligned to electrode Fermi levels. Substitution of $\left(f_D^g, f_S^g, f_D^e, f_S^e \right)$ into (2.21) produces the *I-V-V_G* map, which is shown in Figure 2.11(b). It shows that only four out

(a)

(b)
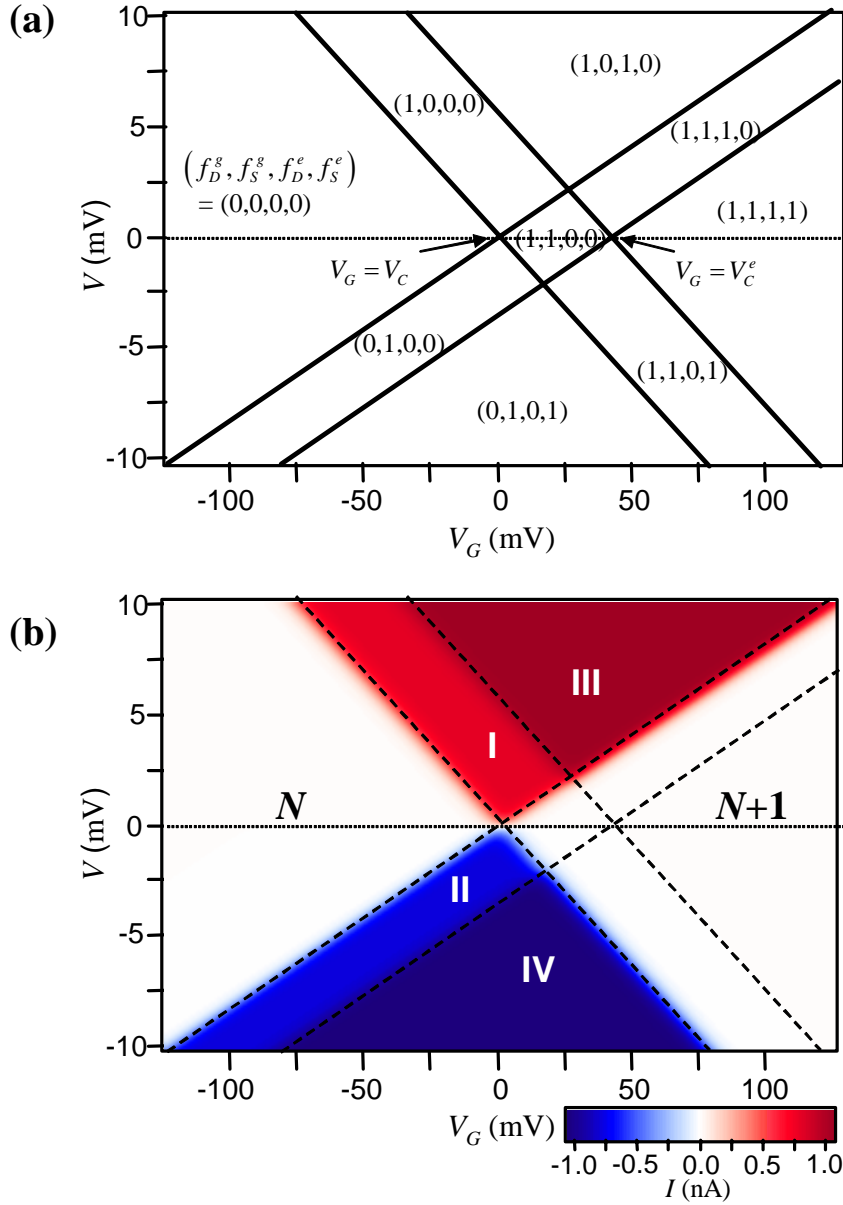
Figure 2.11 Current calculated for a two-level quantum dot. (a) The map of Fermi functions in different regions of V-V_G. (b) Current calculated for the two-level quantum dot. The number of electrons on the dot is shown in each blockade region. The parameters used in this calculation are the same as in Figures 2.5-2.7. The excitation energy for the excited level is 2 meV with the same tunneling rates as for the ground level (10 GHz). The temperature is 1.5 K.

of nine regions conduct and in all of those four regions the ground level is located between the two electrode Fermi levels. In regions I and II, where only the ground level is located in the bias window, the current amplitude becomes $\left|I^{I \ or \ II}\right| = \left|e\right|\Gamma_D^g\Gamma_S^g/\left(\Gamma_D^g+\Gamma_S^g\right) \equiv \left|e\right|\Gamma^g$, the same as (2.11). The current level is different from $\left|e\right|\Gamma^g$

for regions III and IV where both the ground and excited levels are located within the bias window.

$$I^{III} = |e| \frac{\Gamma_S^g \Gamma_D^g \Gamma_S^e \Gamma_D^e \left(1/\Gamma_D^e + 1/\Gamma_D^g\right)}{\left(\Gamma_S^g + \Gamma_D^g\right)\left(\Gamma_S^e + \Gamma_D^e\right) - \Gamma_D^g \Gamma_D^e} = |e| \Gamma^g \frac{\Gamma_S^e + \Gamma_D^e \Gamma_S^e / \Gamma_D^g}{\Gamma_S^e + \Gamma_D^e \Gamma_S^g / \left(\Gamma_S^g + \Gamma_D^g\right)}$$

$$I^{IV} = -|e| \Gamma^g \frac{\Gamma_D^e + \Gamma_S^e \Gamma_D^e / \Gamma_S^g}{\Gamma_D^e + \Gamma_S^e \Gamma_D^g / \left(\Gamma_S^g + \Gamma_D^g\right)}$$

(2.22)

This change in the current level is a direct consequence of the presence of an
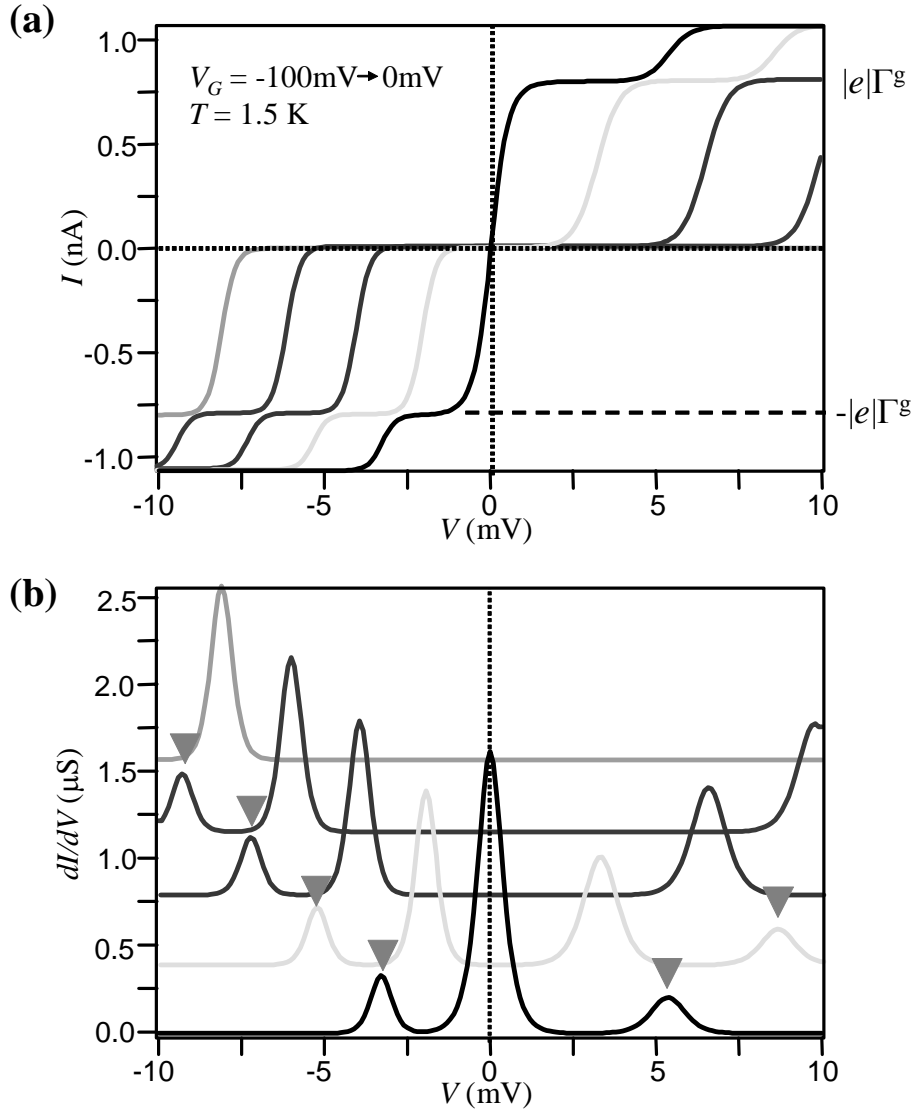
Figure 2.12 The *I-V* curves (a) and *dI/dV-V* curves (b) at different V_G's. Additional current steps and conductance peaks (gray arrows) are observed, which correspond to the excited level of the quantum dot. The conductance curves in (b) are offset by 0.4 µS for clarity. Quantum dot parameters are the same as in Figure 2.11.
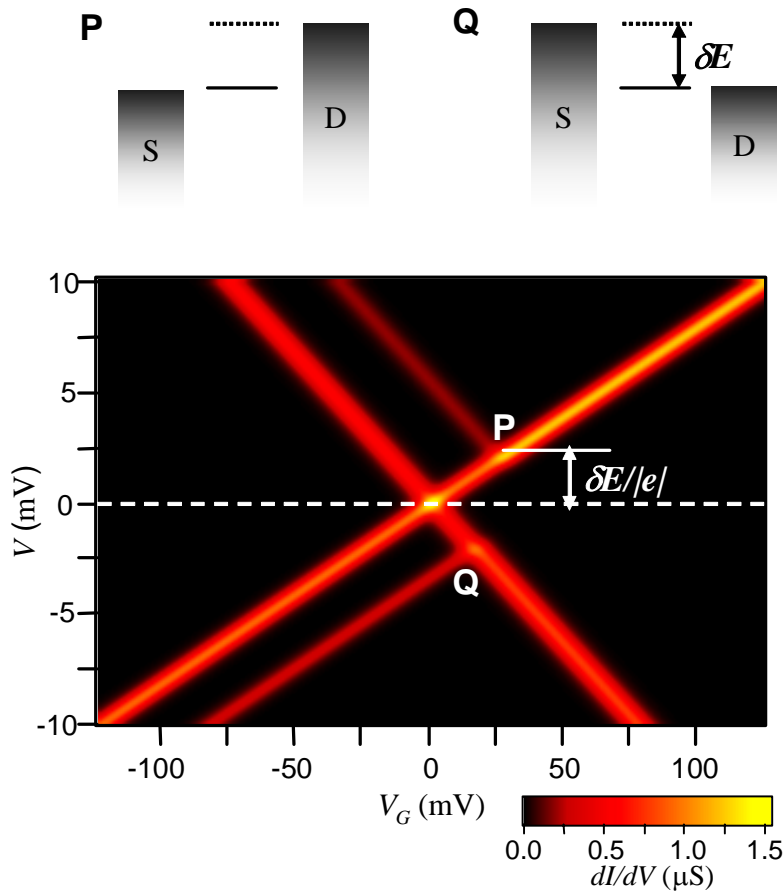
Figure 2.13 The differential conductance plot as a function of V and V_G for a two-level quantum dot. There are two additional dI/dV lines, both representing an alignment event between the excited level and one of the electrode Fermi levels. The excitation energy ($\delta E = 2$ meV) of the excited level is equal to the bias voltage of the intersection between the excited level line and the ground lines (P and Q). The quantum dot parameters are the same as in Figures 2.11 and 2.12. Note that both excited level dI/dV lines intersect the ground level lines at $V_G > V_C$.

excited state. Unlike the case with only the ground level within the bias window, (2.22) shows that the current amplitude is different for positive (region III) and negative bias (region IV). The difference in the current amplitude between region I and III (or between region II and IV) will be represented by a current step in an *I-V* curve taken at a fixed gate voltage and by a *dI/dV* peak in *dI/dV-V* curve (Figure 2.12). Therefore, the *dI/dV-V-* V_G map will show a line along the boundary between regions I and III (also between regions II and IV). Since that boundary corresponds to the excited level aligned to the Fermi level of the drain (or source for the boundary between II and IV) electrode, these *dI/dV* lines enable us to measure the excitation energy $\delta E = U^e(N+1) - U^g(N+1)$

associated with the excited state. For example, the point P in Figure 2.13 corresponds to the energy configuration where the ground level is aligned to the source Fermi level and the excited level to the drain Fermi level. In the energy diagram, it is clear that δE is equal to $|e|V$. Therefore, from the bias voltage where an excited level *dI/dV* line intersects with a ground level *dI/dV* line, we can measure the excitation energy, δE. This method of measuring an excitation energy is routinely used in real quantum dot experiments to study the excitation spectrum of a quantum dot. We also note from Figure 2.13 that both excited level *dI/dV* lines intersect the ground level lines at $V_G > V_C$. In general, this is true for all excited level *dI/dV* lines that correspond to the excited states for the *N+1* electron state (see Figure 2.16(b)).

Before we move on to the next subject, let's see how much a current level increases after the excited level becomes available for electron tunneling in different cases.

Case I: Symmetric tunnel barriers - $\left(\Gamma_S^g = \Gamma_D^g, \ \Gamma_S^e = \Gamma_D^e \equiv k\Gamma_D^g \right)$

When all the tunneling rates are symmetric, the current in the regions III and IV are as follows.

$$I^{III} = -I^{IV} = |e|\Gamma^g \frac{2}{3}(1+k) \tag{2.23}$$

As can be expected from its symmetric tunnel barriers, the current level in the regions III and IV are equal. The current will be larger than the ground state current $|e|\Gamma^g$ when $k > \frac{1}{2}$ but it will be smaller when $k < \frac{1}{2}$. When k is small (therefore low tunneling rates for the excited level), an electron that tunnels into the excited level is "stuck" and the overall current level will be lower than the one without the excited level. In this case, the current will actually decrease once the excited level becomes available and the *dI/dV-V-V_G* plot will show a *dI/dV* line with negative values. This is one mechanism that a quantum dot can show a negative differential conductance (NDC) or equivalently, a negative differential resistance (NDR). However, it requires more sophisticated model to describe the conditions for NDRs. For example, the relaxation

rate from the excited level to the ground level needs to be considered to describe NDRs in real quantum dots.

Case II: Asymmetric tunnel barriers - $\left(\Gamma_S^g / \Gamma_D^g = q, \Gamma_S^e / \Gamma_S^g = \Gamma_D^e / \Gamma_D^g = k\right)$

Many quantum dots have tunnel barriers with different tunnel frequencies. When q becomes large ($q \gg 1$) the current amplitudes that will flow in regions III and IV are as follows.

$$I^{III} = |e|\Gamma^g \frac{1+k}{1+1/(q+1)} \approx |e|\Gamma^g (1+k)$$

$$I^{IV} = -|e|\Gamma^g \frac{1+k}{1+q/(q+1)} \approx -|e|\Gamma^g (1+k)/2$$

(2.24)

Here the current will be approximately twice larger for the positive bias than the negative bias. Figure 2.14(b) explains the origin of this difference using energy diagrams. For positive bias, electrons tunnel onto the quantum dot from the drain and then tunnel off the dot to the source electrode. The current will increase significantly when the excited state becomes available because now electrons have more ways to tunnel onto the dot through the tunnel barrier of the drain side, the thicker barrier that decides the total current level. Compared to the positive bias, the negative bias case where electrons flow from the source to the drain will see smaller current, because an electron on a dot sits in one of the levels before tunneling through the thicker barrier, basically reducing the number of options from two to one.

This case also shows that the size of a current step (or a *dI/dV* peak) corresponding to an excited level in *I-V* curves (*dI/dV-V* curves) can be different for two bias directions. In reality, it is quite common to see an excited level *dI/dV* peak for only one bias direction. In such cases, the *dI/dV* line is stronger for the configuration where the excited level is aligned to the Fermi level of the electrode that has the thicker tunnel barrier. Therefore, it can be used to identify which tunnel barrier is thicker than the other (See Figure 2.14(a)).

In both Case I and II, the amplitude of current steps in *I-V* curves allows us to obtain information about the tunneling rate Γ's for different excited levels. In general,

(a)

(b)
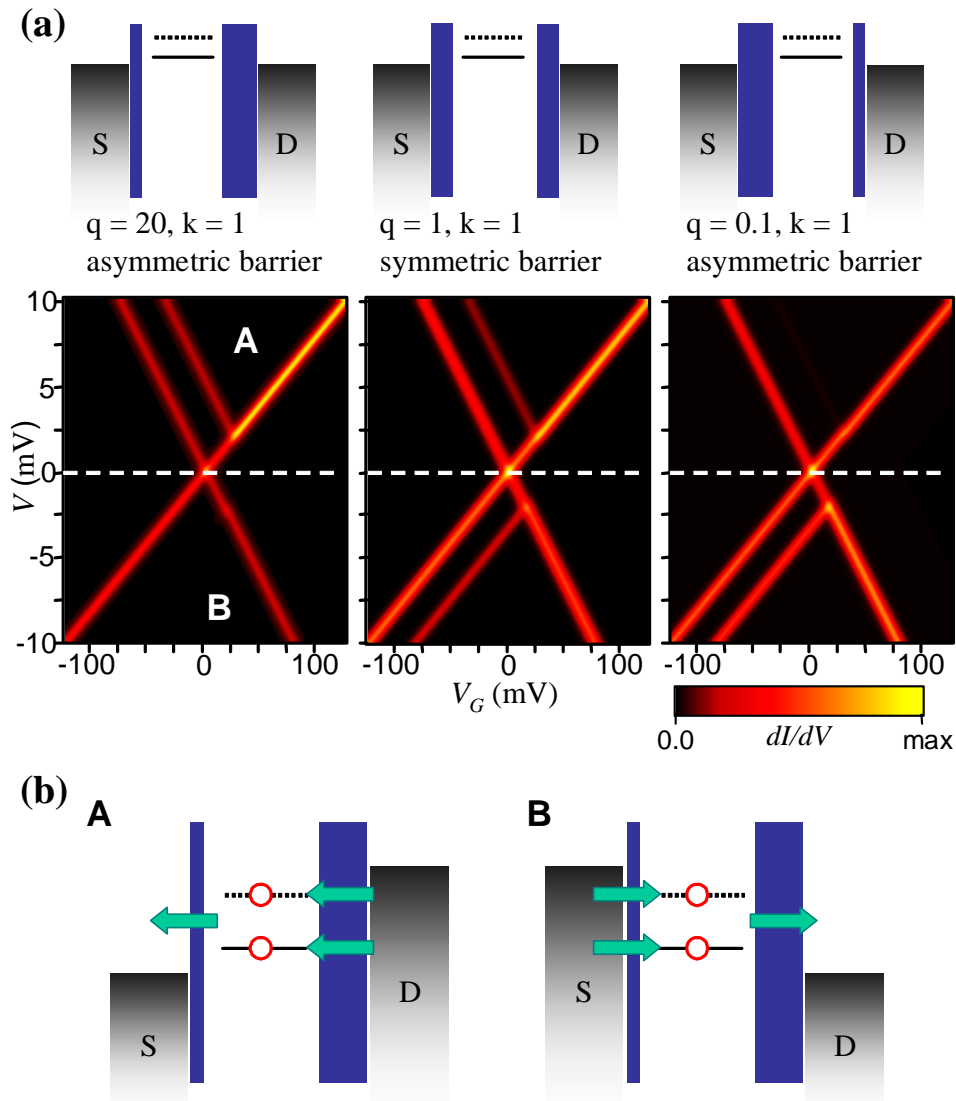
Figure 2.14 Effects of asymmetric tunnel barriers. (a) Conductance plots for three different tunnel barrier configurations. When the tunnel barriers are asymmetric, the excited *dI/dV* line is strong only for one bias direction. (b) The origin of the current asymmetry between regions A and B marked in (a). Current is larger in the region A because an electron tunnels onto either the ground level or to the excited level of the dot through the thicker (drain side) barrier. The number of arrows in the diagram represents the number of tunneling paths that a tunneling electron can use when it tunnels through the barrier.

the current step will be larger for larger Γ's. However, one should carefully set up a model to obtain quantitative information. We will see one such example in Chapter 4.

Example: the Zeeman splitting in a spin-1/2 quantum dot

Until now we have ignored the spin degeneracy of the electronic states of a quantum dot. However, real quantum dots have various degrees of spin degeneracy

depending on *S*, the total spin in a specific charge state. If *S* = 0, it is a singlet and there is no spin degeneracy. If *S* = ½, it is a doublet and there are two spin-degenerate states (S_z = +1/2 and S_z = -1/2) with the same energy. In general, a state with spin *S* has (2*S*+1) degenerate levels.

The two-level quantum dot model just described can be used to study a quantum dot with spin 1/2. Let's first consider a quantum dot with the total spin *S* = 0. When an additional electron tunnels onto the dot it will have a non-zero spin. In many cases it is simply *S* = ½ with two spin-degenerate states. Therefore, it becomes a two-level quantum dot (spin-up and spin-down). When the magnetic field is zero (*B* = 0), the two levels are truly degenerate and all the tunneling rates are identical for both states. Even though it does not have any excited levels (it has two ground levels instead), we still need to use the two-level dot model to accurately describe this case. The current can be obtained from (2.21) by setting all the corresponding quantities for the ground state and the excited states equal.

$$\frac{I}{|e|} = \frac{2\Gamma_S \Gamma_D (f_D - f_S)}{\Gamma_S + \Gamma_D + \Gamma_S f_S + \Gamma_D f_D} \qquad (2.25)$$

The superscripts *e* and *g* are dropped for simplicity. Again, it conducts only in the region where $(f_D - f_S)$ is non-zero as in a single-level quantum dot (compare it with(2.11)). However, the current amplitude of each conducting region is different. The current for the positive (I^+) and negative (I^-) bias is,

$$I^+ = |e|\frac{2\Gamma_S \Gamma_D}{\Gamma_S + 2\Gamma_D}, \quad I^- = -|e|\frac{2\Gamma_S \Gamma_D}{2\Gamma_S + \Gamma_D}. \qquad (2.26)$$

Since the tunneling rates for the source and drain are usually different, I^+ and I^- will be different in general. If one of the tunneling rates is much larger than the other, the ratio between the two current amplitude can be as large as 2. This large current difference can be explained by the same argument that we used in explaining the current asymmetry in the Case II (asymmetric tunnel barriers). The quantum dot conducts better when electrons tunnel onto the dot through a thicker barrier. We also note that from the measured values of I^+ and I^-, one can get Γ_S and Γ_D using (2.26). It is again useful to note that the current amplitude of the positive and negative bias cannot differ by more than two in this case.

(a)

(b)

(c)
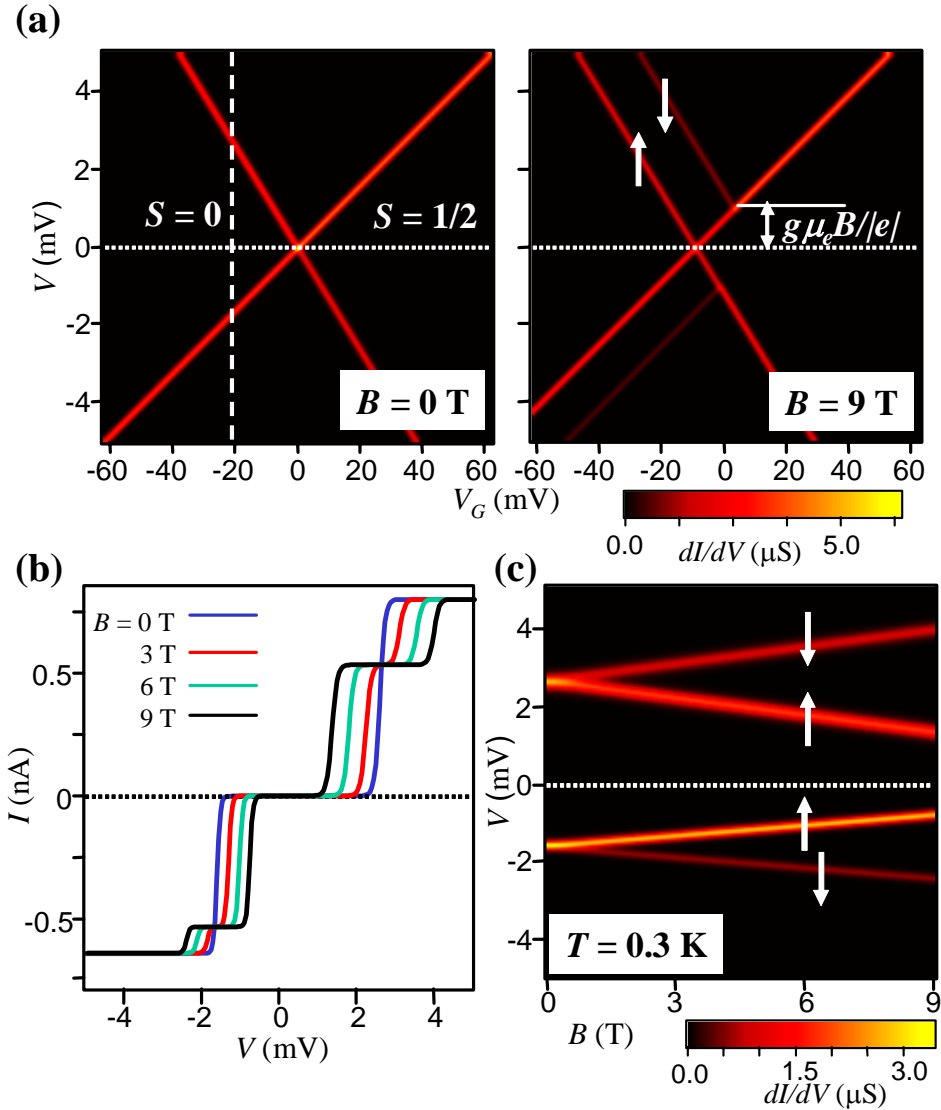
Figure 2.15 The Zeeman splitting of a spin-1/2 quantum dot. (a) The differential conductance plot at $B = 0$ T and 9 T. The Zeeman split dI/dV lines are clearly visible at 9 T. The parameters are $T = 0.3$ K, $E_0 = 0$ ($V_C = 0$ V), C_D:C_S:$C_G = 38$:57:5 ($\alpha = 0.05$), $\Gamma_S = 10$ GHz, $\Gamma_D = 5$ GHz. The spin states for the ground level and the excited level are marked by arrows. (b) *I-V* curves taken at $V_G = -20$ mV (dashed line in (a)) with different magnetic fields. The Zeeman splitting develops additional current steps. The ground level carries the same current for both bias directions but the additional current steps have different amplitude due to the tunnel rate asymmetry. (c) The dI/dV-V-B plot calculated at $V_G = -20$ mV.

When we turn on the magnetic field ($B > 0$), the spin degeneracy is lifted and the two previously degenerate levels will split into two states (the Zeeman splitting). The energy of the spin up state ($S_z = +1/2$) will be $U(N+1) - g\mu_e B/2$ and the energy for the spin-down state ($S_z = -1/2$) will be $U(N+1) + g\mu_e B/2$. Here g is the electron g-factor

and μ_e is the Bohr magneton. The ground level will move down in energy with increasing magnetic fields, while the other level (spin-down) moves up with the total energy difference of $g\mu_e B$. This energy difference is called the Zeeman energy and can be measured using the method explained earlier. It can be read from the bias voltage at the point where a *dI/dV* line corresponding to Zeeman split level intercepts the ground level (see Figure 2.15 (a)).

The quantitative model we developed for a two-level quantum dot can be used for this case by setting $\delta E = g\mu_e B$. For most cases, we can put $\Gamma^g_{S(D)} = \Gamma^e_{S(D)}$, but if the electrodes are magnetic, the tunneling rates can be different for the two spin states.

In Figure 2.15 (b) and (c), we show *I-V* curves and a *dI/dV-V-B* plot for a *S* = ½ quantum dot with asymmetric tunnel barriers at different magnetic fields. The Zeeman splitting is clearly visible for both bias directions and increases with the magnetic field. The second current step in the negative bias direction is smaller due to the asymmetry in the tunnel rates.

2.5 Transport Spectroscopy in a Multi-Level Quantum Dot

In principle, it is possible to solve the rate equations for a quantum dot with many excited levels. However, it is a lengthy calculation and should be done numerically in most cases. We can still qualitatively describe what the solutions would look like and how they describe the transport behaviors of a multi-level quantum dot.

As we saw in previous examples with one- or two-level quantum dots, the electric current flowing through a quantum dot can be decided solely by the values of the electrode Fermi functions evaluated at the energy of each excited or ground level in conjunction with the tunneling rates. Figure 2.16(a) schematically shows this for a quantum dot with five levels: one ground level (μ^0), two lower levels corresponding to excited states for the *N* electron state (μ^{-1} and μ^{-2}), and two higher levels for the *N+1* electron excited states (μ^{+1} and μ^{+2}). For each level, there are two boundary lines crossing *V* = 0 at $V_G = V_C^i$, which correspond to the level aligning to the source or drain Fermi level. When the current is calculated, each region will have different current

amplitude and we will see current steps at the boundaries of any two adjacent regions. As in the previous cases, the current level is non-zero only when the ground level is located between the two electrode Fermi levels and this limits the conducting region to the gray area shown in Figure 2.16(a). Since the current steps are located along the boundaries between different regions, *dI/dV* lines will be present along these boundaries

(a)

$$\cdots\cdots\cdots\cdots\ \mu^{+2} = U_{N+1}^{e2} - U_N^g$$
$$\cdots\cdots\cdots\cdots\ \mu^{+1} = U_{N+1}^{e1} - U_N^g$$
$$\text{————}\ \mu^0 = U_{N+1}^g - U_N^g$$
$$\cdots\cdots\cdots\cdots\ \mu^{-1} = U_{N+1}^g - U_N^{e1}$$
$$\cdots\cdots\cdots\cdots\ \mu^{-2} = U_{N+1}^g - U_N^{e2}$$

(b) *dI/dV-V-V$_G$*
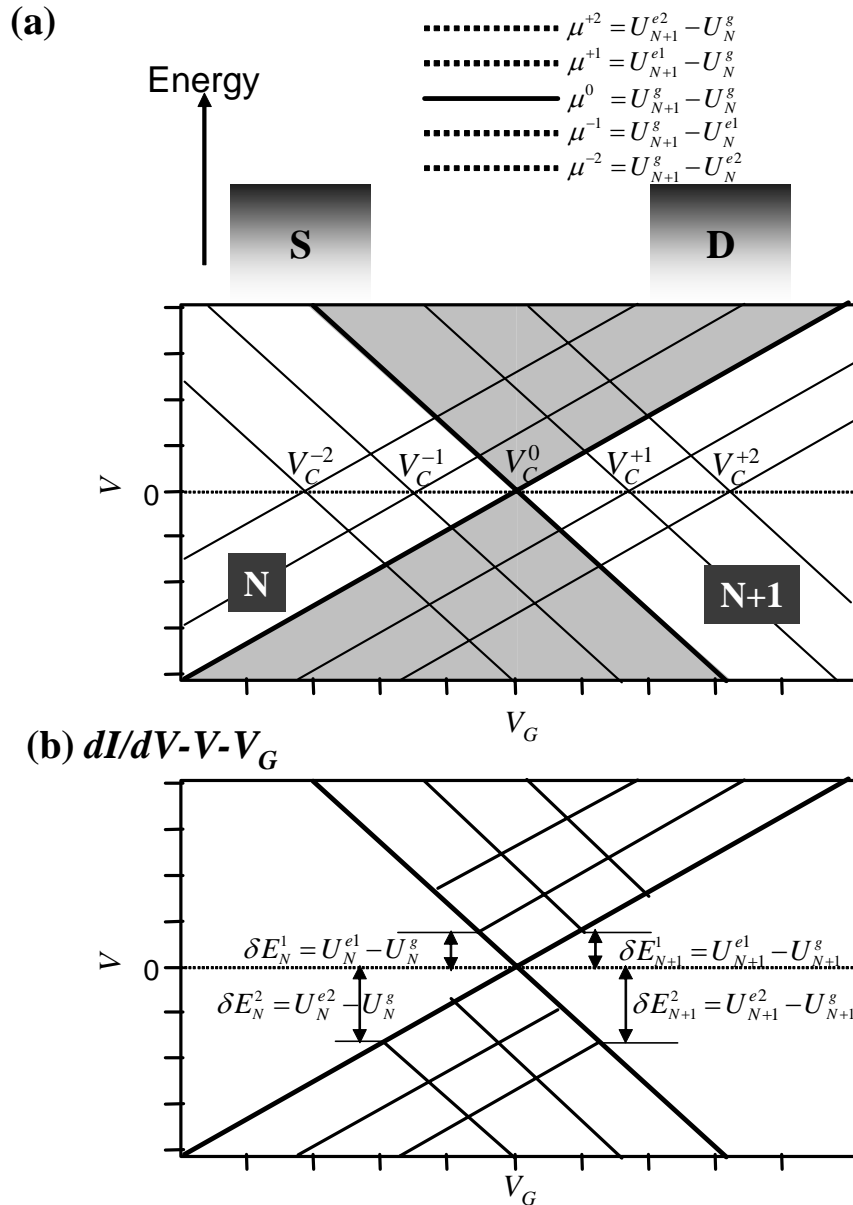
Figure 2.16 A multi-level quantum dot. (a) The energy diagram of a five-level quantum dot is shown. The conducting regions are painted gray in the *V-V$_G$* map. (b) Differential conductance map for the same quantum dot will display multiple excited *dI/dV* lines that correspond to various excited levels. The excitation energies can be measured as shown in the diagram for both charge states. The factor $|e|$ is dropped in the diagram for simplicity.

in the *dI/dV-V-V_G* map. As we can clearly see in Figure 2.16(b), each excited level of the quantum dot is associated with two such *dI/dV* lines; one for positive bias and the other for negative bias (assuming reasonably symmetric tunnel barriers). The excitation energy $\delta E^i_{N(\text{or }N+1)} \equiv U^{ei}_{N(\text{or }N+1)} - U^g_{N(\text{or }N+1)}$ can be read off from the bias of the crossing point between an excited level *dI/dV* line and the ground level *dI/dV* line. It is also important to note that all the excited *dI/dV* lines that end on the *N*+1 electron Coulomb blockade area (right side in Figure 2.16(b)) correspond to excited levels of the *N*+1 electron state and that all the excited *dI/dV* lines that end on the *N* electron Coulomb blockade area (left side) correspond to excited levels of the *N* electron state. Therefore, one can study excitation energies of both *N* and *N*+1 electron states of a quantum dot from the *dI/dV-V-V_G* plot. This allows the transport measurements on a quantum dot to be used as an excellent spectroscopic tool.

We can also obtain information about different tunneling rates associated with each excited level by measuring the intensity of the *dI/dV* lines in the *dI/dV-V-V_G* plot. Again, the *dI/dV* lines will be stronger when the tunneling rates associated with the corresponding excited level are larger.

2.6 Summary and Other Issues

In this chapter we described a theoretical model for a single electron transistor in the quantum dot regime. *I-V* measurements on a quantum dot display Coulomb oscillations and the Coulomb blockade, which occur due to the charge addition energy of an electron to a quantum dot. When excited levels are present in the dot, *I-V* (or *dI/dV-V*) curves will show additional current steps (*dI/dV* peaks) that correspond to the excited levels.

It is possible to study the excitation energy and the tunneling rates associated with each excited level using the Coulomb diamond plot and the amplitude of current steps or *dI/dV* peaks. Therefore, the transports measurements on a quantum dot performed at cryogenic temperatures offer a high-resolution spectroscopy technique that can be used for nanometer-sized objects.

The theory described in this chapter can be developed further to investigate other quantum dots in a variety of device conditions. One important parameter that has not

been included in this chapter is the relaxation from excited states to the ground state. Once an electron occupies an excited state, it can relax to the ground state before tunneling out of the dot. This process will affect the overall current level and should be considered when performing a careful analysis. If the relaxation rate is faster than the slower tunneling rate, then the quantum dot stays in its ground state in most cases (equilibrium process). In some systems, however, electrons tunnel on and off the dot before it relaxes to its ground state and cause non-equilibrium behavior[43].

Another important tunneling process is the co-tunneling process[23]. All the electron processes that have been discussed above are the sequential tunneling process, where an electron tunnels onto a dot and then leaves from it. The co-tunneling process is a second order tunneling process where an electron tunnels through the dot via intermediate levels that are energetically forbidden. This process is sometimes observed in a Coulomb blockade region when the overall conductance of the dot is large in its on state. It has been studied experimentally[44-46] as well as theoretically in various systems and provides a framework for coherent electron transport and tunneling vibrational spectroscopy. The Kondo effect that will be discussed in Chapter 6 is also a second order process that is closely related to this co-tunneling phenomenon.

Chapter 3

Device Fabrication and Experimental Setup

3.1 Introduction: Experimental Techniques for Wiring up Molecules

To perform conductance measurements on an object, one needs at least two electrodes contacting the object - one for the source electrode and the other for the drain. For a macroscopic object, this requires only a very simple experimental setup (*e.g.* a multimeter with a pair of probes). For much smaller objects, as long as they are larger than roughly 10 nm, conductance measurements can be performed using electrodes that are fabricated by standard lithography techniques[47].

However, conductance measurements on single molecules usually require a different experimental scheme, due to their exceedingly small size. Indeed, the molecules we will discuss in the following three chapters (Chapters 4-6) are all smaller than 3 nm. To measure the conductance of such a small molecule, two electrodes (source and drain) are required to have a nm-size gap so that they can be used to "wire up" the molecule. It is not a straightforward task since even the most advanced electron-beam (*e*-beam) lithography techniques still fail to make such structures reproducibly.

People have thus developed various new experimental techniques for wiring up single molecules. They include scanning probe microscopy (SPM) techniques and unconventional fabrication techniques for making nano-electrodes. Figure 3.1 summarizes some of the methods that have been used for studying electron transport in molecules.

One of the most powerful methods is **the SPM technique**[15, 19, 40] (Figure 3.1(a)). In this case, molecules are deposited on top of a conducting surface that acts as one electrode and a metallic scanning probe tip is used as the other electrode. A huge benefit of this technique is that one is allowed to actually "see" the molecules before measuring them. Therefore, it serves as a very versatile tool for studying single molecules. However, it requires a relatively high level of instrumentation and also enough expertise to perform the experiments, especially at cryogenic temperatures. Its

energy resolution is usually poorer than other techniques and it lacks the gate electrode. Especially, the latter is a significant disadvantage when one wishes to study different charge states of the same molecule.

One can circumvent the problems of the SPM techniques by fabricating electrodes with a nm-size gap directly on an insulating surface. **The mechanical break junction technique**[9, 48] (Figure 1.3(b)) has been successfully used to measure the conductance of a single molecule. First, a continuous metallic electrode is fabricated on a flexible

(a) SPM techniques

• STM

• AFM
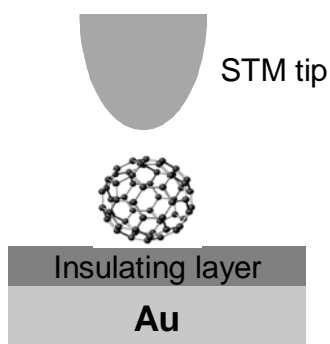
Porath *et al.* PRB (1997)
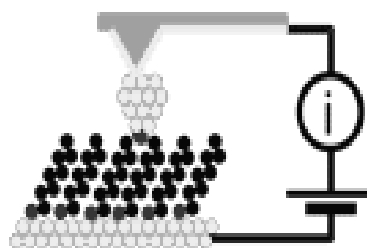
Cui *et al.* Science (2001)

(b) Planar devices (nanoelectrodes)

• mechanical break-junction

• electrodeposition
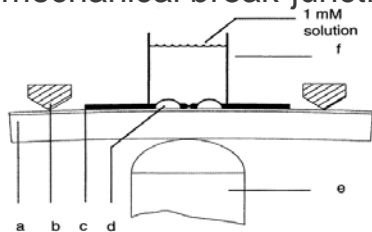
Reed *et al.* Science (1997)
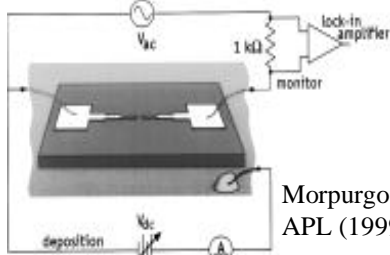
Morpurgo *et al.* APL (1999)

• nanoconstriction

• electromigration

Chen *et al.* Science (1999)
Petta *et al.* APL (2000)
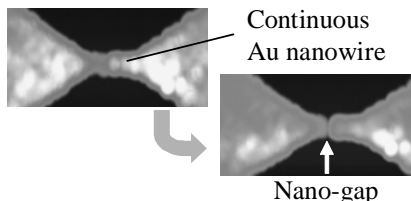
Park *et al.* APL (1999)
Park *et al.* Nature (2000)

Figure 3.1 Various techniques developed for measuring single molecule conductance. (a) Scanning probe microscopy techniques. (b) Fabrication methods for nano-electrodes.

substrate that is subsequently bent to extend the electrode until it breaks. This process can be well controlled to a very fine length resolution, typically below several pm. Until now most experiments that employed this technique lack the gate electrode due to experimental limitations.

People also developed unconventional nanofabrication techniques, two of which are shown in Figure 1.3(b). One can first fabricate two electrodes with a relatively large (>10 nm) separation and grow them electrochemically until they merge. This process, which is called **the electrodeposition technique**[49], can be controlled to produce electrodes with a nm-sized gap. Also shown is **the nanoconstriction technique**[17, 50] (also known as the nanopore technique) that is usually used for studying more than one molecule. In this technique, a small (<10nm) hole is first fabricated in a thin silicon nitride membrane and molecules are sandwiched between the top and bottom electrodes through this hole for electrical measurements. More recently, another fabrication technique was reported by Zhitenev *et al*[51]. In this method, two electrodes are side evaporated to a pulled quartz needle and the electrodes can be connected by molecules near the tip of the needle.

Finally, the technique used in most single molecule experiments described in the following chapters is **the electromigration technique**[52]. First, a continuous wire is fabricated using standard *e*-beam lithography. Then a large bias voltage, typically between 0.5 V and 1 V, is applied to cause a failure of the wire. This process is self-controlled; once the wire fails, current does not flow any more and the gap-opening process induced by the previously large current density stops. Conductance measurement after the electromigration process shows a tunnel conductance smaller than the conductance quantum ($G_0 = 2e^2/h = 77.5$ μS). This suggests that the size of the gap created by this process is small and typically less than 1~2 nm, which is ideal for wiring up a single molecule.

In this chapter, we will discuss various experimental issues regarding the device fabrication and the characterization. First, the fabrication procedure for continuous metal nanowires with gate electrodes will be described (section 3.2). Each wire is used to form two electrodes with a nanometer-sized gap using the electromigration technique. The details of the electromigration process will be described in section 3.3, followed by

discussions on the characterization of the electrodes after the process (section 3.4). Finally, various issues regarding molecule deposition will be discussed (section 3.5) as well as the general transport measurement setup (section 3.6) at the end of this chapter.

The device fabrication procedure is different for carbon nanotube devices because carbon nanotubes are much longer (> 1 μm) than the molecules studied in Chapter 4 through 6. The fabrication process for a carbon nanotube device is therefore described separately in Chapter 7.

3.2 Fabrication of Nanowires and Gate Electrodes

Before explaining the details of the fabrication process, let us remind ourselves of the goal of device fabrication. The schematic of device geometry desired for single molecule experiments is shown in Figure 3.2. Two metal electrodes are located on top of an insulating layer which functions as a gate insulator. The two electrodes are separated by 1~2 nm so that a single molecule can bridge them for electron transport. Below the insulating layer, we find a conducting substrate, which works as the gate electrode. An optical microscope image of a chip (5 mm by 5 mm) that has 36 nanowires is shown in Figure 3.3. Only macroscopic leads are visible in this picture and a continuous nanowire is shown in a separate scanning electron microscope (SEM) image. This nanowire, after it is broken by the electromigration process, will form two electrodes with a nanometer-sized gap.
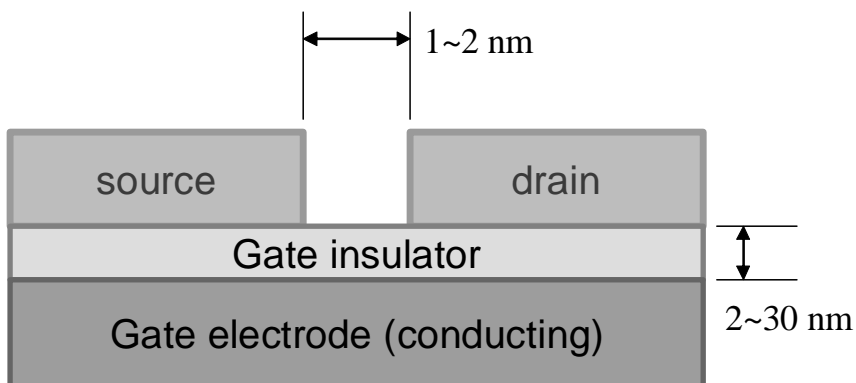
Figure 3.2 A schematic of the nanoelectrodes with a gate. It is not drawn to scale.
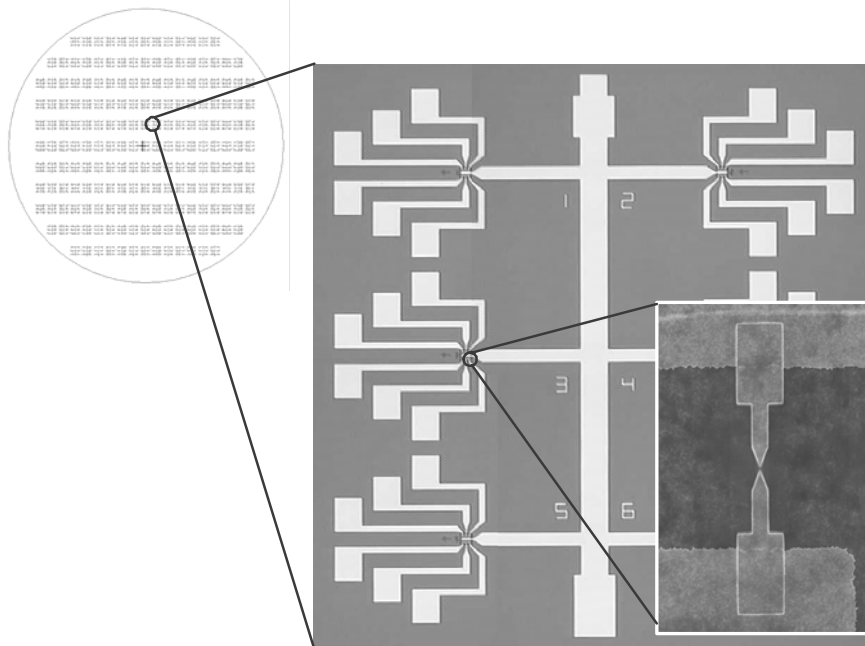
Figure 3.3 An optical microscope image of a chip with 36 nanowires. More than one hundred of these are fabricated on a 4" silicon wafer simultaneously. Only macroscopic gold electrodes are visible in this picture with the vertical bar in the middle serving as the common electrode. Size of the image: 5 mm by 5 mm. Lower inset: An SEM micrograph of a continuous gold nanowire (image size: 20 by 12 μm).

Properties of nanowires

Certain properties are required for the continuous metal wires. First, it should be breakable by the electromigration process briefly described above. It requires that the wires have a fairly small cross section at its smallest. The failure current density for a gold wire is approximately 10^{12} A/m^2[53]. To be able to break them with less than 10 mA, the cross section of the wire should be less than (100 nm)^2.

The thinnest and narrowest part of the wire, the part we will call a nanowire from now on, should also not be too long. The longer it is, the total resistance of the whole wire will be larger, which will require a large bias voltage to achieve the failure current density. This can lead to the destruction of the junction after breaking.

For example, to flow 10 mA at a bias voltage below 0.5 V, the total resistance cannot be larger than 50 Ω. It is a quite stringent condition since there are other parasitic resistances as well. First, the electromigration process is usually performed in a cryostat, which requires resistive wiring for thermal isolation. Second, there is also the resistance

of various wires in the measurement set up. Finally, the nanowires are connected to outside wiring through a thin (<200 nm) film of macroscopic metal electrodes defined by photolithography. These films increase the total resistance typically by several Ohms.

If the cross section of the nanowire is $(10 \text{ nm})^2$, the critical current can be reached with a voltage of 0.5 V for resistance up to 5 kΩ. It is, however, very difficult to define nanowires with a width less than 10 nm and a thickness less than 10 nm. For example, a Au film thinner than 10 nm will be grainy and even discontinuous.

Most wires we used therefore have a width between 20 nm and 200 nm. The thickness is between 10 nm and 20 nm. The length is approximately 200 nm. The typical total resistance of the wire (nanowires resistance plus parasitic resistances) is between 100 Ω and 1 kΩ. It is also important to make the macroscopic wiring film thick enough (>100 nm) in order to reduce the parasitic resistance and also to make the wirebonding easier. If the macroscopic wiring film is too thin (<50 nm), wirebonding can be troublesome. The wire may not stick to the film strongly enough to produce a good electrical connection and the bonding process can even destroy the gate insulator.

Properties of the gate oxide

There are three words that will describe the desired properties of the gate oxide - thinner, smaller and stronger. First, the gate needs to be located very close (less than 50 nm) to the molecule to produce a large gate capacitance. As we discussed earlier (see equation (2.3)), the electrochemical potential of a quantum dot can be controlled by a gate electrode with the gate efficiency set by a capacitance ratio ($\alpha = C_G / C_{total}$). Since the maximum range of an applicable gate voltage is limited (the gate insulator will eventually fail!), it is always advantageous to have good gate efficiency. The relation between the gate capacitance and the thickness of the gate insulator will vary depending on the local device geometry and electrostatics. In a simple parallel capacitor, the capacitance is proportional to $1/r$ where r is the distance between the two plates. However, our experience with different gate insulator thicknesses suggests that the gate efficiency increases by more than just $1/r$ when one thins the gate insulator.

Second, the size of the gate oxide region should be as small as possible. As discussed in the previous paragraph, our capability of changing the electrochemical

potential of a quantum dot depends both on the gate efficiency and the maximum gate voltage we can apply without a gate failure. All the gate oxides that we use in our experiments (SiO_2 and Al_2O_3) are proven to be good insulators up to certain electric field strengths but fail at very high electric fields, typically ~1 V/nm. This implies that one should be able to apply up to 30 V to the gate when one uses a 30 nm thick gate oxide. In reality, the oxide usually fails well below 30 V and in some cases electric current flows between the gate and the source/drain electrodes even at very low biases. This premature gate failure and gate leakage is caused by impurities and pin-holes present in the gate oxide.

To minimize this annoying possibility, one can reduce the overlap area between the gate and the source/drain electrodes. Again, it is not a good idea to make the whole electrode structure (typical total area ~ 0.1 cm^2) on top of a 30 nm gate oxide. Instead, one can reduce the premature gate failure and gate leakage by defining two regions with different gate thicknesses; a small region with a thin gate oxide and all other areas with a thicker (> 200 nm) field oxide. Another reason that one should have an area with a thick field oxide is the wirebonding process. If the oxide is too thin for the wirebonding area, wirebonding process can destroy the oxide and short the gate with source/drain electrodes. A field oxide thicker than 200 nm is usually strong enough to avoid any wirebonding nightmares.

Third, and finally, one should try to grow a good, strong oxide. It is closely related to the problems we discussed above. The density of pin-holes and impurities needs to be minimized to reduce the gate leakage and gate failure. This issue is closely related to the material properties and the details of the fabrication procedure (for example, cleanliness). So far we have used two different materials for the gate oxide. A silicon oxide was grown by dry oxide growth process in a CMOS compatible furnace and an aluminum oxide layer was grown by oxidation of aluminum electrodes in an ambient condition for a day. Both gate oxides performed well enough for our experiments but the aluminum oxide was proven to be more useful thanks to its 2~3 nm thickness.

Fabrication procedure

For past five years, several different device designs have been developed to produce the devices geometry illustrated in Figure 3.2 and 3.3. Main differences among such designs include a different choice of gate/gate oxide material and the fabrication method for nanowires. Describing all these different designs will be tedious and somewhat pointless. In this section, instead, the overall fabrication process for two different device designs will be described, which will explain most fabrication techniques that we have used over the years.

Device design I: Silicon/silicon oxide gate and angle evaporation

The first design shown in Figure 3.4 utilizes the silicon substrate of a silicon wafer as the gate electrode (back gate). We used a degenerately doped silicon wafer to ensure that the substrate stays conducting at cryogenic temperatures. The typical resistivity of the wafer is less than 0.005 $\Omega \cdot cm$. The wafer is covered with ~1 μm of field oxide (SiO_2) pre-grown on top. This thick oxide layer will serve as an insulator between the back gate and macroscopic (> mm) structures that will be subsequently defined on top of it. The first process is defining the gate regions. For a small region (70 μm×70 μm), the field oxide is etched by a wet etching process using buffered HF

1 μm thick SiO_2

degenerately doped Si

70 μm

30 nm thick gate oxide

Pt gate contact

thin Au (30 nm)

thick Au (200 nm)
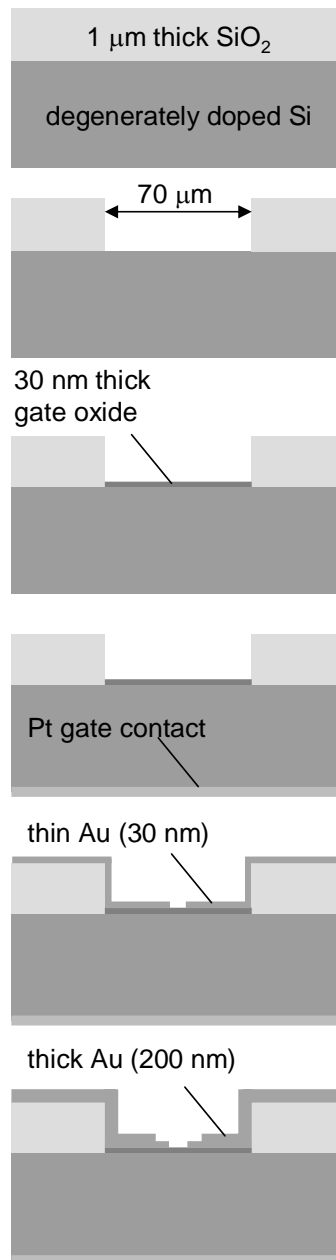
Figure 3.4 The fabrication procedure for the device design I. After step V, it is ready for the fabrication of nanowires (see the next Figure).

step I: defining gate regions (photolithography, wet etching)

step II: gate oxide growth (dry oxide growth process)

step III: back gate contact (wet etching and Pt evaporation)

step IV: thin Au layer (photolithography, lift-off)

**step V**: thick Au layer (photolithography, lift-off)

with a photoresist mask that is defined by a standard photolithography (step I). A 30 nm thick gate oxide is grown by a standard dry oxide growth process in the gate region (step II). The growth of a sacrificial gate oxide layer followed by wet etching is done between steps I and II to reduce the gate oxide impurities and pin-holes. Then the oxide on the back side of the wafer is stripped by HF wet etching and 100 nm of platinum or gold is evaporated to make an electric contact to the back gate (step III). This completes the fabrication of the gate electrode and the gate and field oxide.

The other two electrodes on the surface are fabricated by the following processes. Using the standard photolithography and lift-off, we fabricate macroscopic Au electrodes which run through both the gate oxide region and the field oxide region.   These electrodes are made in two steps. The first thin Au layer was made by evaporating approximately 30 nm of gold with 2 nm of Cr as a sticking layer (step IV). The thick Au layer was then made by evaporating over 200 nm of Au with 2 nm of Cr that overlaps almost all the area covered by the thin Au layer except the edges that will be contacted by nanowires later (step V).   This two-step process is necessary to ensure that the macroscopic electrodes are thick enough to cover the step edges between the thick oxide and the thin gate oxide regions, but thin enough on their ends so that it can be connected to the nanowires easily. The design pattern of the macroscopic electrodes was already shown in Figure 3.3. It has a long vertical electrode that serves as the common electrode for all the wires. There are 36 other macroscopic electrodes grouped into six groups. These 36 electrodes can be wired up separately to allow a conductance measurement between the common electrode and each one of these electrodes.

Finally the nanowires are fabricated using *e*-beam lithography (Figure 3.5). First a bilayer of *e*-beam resist (first MMA/MAA then PMMA) is spun on the surface. Then we expose the target area that will later become nanowires using an electron beam. At this stage, the exposed area is discontinuous in the middle and looks like two needles with >100 nm separation (see Figure 3.5). Carefully timed development of the *e*-beam resists in the MIBK/isopropanol solution will dissolve the PMMA resist in the *e*-beam exposed areas but it will develop to a slightly larger area in the bottom MMA/MAA layer since this layer dissolves in the MIBK solution faster than the PMMA layer. As a result,

we will have a suspended PMMA layer with a hollow tunnel underneath in the MMA/MAA layer.

Viewed from the top, the two exposed areas will still look like two separated needles and a direct evaporation of metal alone will not form a continuous nanowire. To fabricate continuous nanowires, we use an angle evaporation that is described below (see

a *e*-beam exposure

e-beam exposed area

e-beam

PMMA

MMA/MAA

Side view

Top view
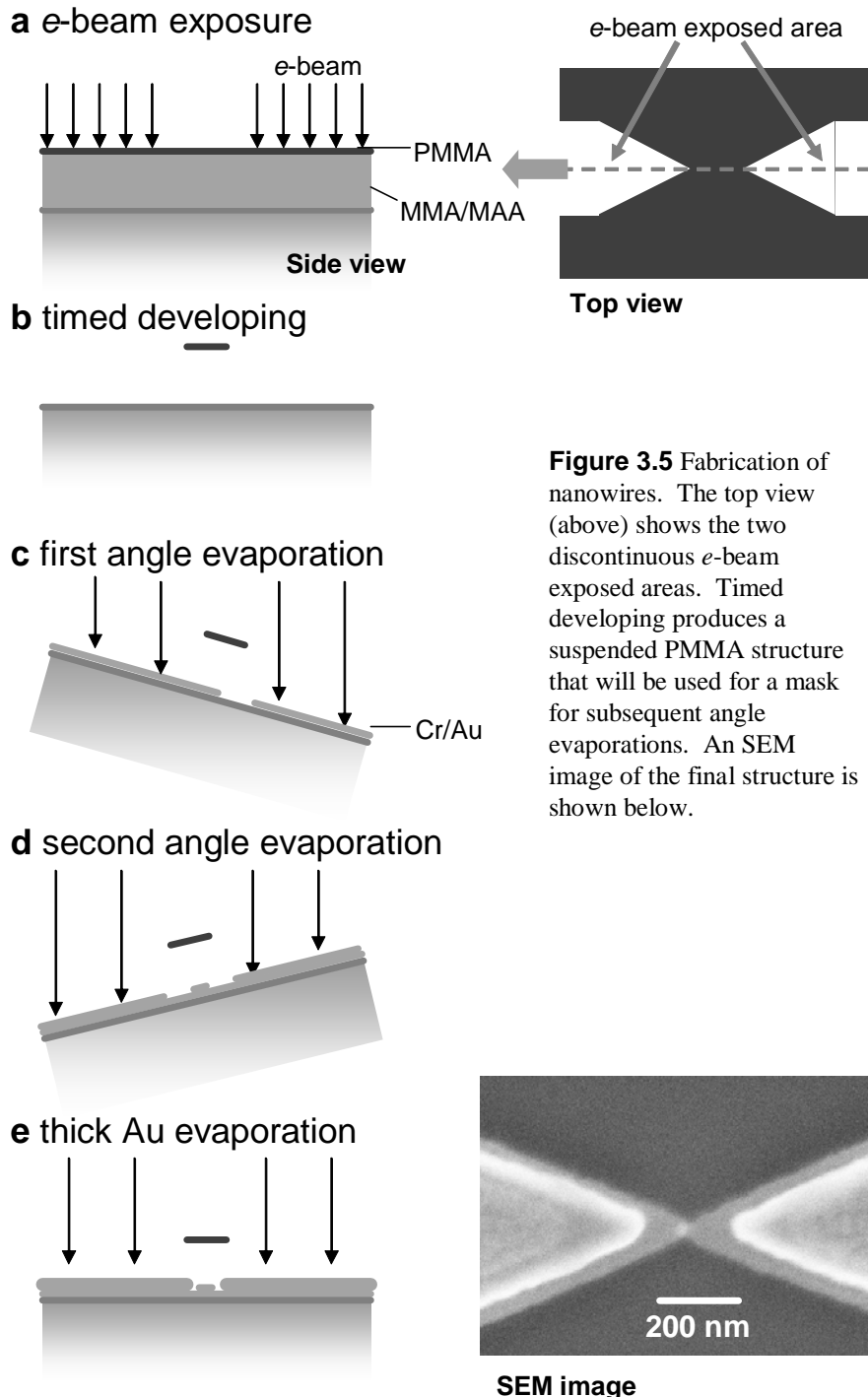
b timed developing

Figure 3.5 Fabrication of nanowires. The top view (above) shows the two discontinuous *e*-beam exposed areas. Timed developing produces a suspended PMMA structure that will be used for a mask for subsequent angle evaporations. An SEM image of the final structure is shown below.

c first angle evaporation

Cr/Au

d second angle evaporation

e thick Au evaporation

200 nm

SEM image

Figure 3.5(c) through (e)). First, the whole wafer is tilted 15 degrees versus the direction of evaporation and 3 nm of Cr and 10 nm of Au is evaporated. Then the wafer is tilted 15 degrees in the opposite direction and again 3 nm of Cr and 10 nm of Au is evaporated. Finally the wafer is rotated back to the original orientation in which its surface is vertical to the evaporation direction. The final evaporation of 3 nm of Cr and 80 nm of Au is done in this orientation. This three-step metal evaporation will leave continuous nanowires with a thin (~15 nm) Au layer with small thicker overlap region in the middle. A liftoff in acetone will leave only the nanowires on the surface. One advantage of this somewhat complicated nanowire fabrication process is that the dimension of the thin region is very small (< 200 nm). In all other sections of the whole current path, the parasitic resistance is minimized by evaporating at lease 100 nm of Au. An SEM image of one finished wire is shown in Figure 3.5.

**Device design II:** Al/Al_2O_3 gate and direct evaporation

Design I has several difficulties. The angle evaporation requires careful parameter controls and can be irreproducible depending on the condition of the *e*-beam system. Also the silicon gate oxide, even though it can be made thinner than 10 nm, is still thicker than aluminum oxide gates (2~3 nm) described below and limits the gate capability. In the device design II, major changes have been made in the gate oxide and evaporation method for the nanowires. The overall fabrication process is illustrated in Figure 3.6.

The silicon wafer used for this design does not require degenerately doped silicon since it is no longer used as a back gate. But it still needs to have a thick (>200 nm) field oxide for electric isolation between all the structures on the surface and the silicon substrate. The field oxide also serves as a protective layer against any wirebonding-induced short between electrodes and the substrate.

The fabrication starts with photolithography and liftoff for macroscopic electrodes. The device pattern is the same as the previous design. It has a vertical common electrode and 36 individual electrodes grouped into six separate groups of electrodes. Among these 36 electrodes, six of them are used to make contacts to the Al/Al_2O_3 gate electrode, as can be seen from the finished device design. The

macroscopic electrodes are again made in two steps; a 20 nm thin Au layer and then a 100 nm thick Au layer that does not cover the edges of the thin Au layer. The edges of the thin Au layer are used to make contact to nanowires and gate electrodes.

Then aluminum gate electrodes 20 nm thick and 2 μm wide are defined using photolithography followed by a low-temperature evaporation on a liquid-nitrogen-cooled evaporation stage. Then the wafer is exposed to air in ambient condition so that it will
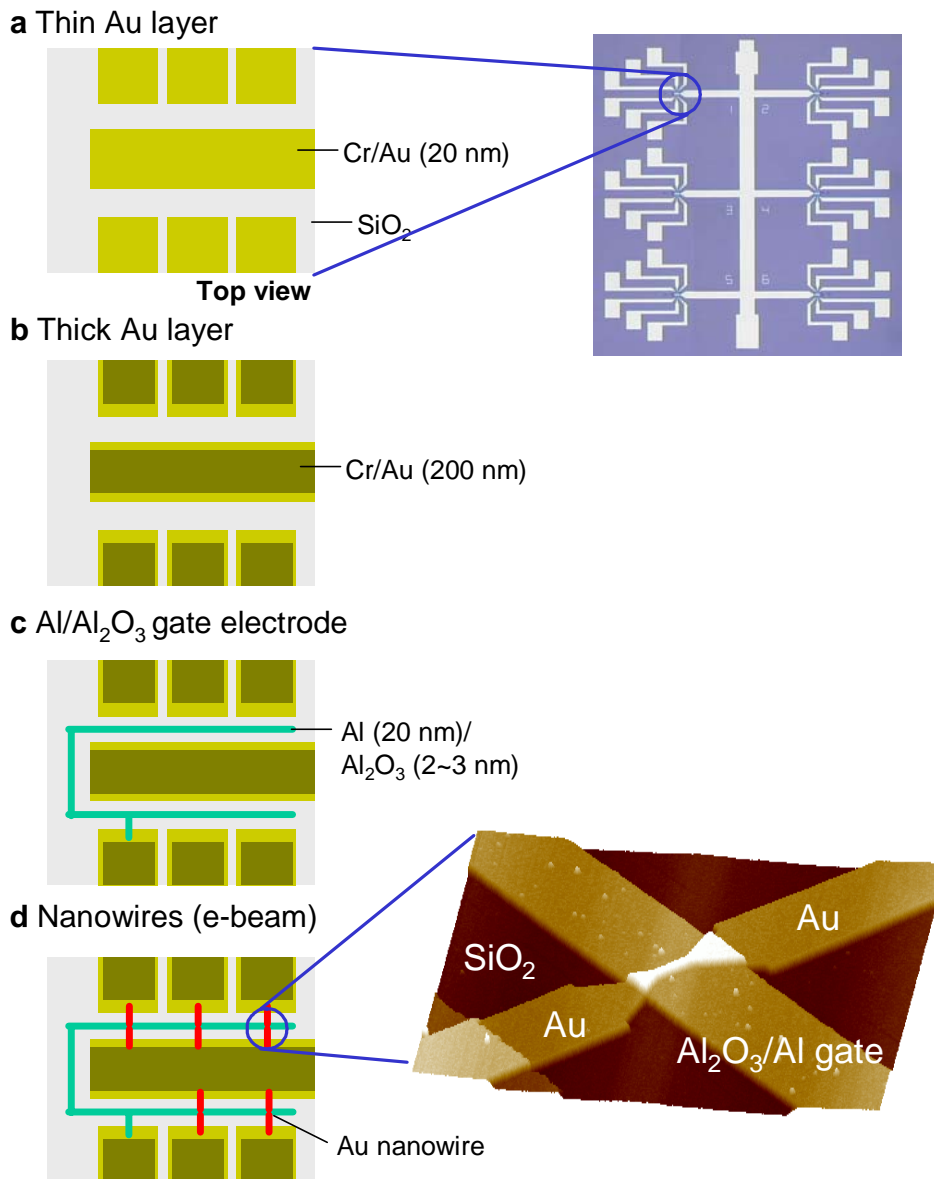
Figure 3.6 Device design II. Al/Al_2O_3 gate electrodes are used instead of silicon oxide. The thin Au, thick Au and Al gate electrodes are made by photolithography and liftoff. After the gate oxidation, nanowires are made using *e*-beam lithography. A topographic AFM image (5 μm by 5μm) is shown at the bottom.

form a native aluminum oxide on the surface of the aluminum electrodes. It is known that this process grows a 2~3 nm thick oxide[34]. Finally the wafer is immersed in acetone overnight for a liftoff. One gate electrode is made for each electrode group so that each chip will have six separate gate electrodes. This design helps to reduce the number of lost devices caused by gate leakage and gate failure since a gate failure or leakage of one gate electrode affects only five nanowires. The low temperature used for the aluminum evaporation tends to crack the photoresist and the surface after a liftoff has small random aluminum wires. It needs to be etched away using an aluminum etchant while the aluminum gate electrode is covered by photoresist.

The nanowires are made by *e*-beam lithography as in the design I but the pattern used for the e-beam lithography is continuous in this case. Therefore it requires no angle evaporation. In terms of e-beam resists, either a PMMA single layer or a PMMA - MMA/MAA bilayer can be used. We evaporate approximately 20 nm of Au with 1~2 nm of Cr as a sticking layer. The *e*-beam pattern that is designed for the nanowires has two tapering needle-like electrodes connected by a thin line. This thin line becomes a nanowire after the *e*-beam process and a liftoff. A topographic AFM image of the finished device is shown in Figure 3.6.

Other materials have been used for the nanowires instead of Au. To date, aluminum and platinum nanowires have successfully formed electrodes with a nm-size gap by the electromigration process.

There are two other issues about the geometry of the nanowires. First, in most of the experiments described in this thesis, a thin (1~2 nm thick) Cr layer was used as a sticking layer so that Au evaporated on top of it adheres well and forms a continuous wire. It, however, raises a question about whether the presence of Cr atoms near the gap formed by the electromigration would affect the device conductance. To test this, we also fabricated nanowires without a Cr layer and measured its properties. Our measurements suggest that its presence does not change the breaking property of the wires or their conductance after the breaking significantly.

Second, different thicknesses of nanowires have been used. Normally we evaporate more than 15 nm of Au for nanowires. It has been suggested that thinner electrodes will allow the target molecules to be located closer to the gate electrode,

increasing the gate efficiency[54]. Au electrodes without a Cr sticking layer tend to form grains and often become discontinuous when made thinner than 10 nm. However, 10 nm thick platinum wires without Cr layer have been successfully made and used for measuring single molecules. Due to lack of enough data, it is not clear whether thin electrodes increase the gate efficiency at this moment.

3.3 Electromigration-induced breaking in nanowires

Figure 3.7 shows the electromigration-induced breaking of the nanowires made
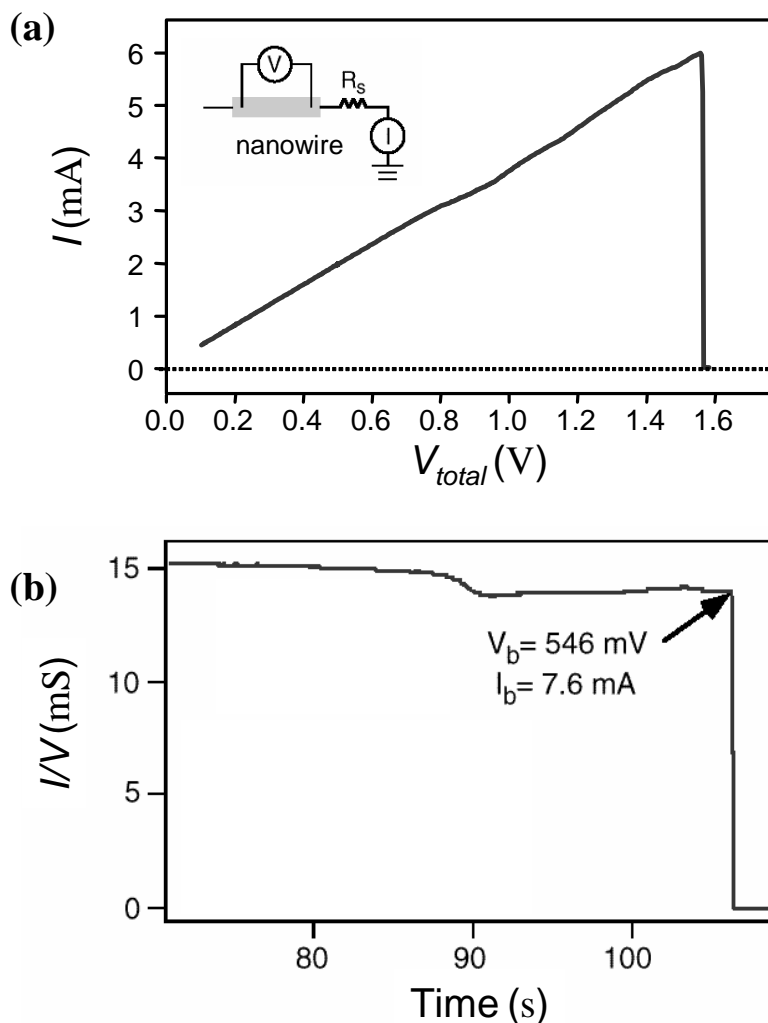
**Figure 3.7** Electromigration induced breaking of a nanowire. (a) The nanowire shows an ohmic behavior until the current level drops to zero at high bias. Note that V_{total} is not equal to the voltage drop across the nanowire. (b) Average conductance (I/V) as a function of time while increasing the bias. It drops to zero at a breaking voltage (V_b) of 546 mV and a breaking current of 7.6 mA.

by the fabrication process in section 3.2. We performed a four-probe measurement as shown in the Figure 3.7(a); the current (I) as well as the voltage drop (V) across the nanowires was measured at the same time.

We plot the current versus the total bias (V_{total}) applied to the circuit in Figure 3.7(a). In this plot, the current keeps increasing until V_{total} reaches 1.56 V and then it suddenly drops to zero. This breaking curve shows that the nanowire behaves like an ohmic conductor up to a certain current density and then fails, forming a physical gap within the nanowire. The breaking process of a similar wire can be seen in a different plot shown in Figure 3.7(b). The average conductance (I/V) instead of current was
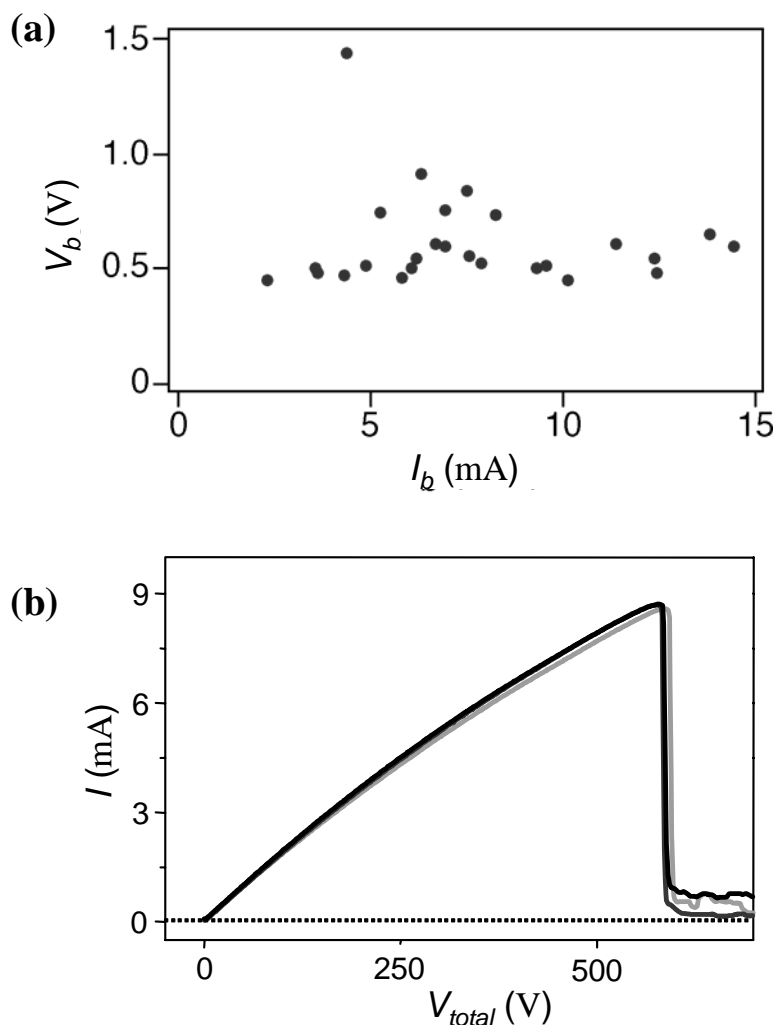
Figure 3.8 The breaking behavior of nanowires. (a) Breaking voltage V_b versus breaking current I_b measured from different nanowires. Most nanowires break near 0.5 V. (b) Breaking curves of three different nanowires made from the same fabrication run show almost identical behavior.

plotted as a function of time while ramping the total bias with a constant rate ($\sim$ 30 mV/s). The average conductance of the wire stays relatively constant until it reaches the critical point at I_b and V_b, where the conductance decreases to near zero suddenly.

The breaking voltage V_b and breaking current I_b measured from $\sim$ 30 nanowires are plotted in Figure 3.8(a). One can clearly see V_b is near 0.5 V in most wires regardless of the breaking current (equivalently, initial resistance). For a nanowire with the length L and the cross section A, the relation between the breaking voltage and the critical current density j_b is as follows:

$$V_b = I_b R = j_b A \cdot \rho L / A = j_b \rho L \qquad (3.1)$$

Here ρ is the resistivity of the nanowire. Since the length of the nanowires is relatively constant near 200 nm, equation (3.1) in conjunction with Figure 3.8(a) shows that the breaking process in the nanowires is dictated by the current density and that the critical current density required for breaking is almost constant over a large spectrum of initial resistance. From the breaking current and the geometry of nanowires ($I_b \sim$ 7 mA for $A \sim$ 15 nm$\times$200 nm), we can estimate $j_b = I_b/A \sim 2 \times 10^{12}\,\mathrm{A/m^2}$, which is similar to the value reported by Durkan *et al*[53]. These behaviors indicate that the main breaking mechanism in the nanowires is electromigration, whose main determinant is the current density as discussed below.

The exact breaking voltage V_b can be slightly different from device to device depending on the nanowire geometry and material choices, but the nanowires that are fabricated in the same fabrication run usually show a very similar breaking voltage. It can be seen from Figure 3.8(b), where breaking curves (I-V_{total}) taken from three different wires made in the same fabrication run show almost identical breaking properties. Thus the wire breaking process shown here is a well-controlled process that can be reproduced over different wires; it is not a random process.

Electromigration process

Electromigration is frequently observed in many metallic structures. When a metal wire is kept under a large current density over a long period of time, it finally fails due to a formation of a gap along the wire. This causes a serious problem in

microelectronic circuits, and there have been many studies[55] about the origins of this failure mechanism, which will be described below.

Electrons traveling in a solid undergo various scattering events caused by impurities, dislocations, and grain boundaries. When an electron changes its motion due to a collision with one such scatterer, it transfers momentum to the scatterer and exerts a force on it. This force can cause the scatterer to move out of its original site. The frequency of these relocation events will be higher for a larger current density. It will be also accelerated at higher temperatures because lattice phonons will help atoms move out of their original site. This mass transport process caused by a large electric current density ("electron wind") is called electromigration.

Black[56, 57] gave a phenomenological description of electromigration, known as the Black equation. It describes the median conductor failure time (MedFT) when it was kept under a set of certain conditions, such as current density and temperature. The equation for a multi-domain wire is as follows:

$$MedFT = Aj^{-n}\exp\frac{E_a}{k_BT} \qquad (3.2)$$

This equation has been tested experimentally for different materials. In (3.2), j is the current density and E_a is the activation energy for the electromigration process. A is a constant that varies according to the geometry and the microstructure of the wire. For Au, E_a is reported to be about 0.9 eV and n is measured near 2 in most reports[55].

The Black equation predicts that the mean failure time is decided mainly by the current density and temperature. From (3.2), a shorter failure time is expected for a larger bias at a constant environment temperature, because at a larger bias, the current density will be larger and the wire temperature will be higher due to Joule heating. Therefore, from these behaviors one can predict the presence of the critical current density (equivalently, critical bias), where the failure time is shorter than a few seconds. This is consistent with the breaking behavior of our wires, which display a sudden failure above a certain bias voltage (V_b) regardless of the initial resistance.

The failure mechanism of gold nanowires was also studied by Durkan *et al*[53]. They concurred that wide (> 100 nm) gold wires break at a typical current density of 2×10^{12} A/m^2 with slight variations depending on detailed wire geometry such as the

width, length, and oxide thickness. The wires failed at lower current density when the oxide is thicker, because it slows down the heat dissipation, causing a higher temperature of the wire.

One important issue is the wire temperature at the breaking current density. Durkan *et al.* estimated it to be near 500 K. More recent experiments by Lambert *et al.*[58] showed that the average local temperature at the breaking current density is approximately 400 K, which will give the lower bound for the temperature of the breaking point. These numbers will vary depending on the actual geometry of the wires and the thickness of the silicon oxide insulator. As Durkan *et al.* pointed out, the oxide thickness is important since it decides the efficiency of heat dissipation through the surface, affecting the local temperature of the wires. The temperature profile along a nanowire changes depending on its length, too. Therefore, the breaking temperature proposed Durkan *et al.* or Lambert *et al.* can provide only a rough estimate for the breaking temperature of our nanowires. However, it is clear that the mechanism of the wire failure in all cases is thermally activated electromigration.
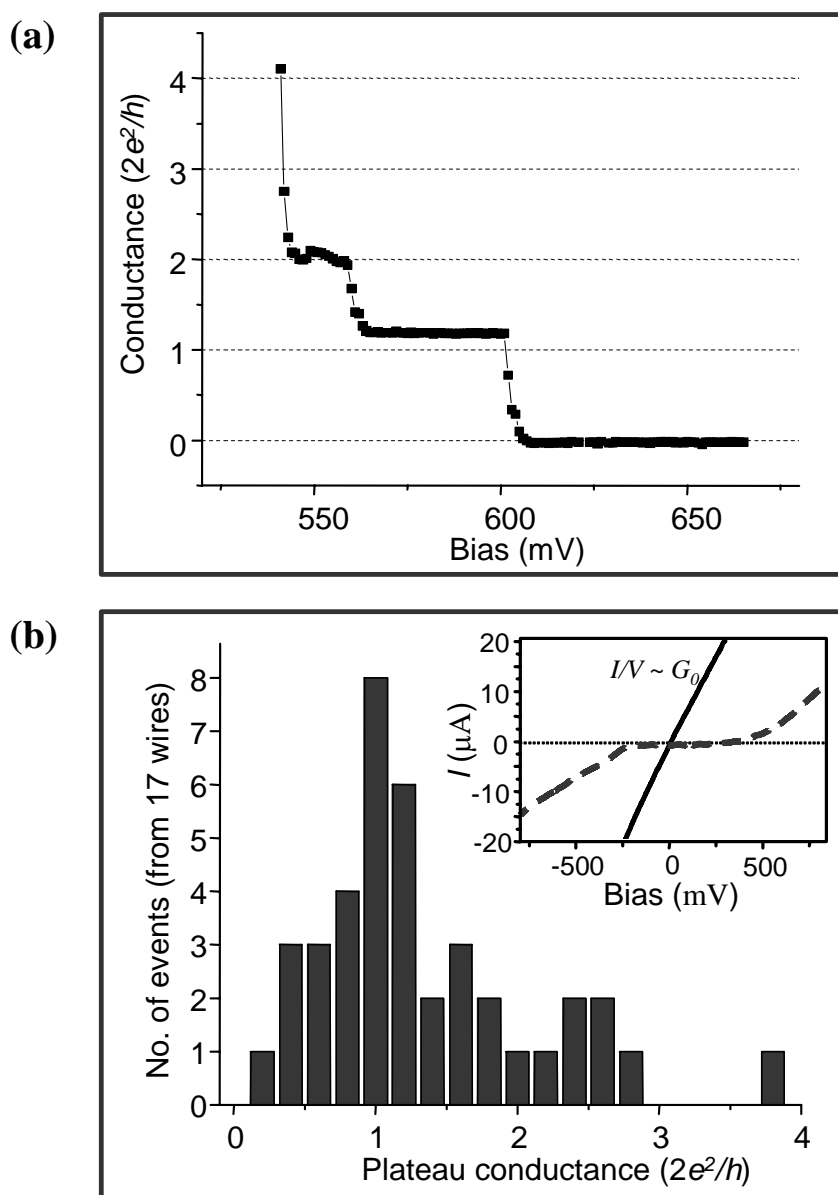
Formation of few-atom contacts

The nanowires can sometimes be broken to form a few-atom contact (Figure 3.9). The breaking process was performed at below 4 K in a liquid helium cryostat in this case. The nanowire shown in Figure 3.9(a) initially breaks to an average conductance of approximately 160 μS and then subsequent increase in bias decreases the conductance to approximately 80 μS. Finally, further bias increase breaks the nanowire to a very large tunnel resistance. The intermediate conductance values measured in this breaking curve are approximate multiples of the conductance quantum, $2e^2/h = 77$ μS. This suggests that the wire breaks first to a configuration where two gold atoms are bridging the two electrodes across the gap and then the number of gold atoms decreases to one when the bias is increased further. It is completely broken when the bias is increased even more, forming a tunnel gap between the two electrodes.

Two *I-V* curves from the same nanowire are shown in the inset to Figure 3.9(b). The *I-V* curve taken after the conductance decreases approximately to the conductance quantum shows an ohmic behavior, which is expected from a single atom contact (solid

curve). It changes after the wire breaks further and it shows a nonlinear *I-V* curve (dashed curve). Again, this suggests that the wire forms a few-atom contact and finally breaks to a tunneling gap that shows a nonlinear tunneling *I-V* curve.

In Figure 3.9(b), a histogram of the intermediate conductance measured from breaking curves of 17 wires is plotted. A prominent peak near $2e^2/h$ is clearly visible in

(a)

(b)

**Figure 3.9** Formation of a single atom contact during the electromigration process. (a) The breaking curve shows two plateaus near multiples of the conductance quantum, suggesting the nanowire formed a few-atom contact. (b) A histogram of the plateau conductance measured from 17 nanowires. It shows a strong peak near the conductance quantum. Inset: *I-V* curves taken at the conductance quantum and after the final breaking.

this histogram, suggesting that the electromigration process in these wires can be controlled to a single-atom contact. The formation of a stable single atom contact was not observed at room temperatures, presumably because of the instability of atomic configurations at higher temperatures.

3.4 Characterization of the Tunnel Gap after Electromigration

As discussed in the previous section, the electromigration process breaks the wires and forms a physical gap within them. The formation of the gap can be seen from images taken by SEM or AFM.

SEM images taken from a wire before and after the breaking are shown in Figure 3.10(a). The presence of a gap between the electrodes is clearly visible after the wire is broken and the size of the narrowest gap is below 5 nm. However, an accurate measurement of the gap size is difficult because it lies below the resolution limit of the SEM. The picture shows that the location of the gap is not always in the middle of the
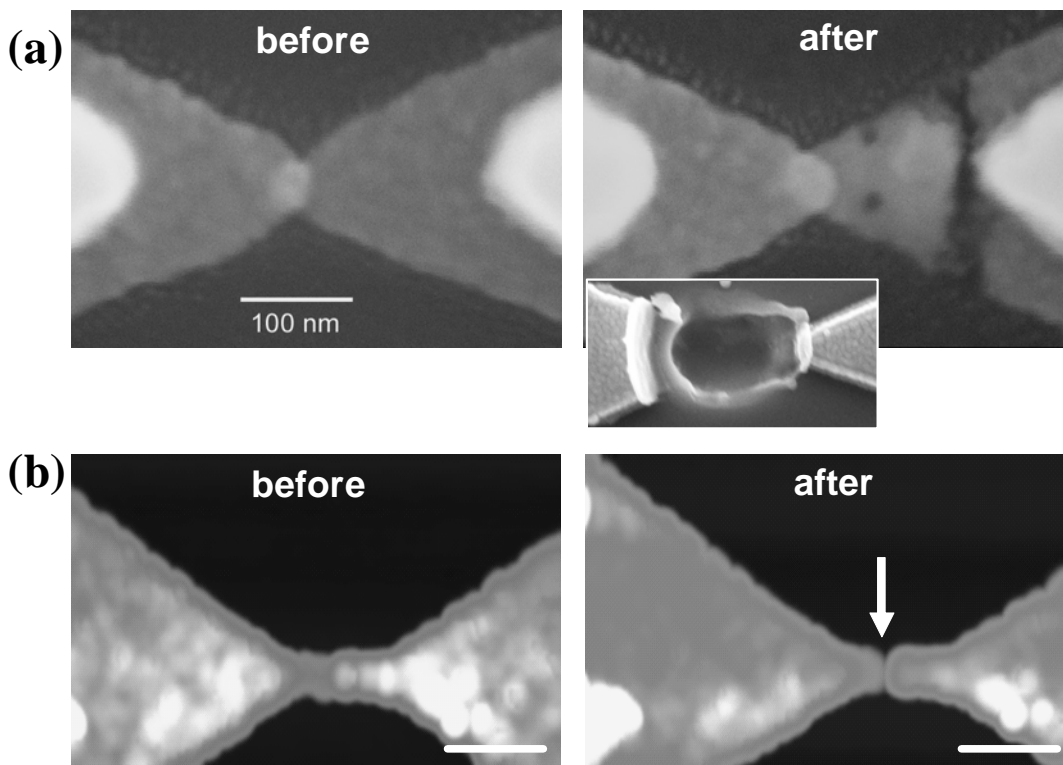
Figure 3.10 STM (a) and AFM (b) images of a nanowire before and after the electromigration-induced breaking process. The wire shown in (a) is fabricated using the design I explained in section 3.2, whereas the wire in (b) was fabricated by the design II. Both images taken after the breaking clearly show a physical gap formed within the nanowire (marked by an arrow in (b)). Scale bar in (b): 200 nm. For comparison, an SEM image of an accidentally broken wire is shown in (a).

wire. This phenomenon has been observed by others[53]. An SEM image of an accidentally broken (by static, most likely) wire is also shown in Figure 3.10(a) for comparison.

Figure 3.10(b) shows topographic AFM images of a wire before and after breaking. Again they clearly show the gap in the middle of the wire, but it is not possible to measure the size of the gap because it is smaller than the size of the AFM tip. In addition, the narrowest point of the gap may lie at the bottom, which an AFM tip cannot reach.

We can identify the location of the tunnel gap using the electrostatic force microscopy (EFM) technique, which allows one to measure the voltage drop across a conducting material. Figure 3.11 shows an EFM image of a wire after it is broken by electromigration process. The voltage drop is abrupt in this image, unlike the gradual voltage drop that can be seen in the EFM image taken before the breaking (not shown). The electrode on the right side (where an AC bias is applied) has a constant electric potential up to the break point without showing any potential drop, whereas the one on the left completely disappeared in the image, showing that the two electrodes are electrically separated. The location of the electrical break matches the location of the physical gap (both locations marked by an arrow) in the wire shown in Figure 3.10(b). This confirms that the tunnel gap actually coincides with the physical gap formed by the electromigration process. It is also clear in this case that the gap is formed near the middle of the wire, where the highest current density and temperature are expected. However, the size of the tunnel gap still cannot be measured using these imaging techniques.
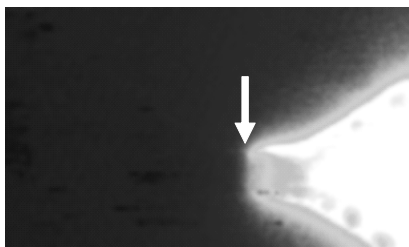
Figure 3.11 An AC-EFM image taken after the wire is broken by electromigration process. The electrode on the right side (bias side) shows up brightly whereas the other electrode completely disappeared. This indicates that the two electrodes are electrically separated by the physical gap (arrow) formed by the electromigration process. (Courtesy of Ji-Yong Park and Markus Brink)

The size of the tunnel gap, therefore, needs to be measured indirectly from its tunnel conductance. Figure 3.12 shows *I-V* curves taken from a nanowire before and after breaking. Before the breaking, the resistance is 40 Ω. Once the nanowire is broken by the electromigration process, its resistance increases to ~80 $G\Omega$ and the *I-V* curve shows nonlinearity. This non-ohmic *I-V* curve with a large resistance is strong evidence for the formation of a tunnel gap in the wire. The resistance is related to the geometry of the tunnel gap.

The width of the tunnel gap can be estimated from measured tunnel conductance. When electric current flows through a tunnel gap, the conductance depends on the width of the tunnel gap, *s*. One can write the relation between the two as follows, assuming a simple one-dimensional model with a WKB approximation.

$$G = G_0 \exp\left(-s/s_0\right) \tag{3.3}$$

In (3.3), G_0 is the quantum of conductance and s_0 is a characteristic length that depends on the work function of gold. When $s = 0$, the conductance will be a quantum of conductance, which corresponds to a single atom contact. As the gap grows larger the conductance across the tunnel gap will decrease exponentially. For gold electrodes, the conductance is known to decrease by one order of magnitude for every one-Angstrom increase in *s*[59].

Figure 3.13 shows a histogram of the tunnel resistance measured from 140 wires broken by the electromigration process. The tunnel resistance varies from ~100 $k\Omega$ to
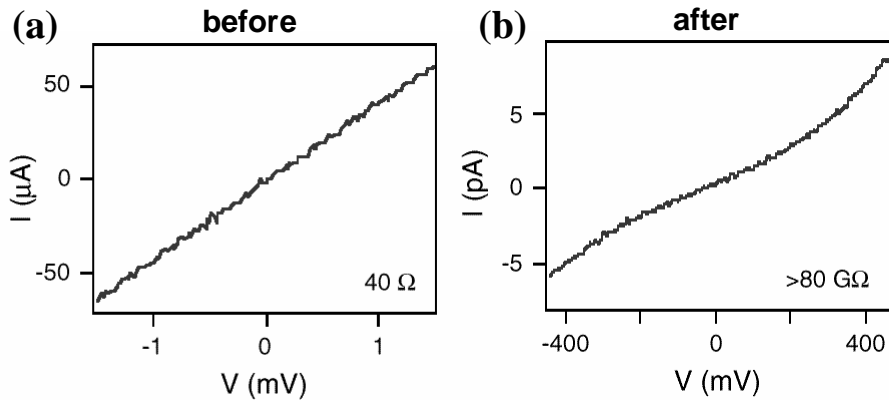
Figure 3.12 The conductance of a Au nanowire before (a) and after (b) the electromigration process. After the process, the resistance of the nanowire increases by many orders of magnitude. The *I-V* curve is nonlinear after the breaking, signifying the formation of a tunnel gap.

~10 GΩ for most nanowires. This wide spectrum in the tunnel resistance, however, corresponds to only ~1 nm variation in *s*. It is also clear that the tunnel distance *s* is most likely within 1~2 nm.

The actual size of the tunnel gap will differ from the value predicted by (3.3) due to many other effects present in the gap such as the image charge interaction and the tunneling through the insulating surface rather than the vacuum. Previous measurements [49, 60] on the tunnel gap between two gold electrodes suggest that the resistance of ~1 nm gap is ~ 1 GΩ. Therefore, the histogram in Figure 3.13 suggests that the median *s* is about 1 nm with a variation of ~1 nm.

These values were confirmed by more recent report by Lambert *et al.*[58] In their report, they used a large bias *I-V* measurement instead of the linear conductance (*V* = 0). Once the bias is larger than the barrier height of the tunnel gap, it is in the well-known Fowler-Nordheim regime where I/V^2 is proportional to $1/V$ with a slope that depends on the gap distance *s*. Lambert *et al.* concluded that *s* is 1.5 +- 0.1 nm for most wires, which is consistent with the values (1~2 nm) inferred from the histogram in Figure 3.13.

The stability of the tunnel resistance is also an important issue. As long as the wires are kept at a liquid helium temperature, the tunnel resistance usually does not change on the time scale of days. However, it changes at room temperature even when it is kept in vacuum. In most Au wires, the tunnel gap widens to such an extent that one cannot measure any current across the tunnel gap after keeping them overnight at room temperature. Compared to Au, the nanoelectrodes made with Pt show better stability at
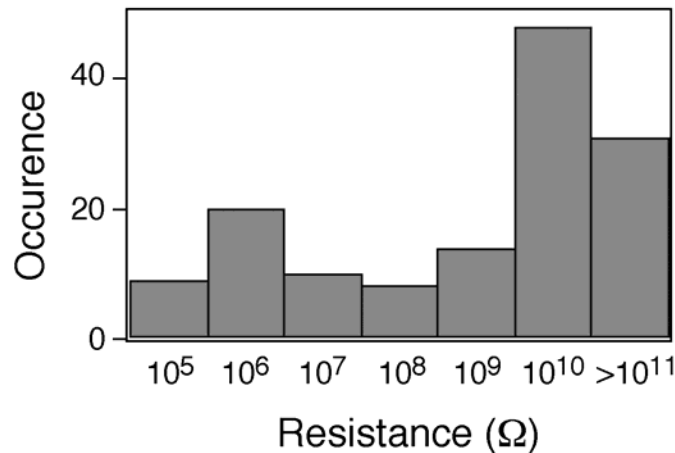

Figure 3.13 A histogram of low bias tunnel resistance of 140 nanowires broken by the electromigration process.

room temperature.   More than half of them show similar tunnel conductance after spending days in vacuum at room temperature.

3.5 Deposition of a molecule in the gap

As discussed in the previous section, nanowires broken by the electromigration process show tunnel resistances that are consistent with a 1~2 nm gap size. Therefore, these electrodes can be used to wire up single molecules in our experiments if the molecules can be located in the gap between the electrodes. The molecule deposition method used to accomplish this objective differs from molecule to molecule and will be explained in detail for each molecule in later chapters. However, the general procedure is summarized below.

First, the continuous wires (before breaking) are carefully cleaned. We begin the cleaning process using typical organic solvents such as acetone, isopropanol, and methylene chloride to remove any organic residue left after all the fabrication steps. Then the chip with the wires is brought into an oxygen plasma cleaner to further eliminate organics. The molecules, which are usually dissolved in a carrier solvent, are deposited onto the wires right after the plasma cleaning. Finally the wires are inserted into a cryostat and broke by the electromigration process to form a tunnel gap. Molecules deposited on the surface of wires before the breaking can be found in the gap by subsequent conductance measurements.
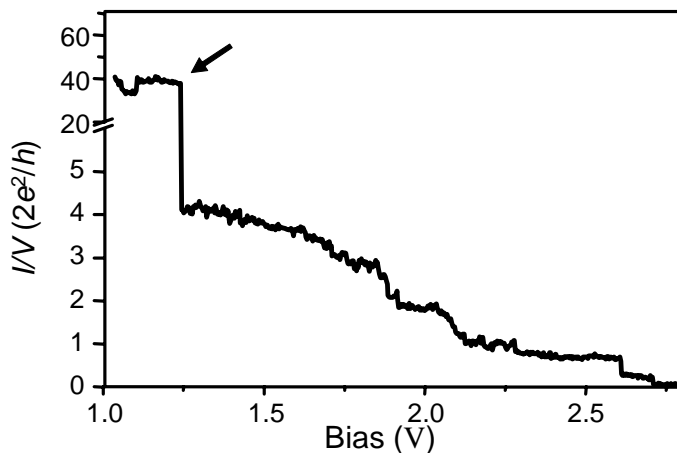

Figure 3.14 The breaking curve of a nanowire with C_{60} molecules deposited on top.
It shows a large residual conductance after major breaking (arrow) occurs.

We sometimes observe the effects of a molecule in the gap during the breaking process. As shown in section 3.3, the conductance of a wire without molecules decreases abruptly once the breaking process begins and the final conductance becomes lower than the conductance quantum. When the wires are broken with molecules deposited on the surface, the breaking curve sometimes shows a significant conductance larger than the conductance quantum even after the wire broke (Figure 3.14). This large residual conductance is often a signature of a molecule incorporated into the gap and many wires that showed the residual conductance after breaking showed Coulomb blockade phenomena in later conductance measurements.

Similar residual conductance is sometimes observed from wires without molecules when the wires are not cleaned thoroughly. Therefore, the breaking curves and the presence of the residual conductance can be used as a measure of the surface cleanliness in test experiments.

The mechanism of incorporation of molecules within the gap is not well understood. One possible explanation is the electrostatic trapping mechanism. Before the breaking, the molecules on the surface of a wire experience a weak local electric field typically less than 10 mV/nm. Once the gap is formed due to the electromigration process, the electric field in the gap region increases to a large value, typically on the order of 1 V/nm. The field strength decreases abruptly as one moves away from the gap region. This strong field localized in the gap region can attract any polarizable molecules
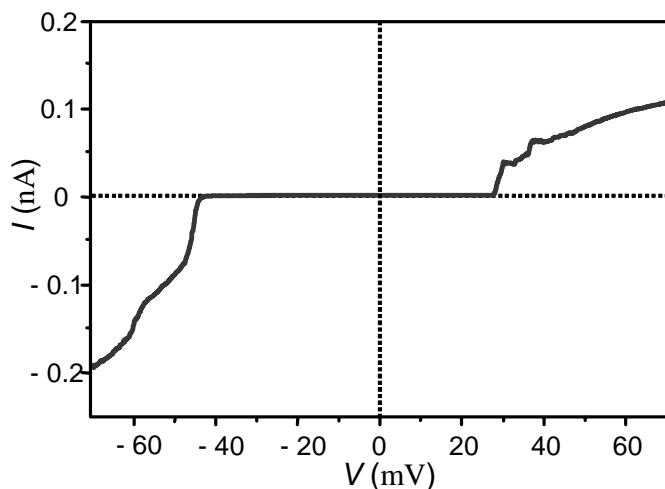
Figure 3.15 A low bias I-V curve taken from a nanowire broken with deposited C_{60} molecules. It shows a Coulomb blockade and additional current steps that can be associated with a single C_{60} molecule located in the gap.

into the gap region. A similar mechanism has been previously used successfully to trap larger objects between two electrodes by other groups[61].

As explained in the previous section, it is extremely difficult to image single molecules located in a tunnel gap. But one can decide whether a molecule is located in the gap by looking at the *I-V* curves measured after the tunnel gap is formed in the wire. Once a molecule is positioned within the gap, the conductance between two electrodes will be affected by the presence of the molecule. The contact between the molecule and the electrodes is usually poor, and it will form two tunnel barriers, each located between the molecule and either electrode. As explained earlier in Chapter 2, the conductance measurement on such a device will be affected by the charging energy of the molecule, showing the characteristic behaviors of a single electron transistor.

Figure 3.15 shows an *I-V* curve taken from a wire that is broken with C_{60} molecules deposited on top. It clearly shows current steps that are absent in the tunnel *I-V* curve of a simple tunnel junction (see Figure 3.12 (b)). The current steps in Figure 3.15 are the result of the charging energy and discrete quantum levels of the C_{60} molecule. Hence, these features indicate the incorporation of a molecule into the gap.

For devices showing the Coulomb blockade, individual devices show different detailed behaviors. This can be seen from a wide variation in such parameters as the overall conductance, the charge degeneracy gate potential (V_C), the energies of excited levels, the intensities of the *dI/dV* lines, and the capacitance values. Such differences among single molecule devices are due to the random nature of the device geometry. Unlike the microelectronic devices fabricated with a well-controlled device geometry, the single molecules in our devices are randomly located in a tunnel gap formed by the electromigration technique. For this reason, we need to rely on device statistics to attribute certain conductance features to the properties of individual molecules. We will see examples of such reproducible features as well as non-reproducible ones in the following chapters.

3.6 Measurement Setup

Most transport measurements and the electromigration process were performed in a liquid helium cooled cryostat with a standard transport measurement setup. Figure 3.16
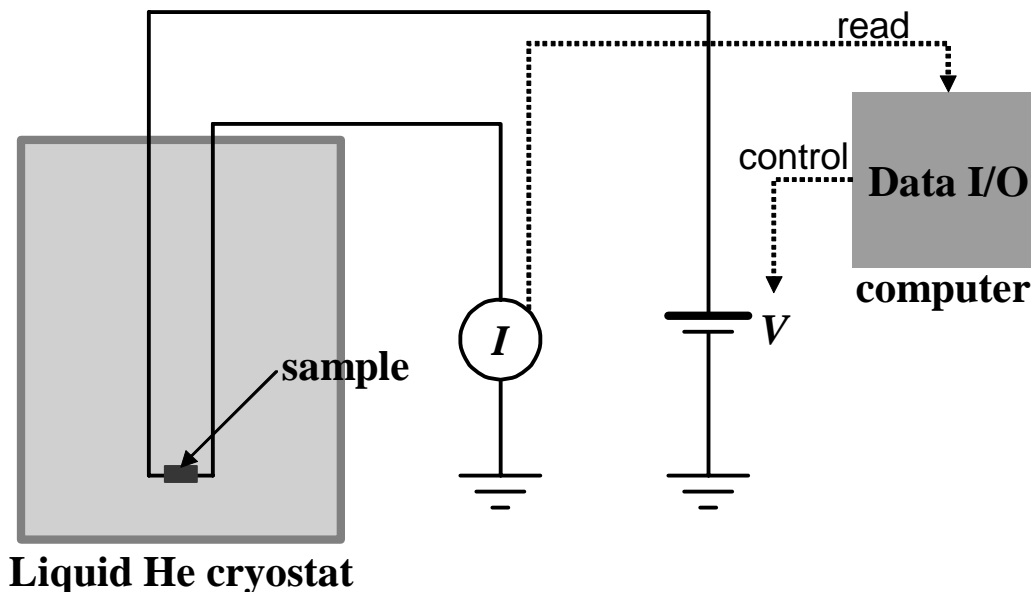
Figure 3.16 A schematic diagram of the low-temperature DC conductance measurement setup.

shows the schematic of the whole measurement setup including the cryostat, device wiring and measurement circuit. Let us go through individual components of the experimental setup one by one.

The liquid helium cryostats

Two major cryostats are used for conductance measurements. The first one is the OXFORD variable temperature insert (VTI) system with a base temperature below 1.5 K (Figure 3.17(a)). The sample sits in a liquid helium can that cools down by pumping the helium gas out of the can. The amount of liquid helium flowing into the can is controlled by a needle valve. The VTI system is relatively simple, requires minimal maintenance, and has a very short sample turn around time (< 2 hrs). Since the cooling power is very high on this system, high resistance wires are not required (wire resistance < 10 Ω). This is ideal for the breaking process, as described in section 3.2. The VTI has a superconducting magnet that can go up to 12 T.

The other cryostat shown in Figure 3.17(b) is the top loading OXFORD dilution refrigerator (DF). The base temperature is below 20 mK and the sample sits in a He3/He4 mixing chamber. Unlike the VTI, the DF requires a heavy maintenance and has a longer sample turn around time (> 5 hrs). The wiring is also resistive (~ 500 Ω), so that only very resistive nanowires (R > 1 kΩ) can be broken in the DF. We can measure

(a)

(b)
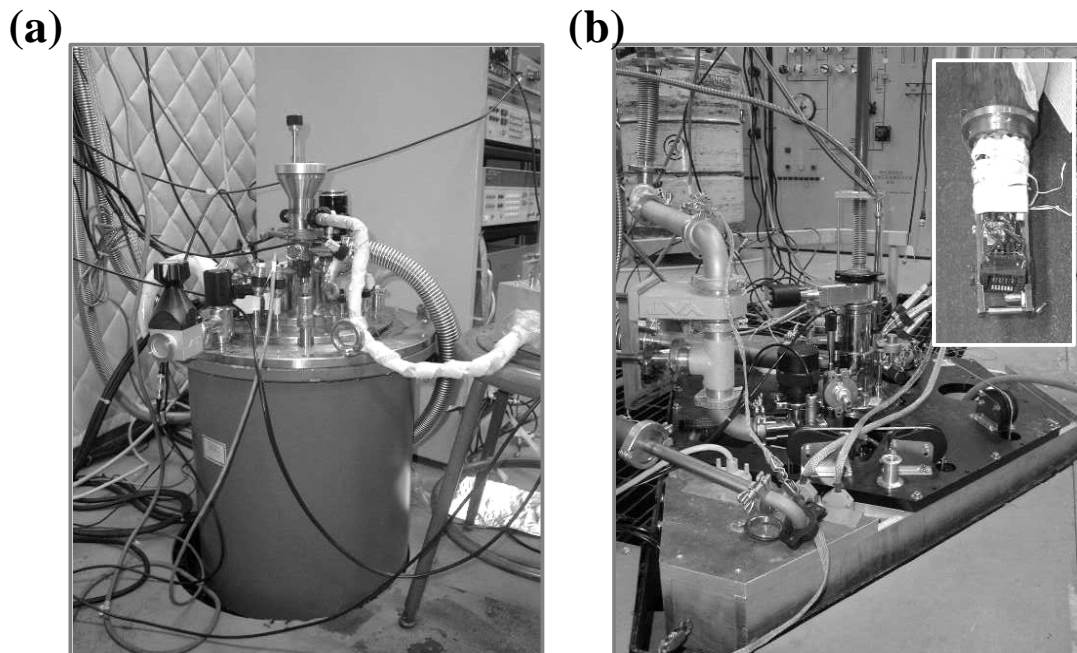
Figure 3.17 The two helium refrigerators used for low temperature conductance measurements. (a) The OXFORD variable temperature insert system with < 1.5 K base temperature. (b) The top loading OXFORD dilution refrigerator with the base temperature lower than 20 mK. Only the top part is shown in the picture. Inset: the sample mount.

low resistance wires in the DF as long as they are broken outside of the DF and then loaded into it. The DF also has a superconducting magnet with a maximum magnetic field of 9 T. In both systems, no special filters were used in the wiring other than a carbon epoxy filter in the DF.

Measurement circuit

Figure 3.18(a) shows a schematic of the measurement circuit for a DC measurement. For a DC *I-V* measurement, we apply a bias to the device and then measure the current flowing through the circuit using a low-noise current preamplifier (DL instruments 1211). The voltage was applied and controlled by a computer-controlled data acquisition card (National Instruments PCI-6052E) with a BNC I/O connector block. The applied bias was directly recorded to the computer simultaneously with the current read from the current preamp using the data acquisition card.

The maximum output voltage of the card is ± 10 V with a resolution of ~0.3 mV. For measurements at helium temperatures (T < 1.5K), a voltage divider (10:1 or 100:1) was always used to decrease the resolution to ~30 μV or ~3 μV.
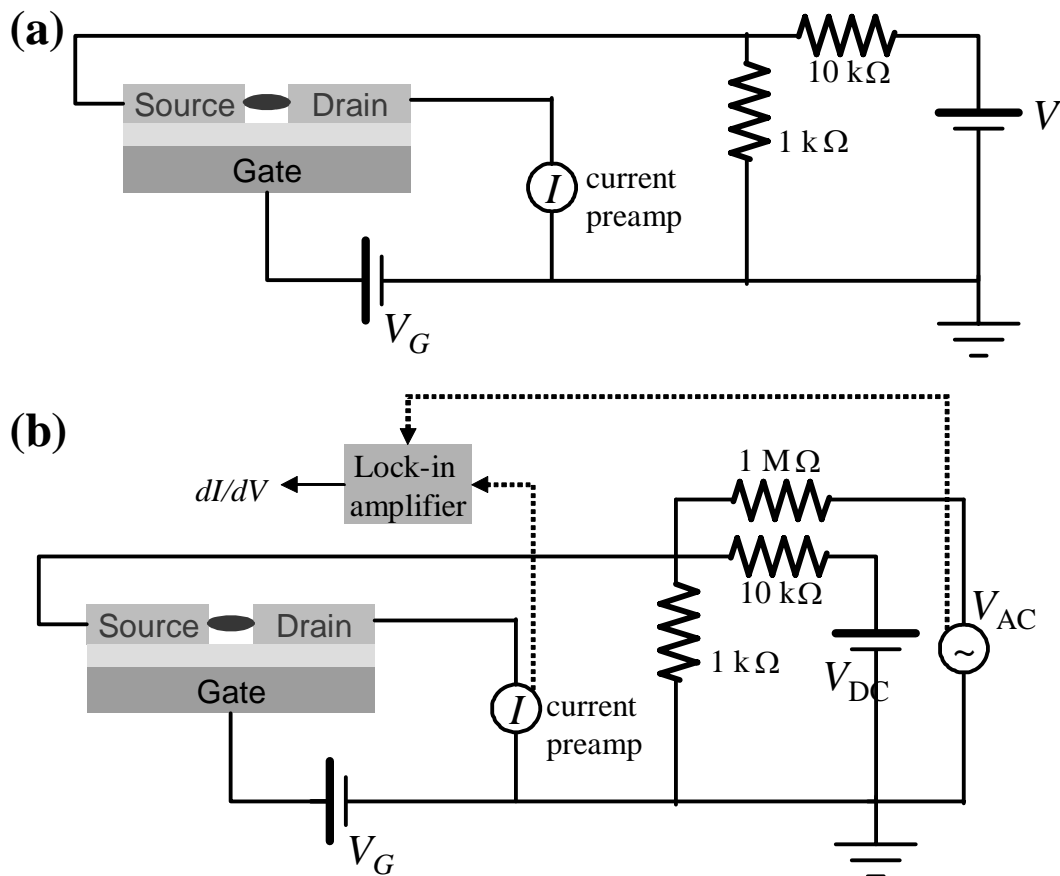
Figure 3.18 The measurement circuit for (a) a DC and (b) AC lock-in conductance measurement.
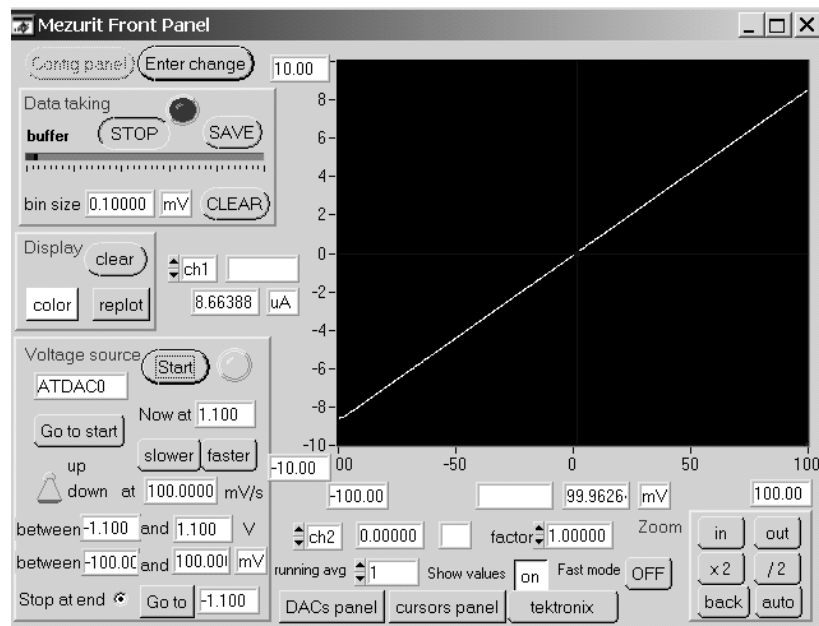

Figure 3.19 The front panel of the data taking program "Mezurit".

Figure 3.18(b) shows a circuit diagram for an AC lock-in measurement. Instead of monitoring the current, the differential conductance (dI/dV) was monitored using a lock-in amplifier (Stanford Research Systems SR844 or EG&G 7265). An AC bias with a small amplitude δV (< k_BT) was applied to the device along with the DC bias. The current was amplified by the current preamplifier and fed into the lock-in amplifier, which measures the AC current. A computer and a data acquisition card are used to produce a DC bias and to record all the data.

Mezurit

Most data presented in this thesis were taken using a program called "Mezurit" (Figure 3.19). It is a C-based program originally developed by Mark Bockrath and David Cobden using the National Instruments LabWindows/CVI programming environment. Mezurit can control two voltage outputs, which are usually used for controlling the source-drain bias and the gate bias. It can also read several analog signals and record them in real time. It is a very versatile program and has many useful functions specially developed for three terminal transport measurements. It is, however, not optimized for fast data taking and also very difficult to customize or expand.

3.7 Summary

In this chapter, we discussed various issues concerning the device design, device fabrication, sample preparations, and the measurement setup. To perform the electromigration-induced breaking successfully, the nanowires are required to meet a certain design criteria (section 3.2) and the gate material and its geometry should be wisely chosen. The wire cleaning process and molecule deposition (section 3.5) is a critical process for successful device fabrication and requires careful parameter control. Finally the electromigration process is used to form two electrodes with a ~nm sized gap that can be bridged by single molecules previously deposited on the surface (section 3.3). Conductance measurements after the breaking show simple tunnel *I-V* curves (section 3.4) or the Coulomb blockade (section 3.5) depending on whether a molecule is located in the gap or not.

Chapter 4

Nano-mechanical Oscillations in a Single C_{60} Transistor

4.1 Introduction

Over the last decade, electron transport through quantum dots has attracted considerable attention from the scientific and engineering community. The electronic motion through these structures is strongly modified by single-electron charging and energy level quantization (Chapter 2). Recently, much effort has been directed toward extending these studies to chemical nanostructures, such as molecules[15, 16, 62-65], nanocrystals[7, 8, 52, 66, 67], and nanotubes[30, 31, 68, 69].

In this chapter we will discuss the fabrication of single-molecule transistors based on individual C_{60} molecules. Transport measurements of single-C_{60} transistors provide evidence for coupling between the center-of-mass motion of C_{60} and single-electron hopping[70], a conduction mechanism that has not been observed in previous quantum-dot studies. This coupling manifests itself as quantized nano-mechanical oscillations of C_{60} against the gold surface. The frequency of this oscillation is determined to be around 1.2 THz, in good agreement with a simple theoretical estimate based on van der Waals and electrostatic interactions between C_{60} and gold electrodes. In general, the coupling between a vibrational mode of a quantum dot and single-electron hopping can be described within the framework of the Franck-Condon process[71] and a simple theoretical model based on this process will be discussed.

This chapter is written based on a previously published paper[32] and parts of the text and the figures presented in this chapter are excerpted from it.

4.2 Sample Preparation

A schematic diagram of an idealized single-C_{60} transistor is shown in Figure 4.1. Single-C_{60} transistors were prepared by depositing a dilute toluene solution of C_{60} onto a
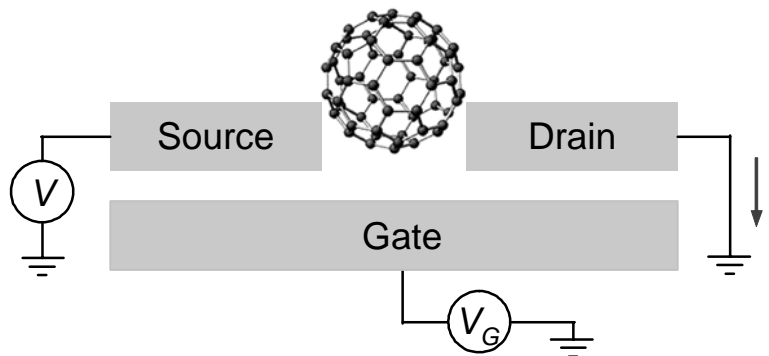
Figure 4.1 An idealized diagram of a single-C_{60} transistor fabricated in the experiment.

pair of connected gold electrodes fabricated using *e*-beam lithography. The toluene solution of C_{60} was made by dissolving 10 mg of C_{60} powder in 3 mL of toluene solvent, which was subsequently sonicated for over 15 minutes and then centrifuged at 4000 rpm for 10 minutes. The C_{60} solution was filtered using 0.2 μm filter, after which a UV spectrum was taken. A five-times diluted solution (~ 1 mM) was used for the actual
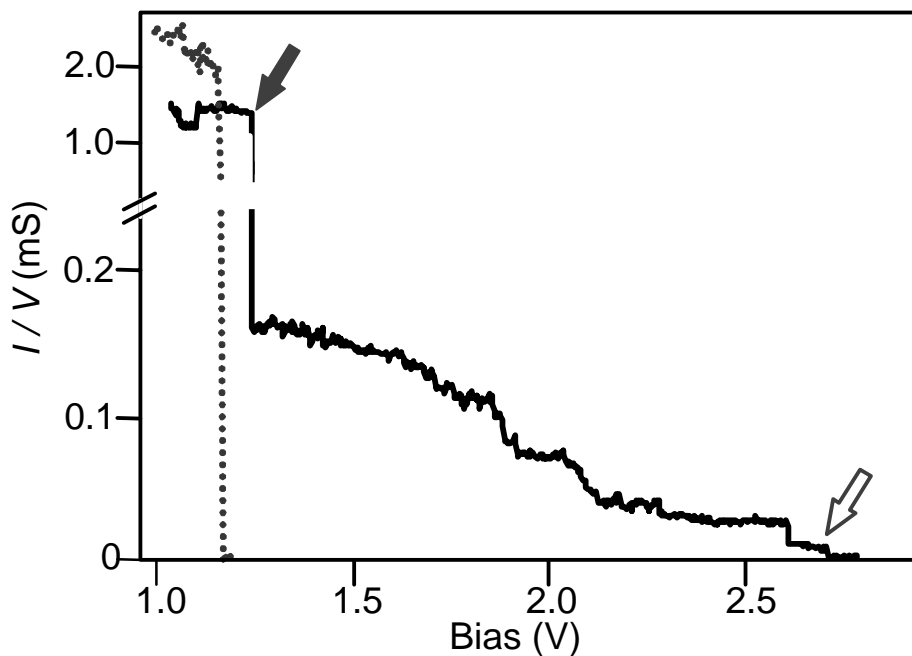
Figure 4.2 Electromigration-induced breaking of the electrodes. A large bias was applied between the electrodes while the current through the connected electrode was monitored (black solid curve). After the initial rapid decrease (solid arrow), the conductance stayed above ~ 0.05 mS up to ~ 2.0 V. This behavior was observed in most single-C_{60} transistors, but it was not observed when no C_{60} solution was deposited (red dotted curve). The bias voltage was increased until the conductance fell low enough to ensure that the current through the junction is in the tunneling regime (open arrow). The low bias measurements were taken after this breaking procedure.

deposition. The C_{60} solution was kept in a quartz vessel to minimize the formation of C_{60} aggregates.

The electrodes are made by the fabrication process described in section 3.2 (device design I). A break-junction technique was then used to create a gap between these electrodes by the process of electromigration. The typical lateral size of the fabricated electrodes was on the order of 100 nm at the point of the gap formation, and the height of the electrodes was 15 nm. Scanning electron microscope images of fabricated electrodes (Figure 3.10(a)) reveal that the gap between two electrodes is not uniform and that the narrowest gap is formed only between small protrusions ($\leq$ 10 nm) of the two gold electrodes. Current-voltage measurements of these electrodes at cryogenic temperatures without deposited C_{60} molecules show that the size of the gap is consistently around 1 nm as discussed in section 3.4. In a significant fraction of the C_{60} devices, the conductance of the junction after initial breaking is substantially enhanced compared to devices with no C_{60} deposited, indicating that C_{60} molecules reside in the junction (see Figure 4.2). The entire structure was defined on a SiO_2 insulating layer on top of a degenerately doped silicon wafer that serves as a gate electrode that modulates the electrostatic potential of C_{60}. All the measurements were performed in a pumped liquid He Cryostat (VTI) with a base temperature below 1.5 K.

4.3 Coulomb Blockade in Single-C_{60} Transistors

Figure 4.3 presents representative current-voltage (*I-V*) curves obtained at 1.5 K from a single-C_{60} transistor at different gate voltages (V_G). The device exhibited strongly suppressed conductance near zero bias voltage followed by step-like current jumps at higher voltages. The voltage width of the zero-conductance region (conductance gap) could be changed in a reversible manner by changing V_G. In ten devices prepared from separate fabrication runs, the conductance gap could be reduced to zero by adjusting V_G, although the gate voltage at which the conductance gap closed (V_C) varied from device to device.

Figures 4.4 and 4.5 show two-dimensional plots of differential conductance (*dI/dV*) as a function of both *V* and V_G for four different devices. Peaks in *dI/dV*, which correspond to the step-like features in Figure 4.3, show up as lines in these plots. As seen
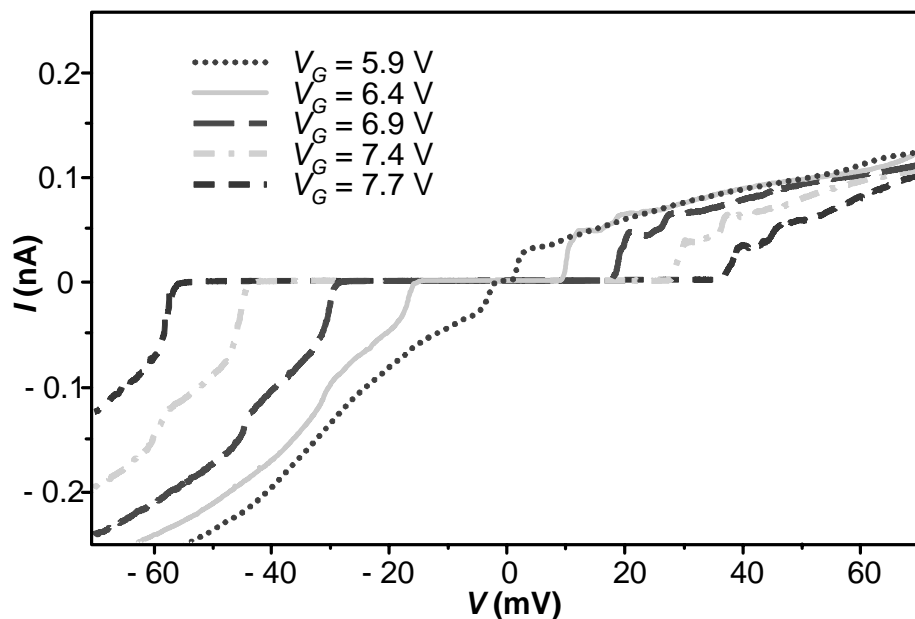
Figure 4.3 Current-voltage (*I-V*) curves obtained from a single-C$_{60}$ transistor at T = 1.5 K. Five *I-V* curves taken at different gate voltages (*V$_G$*) are shown.

clearly in Figures 4.4 and 4.5, the size of the conductance gap and the *dI/dV* peak positions evolve smoothly as V_G is varied. As the gate voltage was varied farther away from V_C in both positive and negative directions, the conductance gap continued to widen and the maximum observed gap exceeded 270 mV (shown in Figure 4.6). Many *dI/dV* peaks outside the conductance gap are also observed.

The *V$_G$*-dependent features described above were not observed in devices when C$_{60}$ was not deposited on the electrodes. In addition, the coverage of C$_{60}$ on the electrodes was such that only ~ 10% of more than 300 fabricated electrodes show *I-V* characteristics different from a simple tunnel junction without C$_{60}$. This low C$_{60}$ coverage ensures that the probability of finding multiple C$_{60}$ molecules bridging two electrodes is small. Furthermore, many different devices exhibited similar conductance characteristics that are consistent with a single nanometer-sized object bridging two electrodes, as explained in detail below. Although C$_{60}$ could not be imaged directly in these devices due to its small size (~7 Å in diameter), these experimental observations indicate that individual C$_{60}$ molecules are responsible for the conductance features observed in the experiment.
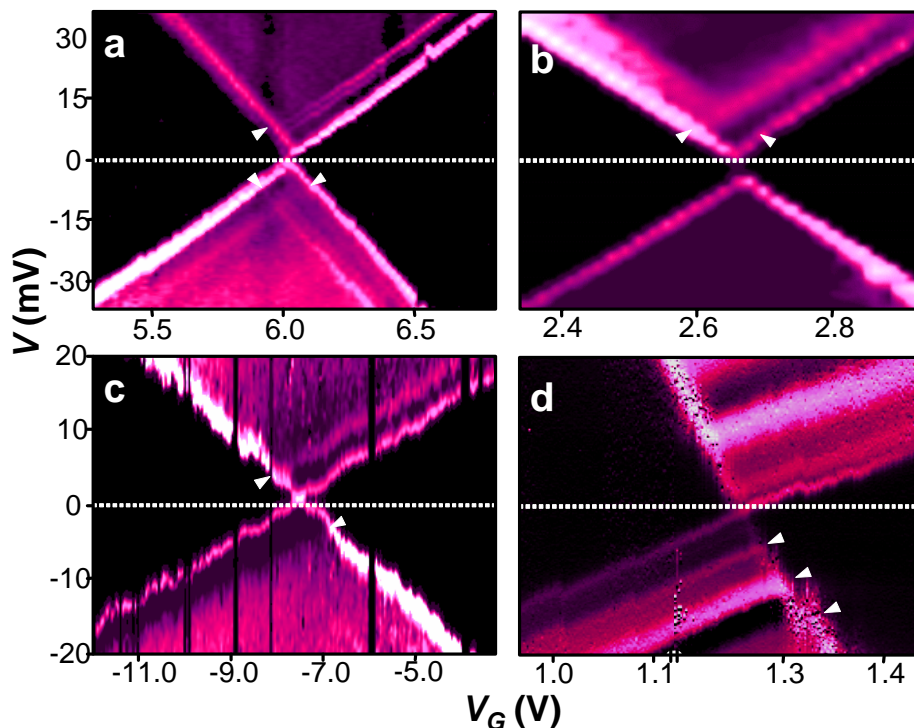
Figure 4.4 Two-dimensional differential conductance (*dI/dV*) plots as a function of the bias voltage (*V*) and the gate voltage (*V_G*) obtained from four different devices prepared from separate fabrication runs. The differential conductance values are represented by the color scale, which changes from black (0 nS) through pink to white (white representing 30 nS in **a, b, c** and 5 nS in **d**). The white arrows mark the point where *dI/dV* lines intercept the conductance gap. During the acquisition of data in **d**, one "switch" where the entire *dI/dV* characteristics shift along the *V_G* axis occurred at *V_G* = 1.15 V. The right portion of plot **d** is shifted along the *V_G* axis to preserve the continuity of the lines.

The global patterns observed in Figures 4.3 - 4.6 can be understood using the Coulomb blockade model described in Chapter 2. The conductance gap observed in the data is a consequence of the finite energy required to add (remove) an electron to (from) C_{60}. This energy cost arises from the combined effect of single-electron charging of C_{60} and the quantized excitation spectrum of the C_{60}-transistor system. The maximum observed gap in the experiment indicates that the charging energy of the C_{60} molecule in this geometry can exceed 270 meV.

The conductance gap changes reversibly as a function of V_G because more positive gate voltage stabilizes an additional electron on C_{60}. The conductance gap disappears at $V_G = V_C$ where the total energy of the system is the same for two different C_{60} charge states. When the gate voltage traverses V_C in the positive direction, the
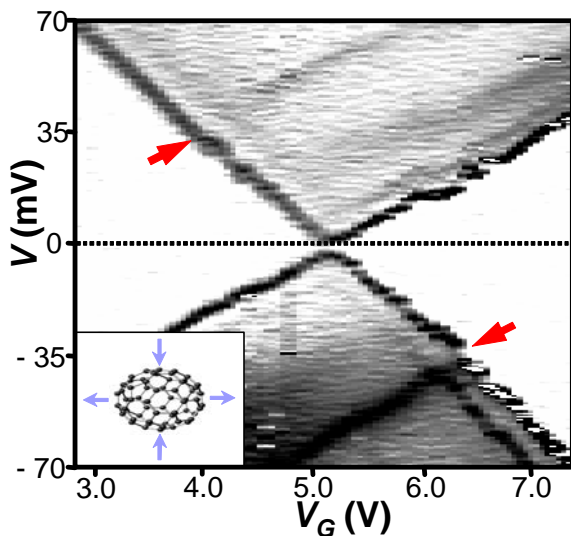
Figure 4.5 A differential conductance plot showing a larger bias-voltage range than those in Figure 4.4. Here two *dI/dV* lines that intercept the conductance gap at $V = 35$ mV are seen clearly (arrows). The energy quantum of this excitation closely matches that of the C_{60} internal vibrational mode shown in the inset.

equilibrium number of charges on C_{60} changes by one electron from C_{60}^{n-} to $C_{60}^{(n+1)-}$, where *n* designates the number of charges on C_{60}. It is determined by both V_G and the local electrochemical environment, that is the work function of the metal electrode and the local charge distribution around C_{60}. While the value of *n* cannot be determined solely from our experimental data, previous electrochemical and photoelectron spectroscopic studies of C_{60} on gold suggest that *n* is most likely zero or one[38].
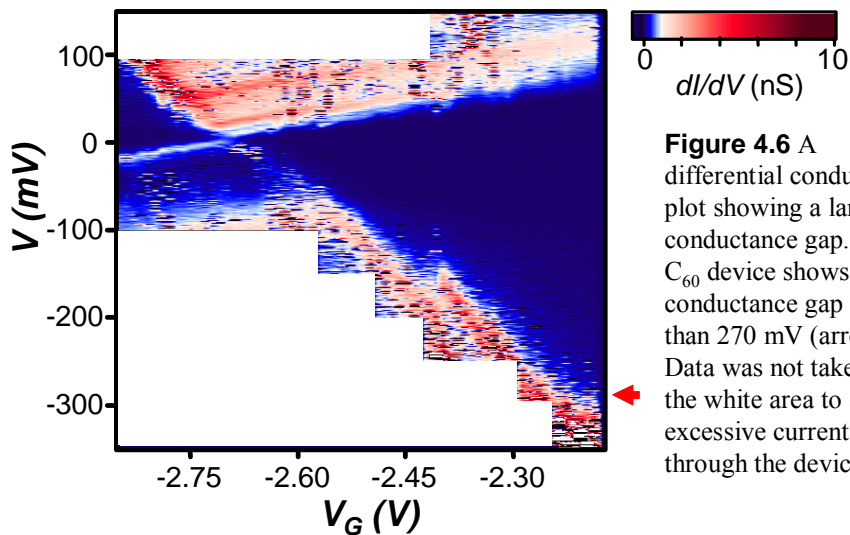
Figure 4.6 A differential conductance plot showing a large conductance gap. This C_{60} device shows a conductance gap larger than 270 mV (arrow). Data was not taken in the white area to avoid excessive current through the device.

The position of each *dI/dV* peak outside the conductance gap in Figures 4.4 and 4.5 provides detailed information on the quantized excitations of the single-C_{60} transistor system as discussed in Chapter 2 (see Figure 2.16). These *dI/dV* peaks appear when a new quantized excitation becomes energetically accessible, providing an electron-tunneling pathway between C_{60} and the gold electrodes. Specifically, each *dI/dV* peak that intercepts the conductance gap on the $V_G > V_C$ side signifies an opening of a new

tunneling pathway where an electron hops onto C_{60}^{n-} to generate $C_{60}^{(n+1)-}$ in its ground or excited states; these peaks therefore probe the excitation energies of the $C_{60}^{(n+1)-}$ ion. Each *dI/dV* peak that ends at $V_G < V_C$ occurs when an electron hops off $C_{60}^{(n+1)-}$ to generate C_{60}^{n-}; these peaks thus probe the ground and excited states of C_{60}^{n-}. As explained in section 2.4, the energy of these quantized excitations can be determined from the bias voltage at which they intercept the conductance gap. These points are marked by the white arrows in Figure 4.4.

4.4 The Center-of-Mass Vibration (5 meV Excitation) in C_{60} Transistors

A remarkable common feature of the different devices is that a quantized excitation is universally observed with an energy of ~5 meV (arrows, Figure 4.4). Moreover, this excitation is observed on both sides of V_C in most devices, indicating that it is an excitation of both charge states of C_{60}. The exact value of this energy quantum varied from device to device and ranged from 3 to 7 meV. This can be seen from the histogram of observed excitation energies, which shows a clear peak centered at 5 meV (Figure 4.7). In some devices, multiple *dI/dV* features with almost identical spacing appear, as seen in Figure 4.4(d).

The observed 5-meV excitation could arise from many possible degrees of freedom of the single-C_{60} transistor system. One possibility, which has been commonly invoked in other nanometer-scale systems, is the excited electronic states of the system. However, this possibility is highly unlikely here because the 5-meV excitation is the
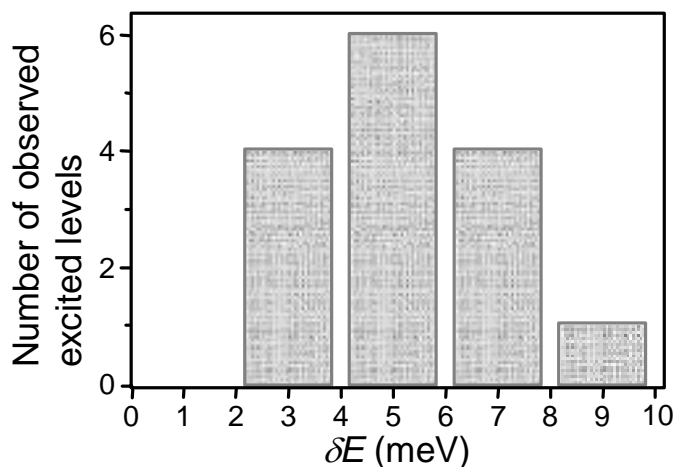
Figure 4.7 The histogram of excited levels observed below 10 meV from eight different C_{60} devices.

same for both charge states of C$_{60}$ and also because multiple excitations with the same spacing are observed. Although the exact electronic-level structures of the C$_{60}^{n-}$ ions are not known experimentally, theoretical calculations predict that the electronic states do not follow such behavior[38] (see Figure 1.6).

A more natural candidate is a vibrational excitation of the C$_{60}$ system coupled to an electron tunneling on and off C$_{60}$. The observation of multiple *dI/dV* features with identical spacing would then result from the excitation of integer numbers of vibrational quanta. Moreover, these vibrational modes would be present irrespective of the charge state of the C$_{60}$.

The internal vibrational modes of the free C$_{60}$ molecule have been extensively studied, both theoretically and experimentally[38, 72]. The lowest-energy mode is one with a vibrational quantum of 33 meV and corresponds to the C$_{60}$ deformation from a sphere to a prolate ellipsoid, as shown in the inset to Figure 4.5. In Figure 4.5, an excitation that likely corresponds to this mode can indeed be seen with an energy of ~35 meV. However, internal vibrational modes cannot account for the observed 5-meV features.

Another possibility is the center-of-mass oscillation of C$_{60}$ located within the confinement potential that binds it to the gold surface, as shown in Figure 4.8. This mode has not been directly measured experimentally. However, previous theoretical and experimental studies have shown that C$_{60}$ is held tightly on gold by van der Waals interactions, with a C$_{60}$-gold binding energy of ~1 eV and a distance of ~6.2 Å between the C$_{60}$ center and the gold surface[38, 73, 74].

The above parameters can be used to determine the shape of the potential that describes the C$_{60}$-gold binding. Assuming that the C$_{60}$-gold interaction can be expressed by the Lennard-Jones form, the binding potential can be obtained by integrating the interaction over all pairs of a C$_{60}$ carbon atom and a gold atom on a plane[74],

$$E(r) = \sum_{all(C,Au)pairs} \left(c_{12}r'^{-12} - c_6 r'^{-6} \right)$$
$$= A\left\{ (r-R)^{-9} - (r+R)^{-9} \right\} - B\left\{ (r-R)^{-3} - (r+R)^{-3} \right\}$$

(4.1)

where R is the radius of C$_{60}$. Using the binding energy (~1 eV) and the equilibrium distance ($r_0 \sim 6.2$ Å), the constants A and B in the binding potential (4.1) can be decided,

and then it can be approximated very well near the equilibrium position by a harmonic potential with an estimated force constant of $k \sim 70$ N/m.

$$E(r) \approx E_{binding} + \tfrac{1}{2}k\left(r - r_0\right)^2 \tag{4.2}$$

Therefore, the C_{60}-gold interaction can be represented by a spring as shown schematically in Figure 4.8. This force constant and the mass M of the C_{60} molecule yield a vibrational frequency of $f = (1/2\pi)(k/M)^{1/2} \sim 1.2$ THz and a vibrational quantum of $hf \sim 5$ meV, where h is the Planck constant.

Adding an additional electron to C_{60} compresses the C_{60}-surface bond due to the interaction between the C_{60} ion and its image charge in the metal and this serves as the excitation mechanism of the center-of-mass vibration of C_{60}. An additional electron on C_{60} results in the shortening of the C_{60}-surface distance by δ, whose value can be estimated as follows when the distance between the additional charge and the image charge (r) is ~1 nm.

$$\delta = F\!\!\Big/\!\!k = \left(\frac{e^2}{4\pi\varepsilon_0 r^2}\right)\!\Big/k \approx \frac{2.3\times10^{-10}\,\text{N}}{70\,\text{N/m}} = 3.3\ \text{pm} \tag{4.3}$$
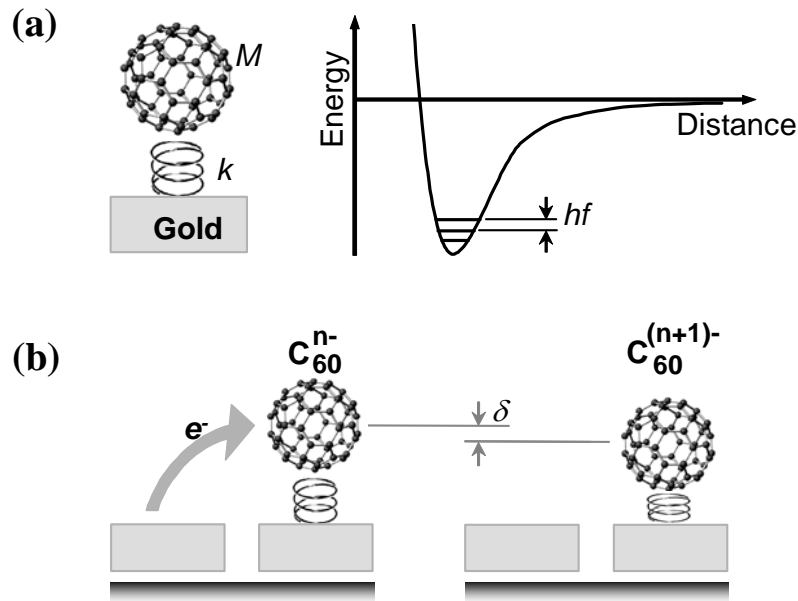
Figure 4.8 Schematic of the center-of-mass oscillation of C_{60}. (a) A C_{60} molecule is bound to the gold surface by the van der Waals and electrostatic interaction. The interaction potential is schematically illustrated in the figure. (b) When an electron jumps on to C_{60}^{n-}, the attractive interaction between the additional electron and its image charge on gold pulls the C_{60} ion closer to the gold surface by the distance δ. This electrostatic interaction results in the mechanical motion of C_{60}.

However, the interaction between the additional electron and the image charge does not significantly change the vibrational frequency. By comparison, the root-mean squared displacement x_m of the C$_{60}$ molecule in the *m*-th vibrational level is given by $x_m = (2m+1)^{1/2} x_0$, where $x_0 = (hf/k)^{1/2} \sim 3$ pm. Although the exact values of these simple estimates change when the second metal electrode is included in the model, the qualitative conclusions of the model remain essentially the same. The present estimates pertain to the situation where the coupling between C$_{60}$ and two electrodes is strongly asymmetric.

The C$_{60}$-surface vibration discussed above can account for the 5-meV conductance features in a unifying fashion. The first *dI/dV* peak at the boundary of the conductance-gap region is observed when an electron hops on or off C$_{60}$ with the system staying in the ground vibrational level. Additional *dI/dV* peaks that intercept the ground *dI/dV* line at $V_G > V_C$ appear when an electron hops onto C$_{60}^{n-}$ to generate C$_{60}^{(n+1)-}$ in excited vibrational states. The *dI/dV* peaks that end on the $V_G < V_C$ side signify, on the other hand, an event where an electron hops off C$_{60}^{(n+1)-}$, leaving C$_{60}^{n-}$ in excited vibrational levels. Multiple *dI/dV* peaks on the same side of V_C indicate that multiple vibrational quanta are excited.

This process is reminiscent of the Franck-Condon processes encountered in electron-transfer and light-absorption processes in molecules, where the vibrational excitation accompanies the electronic motion[71]. We will describe the Franck-Condon process in a single electron transistor more quantitatively in the next section. As we will see in the following section, the vibrational matrix elements for these processes can be readily calculated within the harmonic approximation, and the ratio δ/x_0 determines the number of vibrational quanta typically excited by the tunneling electron. According to the estimates discussed above, $\delta/x_0 \sim 1$ in a single-C$_{60}$ transistor. The number of *dI/dV* peaks visible in Figure 4.4 generally confirms this expectation since only a few *dI/dV* peaks are observed in most devices.

One device that does not follow this general trend is the one shown in Figure 4.4(d). As described previously, this device exhibits many *dI/dV* peaks on both sides of V_C. In addition, the peak intensities do not show simple variations expected from the

single-mode Franck-Condon picture. The anomalous behavior may be related to the highly asymmetric coupling of C_{60} and the two electrodes in this particular device. This asymmetry is demonstrated by the different slopes of the upward and downward *dI/dV* lines in the *V-V_G* plane. The variations of peak intensities may be due to the presence of other degrees of freedom in the system, such as the C_{60} motion perpendicular to the surface normal.

Unexplained features exist in other devices as well. In the data in Figure 4.4(a), a small (≤ 1 meV) energy splitting is observed for many of the lines. This splitting may arise from the C_{60} center-of-mass motion perpendicular to the surface normal discussed above. Unfortunately, the nature of the potential for this motion is not known due to the lack of detailed knowledge of the electrode geometry near C_{60}, and quantitative support of this assignment is thus lacking in this experiment.

4.5 Theory of a Vibrating Quantum Dot

The coupling between tunneling electrons and the center-of-mass motion of C_{60} can be more quantitatively described by extending the Coulomb blockade theory developed in Chapter 2 to accommodate vibrational degrees of freedom of a quantum dot.

In the simple Coulomb blockade model discussed in Chapter 2, the current level of a single-level quantum dot in its on state is decided by the two tunneling rates Γ_S and Γ_D and the current amplitude is $|e|\Gamma$, where $\Gamma = \Gamma_S \Gamma_D/(\Gamma_S + \Gamma_D)$ (equation (2.11)). In this model, these tunneling rates are purely electronic and they are roughly proportional to the electronic wave function overlap between the quantum dot and the electrodes. Once we release the quantum dot so that it can freely move under a certain binding potential, the tunneling rates will change because the lattice wave function can be different before and after the electron tunneling. Therefore, the tunneling rates become modified to take into account the overlap between the two vibrational wave functions.

$$\Gamma_{S(D)} \rightarrow \Gamma_{S(D)} \left| \left\langle \Psi_{after} \middle| \Psi_{before} \right\rangle \right|^2 \qquad (4.4)$$

Here Ψ_{before} and Ψ_{after} are the vibrational wave functions of the quantum dot (a C_{60} molecule in the present experiment) before and after the electron tunneling. It is obvious

(a) Fixed dot   **(b) Vibrating dot**

Tunneling rate: Γ_S & Γ_D $\Gamma_{S(D)} \left| \left\langle \Psi_{after} \middle| \Psi_{before} \right\rangle \right|^2$
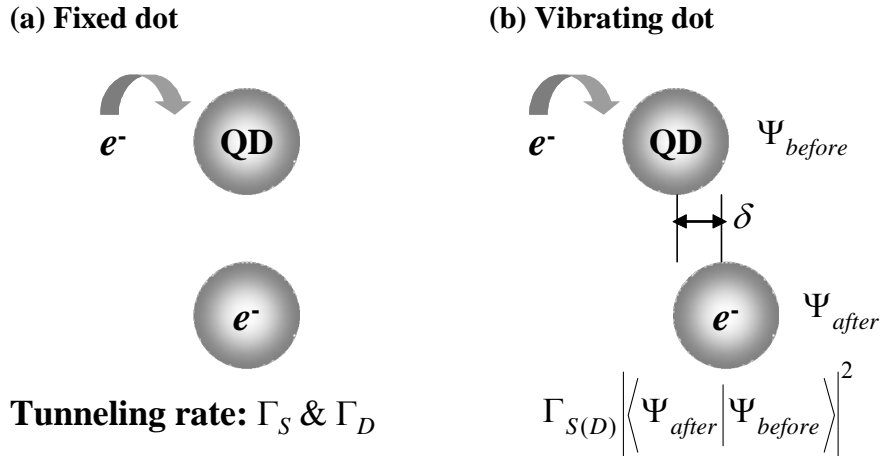
Figure 4.9 Tunneling rates for (a) a fixed quantum dot and (b) a vibrating quantum dot.

that one does not need to consider the vibrational overlap $P = \left| \left\langle \Psi_{after} \middle| \Psi_{before} \right\rangle \right|^2$ when the

dot is fixed since the value will be always 1. The difference between the two cases (a fixed dot and a vibrating dot) is illustrated in Figure 4.9.

The vibrational overlap can be easily calculated when the quantum dot is bound by a simple harmonic potential with the same force constant for both charge states (Figure 4.10). Only the equilibrium position of the quantum dot changes by δ between the two charge states. The overlap between the two vibrational ground states can be readily calculated to produce,
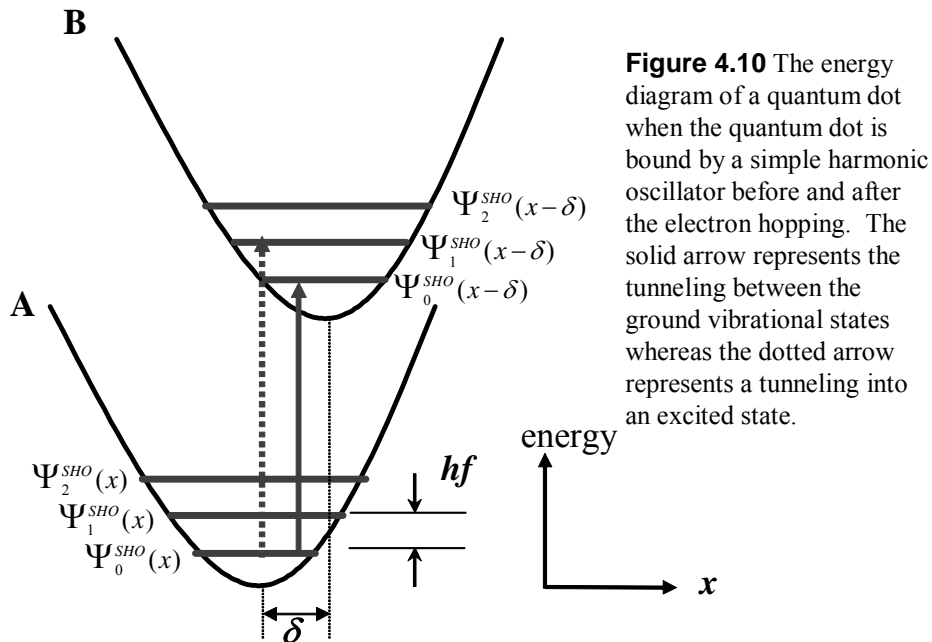
Figure 4.10 The energy diagram of a quantum dot when the quantum dot is bound by a simple harmonic oscillator before and after the electron hopping. The solid arrow represents the tunneling between the ground vibrational states whereas the dotted arrow represents a tunneling into an excited state.

$$P_{00} = \left| \left\langle \Psi_0^{SHO}(x-\delta) \middle| \Psi_0^{SHO}(x) \right\rangle \right|^2 = e^{-g^2/2}, \tag{4.5}$$

where $g = \delta/x_0 = \delta\sqrt{k/hf}$. This ratio between the displacement δ and the ground state vibrational amplitude x_0 is called the Franck-Condon factor. The current that is carried by the ground level becomes exponentially smaller as g grows bigger or equivalently, as the quantum dot moves more upon changing the charge state.

When one of the charge states is in a vibrational excited state, the vibrational overlap can be calculated as follows.

$$P_{n0} = \left| \left\langle \Psi_n^{SHO}(x-\delta) \middle| \Psi_0^{SHO}(x) \right\rangle \right|^2 = e^{-g^2/2} \frac{1}{n!} \left(\frac{g^2}{2} \right)^n \tag{4.6}$$

Assuming the electronic overlap does not change between various vibrational states, P_{n0} will decide the excitation probability for each vibrational excited level when an electron hops on or off the quantum dot. In Figure 4.11, P_{n0} ($n = 0 \sim 10$) for different values of g is plotted. In general, P_{n0} increases with n until $n \sim g^2/2$ and then monotonically decreases. The maximum of P_{n0} can be found near $n \sim g^2/2$ (arrows). In the C_{60} transistor case, g is near 1, which suggests, within this model, that the tunneling will be larger for the ground state than for the excited states (see Figure 4.11). Furthermore, only the lowest excited states will have a large enough excitation probability to be observable in the experiment.

I-V curves can be calculated using (4.6) for a vibrating quantum dot with very asymmetric tunneling rates and electrode capacitances. Five *I-V* curves calculated for different values of g are shown in Figure 4.12. When $g = 0$, it is a fixed quantum dot and its *I-V* curve shows a current step with an amplitude of $|e|\Gamma$ after the Coulomb blockade. As g grows larger, the first current step corresponding to the tunneling between two vibrational ground states becomes smaller. At the same time, other current steps that correspond to vibrational excited states grow larger with increasing g. In the *I-V* curves of a C_{60} device shown in Figure 4.3, the first current step is generally larger than the second current step. This again suggests a small Franck-Condon factor for the C_{60} device.

Other properties of a vibrating quantum dot whose tunneling rates are described by (4.6) can be predicted. One such example is the temperature dependence of a Coulomb oscillation curve. The Coulomb oscillation of a single-level quantum dot was
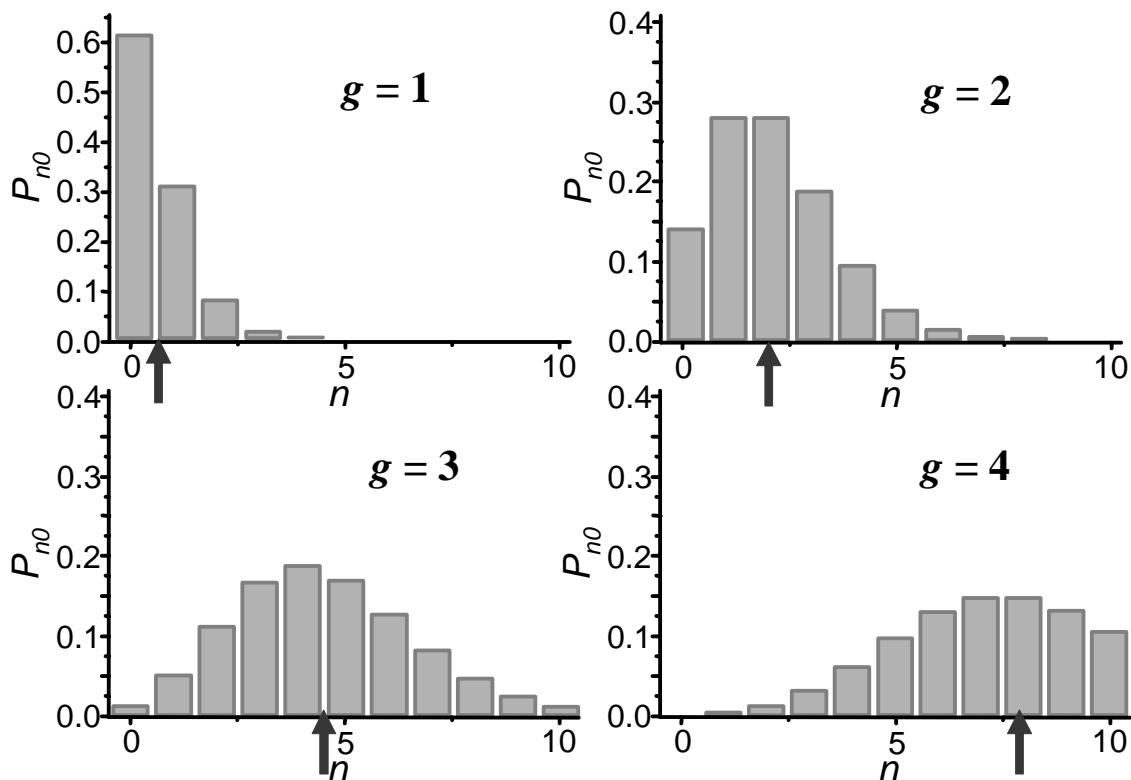
Figure 4.11 The vibrational overlap P_{n0} for different Franck-Condon factors. The arrows mark $g^2/2$.
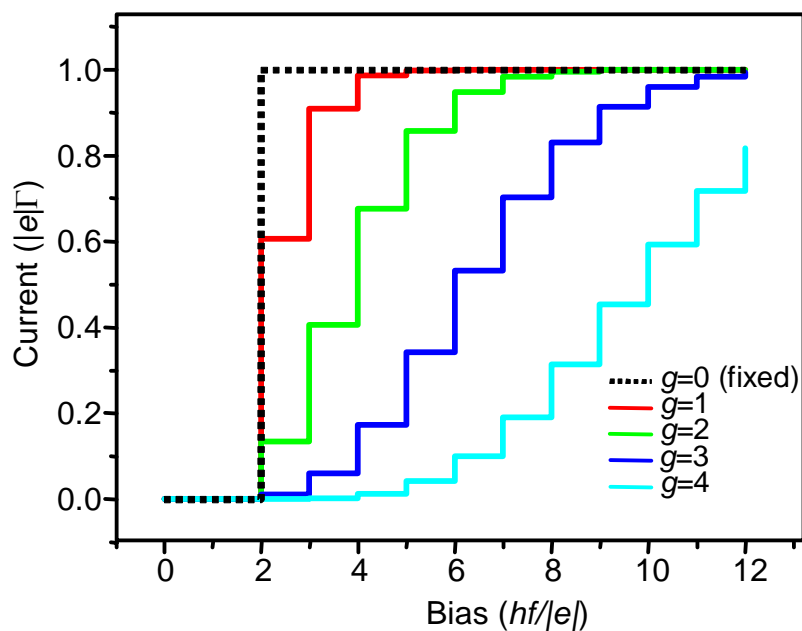
Figure 4.12 *I-V* curves calculated for a quantum dot at 0 K with one vibrational mode with the excitation quantum of *hf*. The calculation is done for a quantum dot with extremely asymmetric tunnel barriers and electrode capacitances. At zero bias, the ground level is assumed to be 2*hf* away from the Fermi level.

described earlier in Chapter 2 (see equation (2.16)). The peak height monotonically decreases with increasing temperature (1/*T* dependence) and the peak width (FWHM) is linearly proportional to the temperature (see Figure 2.8). When there are multiple

vibrational levels present in the quantum dot and all the tunneling rates are described by the vibrational wave function overlap, a different behavior is expected

One can calculate the Coulomb oscillation curve in this case by following the method described in Beenakker *et al*[21]. The result is the following.

$$\left.\frac{dI}{dV}\right|_{V=0} = \frac{e^2\Gamma}{4k_BT}\left(\cosh\left(\frac{|e|\alpha(V_G-V_C)}{2k_BT}\right)\right)^{-2}\sum_{all(m,n)}\frac{2\left(1-e^{-hf/k_BT}\right)}{e^{-mhf/k_BT}+e^{-nhf/k_BT}}P_{mn} \qquad (4.7)$$

Here P_{mn} is the square of the vibrational overlap $\left|\langle\Psi_m(x-\delta)|\Psi_n(x)\rangle\right|$ that can be calculated as follows for a simple harmonic oscillator.

$$\langle\Psi_m^{SHO}(x-\delta)|\Psi_n^{SHO}(x)\rangle =$$
$$e^{-g^2/4}\sqrt{m!n!}\left(\frac{g}{\sqrt{2}}\right)^{m-n}\left[\sum_{k=\max(0,n-m)}^{n}\left(\frac{-g^2}{2}\right)^k\frac{1}{k!(n-k)!(m-n+k)!}\right] \qquad (4.8)$$

Equation (4.7) clearly suggests that the Coulomb oscillation peak (G_{max}) will be no longer proportional to $1/T$. Instead, it can show a non-monotonic behavior depending on the value of g. However, the FWHM will display the linear temperature dependence as in a fixed quantum dot. Figure 4.13 plots calculated G_{max} as a function of temperature for four different values of g. It is clear that the peak height does not follow the $1/T$ dependence any more. It rather decreases more slowly or even shows a dip when g is larger than 2.

For comparison, the Coulomb oscillation peak measured from a C_{60} device is plotted in Figure 4.14 for different temperatures. It shows a monotonic decrease of the peak height with increasing temperature, but it decreases very slowly, changing only by a factor of 2 between 1.5 K and 13 K (left inset). The peak width (FWHM) grows approximately linearly with temperature (right inset). Figure 4.14 clearly shows a departure from the standard behavior of a fixed single-level quantum dot. Instead, it can be qualitatively explained using similar behaviors of a vibrating quantum dot with $g < 2$ as described above.

Further quantitative description of a vibrating quantum dot requires more sophisticated calculation that incorporates various interactions with the environment. For example, any normal mode vibration of a quantum dot can be coupled to the phonon bath of the substrate. This coupling causes the dissipation of the vibrational excitation of the
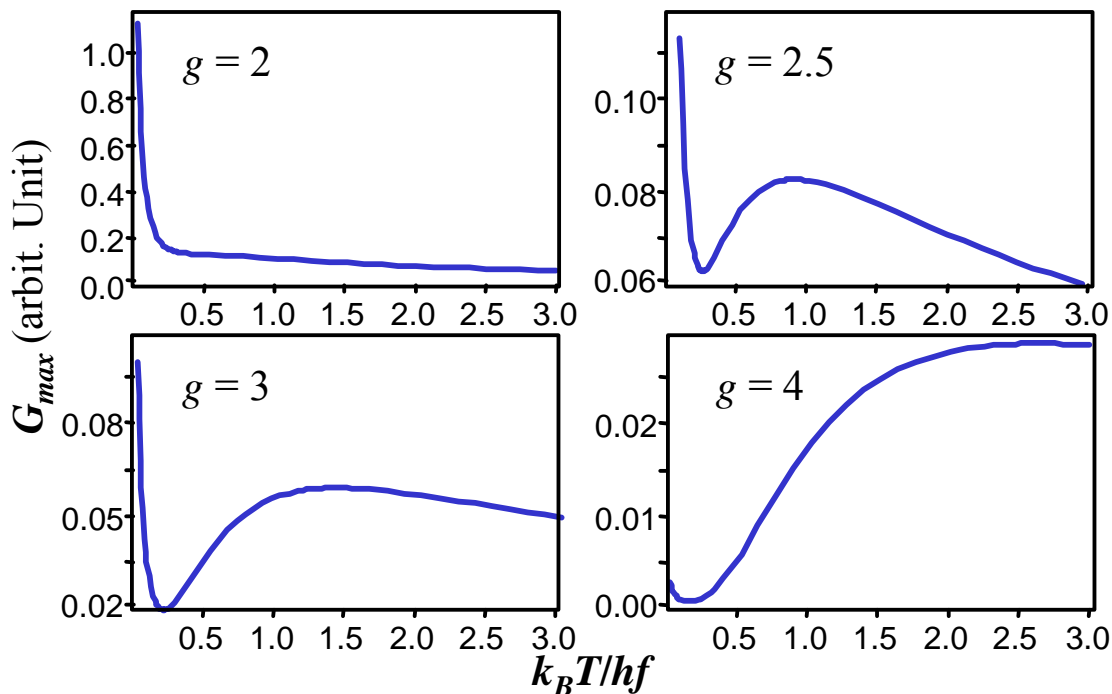
Figure 4.13 The temperature dependence of the Coulomb oscillation peak height with different Franck-Condon factors. When *g* is above 2, it shows a non-monotonic behavior unlike the case with a fixed quantum dot.
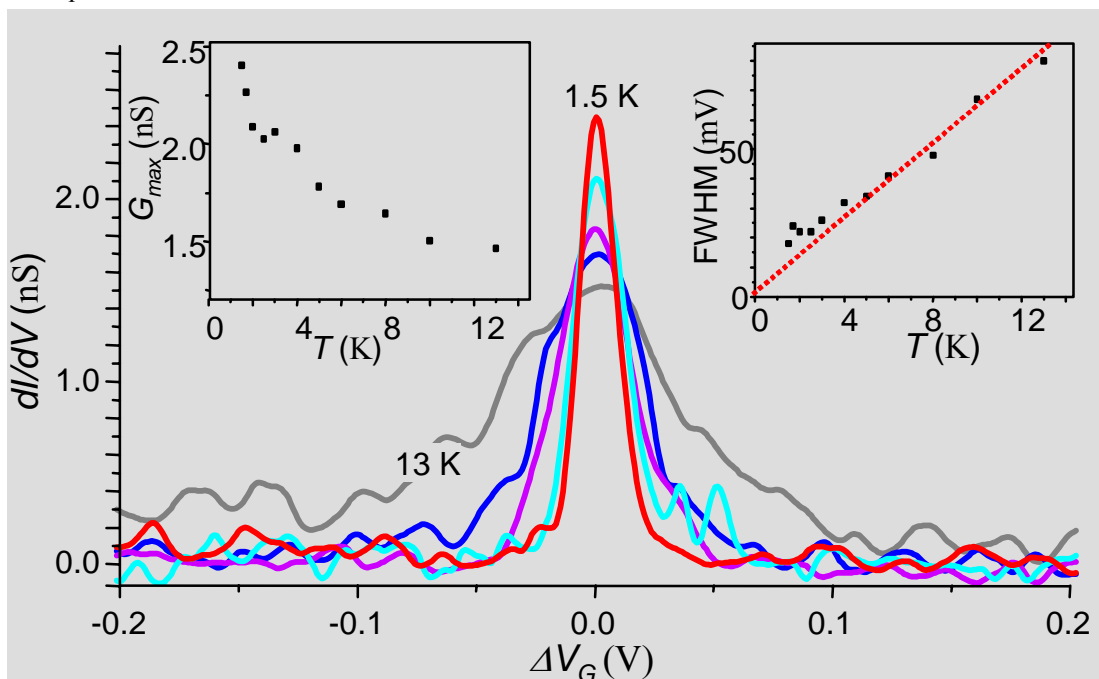
Figure 4.14 The Coulomb oscillation peak measured from a C$_{60}$ device at different temperatures. The curves are shifted in V_G so that the peak is located at 0 V. Measured peak heights and the FWHM are plotted as a function of temperature in the insets.

quantum dot, therefore reducing the quality factor *Q* of the oscillator. In fact, the center-of-mass motion of C$_{60}$ is expected to strongly couple to the substrate and hence will have

a smaller Q. Using a simple physical argument, Braig and Flensberg estimated Q for the C_{60} center-of-mass motion[75].

$$Q \approx \frac{\rho \upsilon_s / \omega_0}{M} = \frac{M_{Au}}{M} \tag{4.9}$$

Here ρ and υ_s are the mass density and the sound velocity of a gold substrate, and $M_{Au} = \rho \upsilon_s / \omega_0$ is the mass of a gold layer located within the wavelength of the phonon mode. Based on (4.9), one gets Q between 1 and 10 for the C_{60} center-of-mass vibration.

Braig and Flensberg[75] also incorporated the coupling with environment into the rate equations and solved them. Using the calculated results, they could qualitatively match the experimental *I-V* curves shown in Figure 4.3, when $g = 1 \sim 2$ and $Q = 2 \sim 6$. Therefore, the center-of-mass vibration of C_{60} molecule is strongly damped (low Q factor) and it finishes the oscillation cycle only several times before dissipation, which limits the lifetime of this vibration to several ps. Compared to this, the typical time scale that the electron resides on the C_{60} molecule is on the order of 100 ps. Therefore, the electron tunneling rate in C_{60} devices is slower that the vibration dissipation and hence it is an equilibrium process. The vibrational excitation created by one tunneling event dissipates before the next tunneling event occurs.

All the discussions above assume that there is only one vibrational mode to the quantum dot, which resembles the C_{60} transistor case. However, molecules in general have more than one vibrational normal mode, including center-of-mass vibrations and intramolecular vibrations. Furthermore, the excitation probability for each vibrational mode can vary according to its normal vectors and the electrostatic environment. The description of the coupling between tunneling electrons and various normal modes of a molecule requires a more general approach than the one presented here.

4.6 Summary

In this chapter, we discussed transport measurements performed on single-C_{60} transistors. They exhibit a Coulomb blockade with a large conductance gap and we also observe quantum excitations of the molecule. The most notable feature is the 5 meV excitation, a signature of the center-of-mass vibration of C_{60} against a gold surface. This

observation serves as an example where a tunneling electron can be used to both excite and probe a nano-mechanical vibration of a single molecule.

This coupling between the tunneling electrons and the molecular vibration can be theoretically addressed using the Franck-Condon model which includes the vibrational wave function overlap into the tunneling rates. This process is expected to be important in electron transport in other single molecules as well. We will see more examples in the following chapters.

Chapter 5

Vibration-Assisted Electron Tunneling in C_{140} Single-Molecule Transistors

5.1 Introduction

In this chapter, we study electron tunneling in single-molecule transistors made from C_{140}, a molecule with a mass-spring-mass geometry chosen as a model system to study electron-vibration coupling. We observe vibration-assisted tunneling at an energy corresponding to the stretching mode of C_{140}. The interaction between a local electric field and the induced dipole moment of the molecule explains why this mode couples better to electron tunneling than do the other internal vibrational modes. We make comparisons between the observed tunneling rates and those expected from the Franck-Condon model.

As we saw from C_{60} transistors in the previous chapter, vibrational modes of molecules can affect the current flow when electrons travel through molecules. Molecular-vibration-assisted tunneling was first measured in the 1960's using devices whose tunnel barriers contained many molecules[76, 77]. Recently, effects of vibrations in single molecules have been measured using a scanning-tunneling microscope[65], single-molecule transistors made using nanofabrication techniques[32, 33] and mechanical break junctions[48]. Theoretical considerations of the coupling of vibrational modes to electron tunneling have predicted a rich range of behaviors, with different regimes depending on the relative magnitudes of the rate of electron flow, the vibrational frequency, and the damping rate of vibrational energy, and also on whether or not electrons may occupy resonant states on the molecule [51, 70, 78-80].

A quantitative analysis of electron-vibration interactions has been difficult to achieve in previous molecular-transistor experiments. In [33], neither the precise nature of the vibrational modes nor their energies was determined independently of transport measurements. In the experiments described in the previous chapter, the "bouncing-ball" mode of a single C_{60} molecule against a gold surface was observed, a mode not intrinsic

to the molecule itself, and one that had not been previously observed in spectroscopic measurements.   In this chapter we discuss single-molecule transistors made using a molecule, C$_{140}$, chosen specifically to have low energy internal vibrational modes that are well understood.   We observe clear signatures of one of these modes and discuss theoretically why it has the strongest coupling to the tunneling electrons.

Most text and figures presented in this chapter are prepared based on Pasupathy, *et al*[81].

5.2 Sample Preparation

The C$_{140}$ molecule consists of two C$_{70}$ balls joined together by two covalent C-C bonds (Figure 5.1(a)).   The vibrational modes of C$_{140}$ have been measured by Raman spectroscopy and modeled numerically[82] (shown in 5.1(b) and (c)).   The six lowest-energy modes are intercage vibrations in which each C$_{70}$ ball moves essentially as a rigid unit, so that the molecule can be thought of as a mass-spring-mass oscillator.   The simple stretching mode is observed most prominently in Raman spectroscopy, with an energy of 11 $\pm$ 0.5 meV.   The other intercage modes involve bending or twisting of the C$_{140}$ molecule, and they are predicted to be at 2.5, 2.7, 4, 15, and 17 meV.   The lowest intracage excitation of a C$_{70}$ molecule by itself is approximately 29 meV[38] and this value does not change significantly in C$_{140}$ (Figure 5.1(b)).   The C$_{140}$ we use was synthesized by pressure treatment of polycrystalline C$_{70}$ at 1 GPa and 200 °C, and purified by chromatography and characterized by C^{13} NMR, Raman and infrared spectroscopy[82].   This process produces predominantly the C$_{2h}$ isomer of C$_{140}$ (Figure 5.1(a)) out of several possible isomers[82].

An atomic force microscope image of our transistor structure is shown in Figure 5.2(a) and its geometry is illustrated in Figure 5.2(b).   A C$_{140}$ molecule bridges source and drain electrodes that are about 1 nm apart.   The molecule is also capacitively coupled to a gate electrode.   To make these devices, we followed the fabrication procedure described in section 3.2 (device design II).   We evaporate an Al pad 20 nm thick and 2 μm wide to serve as the gate electrode, and then oxidize in air to form the gate insulator. On top of the gate we pattern by liftoff a gold wire 200-600 nm long, 20 nm high and 50-
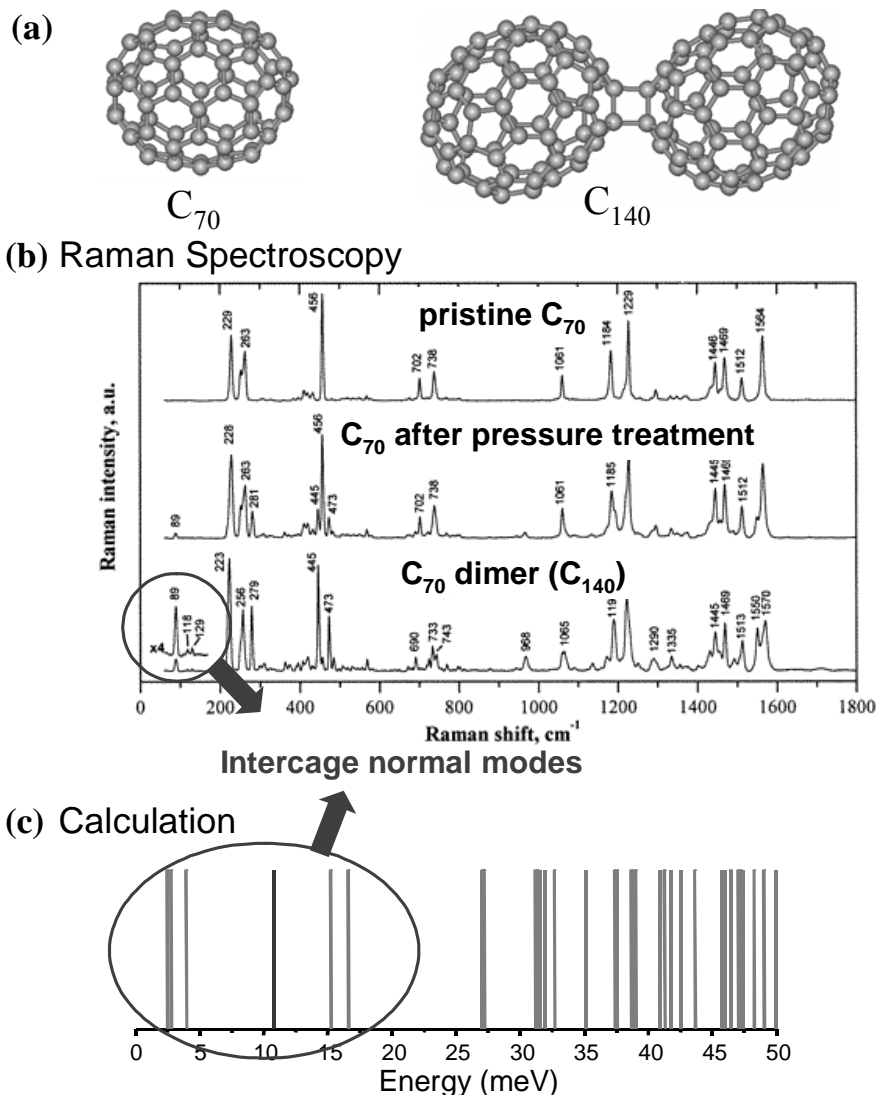
Figure 5.1 Vibrational properties of C_{140} (a) Two fullerene molecules measured in this experiment: C_{70} and C_{140} (b) Vibrational Raman spectroscopy of C_{140} shows low energy modes (< 200 cm^{-1}) that corresponds to intercage vibrations of C_{140}. (c) Normal mode calculation on C_{140} also shows the presence of six such intercage vibrational modes.

100 nm wide with 2-3 nm of Cr as an adhesion layer or a platinum wire having a similar geometry without the adhesion layer.

We deposit approximately 10 μl of a 100 μM solution of C_{140} molecules in *o*-dichlorobenzene onto the device area, and we allow the solvent to evaporate or we blow dry after approximately 10 minutes. After the molecules are deposited, we cool the devices to cryogenic temperatures and use electromigration to create a nm-sized gap in the wire within which a molecule is sometimes trapped. The success rate for incorporating a molecule is approximately 10% for both the gold and platinum wires.

(a)

(b)
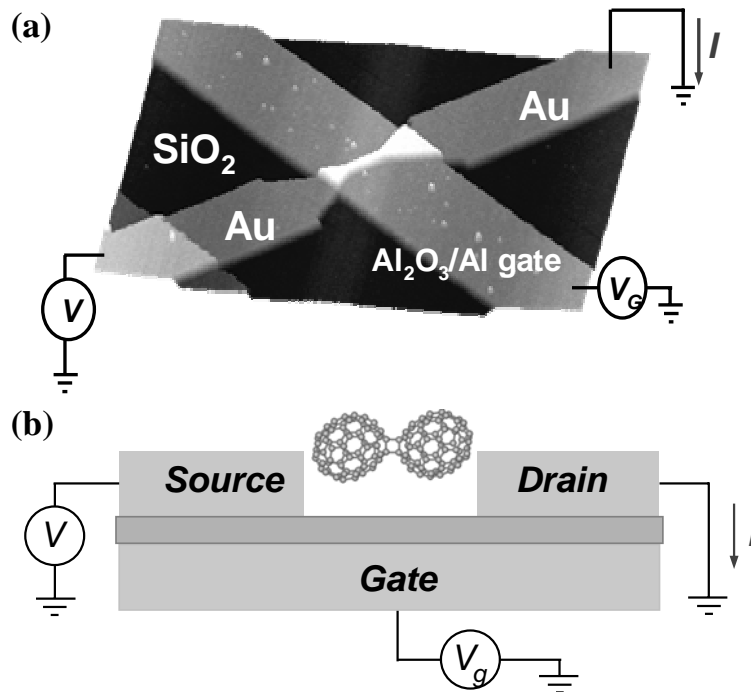
Figure 5.2 (a) A topographic AFM image (5 by 5 μm) of a finished device. (b) A schematic of a C$_{140}$ transistor with the measurement circuit.

The orientation of the molecule in the device is not known and likely varies from device to device. All the measurements were performed in either a pumped He-4 cryostat at 1.5 K or in a dilution refrigerator with an electron base temperature lower than 100 mK.

5.3 Coulomb Blockade in C$_{140}$ Transistors

In Figure 5.3, we show several current versus bias voltage (*I-V*) curves measured from a C$_{140}$ device at different gate voltages (*V$_G$*). The device exhibits Coulomb-blockade behavior; electron flow is suppressed at low voltages because electrons must overcome a charging energy to tunnel on or off the C$_{140}$ molecule. Two-dimensional plots of differential conductance (*dI/dV*) as a function of *V* and *V$_G$* are shown in Figure 5.4 for four of the fourteen C$_{140}$ devices we have examined. The dark areas on the left and right of each plot are the regions of Coulomb blockade. The boundaries of the dark areas show what source-drain voltage is required at a given value of *V$_G$* to enable tunneling via the lowest-energy electronic state of the molecule with one more or one less electron. Tunneling can occur close to *V* = 0 only near one value of gate voltage, *V$_C$*, which varies from device to device because of variations in the local the electrostatic
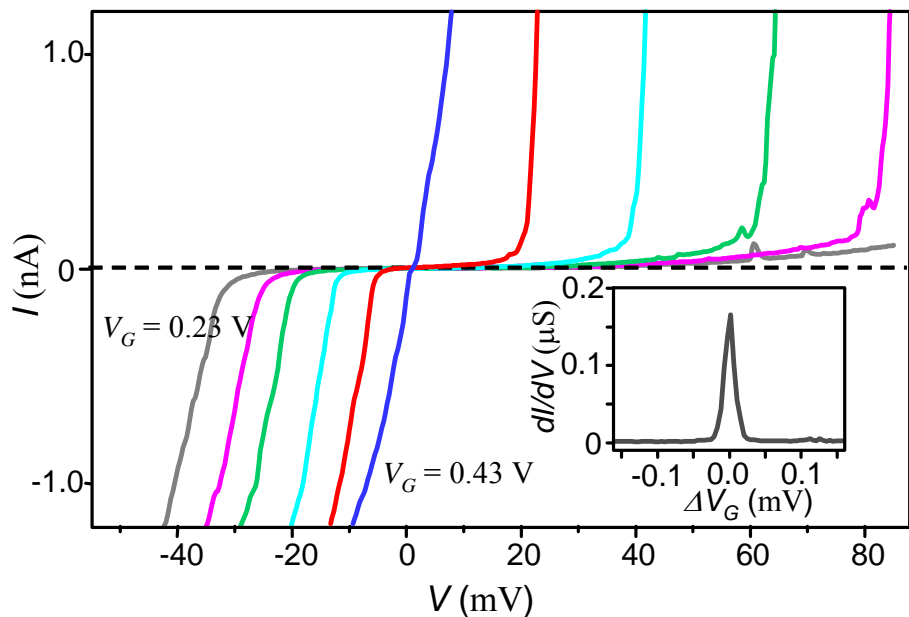
Figure 5.3 *I-V*'s taken from a C_{140} single electron transistor. V_G increases by 0.04 V from gray (0.23V) to blue curve. Inset: the Coulomb oscillation curve from the same device. V_G axis is offset to position the peak at the center.
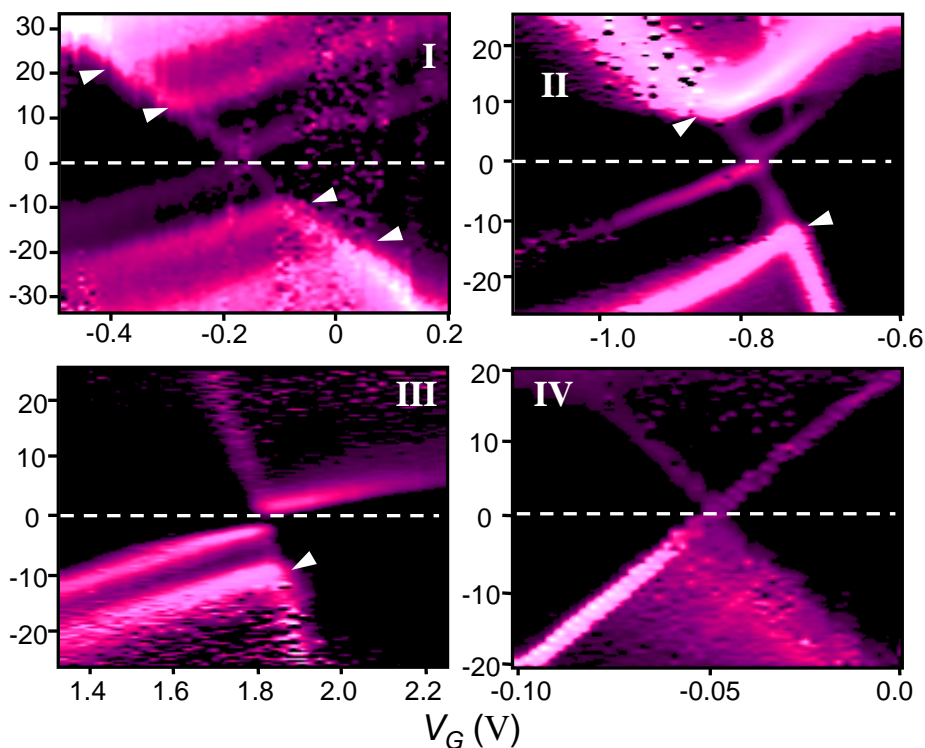
Figure 5.4 Color scale *dI/dV* plots for four C_{140} devices. White arrows indicate excited levels at ~11meV and ~22meV. The conductance is represented by the color scale increasing from black (zero) to white (maximum). The maximum conductance is 200 nS (device I), 600 nS (II), 15 nS (III), and 100 nS (IV), respectively. Measurements were done at 1.5 K for I-III and 100 mK for IV.

environment. Because current flow at low bias occurs only near a value of V_G that is different for each molecule, we can be confident that the current flows through only a single molecule as long as we perform our measurements sufficiently closely to $V_G = V_C$.

Additional *dI/dV* lines are observed in Figure 5.4 at values of $|V|$ larger than the boundary of the Coulomb-blockade regions. As we discussed in Chapter 2, these lines correspond to thresholds for current pathways involving excited quantum states of the molecule. The lines which meet the dark blockade area at $V_G < V_C$ $(V_G > V_C)$ correspond to excited quantum levels of the $V_G < V_C$ $(V_G > V_C)$ charge state. The energy of each excited level can be read off from the bias voltage of the point where the *dI/dV* line intercepts a boundary of the blockade region (white arrows).

5.4 Observation of the Stretching Vibrational Mode (11meV) in C$_{140}$ Transistors

The details of the excited-state energy spectra that we measure differ from device to device. In Figure 5.5(a), we plot a histogram of all of the excited state energies that are resolved below 20 meV in fourteen C$_{140}$ devices; excitations in each charge state are recorded separately. An excitation at 11 ± 1 meV is seen in eleven out of the fourteen devices. In seven of these devices, the 11 meV line is present for both of the accessible charge states, while in four others it is seen for only one. In one sample (device I), well-resolved excited levels are also observed near 22 meV for both charge states, twice the 11 meV energy.

As a control experiment, we also measured eight devices made with single C$_{70}$ molecules. A *dI/dV* plot for one of the C$_{70}$ devices is shown in Figure 5.5(c). A histogram of the observed excited levels for C$_{70}$ devices is shown in Figure 5.5(b). The prominent peak observed near 11 meV for C$_{140}$ is absent in C$_{70}$ devices.

The presence of the 11 meV excitation in C$_{140}$, but not C$_{70}$, indicates that it is an excitation of the entire molecule, and not the C$_{70}$ sub-units. The presence of the same excitation for different charge states of the same molecule, and the observation of an excitation at 2 x 11 meV in one device strongly suggest that the 11 meV excitation is vibrational in nature. A purely electronic excitation should not be the same in both charge states nor appear as multiples of a fundamental excitation. Based on its energy,

(a)

(b)

Excited state energy (meV)

(c)
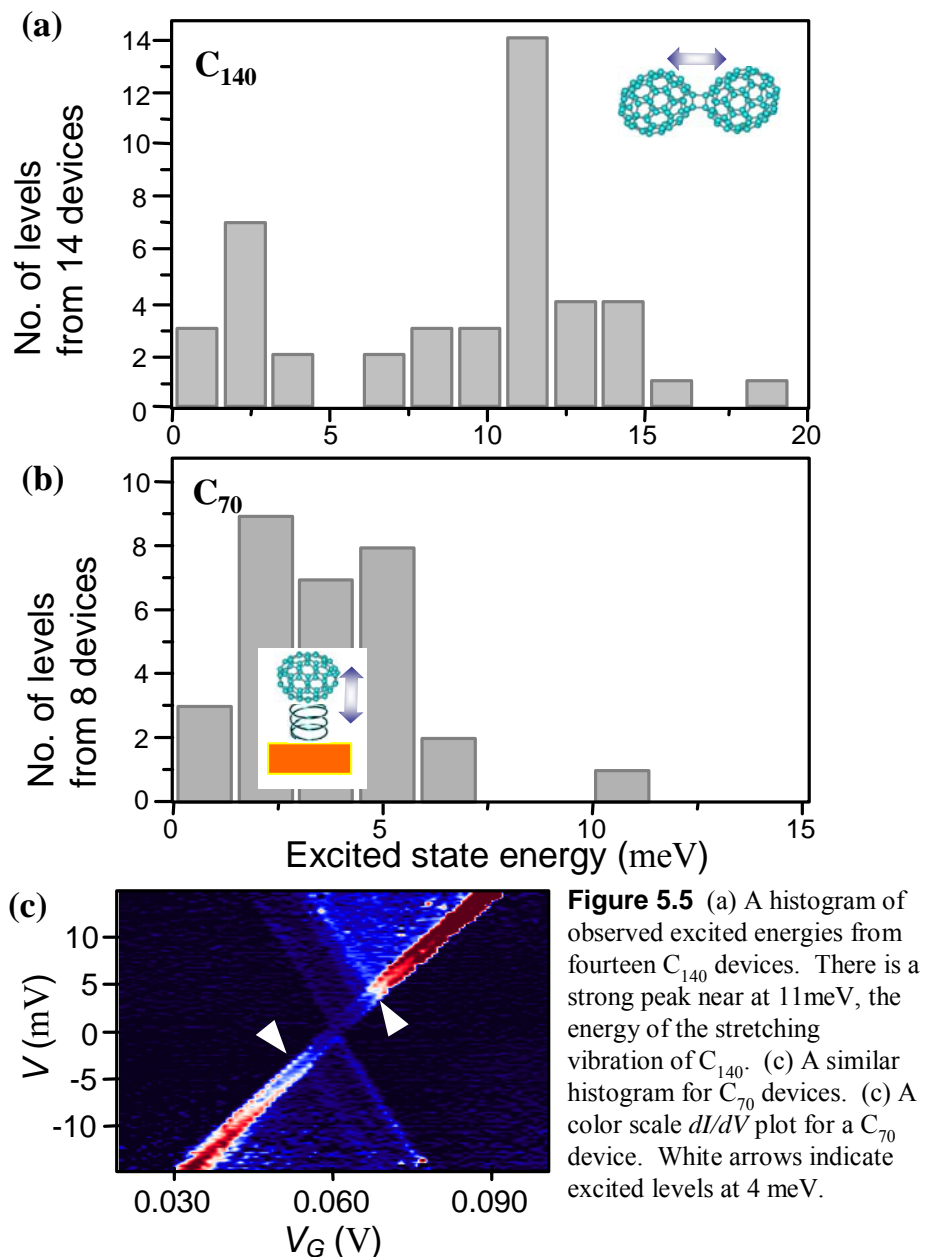
Figure 5.5 (a) A histogram of observed excited energies from fourteen C_{140} devices. There is a strong peak near at 11meV, the energy of the stretching vibration of C_{140}. (c) A similar histogram for C_{70} devices. (c) A color scale dI/dV plot for a C_{70} device. White arrows indicate excited levels at 4 meV.

we identify this excitation with the intercage stretch mode of C_{140}[82]. This is the principal observation in the experiment presented in this chapter.

The C_{70} histogram exhibits excitations below 5 meV. These are likely associated with the bouncing bouncing-ball mode of the molecule, as demonstrated in previous experiments on C_{60} (Chapter 4). For C_{140} devices, sub-5 meV excitations are also observed. These may also arise from the bouncing-ball mode of the entire C_{140} molecule. An alternative candidate is the internal modes of C_{140} at 2.5, 2.7 and 4 meV. We cannot experimentally distinguish between these possibilities. However, calculations (see

below) suggest that the tunneling electrons couple strongly to only the intercage stretch mode, but not the other internal modes. Significantly, peaks in the histogram are not observed near the bending/twisting intercage modes of C$_{140}$ at 15 and 17 meV.

5.5 Excitation Mechanism of the Stretching Vibrational Mode

The coupling between vibrational excitations and an electron tunneling onto or off of a molecule can be understood within the framework of the Franck-Condon model[71]. Basic concepts of this model were already discussed in the previous chapter to explain the coupling between tunneling electrons and the bouncing ball mode of C$_{60}$ (section 4.5).

We will analyze the data from C$_{140}$ devices also within the framework of the Franck-Condon model. C$_{140}$ has a large number of vibrational states we denote by α_j, where α labels the mode of frequency ω_α and j is the number of vibrational quanta excited in the mode. For each vibrational mode, the tunneling electron drives a transition from the ground vibrational state with A electrons to a vibrational state α_j with B electrons, where $B - A = +1$ (-1) for tunneling on (off) the molecule. The energy landscape for a transition from the charge state A to B is illustrated in Figure 5.6(a). The tunneling rate is determined by the overlap of the starting configurational wavefunction, Ψ_g^A, with the one after tunneling, $\Psi_{\alpha_j}^B$:

$$\Gamma_{\alpha_j}^{A \to B} = \Gamma_{electron} P_{\alpha_j}, \text{ where } P_{\alpha_j} = \left| \left\langle \Psi_{\alpha_j}^B \middle| \Psi_g^A \right\rangle \right|^2 \text{ and } \sum_j P_{\alpha_j} = 1. \qquad (5.1)$$

If the electronic contribution $\Gamma_{electron}$ is assumed constant for the different vibrational transitions and if the rate-limiting step for current flow is the $A \to B$ transition, the current step associated with a given vibrational excitation is:

$$\Delta I_{\alpha_j} / \Delta I_g = P_{\alpha_j} / P_g \qquad (5.2)$$

where ΔI_g is the ground state current. In order to predict the size of the current steps, we must therefore calculate the atomic rearrangements that occur when a charge is added to or subtracted from the molecule. We will first perform this calculation for an isolated C$_{140}$ molecule and then discuss effects of the local electrostatic environment, before making comparisons to our measurements.

(a)
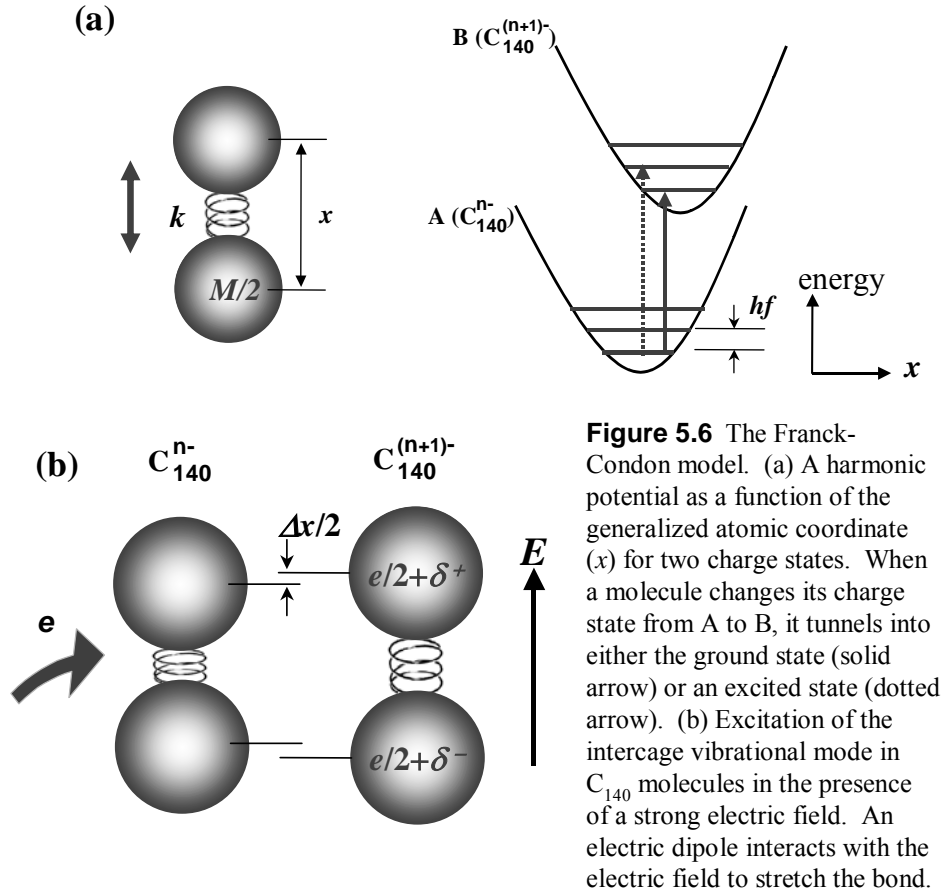
Figure 5.6 The Franck-Condon model. (a) A harmonic potential as a function of the generalized atomic coordinate (x) for two charge states. When a molecule changes its charge state from A to B, it tunnels into either the ground state (solid arrow) or an excited state (dotted arrow). (b) Excitation of the intercage vibrational mode in C_{140} molecules in the presence of a strong electric field. An electric dipole interacts with the electric field to stretch the bond.

For the isolated molecule, we calculate the overlaps P_{α_j} using the semi-empirical method PM3 under Gaussian 03. The charge state of C_{140} in our devices is not known, but since the fullerenes are easily reduced and not easily oxidized[83], we have analyzed the initial charge states $n^- = 0$, 1^-, 2^-, and 3^-.

The PM3 calculations indicate that the probability of tunneling without exciting any of the vibrational degrees of freedom is small. This means that tunneling at low biases is suppressed. The coupling is distributed over all of the vibrational modes, but it is large for a relatively small number. Within our measurement range ($|eV| < 30$ meV) the calculations indicate that the coupling is dominated by a single mode, the 11 meV stretching mode ($\alpha = s$). For the $0 \rightarrow 1^-$ transition, $P_{s1}/P_g = 0.25$. Couplings to all other vibrational modes in the measurement range are found to be smaller by at least a factor 10. The results are qualitatively similar for other charge states.

The physics of the 11 meV stretching mode can be captured using a simple model of the molecule with two masses $M/2$ connected by a spring with a spring constant k, as

illustrated in Figure 5.6(a). The vibrational frequency is $\omega_s = (4k/M)^{1/2}$ and the zero-point rms amplitude of fluctuations in the vibrational coordinate is $x_0 = [2\hbar/(M\omega)]^{1/2} = 2$ pm. The length of the molecule changes by Δx when one charge is added. The Franck-Condon result for the transition probability associated with one quantum of the stretching mode, normalized by the ground-state probability, is

$$P_{s1}/P_g = (\Delta x/x_0)^2/4 \qquad (5.3)$$

Higher-order transitions involving j quanta of a vibrational mode have rates related to the one-quantum transitions:

$$P_{s_j}/P_g = (P_{s1}/P_g)^j/j! \qquad (5.4)$$

In going from the neutral to 1^- charge state for isolated C$_{140}$, PM3 predicts that Δx = -1.9 pm. Equation (5.3) then gives I_{s1}/I_g = 0.23, in good agreement with the full calculation above. Multiple-quanta transitions should be much smaller by Eq. (5.4). For other charge states, the calculated strength of the transition assisted by the stretching mode is weaker, because Δx is smaller: for the $1^- \rightarrow 2^-$ transition Δx = -0.4 pm, for $2^- \rightarrow 3^-$ Δx = -0.1 pm, and for $3^- \rightarrow 4^-$ Δx = -0.3 pm.

The electrostatic environment in the neighborhood of the C$_{140}$ molecule may also play an important role. In general, we expect that the C$_{140}$ molecule will be subject to a strong local electric field E due to image charges, work-function differences, and/or localized charged impurities. For example, an image charge at a distance 0.8 nm generates E = 2 V/nm. We have not succeeded in making quantitative estimates of these field-enhancement effects because the Gaussian 03 implementation of PM3 does not allow for solutions in an external field. However, a local field can be expected to preferentially enhance vibration-assisted tunneling associated with the stretching mode. When an extra electron tunnels onto C$_{140}$, the presence of E will produce unequal charges on the two C$_{70}$ cages, as illustrated in Figure 5.6(b). The rearrangement of charge density within the molecule will produce changes in chemical bonding forces, leading to changes in Δx. In addition, the interaction of E with the charge polarization ($+\delta, -\delta$ in Fig. 5.6(c)) will stretch the C$_{140}$ by a length $\Delta x = E\delta/k$. To estimate the magnitude of this stretching, assume that the charge is fully polarized: $\delta = e/2$, and E = 2 V/nm. Then the
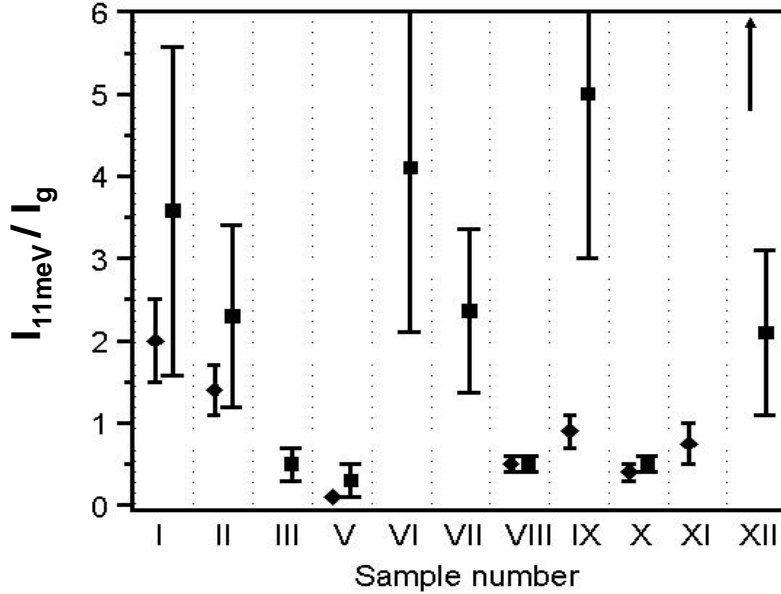
Figure 5.7 Values of $I_{11\text{meV}}/I_g$, the measured current step for the excited-state signal relative to the ground-state current. Values for both charge states n^- (squares) and $(n+1)^-$ (diamonds) are shown. One value is not displayed: for device XII, $I_{11\text{meV}}/I_g = 8 \pm 2.5$ for the $(n+1)^-$- charge state. Samples IV, XIII, and XIV have no visible 11-meV levels.

electrostatic stretching is $\Delta x \sim 1$ pm. Both this stretching and the chemical-bonding rearrangement may therefore produce displacements of comparable magnitude to the values calculated above for isolated C_{140}.

We expect that these electric-field effects will be strongly dependent on the angle between the field and the molecular axis, because C_{140} is most easily polarized along its long axis. This angular dependence means that the strength of the excited-state tunneling at 11 meV could vary significantly between devices because the orientation of the molecule in the junction may vary.

Figure 5.7 shows the measured ratio $\Delta I_{s1}/\Delta I_g$ for all of the devices. These were determined by taking the ratio of the current step height at the 11 meV peak to the current just before the step. In addition to the steps, an overall increasing background was observed that gives significant uncertainties in the step heights. In five of the devices (I, II, V, VIII, and X), the ratios were the same in both charge states, as expected within the simple Franck-Condon picture if the vibrational energies are not altered significantly by the addition of an electron. In three of these devices, $\Delta I_{s1}/\Delta I_g < 0.6$, consistent with the PM3 estimates above. Only the $j = 1$ vibrational state was observed for these three devices, in agreement with theory. For device I, $\Delta I_{s1}/\Delta I_g = 3.6 \pm 2.0$ and 2.0 ± 0.5 for

the n^- and $(n+1)^-$ state, respectively, indicating stronger coupling than expected from our estimate for isolated C$_{140}$. For this sample, additional lines were observed corresponding to the emission of two vibrational quanta ($j = 2$) with amplitudes $\Delta I_{s2}/\Delta I_g =$ 7.3 ± 4 for the n^- charge state and 2.3 ± 1.5 for the $(n+1)^-$ charge state. Equation (5.3) predicts 6.5 ± 4 and 2 ± 1 respectively, in good agreement with the measurements. For device II, strong coupling was also observed, but no $j = 2$ line was resolved, although the increasing background may have masked its presence. Overall, then, this subset of five devices is in reasonable agreement with the Franck-Condon predictions.

In the other devices showing an 11 meV feature, unusual behavior was seen that is not expected within our simple Franck-Condon picture. Large differences were observed in $\Delta I_{s1}/\Delta I_g$ for the two charge states; in many cases, a line was observed only in one charge state (devices III, VI, VII, and XI). In addition, anomalously large values of $\Delta I_{s1}/\Delta I_g$ were observed. These could either reflect strong electron-phonon coupling or an anomalous suppression of tunneling into the ground state by vibrational or other phenomena. Pronounced negative differential resistance was present in one device (VI).

5.6 Summary

In summary, in single-molecule transistors made from C$_{140}$ we observe vibration-assisted tunneling associated with an internal stretching mode of the molecule. The strong coupling of this mode to tunneling electrons, relative to the other molecular modes, is consistent with molecular modeling. Variations in the measured strength of vibration-assisted tunneling between different devices may be associated with an enhancement of the coupling between tunneling electrons and stretching-mode excitations by local electric fields

Chapter 6

Coulomb Blockade and the Kondo Effect in Single Atom Transistors

6.1 Introduction

Using molecules as electronic components is a powerful new paradigm in the science and technology of nanometer-scale systems[12]. Experiments to date have examined a multitude of molecules conducting in parallel[17, 18], or, in some cases, transport through single molecules[5, 6, 15, 40, 62, 84]. In the previous two chapters, we discussed single molecule transistors made from fullerene molecules, where electrons flow by hopping on and off the molecule.

The ultimate limit would be a device where electrons hop on to and off from a single atom between two contacts. In this chapter, we will describe transistors incorporating a transition metal complex designed so that electron transport occurs through well-defined charge states of a single atom. We examine two related molecules containing a Co ion bonded to polypyridyl ligands, attached to insulating tethers of different lengths. Changing the length of the insulating tether alters the coupling of the ion to the electrodes. In the longer molecule, the insulating tether forms a tunnel barrier at the contact and the device shows a Coulomb blockade with a low conductance. In the shorter molecule, we observe the Kondo effect with a high conductance, which indicates that the contacts are more transparent in this molecule.

This chapter is written based on a previously published paper[33]. Part of the text and figures are excerpted from the paper.

6.2 The Molecules and Device Preparation

The molecules that we have investigated are depicted in Figure 6.1. They are coordination complexes in which one Co ion is bonded within an approximately octahedral environment to two terpyridinyl linker molecules with thiol end groups, which confer high adsorbability onto gold surfaces. The two molecules ([Co(tpy-(CH$_2$)$_5$-
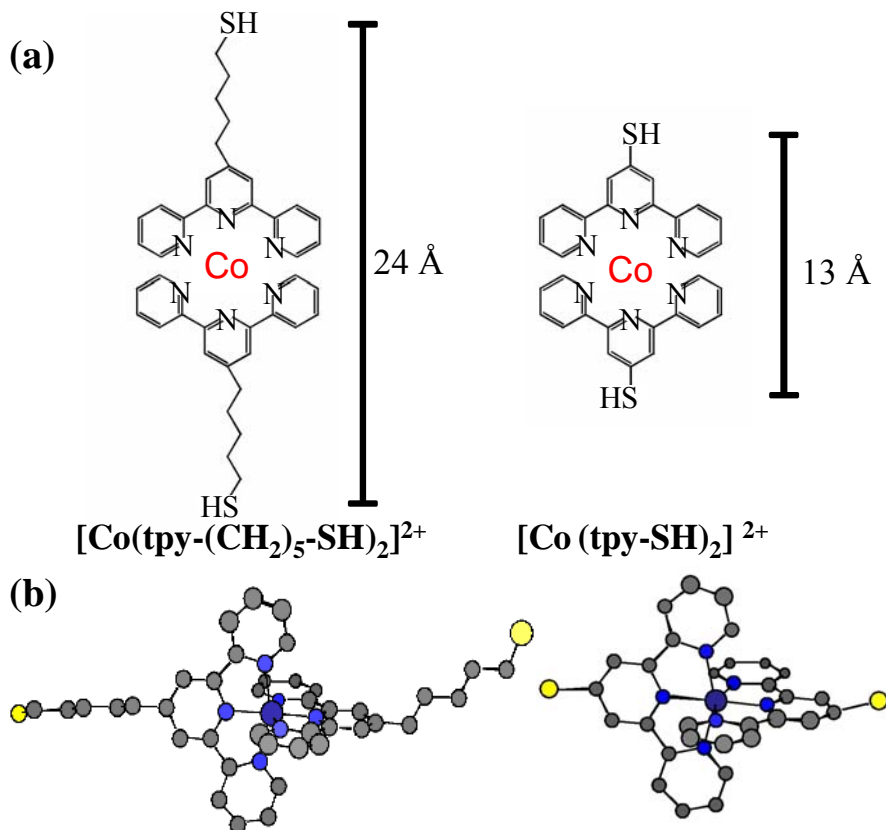
Figure 6.1 The molecules used in this study. (a) The geometry minimized structure of $[Co(tpy-(CH_2)_5-SH)_2]^{2+}$ (where tpy-$(CH_2)_5$-SH is 4'-(5-mercaptopentyl)-2,2':6',2"-terpyridinyl) and $[Co(tpy-SH)_2]^{2+}$ (where tpy-SH is 4'-(mercapto)- 2,2':6',2"-terpyridinyl). The scale bars show the lengths of the molecules as calculated by energy minimization. (b) Three-dimensional structure of the two molecules. The cobalt ion at the center (dark blue) is surrounded by six nitrogen atoms (light blue) in an approximately octahedral environment. The sulfur atoms (yellow) on either end bind to gold strongly. The gray balls are carbon and the hydrogen atoms are not shown.

SH)$_2]^{2+}$ and $[Co(tpy-SH)_2]^{2+}$) differ by a 5-carbon alkyl chain within the linker molecules. The length of the molecule is 24 Å for the longer $[Co(tpy-(CH_2)_5-SH)_2]$ molecule and 13 Å for $[Co(tpy-SH)_2]$.

The synthesis of the longer molecule was described in Maskus *et al*[85]. It was synthesized from an ethanolic solution of tpy-$(CH_2)_5$-SH and aqueous $CoCl_2$. The molecule is stabilized by the strong ligand bonding between the cobalt ion and six pyrine units surrounding it. Likewise, the shorter molecule, $[Co(tpy-SH)_2]^{2+}$, was a complex of cobalt with tpy-SH. The tpy-SH ligand was prepared from 4'-chloro-2,2':6',2" terpyridinyl and sodium ethanethiolate by a nucleophilic aromatic substitution followed

by nucleophilic aliphatic substitution to give the thiolate anion and subsequent protonation to give the desired compound[86, 87].

These molecules were selected because it is known from electrochemical studies that the charge state of the Co ion can be changed from 2+ to 3+ at low energy. A cyclic voltammogram for $[Co(tpy-SH)_2]^{2+}$ adsorbed on a gold electrode in an acetonitrile/supporting electrolyte solution is shown in Figure 6.2, indicating that a positive voltage $V_s \sim +0.25$ V (measured against an Ag/AgCl reference) applied to the solution removes one electron from the ion. Similar results were obtained for $[Co(tpy-(CH_2)_5-SH)_2]^{2+}$. Compared to Co, other metal ions such as Fe and Mn are known to require a larger energy to change the charge state.

Preparation of the single-molecule transistors (schematically shown in Figure 6.3(a)) begins with the thermal growth of a 30 nm SiO_2 insulating layer on top of a degenerately doped Si substrate used as a back gate. Continuous gold wires with a width less than 200 nm, lengths of 200-400 nm and thickness of 10-15 nm are fabricated by electron beam lithography. The detailed fabrication procedure is described in Chapter 3. The final device geometry used in this experiment was obtained by following the fabrication process illustrated in Figure 3.4 with a direct metal evaporation instead of an angle evaporation for the nanowires.

The wires are cleaned with acetone, methylene chloride and oxygen plasma, and placed in a dilute solution of the molecules in acetonitrile for a day or more in order to
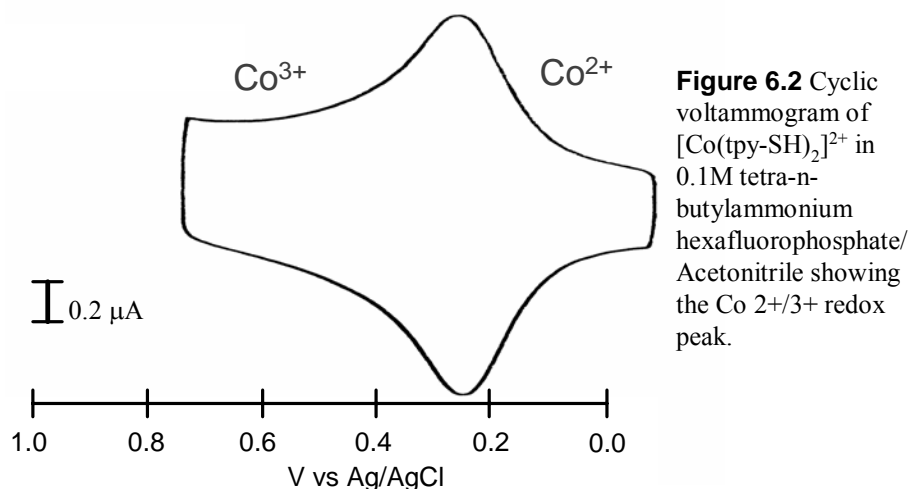
Figure 6.2 Cyclic voltammogram of $[Co(tpy-SH)_2]^{2+}$ in 0.1M tetra-n-butylammonium hexafluorophosphate/ Acetonitrile showing the Co 2+/3+ redox peak.

(a)

(b)
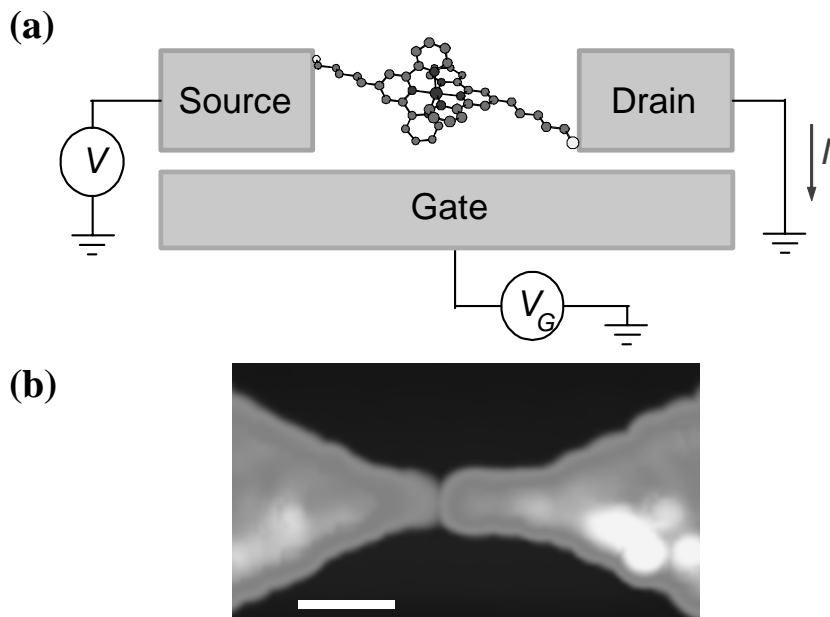
Figure 6.3 (a) A schematic diagram of the device with the longer molecule bridging the two electrodes. (b) A topographic atomic force microscope image of the electrodes with a gap (scale bar, 100nm).

form a self assembled monolayer (SAM) on the Au electrodes. The formation of SAM was later confirmed by the water-contact-angle measurement. The wires coated with molecules are then broken by electromigration, by ramping to large voltages (typically over 0.5 V) at cryogenic temperatures while monitoring the current until only a tunneling signal is present. As we discussed in Chapter 3, this produces a gap ~1-2 nm wide across which a molecule is often found. Electrical characteristics of the molecule are determined by acquiring current versus bias voltage (*I-V*) curves while changing the gate voltage (*V_G*). A topographic AFM image of the electrodes taken after the electromigration process is shown in Figure 6.3(b).

6.3 Coulomb Blockade in [Co(tpy-(CH$_2$)$_5$-SH)$_2$] Transistors

First we discuss the results obtained for the longer molecule, [Co(tpy-(CH$_2$)$_5$-SH)$_2$]. Most measurements were performed in a dilution refrigerator with an electron temperature < 100 mK. In about 10% of 400 broken wires we see *I-V* curves similar to those shown in Figure 6.4. The current is strongly suppressed up to some threshold voltage that depends on V_G and then it increases in steps. In Figure 6.5 we show higher-resolution color-scale plots of the differential conductance *dI/dV* at low bias, as a function
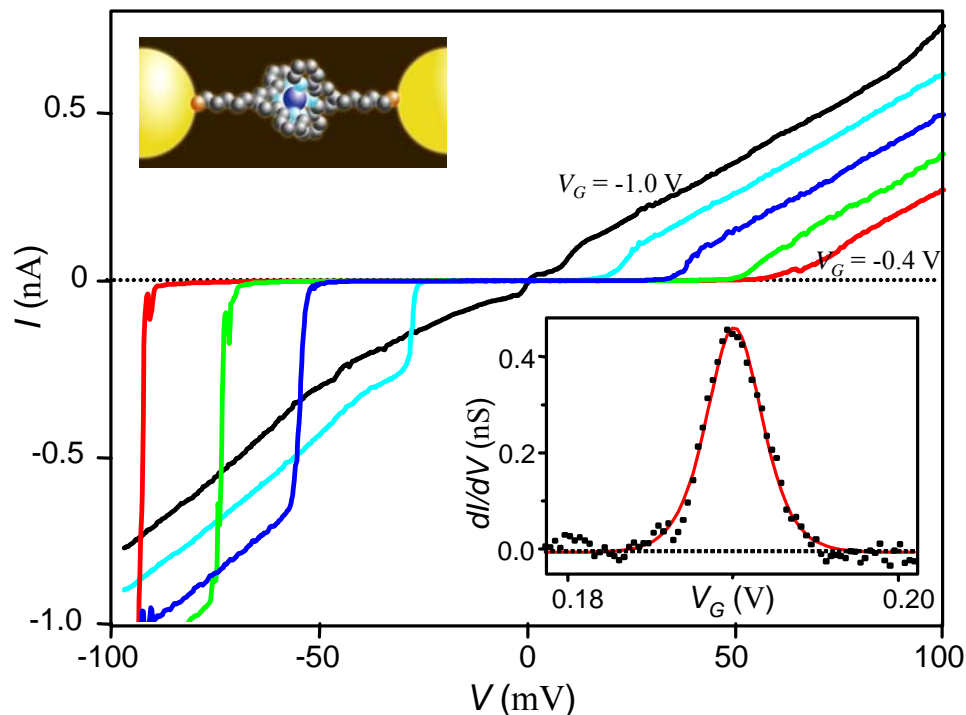
Figure 6.4 *I-V* curves of a $[Co(tpy-(CH_2)_5-SH)_2]^{2+}$ single-electron transistor at different gate voltages from -0.4 V (red) to -1.0 V (black) with $\Delta V_g \sim$ -0.15 V (temperature: 1.5 K). Lower inset: A Coulomb oscillation curve measured from another device. It was taken at 1.5 K and the red line is a theoretical fit with temperature at 1.9 K. Upper inset: a conceptual image of the longer molecule $[Co(tpy-(CH_2)_5-SH)_2]$ connecting two gold electrodes.

of V and V_G for three different devices. The darkest areas on the left and right of the plots indicate the regions of no current. The bright lines located outside of these regions correspond to a fine structure of current steps visible near the voltage thresholds. In Figure 6.6, we also show larger-bias *dI/dV* plots measured from two devices; in (b) the conductance gap keeps opening and exceeds 100 mV.

As we explained in Chapter 2, this behavior is the signature of a single-electron transistor (SET), a device containing a small island which is attached to electrodes by tunnel barriers and whose charge state can be tuned using a gate voltage. In this case the island is a single Co ion. For most values of V_G, the charge state of the ion is stable at low V (dark regions). An electron does not have sufficient energy to tunnel onto the island and therefore current is blocked (Coulomb blockade). The bright lines that define the boundaries of the Coulomb-blockade regions illustrate the tunneling thresholds for transitions between charge states. Conductance in the vicinity of $V = 0$ is allowed at a value of gate voltage V_C where the charge states are degenerate (Coulomb oscillation; see

Figure 6.5 Color-scale plots of differential conductance (*dI/dV*) as a function of the bias voltage (*V*) and the gate voltage (V_G) for three different [Co(tpy-(CH$_2$)$_5$-SH)$_2$] single-electron transistors at zero magnetic field. Black represents zero conductance and white the maximum conductance. The maxima of the scales are 5nS in (a), 10nS in (b), and 500nS in (c). The *dI/dV* values were acquired by numerically differentiating individual *I-V* curves.

Figure 6.6 Large-scale color plots of differential conductance (*dI/dV*) for two different [Co(tpy-(CH$_2$)$_5$-SH)$_2$] single electron transistors. Device (a) is the same device as the one in Figure 6.5 (a) and it shows a strong excited level near 30 meV (arrow). Device (b) displays a large conductance gap exceeding 100 mV. No data was taken in the white rectangular regions. Maximum conductance is 30 nS in (a) and 50 nS in (b).
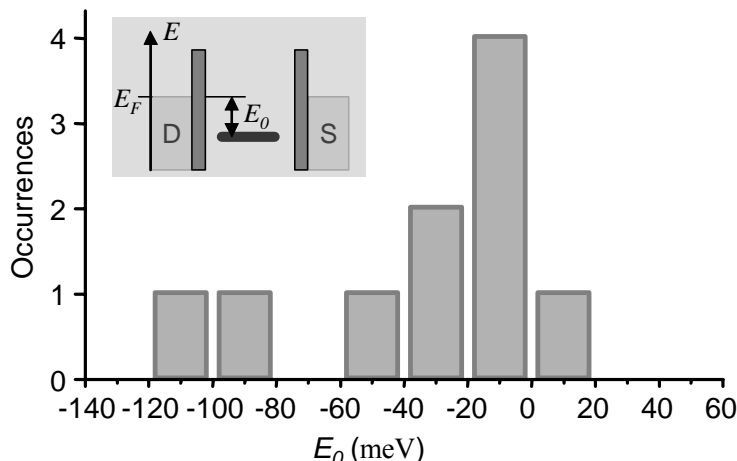
Figure 6.7 Histogram of E_0, the electrochemical potential of the Co^{3+}/Co^{2+} transition measured relative to the electrode Fermi level from nine $[Co(tpy-(CH_2)_5-SH)_2]$ devices. Here negative value corresponds to the case where the molecule is (2+) charge state at $V_G = 0$. The energy diagram is shown in the inset.

the lower inset to Figure 6.4). We label the charge states as Co^{2+} and Co^{3+}, in analogy with the electrochemical measurements, and this is supported by a spin analysis presented below.

In control experiments, this behavior has not been observed for any of 100 bare gold wires or 50 gold wires coated with tpy-$(CH_2)_5$-SH linker molecules alone without Co ions. This provides strong evidence that the island of the SET is indeed the Co ion. We can be confident that the current near each degeneracy point is due to a single molecule because the degeneracy voltage V_C will be different for each molecule due to local variations in the electrostatic environment. The non-blockaded resistance of devices range from 100 MΩ to ~1 GΩ. This is comparable to the resistance measured for alkanedithiol molecules[40] whose length is comparable to the linker molecule used here. These results clearly illustrate that the properties of the molecule are reflected in the electrical properties of the SET.

To test the correspondence between the redox (Co^{2+}/Co^{3+}) potential measured in the cyclic voltammogram (Figure 6.2) and E_0, the electrochemical potential for the Co^{2+}/Co^{3+} transition (see equations (2.4) and (2.5), for a more careful definition), we plot in Figure 6.7 a histogram of E_0 measured from nine different $[Co(tpy-(CH_2)_5-SH)_2]$ single electron transistors. E_0 can be measured from transport data using equation (2.5). For most devices, E_0 as well as V_C has a negative value, which indicates that the charge state of the cobalt ion is 2+ at $V_G = 0$. This is consistent with the electrochemical result

(Figure 6.2), where the redox peak is found at a positive potential. However, the number of devices used for the histogram is not large enough to develop a strong correspondence. For most devices, V_C changes significantly (sometimes over 1 V) after a series of V_G scans due to changes in local electrostatic environment, and hence the error associated with measured V_C values is large.

Vibrational excited levels

Additional lines in Figure 6.5 running parallel to the tunneling thresholds indicate the contributions of excited states to the tunneling current. Lines that end in the Co^{3+} (Co^{2+}) blockade region correspond to excited levels of the Co^{3+} (Co^{2+}) charge state. The pattern of excited states is qualitatively, but not quantitatively, similar from molecule to molecule. Typically we observe several lines at energies below 6 meV. No additional lines are resolved between ~6-30 meV, at which point additional strong peaks are sometime seen (see Figure 6.6 (a)).

A notable feature of the excited-state spectra is that the pattern of low-lying excitations is the same for both charge states of a given molecule. This, together with the small energy scale, suggests that the low-energy excitations are not associated with different electronic configurations. In order to test whether the excitations may be associated with the emission of a phonon, we have calculated the normal modes of the molecule using a quantum chemistry package (HyperChem 7.0). The simulations show normal modes with energies beginning at approximately 1 meV, with a density of ~2 modes/meV, in reasonable consistency with our observations. However, depending on how the molecule is held by the electrodes, the normal mode structure is expected to change. Therefore, it is difficult to find the correspondence between the excited levels observed in Figure 6.5 and theoretical normal modes in these devices, unlike in the fullerene devices we studied in Chapter 4 and 5.

Magnetic field studies: Zeeman splitting

We have applied a magnetic field B to determine the magnetic state of the Co ion. Figure 6.8(a) shows a color plot of dI/dV at a magnetic field of 6T for the same device as in Figure 6.5(a). A new excited Co^{2+} level, denoted by a triangle, has split from the Co^{3+}

to Co^{2+} ground-state transition. The energy difference between these two states is linear in *B*, with a slope corresponding to a g-factor of 2.1±0.2 as shown in Figure 6.8(b). There is no corresponding Co^{3+} excited state splitting from the Co^{2+} to Co^{3+} ground-state transition.

As we discussed in section 2.4 (see Figure 2.15), these results indicate that the Co^{2+} state is spin-degenerate, while the Co^{3+} state is not. An unambiguous identification of the Co^{2+} ground state as S=1/2 and the Co^{3+} ground state as S=0 is indicated by an

(a) **(b)**
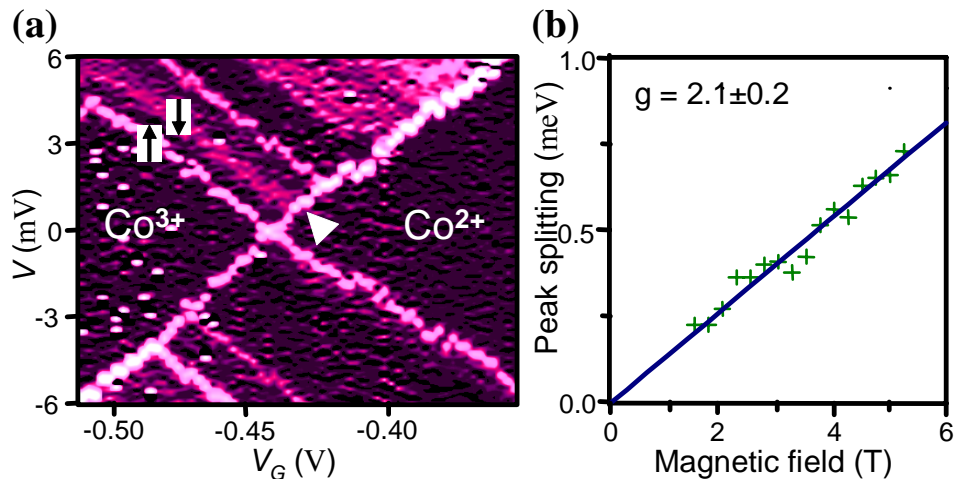
Figure 6.8 Magnetic field dependence of the tunneling spectrum of a [Co(tpy-(CH$_2$)$_5$-SH)$_2$] single-electron transistor. (a) Differential conductance plot of the device shown in Figure 6.5(a) at a magnetic field of 6 Tesla. There is an extra level (indicated with the triangle) seen due to the Zeeman splitting of the lowest energy level of Co^{2+}. The arrows denote the spin of the tunneling electron. (b) Magnitude of the Zeeman splitting as a function of magnetic field.
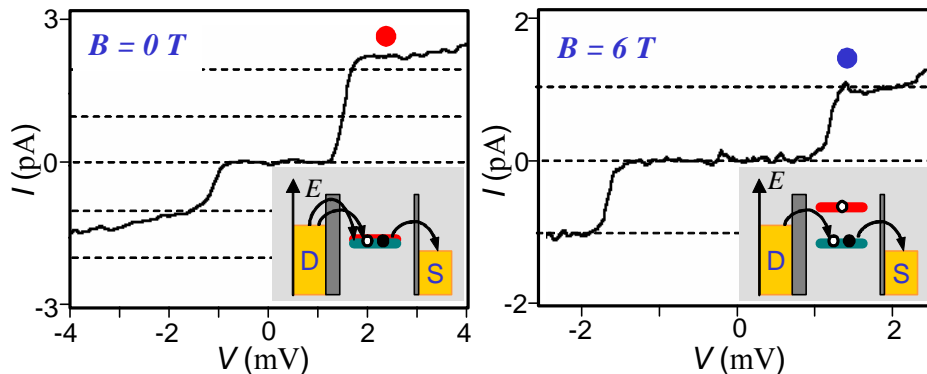
Figure 6.9 The tunneling current amplitude is approximately 2 pA (red dot) for positive bias at zero magnetic field, which is twice as large as the one at 6 T (blue dot). This can be compared to the current amplitude on the negative bias side, which is similar for both cases. This can be explained using a doubly-degenerate quantum level (S = ½) with very asymmetric tunnel barriers as shown in the diagram. The degeneracy is lifted with a magnetic field (Zeeman splitting), leaving only one level carrying the current.

analysis of the tunneling current amplitudes (see Figure 6.9). The lower-energy Zeeman-split state in Figure 6.8(a) carries a current of 1.0 pA, and the second is nearly equal, 0.8 pA. Nearly equal currents are expected for S=0 to S=1/2 tunneling, for a tunneling threshold across the higher-resistance tunnel junction[41, 88]. For any higher spin, the current carried by the second state would be suppressed by a Clebsch-Gordan coefficient by at least a factor of 2 compared to the first state[89].

The electronic structure inferred above is consistent with the expected electronic structure of the Co ion if its angular momentum is quenched due to the binding to ligand molecules. A Co^{2+} ion ($3d^7$) has an odd number of electrons and possesses Kramers'-degenerate states that will split in a magnetic field, while Co^{3+} ($3d^6$) has an even number of electrons and may have a total spin S=0 so that it will not undergo Zeeman splitting. Previous magnetization studies in bulk material suggest that Co^{2+} in the molecule is S=1/2 at cryogenic temperatures[90]. Our measurements provide a confirmation of this result.

6.4 The Kondo Effect in [Co(tpy-SH)$_2$] Transistors

We now turn to the results for the shorter molecule, [Co(tpy-SH)$_2$] where we expect significantly larger conductances due to the shorter tether length. In fact, we observe conductances large enough that we can see directly when a molecule becomes inserted in the gap between the electrodes (Figure 6.10). During the course of electromigration, the conductance initially decreases below the conductance quantum ($2e^2/h$), indicating a tunneling gap between the electrodes. If the voltage is increased further, the current often suddenly increases by up to a factor of 10 (red dot, Figure 6.10(a)). The low bias conductance curves measured before and after such event are shown in Figure 6.10(c). The conductance after the current jump (solid dot, ~ 50 µS) is approximately five times larger than the one measured before the current jump (open dot ~ 10 µS) and it sometimes shows a peak near zero bias, a behavior we will discuss below in detail. The behavior described in Figure 6.10 is not observed for bare gold electrodes. We therefore interpret the jump as the inclusion of at least one molecule in the gap between electrodes[61]. We stop the electromigration process once this happens and study the devices at lower *V*.

The differential conductance *dI/dV* for one [Co(tpy-SH)₂] device is shown in Figure 6.11(a). The most striking property is a peak in *dI/dV* at $V = 0$. The peak becomes smaller with increasing temperature and it shows a logarithmic temperature dependence between 3 and 20K (Figure 6.11(b)). The peak also splits in an applied magnetic field (Figure 6.12(a)), with a splitting equal to $2g\mu_B B$, where $g \sim 2$ and μ_B is the Bohr magneton. The peak spitting in a magnetic field is more pronounced in the device shown in Figure 6.12(b). The peak splitting is linear in *B* and the measured g-factor is 2.0 ± 0.05, which is consistent with the value measured from the longer molecule (see the

(a)

(b)

(c)
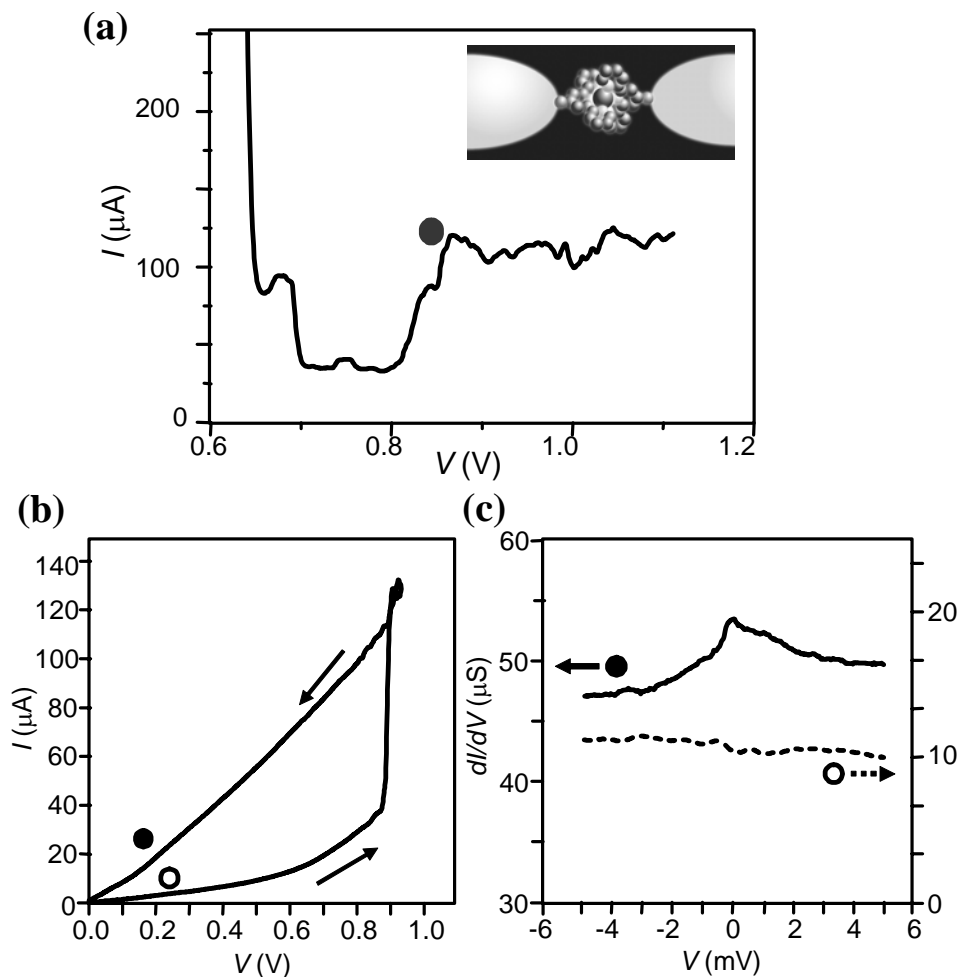
Figure 6.10 The electromigration process with the shorter molecule [Co(tpy-SH)₂]. (a) Breaking trace of a gold wire with adsorbed [Co(tpy-SH)₂] at 1.5K. After the wire is broken the current level suddenly increases (dot) due to the incorporation of a molecule in the gap. Inset: a conceptual image of a [Co(tpy-SH)₂] molecule connecting two gold electrodes. (b), (c) After a wire is initially broken to a tunnel conductance, its low bias conductance was measured to be ~10 μS ((c), dotted curve). When the bias was increased to approximately 0.9 V the current suddenly increases (b), after which the conductance is ~50 μS ((c), solid curve) and shows a peak near zero bias.
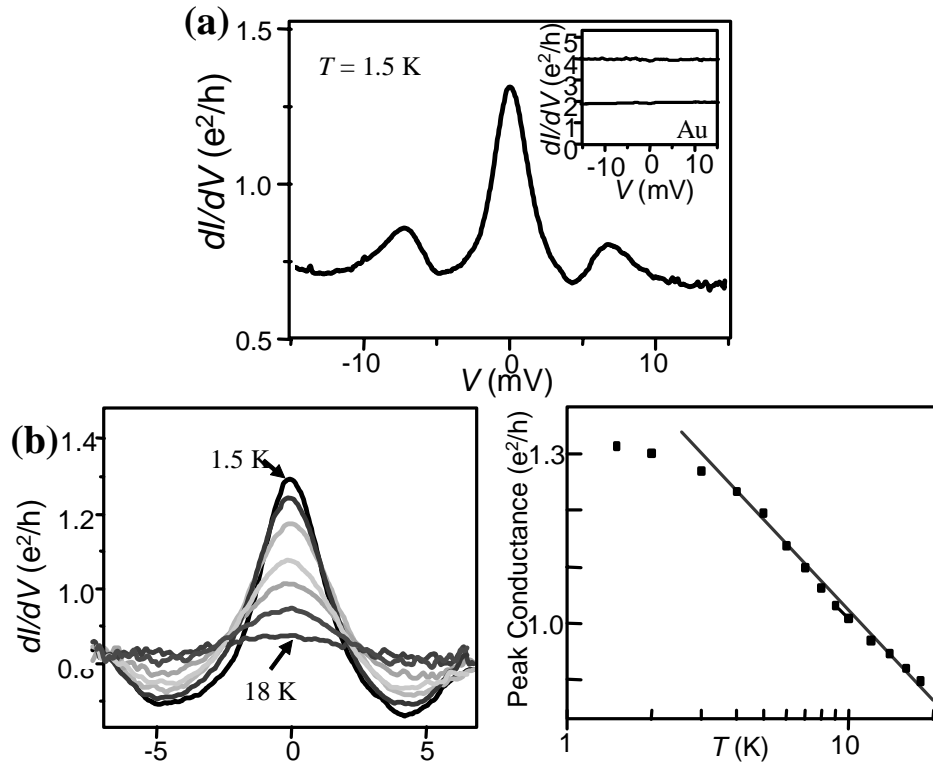
Figure 6.11 The Kondo effect in $[Co(tpy\text{-}SH)_2]^{2+}$ devices. (a) Differential conductance of a $[Co(tpy\text{-}SH)_2]^{2+}$ device at 1.5 K showing a Kondo peak. The inset shows *dI/dV* plots for bare gold point contacts for comparison. (b) The temperature dependence of the Kondo peak for the device shown in (a). The right panel shows the *V*=0 conductance as a function of temperature. The peak height decreases approximately logarithmically with temperature and vanishes around 20 K.

previous section).

In approximately 30% of ~100 wires broken with the molecule, this peak has been clearly observed with the temperature and field dependence described above. As a control experiment, we measured more than 150 gold wires with or without Cr sticking layer. Enhanced zero bias conductance was observed in less than 8 % of them, but most of them did not show the temperature and field dependence observed in the wires with the molecule. This indicates that the conductance behavior observed in $[Co(tpy\text{-}SH)_2]$ devices arises from the presence of the molecule and it is different from the zero-bias anomaly we sometimes observed from bare gold wires.

The logarithmic temperature dependence and the magnetic-field splitting in $[Co(tpy\text{-}SH)_2]$ devices indicate that the peak is due to the Kondo effect[59]. The Kondo effect is a bound state that forms between a local spin on an island and the conduction electrons in the electrodes that enhances the conductance at low biases. The observation

(a)

(b)
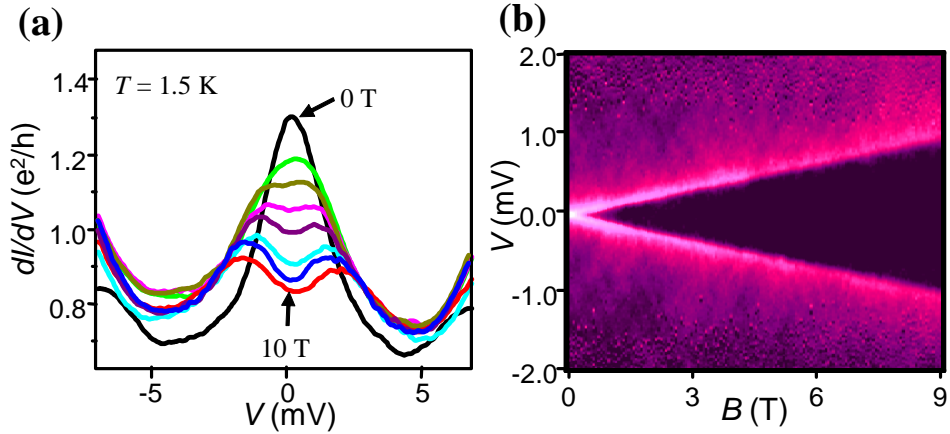
Figure 6.12 Magnetic field dependence of the Kondo peak in [Co(tpy-SH)$_2$]$^{2+}$ devices. (a) The Kondo peak splits with magnetic field (the same device as shown in Figure 6.11). (b) A color scale *dI/dV* plot as a function of *V* and *B* measured from a different device at 100 mK. The peak splitting is $2g\mu_B B$ *with* g = 2.0.
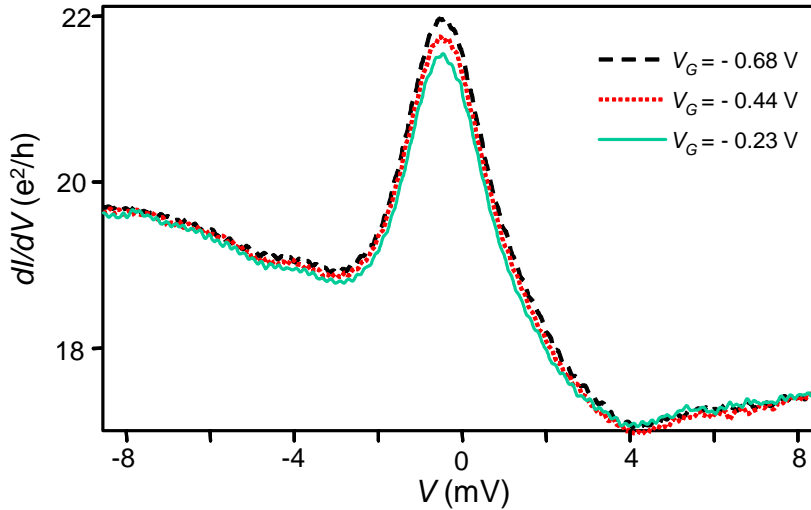
Figure 6.13 The V_G dependence of the Kondo peak in a [Co(tpy-SH)$_2$]$^{2+}$ device is shown. The peak conductance becomes larger at more negative gate voltages, indicating that the energy of the electronic state on the Co ion is tuned closer to the Fermi level.

of the Kondo effect is consistent with the identification of $S = 1/2$ for the Co^{2+} ion given above.

The Kondo effect in single electron transistors was previously observed in a quantum dot formed in a semiconducting heterostructure or a carbon nanotube[91-93]. The strength of the Kondo coupling is dictated by T_K, the Kondo temperature. It is roughly the temperature at which a Kondo peak disappears and depends on several quantum dot parameters such as the charging energy (E_C), electronic coupling (Γ) and μ, the electrochemical potential measured from the electrode Fermi level[92].

$$T_K = \frac{\sqrt{\Gamma E_C}}{2} e^{\pi \mu (\mu + E_C)/\Gamma E_C} \tag{5.5}$$

The Kondo temperature can be estimated from the width of the Kondo peak measured at temperatures low enough that the peak does not change any more. By setting the low-T full-width at half-maximum of the Kondo peak equal to $2k_B T_K//e/$[93], we estimate that T_K in different [Co(tpy-SH)$_2$] devices varies typically between 10 and 25 K. These are large Kondo temperatures compared to the ones previously reported from other systems. It indicates that the coupling between the localized state and the island is strong, consistent with the high conductances found for the shorter linker molecule. Liang *et al.*[34] also observed a strong Kondo effect from single electron transistors made from a divanadium molecule.

From equation (5.5), one expects that the Kondo temperature will change with V_G, since the electrochemical potential μ can be controlled by changing V_G (see equation (2.3)). In three devices the gate coupling was strong enough that T_K was increased by sweeping V_G to more negative values, indicating that the energy of the electronic state on the ion is tuned closer to the Fermi level. Figure 6.13 shows the V_G dependence of the Kondo peak of one such device. However, in most other devices the gate effect is not observed, which is most likely due to the strong coupling with electrodes and a relatively weak gate coupling.

6.5 Summary

In this chapter, we have discussed transistors made from single molecules in which one cobalt ion is connected to gold electrodes by organic barriers. By tuning the length of the organic barrier we are able to control the coupling between the ion and the electrodes. For relatively long linker molecules, giving weak coupling, the molecule functions as a quantum dot. For stronger coupling, we observe Kondo-assisted tunneling. This experiment shows that the properties of a molecular transistor can be controlled by the chemical properties of the molecule.

The ability to design the electronic states of a molecular device using chemical techniques, together with the ability to measure individual molecules, will play an important role in molecular electronics and in the physics of nanometer-scale systems.

Chapter 7

Electrical Conductance of Single-Wall Carbon Nanotubes

7.1 Overview

In the previous three chapters, we studied electrical conductance of molecules that are smaller than 3nm. Those molecules form tunnel barriers at the contact with the leads; electrons tunnel on and off a molecule to flow current. Due to a large charging energy combined with the presence of tunnel barriers, the devices made from these small molecules form a quantum dot and electron transport was described using the Coulomb blockade theory discussed in Chapter 2.

In this chapter, we discuss electrical conductance of semiconducting single-wall carbon nanotubes (SWNTs), which allow us to study electron transport in other regimes. Especially, they can be studied in ambient conditions thanks to their thermal and chemical stability.

After a brief introduction to carbon nanotubes (section 7.2), we discuss low temperature behaviors of SWNT devices (section 7.3). In this case, the contacts are poor and they display the Coulomb blockade behavior due to the charging energy of the nanotube. However, contact effects in a semiconducting SWNT device sometimes leads to the formation of a multiple-dot configuration when the main body of the SWNT is electron (n)-doped.

We then study the room temperature field effect transistor (FET) behavior of SWNT devices with better contacts. An electrolyte gate with a good gate coupling is used instead of a back gate. In this regime, the high mobilities, low contact resistances, and excellent gate coupling of these devices yield device characteristics that significantly exceed previous reports.

This chapter is written based on two previously published papers[94, 95]. Most figures and texts in sections 7.3-7.4 are excerpted from the two papers.

7.2 Introduction to Carbon Nanotubes

A carbon nanotube is a carbon-based tube-like molecule that is a rolled-up graphene sheet[38]. Multi-wall carbon nanotubes were first made by Iijima[96] in 1991. Later Iijima *et al*. and Bethune *et al*.[97, 98] also reported a SWNT (shown in Figure 7.1). One unique property of a SWNT is its aspect ratio; most SWNTs have a diameter less than several nanometers, but they can be as long as several hundreds of micrometers[99]. Therefore, electrons in a SWNT are confined within several nanometers in two directions but they can travel freely in the third direction, which makes a SWNT a prototypical one-dimensional (1D) conductor[68].

Electrical conductance of SWNTs

Electrical conductance of a SWNT has been intensely studied the last several years and many key experimental results were reported. Many of them can be found in several recent review papers[4-6].

Depending on how a graphene sheet is rolled up, a SWNT can become a metal or a semiconductor. This remarkable electronic property of a SWNT stems from the unusual band structure of a graphene sheet. A single graphene sheet has cone-shaped conduction and valence bands, which meet at the Fermi energy to form point-like Fermi surfaces (Fermi points). Since electrons in a SWNT can move freely only along the tube axis, they form 1D subbands. A SWNT becomes a metal if there exists a subband that crosses one of the Fermi points of a graphene sheet. Otherwise, a SWNT has a bandgap at the Fermi energy and becomes a semiconductor. More detailed explanation of the

(a) **(b)**
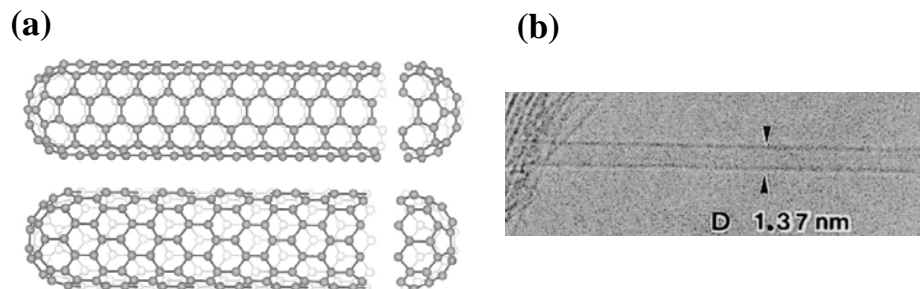
Figure 7.1 Single-wall carbon nanotubes (SWNTs). (a) Images of two SWNTs with different chirality. The top one is metallic whereas the bottom one is semiconducting. (images from Smalley web gallery) (b) An electron micrograph of a SWNT with a diameter ~ 1.4 nm (Iijima *et al*., Nature (1993)).

electronic structure of SWNTs can be found in existing review papers[4-6].

When a SWNT is a metal, it has two 1D electron subbands (+k and -k) that meet at the Fermi energy (see the inset to Figure 7.2(a)). On the contrary, when a SWNT is semiconducting, there is a band gap E_g, between the conduction band and the valence band. In the language of the molecular orbital theory, E_g corresponds to the HOMO-LUMO gap of a molecule. It is known that the size of E_g is inversely proportional to the diameter of a nanotube, d [38, 100].

$$E_g = \frac{0.8 \text{ eV}}{d \text{ [nm]}} \tag{7.1}$$

In both cases, additional electron subbands can be found at much higher or much lower energy (typical energy scale ~ eV).

Electrical conductance of a SWNT shows different behaviors depending on whether it is metallic or semiconducting. The room temperature conductance versus the gate voltage V_G curve is shown in Figure 7.2 for each case. In a metallic nanotube, the conductance shows little dependence to V_G as expected from its band structure. On the contrary, a semiconducting nanotube shows a strong V_G dependence. It conducts well when the Fermi level is located in the valence band (p-doped regime) and the conductance keeps decreasing as the Fermi level approaches the band gap region. The conductance increases again when the Fermi level is in the conduction band (n-doped regime). Such conductance behavior allowed the fabrication of FETs made from

(a) Metallic nanotubes   **(b)** Semiconducting nanotubes
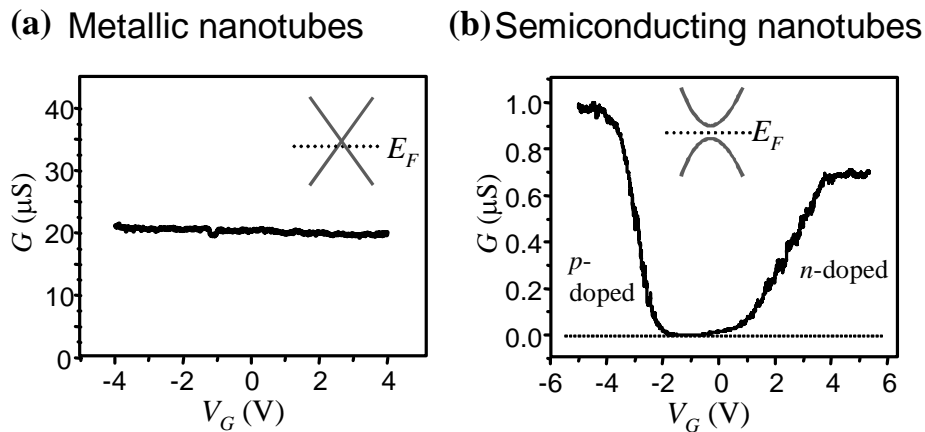
Figure 7.2 Electrical conductance of carbon nanotubes. (a) Conductance of metallic nanotubes does not depend on the gate voltage V_G. (b) Conductance of semiconducting nanotubes shows a strong gate dependence. A schematic band diagram for each case is shown in the inset.

SWNTs, which have been intensely investigated[101-106] since they were first made in 1998[69].

At low temperatures, SWNT devices show Coulomb oscillations due to the charge addition energy $E_C + \Delta E$ of nanotubes[30, 31]. In this regime, a SWNT serves as a dot over which an electron is delocalized. Therefore, the charging energy E_C can be roughly estimated from the length of the tube L, using,

$$E_C \approx \frac{e^2}{4\pi\varepsilon_0 L} = \frac{1.44 \text{ meV}}{L\,[\mu\text{m}]}. \tag{7.2}$$

This gives an order-of-magnitude estimate of E_C. The electronic excitation energy ΔE, on the other hand, can be obtained for a metallic nanotube from the dispersion dE/dk at the Fermi level[38, 107, 108].

$$\Delta E \approx \left(\frac{dE}{dk}\right)_{E=E_F} \frac{\Delta k}{2} \approx \left(\frac{dE}{dk}\right)_{E=E_F} \frac{\pi}{L} \approx \frac{0.5 \text{ meV}}{L\,[\mu\text{m}]} \tag{7.3}$$

From (7.2) and (7.3), we see that the charging energy is roughly three times larger than ΔE regardless of the length of a nanotube. This length independent behavior is a consequence of the 1D electronic structure of a SWNT. We also expect a SWNT shorter than 1 μm to form a quantum dot at liquid helium temperatures since both E_C and ΔE are larger than $k_B T$.

Fabrication of SWNT devices

Since carbon nanotubes are much longer than other small (< 3nm) molecules, they can be wired up using conventional lithography techniques. Details of the fabrication procedure for a SWNT device, however, vary depending on the nanotube synthesis, deposition and wiring-up scheme.

Here we will discuss the fabrication procedure that employs the CVD (chemical vapor deposition) nanotube growth[109] method and alignment marks fabricated by *e*-beam lithography. The overall fabrication procedure is illustrated in Figure 7.3. Similar procedures were used for the fabrication of devices that will be discussed in the following sections.
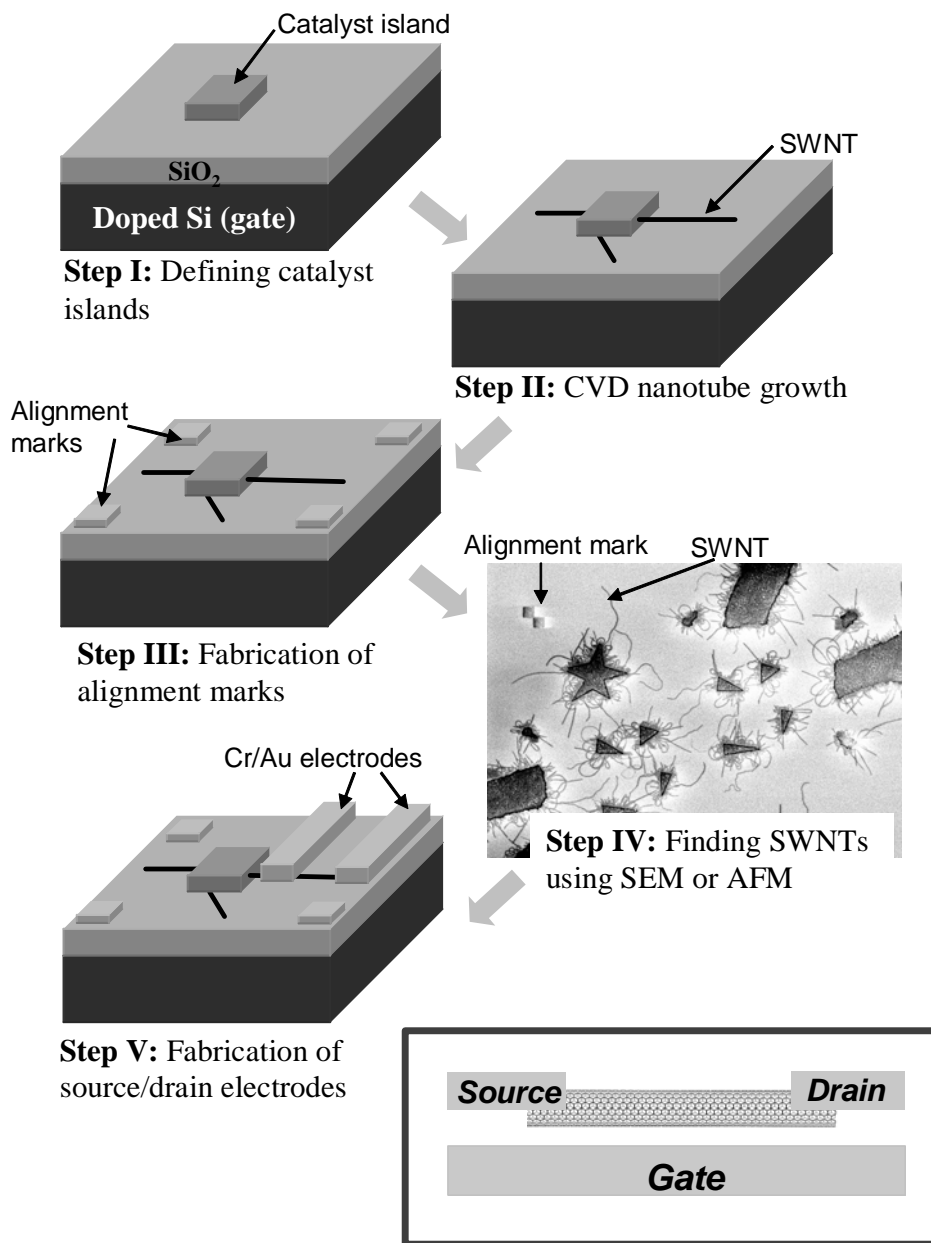
Figure 7.3 A fabrication procedure for a carbon nanotube device. The schematic of a finished device is shown at the bottom.

The fabrication begins with defining islands of catalyst islands (composed mainly of Fe and alumina nanoparticles) on a silicon wafer covered with a silicon oxide (step I). The catalyst islands ($\sim$ 2 by 2 μm) were defined using an *e*-beam lithography followed by lift-off. The silicon substrate is degenerately doped, so that it can serve as a gate electrode at cryogenic temperatures. A chip with catalyst islands is then inserted into a tube furnace, where nanotubes are grown at $\sim$ 900 °C in a methane flow (step II). For

proper growth conditions, this CVD technique produces predominantly single-wall nanotubes[109].

To wire up tubes grown on the chip, we first make gold alignment marks using *e*-beam lithography and lift-off (step III). Then nanotubes are located relative to these alignment marks using SEM or AFM images (step IV). Finally, gold electrodes are fabricated to contact nanotubes by another *e*-beam lithography and lift-off (step V), completing a nanotube device illustrated in Figure 7.3. In other cases (section 7.4), electrodes are deposited right after the nanotube growth (step II) to randomly contact them[95]. This alternative procedure can mass-produce nanotube devices in one fabrication run, but each device may have more than one conducting nanotube. Therefore, the number of nanotubes conducting in each device needs to be confirmed by other means (*e.g.* SEM or AFM).

7.3 Formation of a *p*-type Quantum Dot at the End of an *n*-type Nanotube

Semiconducting SWNTs were initially shown to operate as hole (*p*-type) FET devices[69, 102], with the metallic contacts serving as *p*-type contacts to the 1D hole gas. Subsequently, electron-donating dopants such as potassium were used to create electron doped (*n*-type) devices and *p-n* junctions[110-113]. The initial signatures of *n*-type behavior have been seen in previous experiments on strictly field-effect (gated) devices[103], but before the work presented here there had not been a systematic study of both *p*- and *n*-type behavior using only field effect doping.

Here a back gate is used to study both *p*- and *n*-type transport in the same nanotube device. A schematic diagram of the SWNT device is shown in Figure 7.4(a). This device is prepared using the fabrication procedure described in the previous section. Figure 7.4(b) shows the current (I) through the nanotube versus the gate voltage (V_G) and source drain bias (V). The large dark region in the center corresponds to the Fermi level in the bandgap of the tube. The region on the left corresponds to *p*-type conduction, while the data on the right to *n*-type conduction. These regimes are illustrated schematically in Figure 7.6.

(a)

Figure 7.4 (a) Schematic diagram of the device. The thickness of the insulating silicon oxide layer is 500 nm. (b) Current as a function of the bias (*V*) and the gate voltage measured at 77 K. Current is zero for black regions and the maximum (100 nA) for dark red regions. A non-conducting bandgap region (black) separates *p*-type (left) and *n*-type (right) region.

(b)

Figure 7.5 Conductance as a function of the gate voltage (V_G) at 30K. Coulomb oscillation peaks are observed when $V_G > 3$ V (*n*-type).

p- and *n*-type transport in a SWNT

We begin by discussing the *p*-type region. At low temperatures, Coulomb oscillations are seen (Figure 7.6(c)) with a period in gate voltage $\Delta V_G \sim 9$ mV. Using standard Coulomb blockade analysis of linear and nonlinear transport[26] as described in Chapter 2, we can determine the charging energy, $E_C = 3$ meV, and barrier resistances, R(right) ~ 1 MΩ and R(left) < 100 kΩ. The capacitive couplings of the nanotube quantum dot to the gate, right and left electrodes are 18 aF, 15 aF, and 16 aF, respectively. These measurements indicate that the entire 1.5 μm long carbon nanotube acts like a single quantum dot with tunnel barriers for entering and exiting the tube. As

we discussed in the previous section, this behavior has been seen previously in long metallic nanotubes[30, 31]. Furthermore, the right tunnel barrier is observed to be the dominant one. Because of the small charging energy, at temperatures higher than 5 K, the Coulomb oscillations were washed away, and the linear conductance showed almost no gate dependence, except very near turn-off (Figure 7.5).

Let us now turn to *n*-type operation. The device conducts in this region, but with a conductance that is a factor of 5-10 smaller. Most surprisingly, Coulomb oscillations with much larger gate voltage period, $\Delta V_G \sim 200$ mV, are observed, as seen in Figure 7.5. These oscillations are well-defined at 30 K, long after the Coulomb oscillations observed in the *p*-type region have been washed out, and they persist to ~ 100 K. This, combined with nonlinear measurements such as those shown in Figure 7.7, yields a charging energy of approximately 50 meV. This indicates the presence of a quantum dot approximately ten times smaller than the one formed in the *p*-type region.

Formation of an end-dot

The *n*-type behavior described above can be easily understood using the band diagrams in Figure 7.6. At large positive V_G, the center of the tube is electrostatically doped *n*-type. However, the contacts still dope the ends of the tube *p*-type and screen out the effects of the gate. The net result is the formation of a small *p*-type quantum dot at the end of the nanotube. It is confined on one side by the tunnel barrier to the metallic electrode and on the other by the depletion region between the *p*- and *n*- type regions of the nanotube. In general, we expect the formation of two end-dots, one at each end of the nanotube. However, the transport properties shown above can be understood by considering only one end-dot. This is because the tunnel barrier to the right contact is much larger than the one to the left contact (as determined from measurements in the *p*-type region – see above). As a result, the *p*-type dot formed at the right high resistance contact dominates transport. The dot at the left contact is well coupled to the electrode and effectively behaves like an extension of the electrode under most circumstances[114-116]. From the measured charging energy and period in V_G, we estimate the size of the end-dot to be ~ 100 nm. A theoretical estimate of the size of this dot would require

(a) p - type

(b) n - type

(c)

(d)
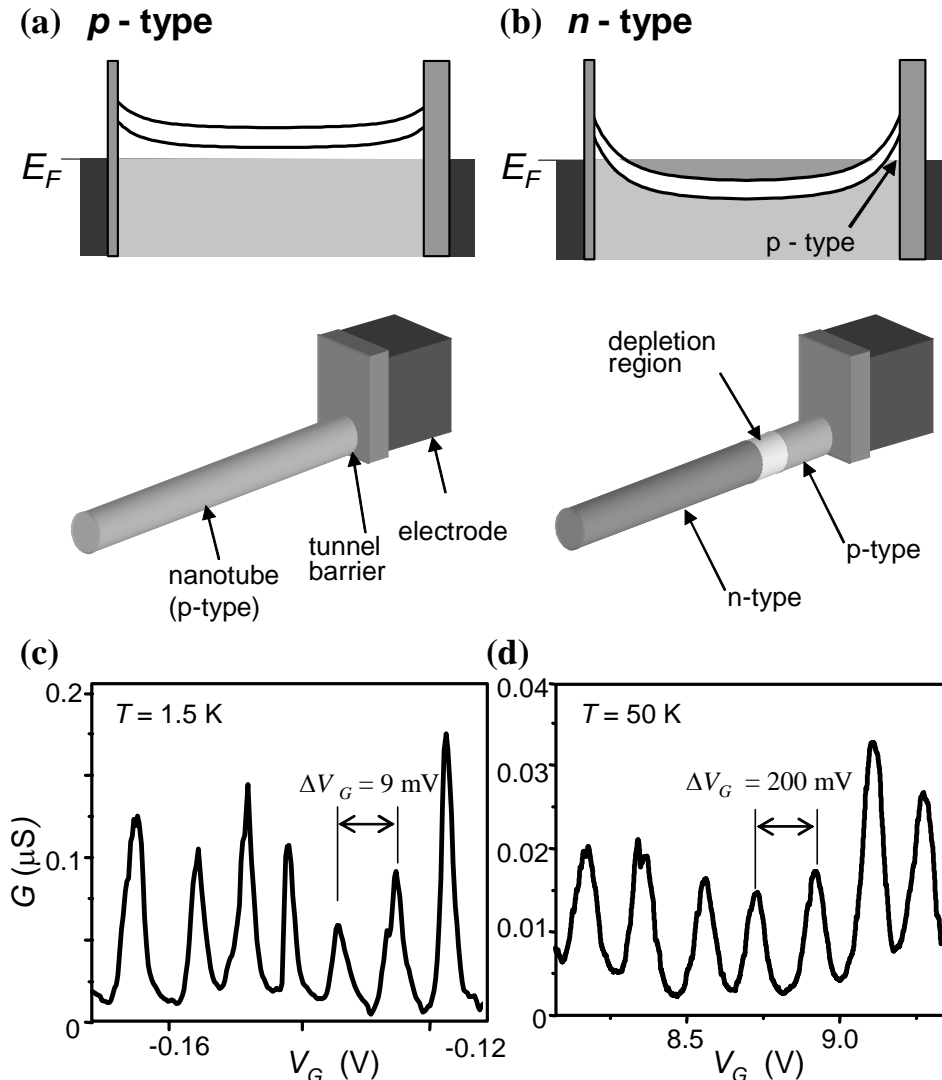
Figure 7.6 Band diagrams and schematic pictures of a semiconducting nanotube device when it is field doped (a) p-type and (b) n-type. Note that the right barrier is thicker than the left. (c) Coulomb oscillations in p-type regime at 1.5 K. The gate period is 9mV. (d) Coulomb oscillations in n-type regime at 50 K. The gate period is approximately 200 mV.

detailed modeling, but this size is roughly consistent with the distance to the gate divided by the dielectric constant of SiO_2, d ~ (500 nm) / 3.8 ~ 130 nm.

Similar behavior – the formation of a large charging energy quantum dot - has recently been reported in two experiments on potassium doped devices[112, 113]. The tentative explanation given was an inhomogeneous-doping-induced dot formed inside a tube. This explanation is highly unlikely in the current experiment because no dopants were used. Furthermore, local potential variations induced by chemical inhomogeneity or impurities are not likely to explain our data, for two reasons. The first is that the

measurements in the p-type region show that there are no large scattering centers along the length of the tube. Second, the persistence of the Coulomb oscillations over a very wide range in V_G (see Figure 7.5) is inconsistent with a quantum dot formed in a shallow potential minimum. Indeed, we believe that the physical origin of the dots observed in the previous experiments is the same as that found here. The contacts doped the end of the tube *p*-type, while the potassium doped the remainder *n*-type, forming an end-dot. This model thus provides a simple and consistent picture of all of the experiments to date on *n*-type samples.

Double-dot behaviors

Other consequences follow from the picture of the nanotube in the *n*-type region represented in Figure 7.6(b). In addition to the *p*-type dot at the end, we would expect a longer, *n*-type dot to be formed in the center of the tube. Indeed, low-*T* measurements reveal a clear signature of a second dot in series with the first. This is evident from the data in Figure 7.7, where a gray scale plot of the differential conductance versus V and V_G at $T = 1.5$ K is shown. The boundary of the large Coulomb gap associated with the end-dot exhibits a sawtooth structure, and a series of lines are observed with a periodic spacing in $\Delta V_G \sim$ 22 mV. Note that these lines are not parallel to the boundaries of the
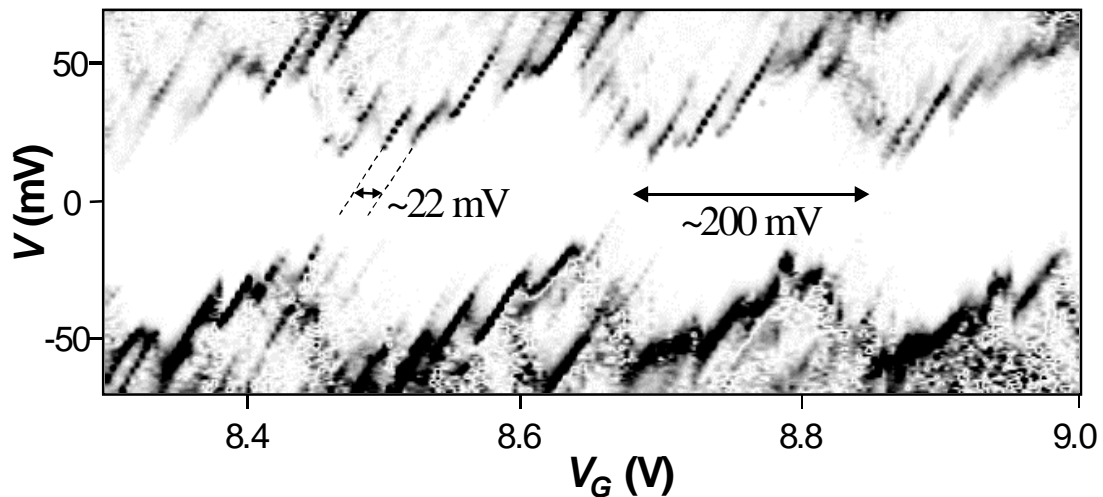
Figure 7.7 Differential conductance plot as a function of V and V_G in the *n*-type regime. The conductance is zero for white regions and the maximum conductance (black) is 0.1 µS. Two periodic features are present. There are Coulomb diamonds with a charging energy ~50 meV and a gate period $\Delta V_G \sim$ 200 mV. Along the edge of these diamonds, another periodic feature with $\Delta V_G \sim$ 22mV period is observed. This corresponds to single-electron charging of the main nanotube dot.

3D MOSFET

2D Gated GaAs heterostructure

1D Semiconducting SWNT
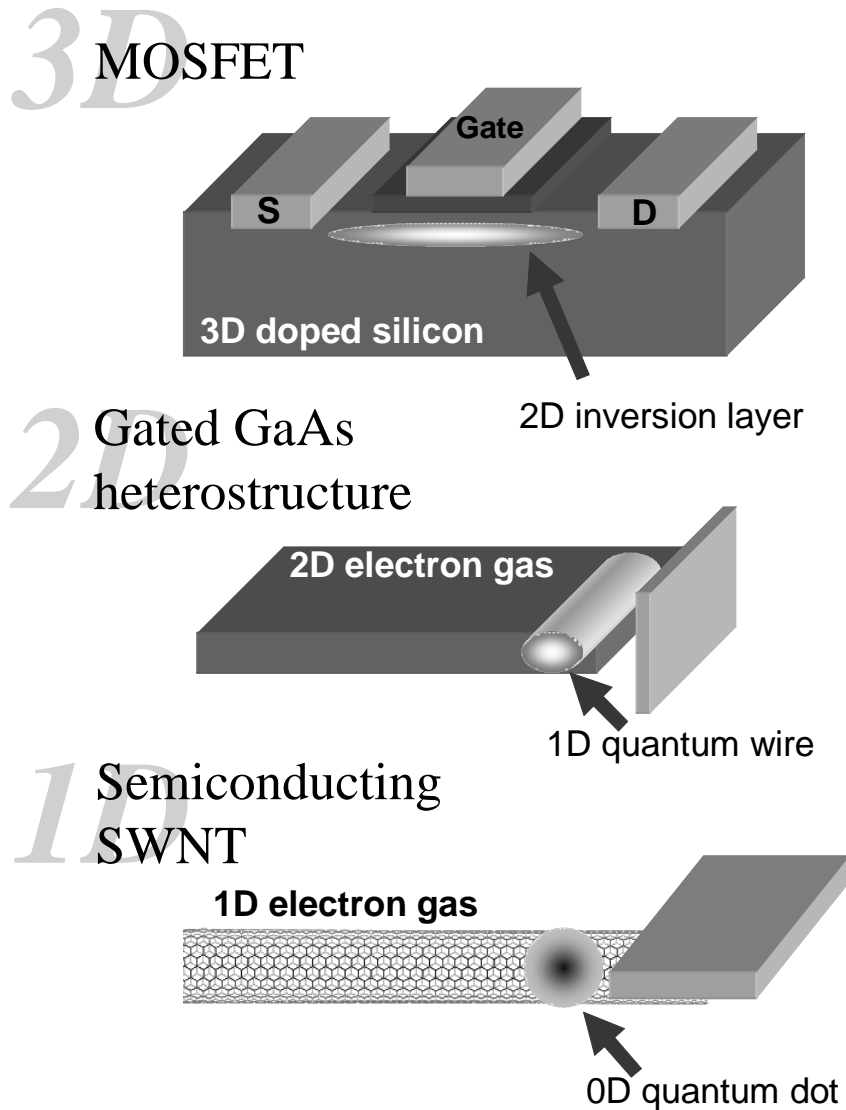
Figure 7.8 Formation of reduced dimensional structures in semiconducting materials.

Coulomb blockade diamonds. This indicates that they are not excited states of the small dot, but rather associated with charging of a second, larger dot in series with the first. Transport through the device is thus dominated by Coulomb charging through two dots in series, with one dot approximately ten times larger than the other. The period in ΔV_G of the larger dot is of the same order of magnitude of that observed in the p-type region, again indicating that it arises from the large n-type center portion of the tube.

Two quantum dots in series have been widely studied in previous experiments on lithographically patterned dots[26]. A number of novel phenomena, such as negative differential resistance (NDR) due to the alignment of the energy levels of the two dots,

have been observed. We indeed observe dramatic NDR in this device (not shown), further supporting the overall picture outlined here.

These experiments demonstrate that a 0D quantum dot can be electrostatically formed at the end of a 1D semiconductor. This is the final step in a now well-established trend in semiconductor physics (Figure 7.8). Two dimensional electron gases at the boundary of 3D semiconductors (*e.g.* MOSFETs) are well known[117], and are of tremendous fundamental and practical interest. One-dimensional electron gases have also been created at the edge of 2D systems[114]. Continuing this trend to 0D provides a simple and controlled way to create a very small quantum dot at the end of a 1D semiconductor.

7.4 High Performance Electrolyte-Gated Carbon Nanotube Transistors

We now turn to room temperature measurements of semiconducting carbon nanotubes. Unlike the low temperature measurements described in the previous section, Coulomb oscillations disappear at a room temperature and carbon nanotube devices function as field effect transistors (FETs) as reported by other groups[69, 102].

The reported properties of nanotube FETs have varied widely due to variations in the quality of the nanotube material, the device geometry, and the contacts. Optimizing their properties is crucial for applications in both electronics and in chemical and biological sensing. For electronic applications, a number of parameters dictate the performance of an FET, such as the mobility and the transconductance. For sensing[118, 119], the ability to work in the appropriate environment (*e.g.* salty water for biological applications) is critical.

The nanotube devices were prepared following a procedure[95] similar to the one described in section 7.2 (see Figure 7.9(a) and (b)). An anneal at 600°C for 45 minutes in an argon environment was used to improve the contact resistance between the tubes and the electrodes (typically by an order of magnitude).

Electrolyte-gated nanotube FETs

In the experiments discussed in this section, we measure the conductance through the tube using an electrolyte as a gate, as schematically shown in Figure 7.9(c). This
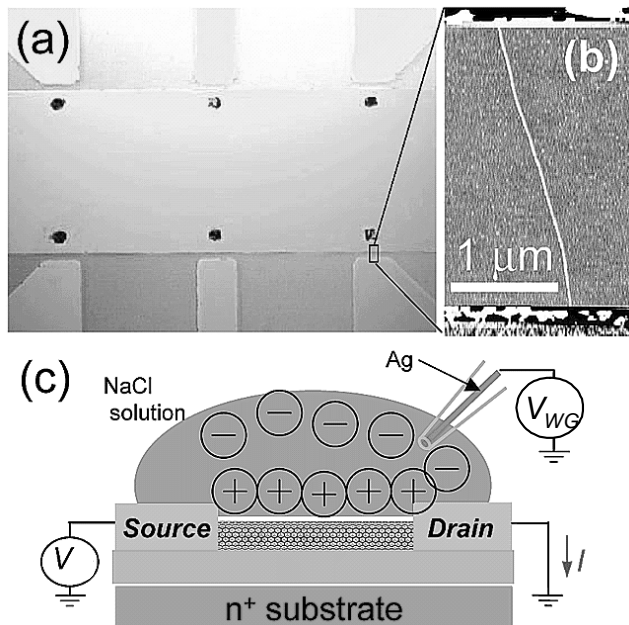
Figure 7.9 (a) Optical micrograph of the device. Six catalyst pads (dark) can be seen inside area of the common electrode. Correspondingly, there are six source electrodes for electrical connection to tubes. (b) AFM image of a tube between two electrodes. The tube diameter is 1.9 nm. (c) Schematic of the electrolyte gate measurement. A water-gate voltage V_{WG} is applied to droplet through a silver wire.

approach was first used by Kruger *et al.*[120] to study multi-wall nanotubes. A micropipette is used to place a small (~ 10-20 micron diameter) water droplet over the nanotube device. A voltage V_{WG} applied to a silver wire in the pipette is used to establish the electrochemical potential in the electrolyte relative to the device. For -0.9 V < V_{WG} < 0.9 V, the leakage current between the water and the Au electrodes/SWNT was negligible (less than 1 nA); the electrolyte then functions as a well-insulated liquid gate. Above this range, the electrolyte reacts with the Au electrodes and destroys the device.

The main panels of Figure 7.10 show the low-bias conductance G vs. V_{WG} for three nanotubes with increasing diameters, where the electrolyte is 10 mM NaCl. The conductance is large at negative V_{WG}, corresponding to *p*-type conduction in the tube, decreasing approximately linearly to zero. It remains near zero for a range near 0 V, and then increases again at positive V_{WG}. This corresponds to *n*-type transport. In the *n*-type region, the conductance is significantly less than in the *p*-type region, particularly for smaller diameter SWNTs.

Note that the size of the gap between *n*- and *p*- behavior decreases with increasing the diameter of the tube, as does the on-state conductance in *n*-type region compared to the *p*-region. This is evident from the traces of G vs V_{WG} in Figure 7.10. The suppression of *n*-type transport in small diameter tubes results from the fact that, under ambient conditions, Au contacts form *p*-type contacts to the tube. As we already

discussed in the previous section, depletion barriers thus form at the contacts in *n*-type operation, creating a large contact resistance to the tube. This barrier is larger the larger the bandgap of the tube. As a result of these contact issues for *n*-type operation, we will concentrate our analysis on *p*-type operation.

High mobility in nanotube FETs

The conductance change in the linear *p*-region for the device in Figure 7.10(a) is $dG/dV_{WG} \sim 1 \ e^2/h$/V. Measurements from many other devices show similar behavior, with no obvious correlation between dG/dV_{WG} and the diameter of the tube or the salt concentrations. For comparison, *G* versus back-gate voltage V_{BG} applied to the substrate for the same device in operating in vacuum is shown in the inset, yielding $dG/dV_{BG} \sim$ 0.08 e^2/h/V. The electrolyte gate is therefore ~ 10 times more effective in modulating the conductance of the tube than the back gate. dG/dV_{WG} is also an order of magnitude larger than values obtained using thin-oxide back-gates[104] and top-gates[106].

To quantitatively describe the transport in the *p*-region, we note that, in the incoherent limit, the total resistance of a SWNT with one subband occupied is the sum of three contributions, $R = h/4e^2 + R_c + R_t$. The term $h/4e^2$ is the quantized contact resistance expected for a 1D system with a fourfold-degenerate subband. In addition, imperfect contacts to the tube can give rise to an extra contact resistance R_c. Finally, the presence of scatters in the tube contribute a Drude-like conductance:

$$G_t = 1/R_t = C_G '|V_G - V_{G0}| \mu / L \qquad (7.4)$$

where C_G' is the capacitance per unit length of the tube, V_G is the gate voltage (back or electrolyte), V_{G0} is the threshold gate voltage at which the device begins to conduct, and μ is the mobility. At low $|V_G - V_{G0}|$, the device resistance is dominated by the intrinsic tube conductance G_t, which increases linearly with increasing V_G if μ is a constant. At large $|V_G - V_{G0}|$, the device resistance saturates due to either the contact resistances or a V_G-independent tube resistance.

Using the equation for G_t given above, the mobility of carriers can be inferred if the capacitance per unit length of the SWNT is known. For the case of vacuum operation, the capacitance to the back-gate C_{BG}' can be estimated from electrostatics[102]
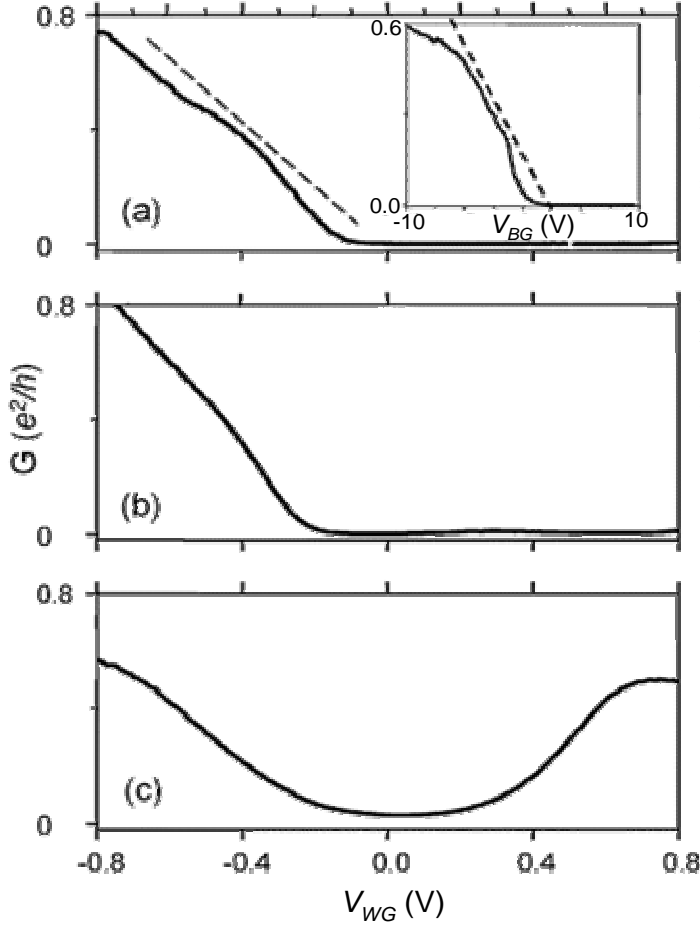
Figure 7.10 Conductance G versus water gate voltage V_{WG} for three tubes with lengths and diameters given by: (a) $L = 1$ μm, $d = 1.1$ nm, (b) $L = 1.4$ μm, $d = 3$ nm and (c) $L = 2.2$ μm, $d = 4.3$ nm. Inset to (a): G versus the back-gate voltage V_{BG} for same device measured in vacuum; the slopes of linear regimes are given by the dashed lines.

r inferred from Coulomb-blockade measurements[30, 31, 121], yielding estimates from 1- 3×10^{-11} F/m. Using a value $C_{BG}' = 2 \times 10^{-11}$ F/m, we obtain an inferred mobility μ ~ 1,500 cm^2/V-s for the vacuum data in Figure 7.10(a). Mobilities in the range of 1,000 - 4,000 cm^2/V-s are routinely obtained, with a few devices showing much higher values. The mobilities reported here are significantly higher than those for holes in Si MOSFETs ($\mu < 500$ cm^2/V-s), indicating that SWNTs are remarkably high-quality semiconducting materials.

High mobility in electrolyte-gated nanotube FETs

For electrolyte gating, a simple estimate of the electrostatic capacitance between the tube and ions is given by: $C_{eWG}' = 2\pi\varepsilon\varepsilon_0 / \ln(1 + 2\lambda_D / d)$ ~ 7 x 10^{-9} F/m for typical values of the dielectric constant and Debye screening length for salty water: $\varepsilon = 80$ and λ_D ~ 1 *nm*. This value is more than 2 orders of magnitude larger than the back gate

capacitance given above. There is an additional contribution to capacitance that is relevant in this case, however. The total capacitance, which relates the electrochemical potential difference applied between the tube and the gate to the charge on the tube, has both electrostatic and quantum (chemical) components: $1/C' = 1/C_e' + 1/C_Q'$, where C_e' is the electrostatic capacitance and $C_Q' = e^2 g(E)$, where $g(E)$ is the density of states for the SWNT. For a 1D tube, $g(E)$ is given by:

$$g(E) = \frac{4}{\pi \hbar v_F} \frac{\sqrt{E^2 - (E_g/2)^2}}{E} \tag{7.5}$$

where $E > E_g/2$ is the energy of the electron measured relative to the center of the bandgap. The quantum capacitance is therefore of order: $C_Q' = 4e^2/\pi \hbar v_F = 4 \times 10^{-10}$ F/m for one subband occupied in the tube

Note that it is the *smaller* of C_Q' and C_e' that dominates the overall capacitance C'. For the case of back-gating, C_{eBG}' is nearly an order of magnitude smaller than C_Q' and therefore C_{eBG}' dominates. For water gating, on the other hand, C_Q' is an order of magnitude smaller than C_{eWG}' so C_Q' dominates. In principle, C_Q' goes to zero at the subband bottom, but thermal effects and the electrostatic capacitance C_e' will smear this out in the total capacitance C'. Numerical calculations indicate that to a good approximation, $C_{WG}' \sim 4e^2/\pi \hbar v_F$ except very near turn-on.

We therefore make the approximation $C_{WG}' \sim 4e^2/\pi \hbar v_F$, which should be an upper bound for the true capacitance when only one subband is occupied. We can then infer the mobilities of the tubes under electrolyte gating; for the data in Figure 7.10(a), this gives μ


V (V)

0.4 V

0.4 V

-0.4 V

V$_{WG}$ (V)
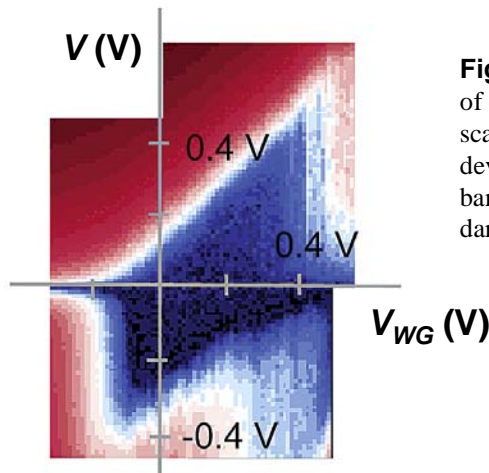
Figure 7.11 Colorscale plot of current on a logarithmic scale versus V_{WG} and V for the device of Figure 7.10(b). The band gap region is given by the dark trapezoid at the center.

~ 1,000 cm^2/V-s. This is in good agreement with the mobility obtained for the same device in vacuum, $\mu = 1,500$ cm^2/V-s. This agreement implies that (a) the mobility of the tube is not dramatically affected by the electrolyte, and (b) the elecrolyte-tube capacitance is near the quantum capacitance. These measurements illustrate that water-gated nanotube FETs approach the ultimate limit where the capacitance is governed by quantum effects and not electrostatics.

Transconductance of electrolyte-gated nanotube FETs

We now discuss the nonlinear transport performance characteristics of water-gated nanotubes. Figure 7.11 shows a color-scale plot of the current amplitude of the device shown in Figure 7.10(b) as a function of both V and V_{WG}. The low conductance region corresponding to the band gap of the tube is clearly seen, with *p*- and *n*- type conductance observed at negative and positive V_{WG}'s respectively. The low- conductance region is trapezoidal in shape, with the boundaries given by a line with slope $dV/dV_{WG} \cong 1$. Figure 7.12 shows *I-V* curves at different V_{WG}'s in the *p*-region. The current initially rises linearly with V and then becomes constant in the saturation region. The transconductance in the saturation region, $g_m = dI/dV_{WG}$, grows approximately linearly with $\left|V_{WG} - V_{WG0}\right|$, as shown in the inset, reaching a value of 20 μA/V. Measurements on other samples give comparable results. This transconductance is approximately one order of magnitude larger than the highest values previously reported for SWNT transistors[103, 106].
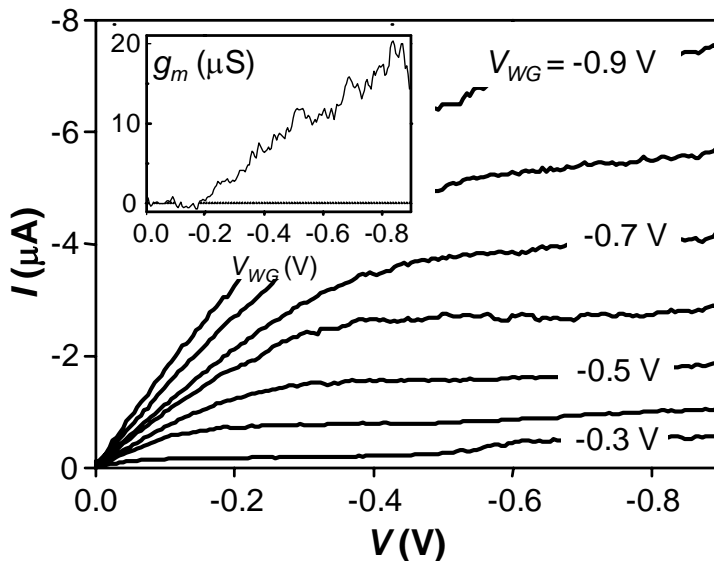
Figure 7.12 *I-V* characteristics of the device shown in Figure 7.10 (b) at different water-gate voltages ranging from –0.9 V to –0.3 V in 0.1 V steps (top to bottom). The inset shows the transconductance $g_m = dI/dV_{WG}$ taken at $V = -0.8$ V.

The large g_m follows directly from the high mobility and large gate capacitance found above. From standard FET analysis, $g_m = C_g'/V_G\text{-}V_{G0}/\mu/L$. Using the linear-response measurements above, this equation predicts a g_m of 27 µA/V at an overvoltage of 0.7 V, in reasonable agreement with the measured value. Normalizing the transconductance to the device width of ~ 3 nm gives g_m/W ~ 7 µS/nm. This is an order of magnitude greater than the transconductance per unit width for current-generation MOSFETs. The results above show that nanotubes have very high transconductances. The ultimate limit would be a ballistic nanotube transistor with a gate capacitance given by C_Q': $g_m = 4e^2/h = 150\ \mu$A/V. The transistors reported here are within a factor of 5-10 of this limit.

7.5 Summary

In this chapter we studied electrical conductance of semiconducting SWNTs in two different temperature regimes.

At low temperatures (section 7.3), the charging energy dominates electron transport and we observe Coulomb oscillations both in *p*-type and *n*-type regime. In *n*-type regime, a small *p*-type end-dot with a large charging energy is formed near the contact because the contacts dope the ends of the tube *p*-type. Therefore, we see transport behaviors that correspond to a double-quantum dot. This provides us a reliable way to fabricate very small quantum dots with a large charging energy. There are applications of this in many areas, including high-temperature Coulomb blockade devices, the creation of multiple-dot structures, and novel scanned probe systems where a quantum dot is formed at the end of a nanotube AFM tip.

The room temperature studies (section 7.4) of nanotube FETs with an electrolyte gate revealed that a SWNT is an excellent semiconducting material with a high mobility and transconductance. The excellent device characteristics of SWNT transistors in salty water also indicate that they may be ideal for biosensing applications. Since a SWNT has dimensions comparable to typical biomolecules (*e.g.* DNA, whose width is approximately 2 nm), they should be capable of electrical sensing of single biomolecules. The large transconductances indicate that the signal from single molecules should be readily observable.

Chapter 8

Conclusion

8.1 Summary

In the previous four chapters (Chapters 4 through 7), we have discussed examples of single molecule transistors that are made from various molecules, including fullerenes, single cobalt molecules, and carbon nanotubes.

To measure such small molecules (< 3nm, except carbon nanotubes), we developed the electromigration junction technique (Chapter 3) to fabricate electrodes with a nanometer-sized gap. In the experiments of this thesis, these nanoelectrodes were successfully used to "wire-up" various single molecules. The development of this experimental tool for single molecule measurements is one of the main conclusions of this thesis.

Single molecule devices made from different molecules exhibited several common behaviors. First, single molecules in our devices form quantum dots due to a large charging energy and the energy level quantization. Second, the overall conductance of a single molecule device is dominated by the properties of the contacts between the dot (the molecule) and the electrodes. These common properties are described below in further detail.

We also observe different characteristics that reflect the unique properties of each molecule as discussed below. This shows that the transport measurement technique described in this thesis can be used more generally to study electron transport properties of a variety of molecules and to investigate the coupling between various quantum excitations of a molecule and its electronic degree of freedom.

Single electron transport and the Coulomb blockade

The entire single molecule devices described in this thesis, when measured at cryogenic temperatures, exhibited Coulomb blockade. This shows that single molecules formed a dot, thanks to their large charging energies. This allows us to analyze the data

from single molecule devices using the standard Coulomb blockade theory described in Chapter 2.

The overall conductance of most single molecule transistors is significantly lower than the conductance quantum e^2/h. This is due to a large tunnel contact resistance between the molecule and the electrodes, which is consistent with the formation of a single electron transistor.

Quantum excitations and *dI/dV* peaks

In most single molecule transistors, we could resolve additional *dI/dV* peaks outside of Coulomb blockade areas. These additional peaks correspond to quantum excitations of the device. Traveling electrons tunnel on and off the molecule using well defined quantum states, and useful information on individual quantum states can be learned from the measured properties of corresponding *dI/dV* peaks.

The origin of the quantum excitation can be electronic, magnetic, or vibrational. Due to variations in the local environment of each single molecule device, the observed excitation spectrum usually differs from device to device. However, there are reproducible conductance features over many different devices, which allow one to identify the origin of the responsible quantum excitations and the excitation mechanism.

Vibrational excitations and the Franck-Condon model

A vibrational excitation is the one that is the most frequently observed. When an electron tunnels on to or off from a molecule, the molecular equilibrium configuration undergoes a certain change that also reflects the change in the local electrostatic environment.

The *dI/dV* features that correspond to a vibrational excitation are usually charge state independent and sometimes show multiples of the principle excitation. In C_{60} devices, the C_{60} center-of-mass vibration against a gold surface (the bouncing-ball mode) was observed near 5 meV, which is consistent with a simple ball-and-spring model. In C_{140} devices, the intercage stretching mode was the most prominent one, and was observed near 11 meV. In both cases, the Franck-Condon model provides a theoretical platform for analyzing the data. Using this model, we can obtain detailed information on

each vibrational mode, such as the vibrational excitation probability and the *Q*-factor of the mode.

However, the specific nature of the responsible vibrational mode is not always identifiable, as is the case with the single Co molecules. In this case, the number density of the normal modes is too high and the eigenenergy is very susceptible to the local environment, both of which prevent us from identifying the exact origin of the vibrational conductance features observed from these devices.

Contact with electrodes and the Kondo effect

The overall conductance of a single molecule transistor is determined by the tunnel resistances of the contacts. In general, the contact between a molecule and the electrodes are observed to be poor and the overall conductance is significantly lower than the conductance quantum. Within the experimental scheme of this thesis, one usually does not have a good control over how a molecule is contacted by electrodes. Therefore, the conductance varies from device to device even for the devices made with the same molecule.

However, in the experiments with single Co molecules with different lengths (Chapter 6), we demonstrated how one could control the overall resistance by changing the length of the insulating linker group of the molecule. When a shorter linker group was used instead of a longer one, the overall conductance of the device increased by several orders of magnitude. Furthermore, we observed the Kondo effect from these devices, which can be explained by the large coupling between the single Co molecule and the electrodes.

8.2 Future Directions

The experiments described in this thesis are still somewhat simple in a couple of ways. First, the electrodes are made with noble metals - mainly Au and sometimes Pt. For this reason, all the devices measured to date have nonmagnetic electrodes with identical Fermi levels for the left and right electrodes. Second, the molecules studied in this thesis have electrons delocalized over the entire molecule or have only one active

part over which an additional electron is located. Therefore, these molecules can be thought of as a single quantum dot.

Naturally, one interesting direction is to make more sophisticated electrodes. In other words, one can incorporate "functionality" to the electrodes. One example of such electrodes is recently reported by Deshmukh *et al*[122]. In [122], Deshmukh *et al*. fabricated each electrode in a pair with a different metal (*e.g.* one electrode with Au and the other with Cu). This allows one to make asymmetric junction, having electrodes with different Fermi levels. One can also make the electrodes using magnetic or superconducting materials. Single electron transistors made with nanoparticles were previously studied using such electrodes[43, 88], and interesting behaviors were observed in those experiments.

Another exciting direction is to design single molecules with more complex

(a) $M_2(tppz)(tpy\text{-}SH)_2$

(b)
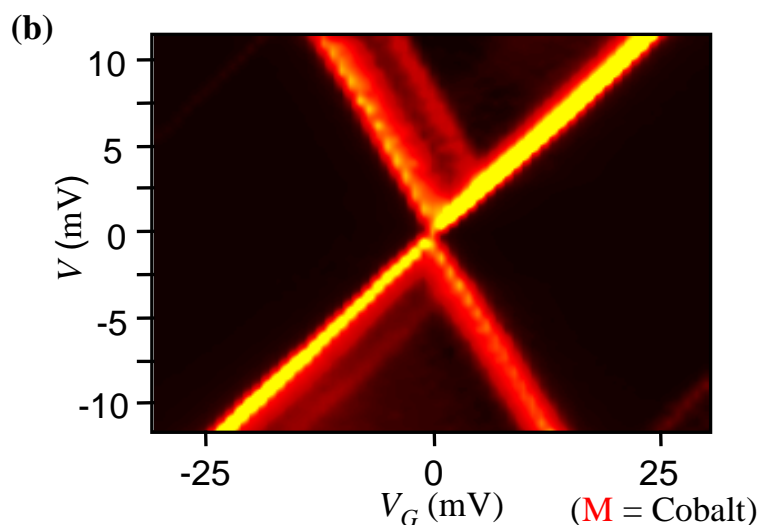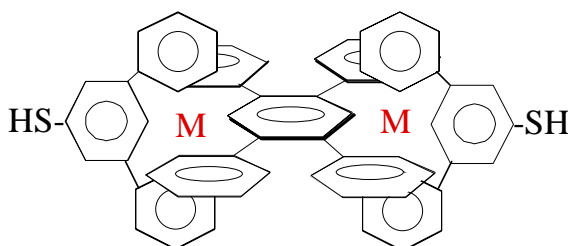
Figure 8.1 A single molecule transistor with two metal atoms. (a) A schematic of $M_2(tppz)(tpy\text{-}SH)_2$, where M, tppz, and tpy-SH represent a metal atom, tetra-2-pyridyl-1,4-pyrazine, and 4'-(mercapto)- 2,2':6',2"-terpyridinyl, respectively. (b) A conductance plot measured from a device with a molecule shown in (a) with two cobalt atoms.

electronic properties. As mentioned in the beginning of this thesis, one unique property of molecules as active electronic elements is their vast diversity and functionality. These diverse properties will be reflected to the conductance properties of single molecule devices. Therefore, designing molecules with desirable properties and incorporating them into electronic devices is a goal that will have a huge impact on the scientific and industrial communities. One experiment in this direction, even though still simple, is described in Figure 8.1. In this experiment, a molecule that is similar to the single Co molecule of Chapter 6 is measured using a similar device geometry. The molecule shown in Figure 8.1(a) has two metal atoms instead of one and the coupling between the two Co atoms can be controlled by using different linkers between them. One can develop even more complex molecules based on the same scheme. For example, a synthesis procedure for making a series of molecules with multiple metal atom centers is described in [85].

Figure 8.1(b) presents a conductance plot measured from a double Co molecule (M = Co). Since the coupling between the two Co atoms is strong, the molecule is still expected to form a single quantum dot in this case.

8.3 Concluding Remarks

In this thesis we discussed the fabrication and the measurements of single molecule transistors where electrons tunnel one by one through the molecule. We found that electrical conductance changes depending on how tunneling electrons interact with various quantum excitations of the molecule. One can apply the results of this thesis to investigate the electronic motion in single molecules and also to design new molecules that have useful properties for novel electronic devices.

References

1. Datta, S., *Electronic Transport in Mesoscopic Systems*. Cambridge studies in semiconductor physics and microelectronic engineering, ed. H. Ahmed, M. Pepper, and A. Broers. 1995, Cambridge, UK: Cambridge.

2. Kastner, M.A., *Artificial Atoms.* Physics Today, 1993. 46(1): p. 24-31.

3. Reed, M.A., *Quantum Dots.* Scientific American, 1993. 268(1): p. 118-123.

4. McEuen, P.L., M.S. Fuhrer, and H.K. Park, *Single-walled carbon nanotube electronics.* IEEE Transactions on Nanotechnology, 2002. 1(1): p. 78-85.

5. Dekker, C., *Carbon nanotubes as molecular quantum wires.* Physics Today, 1999. 52(5): p. 22-28.

6. McEuen, P.L., *Single-wall carbon nanotubes.* Physics World, 2000. 13(6): p. 31-36.

7. Klein, D.L., et al., *An approach to electrical studies of single nanocrystals.* Applied Physics Letters, 1996. 68(18): p. 2574-2576.

8. Klein, D.L., et al., *A single-electron transistor made from a cadmium selenide nanocrystal.* Nature, 1997. 389(6652): p. 699-701.

9. Reed, M.A., *Molecular-scale electronics.* Proceedings of the IEEE, 1999. 87(4): p. 652-658.

10. Petty, M.C., M.R. Bryce, and D. Bloor, *Introduction to Molecular Electronics*. 1995, New York: Oxford.

11. Aviram, A. and M.A. Ratner, *Molecular Electronics: Science and Technology*. 1998, New York: New York Academy of Sciences.

12. Aviram, A. and M.A. Ratner, *Molecular Rectifiers.* Chemical Physics Letters, 1974. 29(2): p. 277-283.

13. Fagan, P.J. and M.D. Ward, *Building Molecular-Crystals.* Scientific American, 1992. 267(1): p. 48-54.

14. Joachim, C. and J.F. Vinuesa, *Length dependence of the electronic transparence (conductance) of a molecular wire.* Europhysics Letters, 1996. 33(8): p. 635-640.

15. Bumm, L.A., et al., *Are single molecular wires conducting?* Science, 1996. 271(5256): p. 1705-1707.

16. Joachim, C. and J.K. Gimzewski, *An electromechanical amplifier using a single molecule.* Chemical Physics Letters, 1997. 265(3-5): p. 353-357.

17. Chen, J., et al., *Large on-off ratios and negative differential resistance in a molecular electronic device.* Science, 1999. 286(5444): p. 1550-1552.

18. Collier, C.P., et al., *Electronically configurable molecular-based logic gates.* Science, 1999. 285(5426): p. 391-394.

19. Joachim, C., et al., *Electronic Transparency of a Single C_{60} Molecule.* Physical Review Letters, 1995. 74(11): p. 2102-2105.

20. Liang, W.J., et al., *Fabry-Perot interference in a nanotube electron waveguide.* Nature, 2001. 411(6838): p. 665-669.

21. Beenakker, C.W.J., *Theory of Coulomb-Blockade Oscillations in the Conductance of a Quantum Dot.* Physical Review B, 1991. 44(4): p. 1646-1656.

22. Averin, D.V. and K.K. Likharev, *Coulomb Blockade of Single-Electron Tunneling, and Coherent Oscillations in Small Tunnel-Junctions.* Journal of Low Temperature Physics, 1986. 62(3-4): p. 345-373.

23. Grabert, H. and M.H. Devoret, *Single Charge Tunneling.* 1991: Plenum Press.

24. Kouwenhoven, L.P. and P.L. McEuen, in *Nano-Science and Technology*, G. Timp, Editor. 1997, AIP Press.

25. Meirav, U. and E.B. Foxman, *Single-electron phenomena in semiconductors.* Semiconductor Science and Technology, 1996. 11(3): p. 255-284.

26. Kouwenhoven, L.P., et al., *Electron transport in quantum dots*, in *Mesoscopic Electron Transport*, L.L. Sohn, L.P. Kouwenhoven, and G. Schoen, Editors. 1997, Plenum: New York and London. p. 105-214.

27. Fulton, T.A. and G.J. Dolan, *Observation of Single-Electron Charging Effects in Small Tunnel-Junctions.* Physical Review Letters, 1987. 59(1): p. 109-112.

28. Scottthomas, J.H.F., et al., *Conductance Oscillations Periodic in the Density of a One- Dimensional Electron-Gas.* Physical Review Letters, 1989. 62(5): p. 583-586.

29. Reed, M.A., et al., *Observation of Discrete Electronic States in a Zero-Dimensional Semiconductor Nanostructure.* Physical Review Letters, 1988. 60(6): p. 535-537.

30. Tans, S.J., et al., *Individual single-wall carbon nanotubes as quantum wires.* Nature, 1997. 386(6624): p. 474-477.

31. Bockrath, M., et al., *Single-electron transport in ropes of carbon nanotubes.* Science, 1997. 275(5308): p. 1922-1925.

32. Park, H., et al., *Nanomechanical oscillations in a single-C_{60} transistor.* Nature, 2000. 407(6800): p. 57-60.

33. Park, J., et al., *Coulomb blockade and the Kondo effect in single-atom transistors.* Nature, 2002. 417(6890): p. 722-725.

34. Liang, W.J., et al., *Kondo resonance in a single-molecule transistor.* Nature, 2002. 417(6890): p. 725-729.

35. Green, W.H., et al., *Electronic structures and geometries of C_{60} anions via density functional calculations.* Journal of Physical Chemistry, 1996. 100(36): p. 14892-14898.

36. Seifert, G., K. Vietze, and R. Schmidt, *Ionization energies of fullerenes - Size and charge dependence.* Journal of Physics B-Atomic Molecular and Optical Physics, 1996. 29(21): p. 5183-5192.

37. Anderson, P.A., *Work Function of Gold.* Physical Review, 1959. 115(3): p. 553-554.

38. Dresselhaus, M.S., G. Dresselhaus, and P.C. Eklund, *Science of Fullerenes and Carbon Nanotubes.* 1996, New York: Academic.

39. Dhirani, A., et al., *Self-assembled molecular rectifiers.* Journal of Chemical Physics, 1997. 106(12): p. 5249-5253.

40. Cui, X.D., et al., *Reproducible measurement of single-molecule conductivity.* Science, 2001. 294(5542): p. 571-574.

41. Bonet, E., M.M. Deshmukh, and D.C. Ralph, *Solving rate equations for electron tunneling via discrete quantum states.* Physical Review B, 2002. 6504(4): p. art. no.-045317.

42. Kouwenhoven, L.P., et al., *Excitation spectra of circular, few-electron quantum dots.* Science, 1997. 278(5344): p. 1788-1792.

43. Deshmukh, M.M., et al., *Magnetic anisotropy variations and nonequilibrium tunneling in a cobalt nanoparticle.* Physical Review Letters, 2001. 8722(22): p. art. no.-226801.

44. Pasquier, C., et al., *Quantum Limitation on Coulomb Blockade Observed in a 2d Electron-System.* Physical Review Letters, 1993. 70(1): p. 69-72.

45. Eiles, T.M., et al., *Thermal Enhancement of Cotunneling in Ultra-Small Tunnel- Junctions.* Physical Review Letters, 1992. 69(1): p. 148-151.

46. Geerligs, L.J., D.V. Averin, and J.E. Mooij, *Observation of Macroscopic Quantum Tunneling through the Coulomb Energy Barrier.* Physical Review Letters, 1990. 65(24): p. 3037-3040.

47. Rai-Choudhury, P., *Microlithography.* Handbook of Microlithography, Micromachining, and Microfabrication. Vol. 1. 1997: SPIE press, IEEE.

48. Smit, R.H.M., et al., *Measurement of the conductance of a hydrogen molecule.* Nature, 2002. 419(6910): p. 906-909.

49. Morpurgo, A.F., C.M. Marcus, and D.B. Robinson, *Controlled fabrication of metallic electrodes with atomic separation.* Applied Physics Letters, 1999. 74(14): p. 2084-2086.

50. Petta, J.R., D.G. Salinas, and D.C. Ralph, *Measurements of discrete electronic states in a gold nanoparticle using tunnel junctions formed from self-assembled monolayers.* Applied Physics Letters, 2000. 77(26): p. 4419-4421.

51. Zhitenev, N.B., H. Meng, and Z. Bao, *Conductance of small molecular junctions.* Physical Review Letters, 2002. 88(22): p. art. no.-226801.

52. Park, H., et al., *Fabrication of metallic electrodes with nanometer separation by electromigration.* Applied Physics Letters, 1999. 75(2): p. 301-303.

53. Durkan, C., M.A. Schneider, and M.E. Welland, *Analysis of failure mechanisms in electrically stressed Au nanowires.* Journal of Applied Physics, 1999. 86(3): p. 1280-1286.

54. Park, H., *Personal communication.*

55. Young, D. and A. Christou, *Failure-Mechanism Models for Electromigration.* Ieee Transactions on Reliability, 1994. 43(2): p. 186-192.

56. Black, J.R., *Electromigration Failure Modes in Aluminum Metallization for Semiconductor Devices.* Proceedings of the Ieee, 1969. 57(9): p. 1587-&.

57. Black, J.R., *Electromigration - a Brief Survey and Some Recent Results.* Ieee Transactions on Electron Devices, 1969. ED16(4): p. 338-&.

58. Lambert, M.F., et al., *Fabrication and characterization of sub-3 nm gaps for single-cluster and single-molecule experiments.* Nanotechnology, 2003. 14: p. 772-777.

59. Wolf, E.L., *Principles of Electron Tunneling Spectroscopy.* 1989, Oxford: Oxford Univ. Press.

60. Zhou, C., et al., *Microfabrication of a Mechanically Controllable Break Junction in Silicon.* Applied Physics Letters, 1995. 67(8): p. 1160-1162.

61. Bezryadin, A., C. Dekker, and G. Schmid, *Electrostatic trapping of single conducting nanoparticles between nanoelectrodes.* Applied Physics Letters, 1997. 71(9): p. 1273-1275.

62. Reed, M.A., et al., *Conductance of a molecular junction.* Science, 1997. 278(5336): p. 252-254.

63. Datta, S., et al., *Current-voltage characteristics of self-assembled monolayers by scanning tunneling microscopy.* Physical Review Letters, 1997. 79(13): p. 2530-2533.

64. Porath, D., et al., *Tunneling spectroscopy of isolated C_{60} molecules in the presence of charging effects.* Physical Review B, 1997. 56(15): p. 9829-9833.

65. Stipe, B.C., M.A. Rezaei, and W. Ho, *Single-molecule vibrational spectroscopy and microscopy.* Science, 1998. 280(5370): p. 1732-1735.

66. Banin, U., et al., *Identification of atomic-like electronic states in indium arsenide nanocrystal quantum dots.* Nature, 1999. 400(6744): p. 542-544.

67. Kim, S.H., et al., *Individual and collective electronic properties of Ag nanocrystals.* Journal of Physical Chemistry B, 1999. 103(47): p. 10341-10347.

68. Bockrath, M., et al., *Luttinger-liquid behaviour in carbon nanotubes.* Nature, 1999. 397(6720): p. 598-601.

69. Tans, S.J., A.R.M. Verschueren, and C. Dekker, *Room-temperature transistor based on a single carbon nanotube.* Nature, 1998. 393(6680): p. 49-52.

70. Gorelik, L.Y., et al., *Shuttle mechanism for charge transfer in Coulomb blockade nanostructures.* Physical Review Letters, 1998. 80(20): p. 4526-4529.

71. Schatz, G.C. and M.A. Ratner, *Quantum Mechanics in Chemistry.* 1993, Englewood Cliffs: Prentice Hall.

72. Heid, R., L. Pintschovius, and J.M. Godard, *Eigenvectors of internal vibrations of C_{60}: Theory and experiment.* Physical Review B, 1997. 56(10): p. 5925-5936.

73. Chavy, C., C. Joachim, and A. Altibelli, *Interpretation of Stm Images - C_{60} on the Gold(110) Surface.* Chemical Physics Letters, 1993. 214(6): p. 569-575.

74. Ruoff, R.S. and A.P. Hickman, *Vanderwaals Binding of Fullerenes to a Graphite Plane.* Journal of Physical Chemistry, 1993. 97(11): p. 2494-2496.

75. Braig, S. and K. Flensberg, *Vibrational sidebands and dissipative tunneling in molecular transistors.* cond-mat/0303236, 2003.

76. Jaklevic, R.C. and J. Lambe, *Molecular Vibration Spectra by Electron Tunneling.* Physical Review Letters, 1966. 17(22): p. 1139-&.

77. Lambe, J. and R.C. Jaklevic, *Molecular Vibration Spectra by Inelastic Electron Tunneling.* Physical Review, 1968. 165(3): p. 821-&.

78. Glazman, L.I. and R.I. Shekhter, *Inelastic Resonance Tunneling of Electrons through a Potential Barrier.* Zhurnal Eksperimentalnoi I Teoreticheskoi Fiziki, 1988. 94(1): p. 292-306.

79. Wingreen, N.S., K.W. Jacobsen, and J.W. Wilkins, *Inelastic-Scattering in Resonant Tunneling.* Physical Review B, 1989. 40(17): p. 11834-11850.

80. Boese, D. and H. Schoeller, *Influence of nanomechanical properties on single-electron tunneling: A vibrating single-electron transistor.* Europhysics Letters, 2001. 54(5): p. 668-674.

81. Pasupathy, A.N., et al., *Vibration-assisted electron tunneling in C_{140} single-molecule transistors.* to be published, 2003.

82. Lebedkin, S., et al., *Structure and properties of the fullerene dimer C_{140} produced by pressure treatment of C_{70}.* Journal of Physical Chemistry B, 2000. 104(17): p. 4101-4110.

83. Echegoyen, L. and L.E. Echegoyen, *Electrochemistry of fullerenes and their derivatives.* Accounts of Chemical Research, 1998. 31(9): p. 593-601.

84. Kergueris, C., et al., *Electron transport through a metal-molecule-metal junction.* Physical Review B, 1999. 59(19): p. 12505-12513.

85. Maskus, M. and H.D. Abruna, *Synthesis and characterization of redox-active metal complexes sequentially self-assembled onto gold electrodes via a new thiol-terpyridine ligand.* Langmuir, 1996. 12(18): p. 4455-4462.

86. Testaferri, L., et al., *Simple Syntheses of Aryl Alkyl Thioethers and of Aromatic Thiols from Unactivated Aryl Halides and Efficient Methods for Selective Dealkylation of Aryl Alkyl Ethers and Thioethers.* Synthesis-Stuttgart, 1983(9): p. 751-755.

87. Mathis, J.M. and A.J. Pallenberg, *Preparation of novel, functionalized 1,10-phenanthrolines.* Synthetic Communications, 1997. 27(17): p. 2943-2951.

88. Deshmukh, M.M., et al., *Equilibrium and nonequilibrium electron tunneling via discrete quantum states.* Physical Review B, 2002. 65(7): p. art. no.-073301.

89. Akera, H., *Coulomb staircase and total spin in quantum dots.* Physical Review B, 1999. 60(15): p. 10683-10686.

90. Oshio, H., et al., *Electronic relaxation phenomena following Co-57(EC)Fe-57 nuclear decay in Mn-II(terpy)(2) (ClO4)(2)center dot(1)/2H2O and in the spin crossover complexes Co-II(terpy)(2) X-2 center dot nH(2)O (X = Cl and ClO4): A Mossbauer emission spectroscopic study.* Inorganic Chemistry, 2001. 40(6): p. 1143-1150.

91. Goldhaber-Gordon, D., et al., *Kondo effect in a single-electron transistor.* Nature, 1998. 391(6663): p. 156-159.

92.   van der Wiel, W.G., et al., *The Kondo effect in the unitary limit.* Science, 2000. 289(5487): p. 2105-2108.

93.   Nygard, J., D.H. Cobden, and P.E. Lindelof, *Kondo physics in carbon nanotubes.* Nature, 2000. 408(6810): p. 342-346.

94.   Park, J.W. and P.L. McEuen, *Formation of a p-type quantum dot at the end of an n-type carbon nanotube.* Applied Physics Letters, 2001. 79(9): p. 1363-1365.

95.   Rosenblatt, S., et al., *High performance electrolyte gated carbon nanotube transistors.* Nano Letters, 2002. 2(8): p. 869-872.

96.   Iijima, S., *Helical Microtubules of Graphitic Carbon.* Nature, 1991. 354(6348): p. 56-58.

97.   Bethune, D.S., et al., *Cobalt-Catalyzed Growth of Carbon Nanotubes with Single-Atomic-Layerwalls.* Nature, 1993. 363(6430): p. 605-607.

98.   Iijima, S. and T. Ichihashi, *Single-Shell Carbon Nanotubes of 1nm Diameter.* Nature, 1993. 363(6430): p. 603-605.

99.   Kim, W., et al., *Synthesis of ultralong and high percentage of semiconducting single-walled carbon nanotubes.* Nano Letters, 2002. 2(7): p. 703-708.

100.   Wildoer, J.W.G., et al., *Electronic structure of atomically resolved carbon nanotubes.* Nature, 1998. 391(6662): p. 59-62.

101.   McEuen, P.L., et al., *Disorder, pseudospins, and backscattering in carbon nanotubes.* Physical Review Letters, 1999. 83(24): p. 5098-5101.

102.   Martel, R., et al., *Single- and multi-wall carbon nanotube field-effect transistors.* Applied Physics Letters, 1998. 73(17): p. 2447-2449.

103.   Zhou, C.W., J. Kong, and H.J. Dai, *Electrical measurements of individual semiconducting single-walled carbon nanotubes of various diameters.* Applied Physics Letters, 2000. 76(12): p. 1597-1599.

104.   Bachtold, A., et al., *Logic circuits with carbon nanotube transistors.* Science, 2001. 294(5545): p. 1317-1320.

105.   Javey, A., M. Shim, and H.J. Dai, *Electrical properties and devices of large-diameter single- walled carbon nanotubes.* Applied Physics Letters, 2002. 80(6): p. 1064-1066.

106.   Wind, S.J., et al., *Vertical scaling of carbon nanotube field-effect transistors using top gate electrodes.* Applied Physics Letters, 2002. 80(20): p. 3817-3819.

107.   Saito, R., et al., *Electronic-Structure of Chiral Graphene Tubules.* Applied Physics Letters, 1992. 60(18): p. 2204-2206.

108.   Hamada, N., S. Sawada, and A. Oshiyama, *New One-Dimensional Conductors - Graphitic Microtubules.* Physical Review Letters, 1992. 68(10): p. 1579-1581.

109.   Kong, J., et al., *Synthesis of individual single-walled carbon nanotubes on patterned silicon wafers.* Nature, 1998. 395(6705): p. 878-881.

110.   Lee, R.S., et al., *Transport properties of a potassium-doped single-wall carbon nanotube rope.* Physical Review B, 2000. 61(7): p. 4526-4529.

111. Bockrath, M., et al., *Chemical doping of individual semiconducting carbon-nanotube ropes.* Physical Review B, 2000. 61(16): p. 10606-10608.

112. Kong, J., et al., *Alkaline metal-doped n-type semiconducting nanotubes as quantum dots.* Applied Physics Letters, 2000. 77(24): p. 3977-3979.

113. Zhou, C.W., et al., *Modulated chemical doping of individual carbon nanotubes.* Science, 2000. 290(5496): p. 1552-1555.

114. Dignam, M.M., et al., *One-Dimensional Quantum-Wire States Probed by Resonant Electron-Tunneling.* Physical Review B, 1994. 49(3): p. 2269-2272.

115. Ruzin, I.M., et al., *Stochastic Coulomb Blockade in a Double-Dot System.* Physical Review B, 1992. 45(23): p. 13469-13478.

116. Chandrasekhar, V., Z. Ovadyahu, and R.A. Webb, *Single-Electron Charging Effects in Insulating Wires.* Physical Review Letters, 1991. 67(20): p. 2862-2865.

117. Ando, T., A.B. Fowler, and F. Stern, *Electronic-Properties of Two-Dimensional Systems.* Reviews of Modern Physics, 1982. 54(2): p. 437-672.

118. Kong, J., et al., *Nanotube molecular wires as chemical sensors.* Science, 2000. 287(5453): p. 622-625.

119. Cui, Y., et al., *Nanowire nanosensors for highly sensitive and selective detection of biological and chemical species.* Science, 2001. 293(5533): p. 1289-1292.

120. Kruger, M., et al., *Electrochemical carbon nanotube field-effect transistor.* Applied Physics Letters, 2001. 78(9): p. 1291-1293.

121. Cobden, D.H., et al., *Spin splitting and even-odd effects in carbon nanotubes.* Physical Review Letters, 1998. 81(3): p. 681-684.

122. Deshmukh, M.M., et al., *Fabrication of asymmetric electrode pairs with nanometer separation made of two distinct metals.* Nano Letters, 2003. 3(10): p. 1383-1385.